

UNIVERSITY OF CALIFORNIA

Los Angeles

**The Universe as Viewed from Star Forming
Galaxies over the Past Ten Billion Years**

A dissertation submitted in partial satisfaction
of the requirements for the degree
Doctor of Philosophy in Astronomy

by

Chun Ly

2010

© Copyright by
Chun Ly
2010

The dissertation of Chun Ly is approved.

An Yin

Alice E. Shapley

Edward L. Wright

James E. Larkin

Matthew A. Malkan, Committee Chair

University of California, Los Angeles

2010

*To my Mom for giving me everything, and
to Mark Ratkovic, my high school teacher, good friend,
and my first astronomy mentor.*

TABLE OF CONTENTS

1	Introduction	1
1.1	SFR Measurements and Outstanding Problems	3
1.1.1	Calibrating SFR Indicators at High Redshifts	3
1.2	A Census of Star Formation at $z = 1 - 3$	5
1.2.1	Broad-band Photometric Selection	6
1.2.2	A Photometric Redshift Approach	6
1.3	Adopted Conventions	7
2	The Subaru Deep Field Narrow-band Survey: Measurements at Redshifts of 0.07 to 1.47	9
2.1	Observations	12
2.1.1	Optical Imaging	12
2.1.2	Spectral Identification of NB Emitters	13
2.1.3	Previous Subaru/FOCAS Spectroscopy	15
2.1.4	DEIMOS Spectroscopy of NB816 and NB921 Emitters	21
2.1.5	NB Excess Predictions from Sloan Digital Sky Survey	25
2.2	Results	25
2.2.1	Broad-band Color Selection	26
2.2.2	Averaged Spectral Energy Distributions	34
2.2.3	The Luminosity Function	35
2.2.4	Completeness of the Luminosity Functions	40

2.2.5	Correcting for Dust Extinction	44
2.2.6	The Star Formation Rate Density	45
2.3	Comparison with Other Studies	50
2.3.1	H α Emitters	50
2.3.2	[O III] and [O II] Emitters	53
2.4	Discussion	53
2.4.1	Differences between NB704 and NB711 LFs	53
2.4.2	Evolution of the LF and SFR Densities	54
2.4.3	Future Work	55
2.5	Conclusion	56
3	Hα Star Formation Rates at $z \approx 0.8$ from the NewHα Survey .	60
3.1	The NewH α Survey	62
3.1.1	Near-IR Narrow-band Observations and Data Reduction .	62
3.1.2	Identification of Emission-Line Galaxy Candidates	64
3.1.3	IMACS Spectroscopy	68
3.1.4	Public Ancillary Data	70
3.2	Selection of H α Emitters and Line Measurements	70
3.2.1	Selection of H α Emitters	70
3.2.2	Comparison of Photometric Selection with Spectroscopic Redshifts	72
3.2.3	Deriving Emission-Line Flux and Luminosity Measurements	74
3.3	Completeness of the Survey	80

3.3.1	Monte Carlo Simulations	80
3.3.2	Effective Volume	83
3.4	Results	84
3.4.1	Luminosity Function and Star Formation Rate Densities	84
3.5	Comparisons with Other Near-Infrared H α Studies	92
3.6	Discussion	96
3.7	Future Work	98
3.8	Conclusions	101
4	Lyman Break Galaxies at $z \approx 1.8 - 2.8$	104
4.1	Observations	106
4.1.1	<i>GALEX/NUV</i> Imaging of the SDF	106
4.1.2	Follow-up Spectroscopy	107
4.1.3	Spectroscopic Identification of Sources	114
4.1.4	Additional Spectra with Subaru/MOIRCS	121
4.1.5	Summary of Observations	125
4.2	Photometric Selection of <i>NUV</i> -dropouts	125
4.2.1	Revised <i>NUV</i> Photometric Catalogs	126
4.2.2	Broad-band Color Selection	127
4.3	Contamination and Completeness Estimates	128
4.3.1	Removal of Foreground Stars	128
4.3.2	Contamination from $z < 1.5$ Interlopers	133
4.3.3	Modelling Completeness and Effective Volume	136

4.3.4	Summary of Survey Completeness and Contamination	137
4.4	Results	141
4.4.1	The 1700Å UV Luminosity Function	141
4.4.2	The Luminosity and Star-Formation Rate Densities	142
4.4.3	Summary of Results	145
4.5	Comparisons with other Studies	145
4.5.1	UV-selected Studies at $z \sim 2 - 3$	149
4.5.2	Evolution in the UV Luminosity Function and Density	151
4.6	Discussion	154
4.7	Conclusions	157
5	A Census of Star-Forming Galaxies at $z = 1 - 3$	160
5.1	Subaru Deep Field Multi-Wavelength Observations	161
5.1.1	Subaru/Suprime-Cam Data	162
5.1.2	UKIRT/WFCAM Data	164
5.1.3	Mayall/MOSAIC Data	164
5.1.4	<i>GALEX/NUV</i> and <i>FUV</i> Data	165
5.1.5	Mayall/NEWFIRM Data	166
5.2	Synthesizing Multi-band Data	166
5.2.1	The Identification of Stars	171
5.3	Photometric Redshifts and SED Modelling	173
5.3.1	Photometric Redshifts	173
5.3.2	SED Modelling	181

5.4	Photometric Techniques to Identify $z = 1 - 3$ Galaxies	182
5.4.1	The BX and BM Selection	182
5.4.2	The BzK Selection	189
5.4.3	The LBG Selection	193
5.4.4	Summary	198
5.5	Results	199
5.5.1	The Physical Properties of $z = 1 - 3$ Galaxies	199
5.5.2	A Direct Comparison of Photometric Selection Techniques	202
5.5.3	The Star-Formation Rate Density from the Census	216
5.5.4	The Completeness of Photometric Selection Techniques . .	218
5.6	Discussion	219
5.7	Future Work	221
5.8	Conclusions	223
6	The State of Star Formation Rate Estimates and Conclusions	227
6.1	SFR Estimates from Cosmological Simulations	227
6.2	A Comparison between Theory and Observation	228
6.3	Potential Problems with Observations	230
6.3.1	Cosmic Variance	230
6.3.2	Dust Attenuation	232
6.3.3	The Faint-end Slope	233
6.3.4	Using [O II] and [O III] as SFR Indicators	234
6.4	Potential Problems with Numerical Simulations	234

6.4.1	Resolution	234
6.4.2	Pitfalls of Semi-Analytical Models	235
6.5	Star Formation at Higher Redshifts	235
A	Chapter 4: Individual Sources of Special Interest	237
B	Chapter 5	242
B.1	Unique Sources from Photometric Selection	242
B.2	Additional Tables	243

LIST OF FIGURES

2.1	NB704, NB711, NB816, and NB921 excess plots	14
2.2	Spectra of NB921 emitters from FOCAS	16
2.3	DEIMOS spectra of identified line-emitting galaxies	22
2.4	Spectra of the twenty fortuitous sources	24
2.5	Two-color diagrams of NB704 and NB711 emitters	29
2.6	Two-color diagrams for NB816 emitters	30
2.7	Two-color diagrams for NB921 emitters	31
2.8	Spectral energy distributions for NB emitters	34
2.9	Comparison between spectroscopic and photometric line fluxes . .	37
2.10	The luminosity function for H α emitters at $z < 0.4$	39
2.11	The luminosity function for [O III] emitters	41
2.12	The luminosity function for [O II] emitters	42
2.13	[O III]-H α flux ratio for NB704+921 emitters	48
2.14	Evolution of Schechter LF parameters and SFR density	49
2.15	Optical colors for Hawaii HDF-N galaxies	52
3.1	Identification of NB1187 excess emitters	67
3.2	Color selection of SXDS H α emitters	73
3.3	Color selection of COSMOS H α emitters	74
3.4	H α equivalent widths and emission-line fluxes	75
3.5	Correction for [N II] contamination	78
3.6	NewH α survey's completeness	82

3.7	Effective surveyed volume	84
3.8	The observed H α luminosity function	85
3.9	The extinction-corrected H α luminosity function at $z \sim 0.81$	86
3.10	Field-to-Field Variations in the NewH α survey	87
3.11	Confidence contours for the Schechter fit	90
3.12	The selection of NB excess emitters by Sobral et al. (2009)	93
3.13	The SFR density from H α surveys	97
3.14	Redshift evolution in Schechter parameters	99
4.1	Postage stamps for some <i>NUV</i> -dropouts	108
4.2	Examples of cross-correlation power spectra	117
4.3	LRIS spectra of confirmed <i>NUV</i> -dropouts from the ver. 1 catalog with known redshifts	119
4.4	Same as Figure 4.3, but some spectra do not have Ly α emission .	120
4.5	Same as Figures 4.3 and 4.4	121
4.6	Same as Figures 4.3 and 4.4	122
4.7	Same as Figure 4.6	123
4.8	Same as Figures 4.6 and 4.7	124
4.9	<i>NUV</i> – <i>B</i> and <i>B</i> – <i>V</i> colors for $22.0 < V_{\text{auto}} < 25.3$ sources . . .	129
4.10	Two color-color diagrams for rank 10 point-like objects	131
4.11	Photometric properties of rank 10 point-like objects	133
4.12	Narrow-band emitters that meet the <i>NUV</i> -dropout criteria	135
4.13	Modelled <i>NUV</i> – <i>B</i> and <i>B</i> – <i>V</i> colors for <i>NUV</i> -dropouts	139

4.14	Monte Carlo completeness estimates	140
4.15	The <i>observed</i> V -band luminosity function for NUV -dropouts	143
4.16	Confidence contours of Schechter fits	144
4.17	Comparisons of the LBG LF with other LFs	150
4.18	Compiled Schechter parameters of LBG and BX studies versus redshift	152
4.19	UV specific luminosity densities as a function of redshift	153
4.20	Surface densities and redshift distributions for $z \sim 2$ BXs and LBGs	156
5.1	Multi-wavelength SDF coverage	163
5.2	Point spread function for SDF data	167
5.3	Comparison between single- and multi-image source extraction . .	170
5.4	The selection of stars using the Δ method	172
5.5	Comparison of photometric and spectroscopic redshifts	175
5.6	Photometric redshift uncertainties	176
5.7	Accuracy of photometric redshifts without K data	177
5.8	SDF photometric redshift distribution	178
5.9	Broad-band colors for the photometric samples	180
5.10	Comparison of the $U_nG\mathcal{R}$ and $UBVR_{\text{C}}i'$ systems	184
5.11	BX transformation for $U_nG\mathcal{R}$ to $UBV - R_{\text{C}}i'$	185
5.12	Similar to Figure 5.11	186
5.13	Selection of BX and BM galaxies	188
5.14	Redshift distribution for BXs, BMs, and $z \sim 3$ LBGs	189

5.15	Surface density of BX and U -dropouts	190
5.16	Selection of BzK galaxies	191
5.17	Photometric redshift for BzK galaxies	192
5.18	Magnitudes for a subset of BzK galaxies	192
5.19	Selection of U -dropout galaxies	195
5.20	Selection of NUV -dropouts and photometric redshifts	197
5.21	Selection of FUV -dropouts	198
5.22	Photometric selection completeness	201
5.23	Physical properties of $z = 1 - 3$ galaxies	203
5.24	Venn diagram of galaxy population overlap	206
5.25	Same as Figure 5.24	207
5.26	Sample overlap: $B - z'$ and $z' - K$ colors	210
5.27	Overlap fraction between sBzK and UV-selected galaxies	211
5.28	Sample overlap: $U - BV$ and $BV - R_{\mathrm{C}}i'$ colors	213
5.29	Sample overlap: $NUV - B$ and $B - V$ colors	215
5.30	SFR density from the census sample	217
5.31	Photo- z distribution for photometrically selected galaxies	220
6.1	The cosmic star formation history	231
A.1	Optical images for 179350	238
A.2	Spectra for 62056 and 72012	239
A.3	The B -band image cropped to $20''$ on a side and centered on 62056	239
A.4	Postage stamp images ($10''$ on a side) for 72012	241

LIST OF TABLES

2.1	Photometric Properties of Spectroscopically Confirmed Narrow-Band Line-Emitting Galaxies	17
2.1	Photometric Properties of Spectroscopically Confirmed Narrow-Band Line-Emitting Galaxies	18
2.2	Continuation of Table 2.1	19
2.2	Continuation of Table 2.1	20
2.3	Summary of All 75 Spectra.	23
2.4	Redshift Ranges, Comoving Volumes, and Luminosity Distances .	26
2.5	Schechter Fits and Inferred SFR Densities	57
2.6	Continuation of Table 2.5	57
2.7	Compilation of Emission-line Observed SFR Density Measurements	58
2.8	Compilation of Emission-line Extinction-Corrected SFR Density Measurements	59
3.1	Summary of NEWFIRM Imaging	65
3.2	Summary of Photometric and Spectroscopic Samples	68
3.3	Properties for Some H α Emitters	76
3.4	H α Luminosity Function at $z \sim 0.81$	89
3.5	Compilation of H α SFR densities	100
4.1	Properties of Spectroscopically Targeted <i>NUV</i> -dropouts and BzKs	109
4.1	Properties of Spectroscopically Targeted <i>NUV</i> -dropouts and BzKs	110
4.2	Continuation of Table 4.1	111

4.2	Continuation of Table 4.1	112
4.3	Summary of Spectroscopic Observations	126
4.4	LBG Effective Volume Estimates	138
4.5	Compilation of UV Luminosity Functions	147
4.6	Compilation of UV Luminosity Densities	148
5.1	Summary of SDF Multi-Wavelength Data	162
5.2	Summary of Photometric Redshift Uncertainties	179
5.3	Summary of Photometric Selection Samples	183
5.4	Summary of Photometric Selection Census Surveys	204
B.1	Summary of Wave-band Detection for the 5BK3 σ Sample	244
B.2	Summary of Photometric Technique Overlap: Shallow Sample	245
B.3	Summary of Photometric Technique Overlap: Faint Sample	245

ACKNOWLEDGMENTS

Over the past ten years, I have had the fortunate opportunity to develop into a professional astronomer, and this would not be possible without the positive influences of past instructors, advisors, and mentors at the undergraduate and graduate level. First and foremost, I am indebted to my Ph.D advisor, Matthew A. Malkan. He has shared his experiences and knowledge and have been patient throughout my graduate career. I would also like to acknowledge Janice C. Lee, Nobunari Kashikawa, Kazuhiro Shimasaku, and Leonidas Moustakas. They have collaborated closely with me on different aspects for my dissertation and greatly extended the breath of my research.

Prior to coming to UCLA, I had many research opportunities that spanned a broad range of topics. My past advisors include Dr. Robert Craig Walker, Prof. Michael S. Brotherton, Dr. David S. DeYoung, and Prof. Jill Bechtold. They taught me everything from the synthesis of radio data to the physics of jets to writing peer-refereed papers.

I would also like to thank the (1) UCLA's Physics and Astronomy Department, (2) Astronomy Department at the University of Arizona, (3) Carnegie Observatories, (4) NASA's Jet Propulsion Laboratory in Pasadena, California, and (5) the National Optical Astronomy Observatory. These institutions have provided excellent academic experiences and/or resources to complete my dissertation.

This dissertation would not be possible without financial support from a Eugene V. Cota-Robles Fellowship, and NASA grant NNX08AW14H through their Graduate Student Researcher Program.

Access to several astronomical facilities (Subaru telescope, Keck Observatory,

Kitt Peak National Observatory) was required to complete my dissertation, and these facilities would not be possible without dedicated staff scientists and engineers. The Keck Observatory was made possible by the generous financial support of the W.M. Keck Foundation. I wish to recognize and acknowledge the very significant cultural role and reverence that the summit of Mauna Kea has always had within the indigenous Hawaiian community. We are most fortunate to have the opportunity to conduct observations from this mountain. We gratefully acknowledge NASA's support for construction, operation, and science analysis for the *GALEX* mission. We thank the Hectospec instrument and queue-mode scientists and the MMT operators for their excellent assistance with the observations. Public Access MMT time is available through an agreement with the National Science Foundation.

VITA

1982	Born, Galang, Jakarta, Indonesia.
2001	Inducted, Phi Eta Sigma National Honor Society University of Arizona Tucson, Arizona
2003	Galileo Circle Scholar University of Arizona Tucson, Arizona
2004	B.S. (Astronomy) and B.S. (Physics) University of Arizona Tucson, Arizona
2003-2004	NASA Arizona Space Grant Researcher
2004	Eugene V. Cota-Robles Fellowship Department of Physics and Astronomy University of California, Los Angeles
2004-2005	Teaching Assistant Department of Physics and Astronomy University of California, Los Angeles
2005	Departmental Outstanding Teaching Assistant Award Department of Physics and Astronomy University of California, Los Angeles

2006	M.S. (Astronomy) University of California, Los Angeles
2005-2008	Graduate Student Researcher Department of Physics and Astronomy University of California, Los Angeles
2008	Summer Graduate Student Researcher The Observatories, Carnegie Institute of Washington Pasadena, California
2008-2010	NASA Graduate Student Researchers Program Fellowship
2009	American Astronomical Society Chambliss Astronomy Achievement Student Award
2010	Giacconi Postdoctoral Fellowship Space Telescope Science Institute Baltimore, Maryland

PUBLICATIONS

Doherty, M., Tanaka, M., DeBreuck, C., Ly, C., Kodama, T., Kurk, J., Seymour, N., Stern, D., Vernet, J., Kajisawa, M., Tanaka, I., Venemans, B., “Optical and near-IR spectroscopy of candidate red galaxies in two $z \sim 2.5$ proto-clusters”, 2010, *Astronomy & Astrophysics*, 509, 83

Acciari, V. A., et al.; “Radio Imaging of the Very-High-Energy γ -Ray Emission Region in the Central Engine of a Radio Galaxy”, 2009, Science, 325, 444

Ly, C., Malkan, M. A., Woo, J.-H., Treu, T., Kashikawa, N., Shimasaku, K., Yoshida, M., “Lyman Break Galaxies at $z \approx 1.8 - 2.8$: GALEX/NUV Imaging of the Subaru Deep Field”, 2009, The Astrophysical Journal, 697, 1410

Hatsukade, B., Iono, D., Motohara, K., Nakanishi, K., Hayashi, M., Shimasaku, K., Nagao, T., Tamura, Y., Malkan, M. A., Ly, C., Kohno, K., “A Search for Molecular Gas toward a BzK-selected Star-forming Galaxy at $z = 2.044$ ”, 2008, Publications of the Astronomical Society of Japan, 61, 487

Hayashi, M., Motohara, K., Shimasaku, K., Onodera, M., Uchimoto, Y. K., Kashikawa, N., Yoshida, M., Okamura, S., Ly, C., Malkan, M. A., “Star Formation Rates and Metallicities of K-selected Star Forming Galaxies at $z \sim 2$ ”, 2008, The Astrophysical Journal, 691, 140

Nagao, T., Sasaki, S. S., Maiolino, R., Grady, C., Kashikawa, N., Ly, C., Malkan, M. A., Motohara, K., Murayama, T., Schaerer, D., Shioya, Y., Taniguchi, T., “A Photometric Survey for Ly-[He ii] Dual Emitters: Searching for Population III Stars in High-redshift Galaxies”, 2008, The Astrophysical Journal, 680, 100

Nagao, T., Murayama, T., Maiolino, R., Marconi, A., Kashikawa, N., Ajiki, M., Hattori, T., Ly, C., Malkan, M., Motohara, K., Ohta, K., Sasaki, S., Shioya, Y., Taniguchi, Y., “High-redshift Ly α emitters with a large equivalent width: Properties of i-dropout galaxies with an NB921-band depression in the Subaru

Deep Field”, 2007, *Astronomy & Astrophysics*, 468, 877

Ly, C., Walker, R. C., Junor, W., “High Frequency VLBA/VLBI Imaging of M87”, 2007, *The Astrophysical Journal*, 660, 200-205

Ly, C., Malkan, M., Kashikawa, N., Shimasaku, K., Doi, M., Nagao, T., Iye, M., Kodama, T., Morokuma, T., Motohara, K., “The Luminosity Function and Star Formation Rate Between Redshifts of 0.07 and 1.47 for Narrow-band Emitters in the Subaru Deep Field”, 2007, *The Astrophysical Journal*, 657, 738-759

Kashikawa, N., Shimasaku, K., Malkan, M. A., Doi, M., Matsuda, Y., Ouchi, M., Taniguchi, Y., Ly, C., Nagao, T., Iye, M., Motohara, K., Murayama, T., Murozono, K., Narai, K., Ohta, K., Okamura, S., Sasaki, T., Shioya, Y., Umemura, M., “The End of the Reionization Epoch Probed by Lyman-Alpha Emitters at $z = 6.5$ in the Subaru Deep Field”, 2006, *The Astrophysical Journal*, 648, 7

Shimasaku, K., Kashikawa, N., Doi, M., Ly, C., Malkan, M. A., Matsuda, Y., Ouchi, M., Hayashino, T., Iye, M., Motohara, K., Murayama, T., Nagao, T., Ohta, K., Okamura, S., Sasaki, T., Shioya, Y., Taniguchi, Y., “Ly α Emitters at $z = 5.7$ in the Subaru Deep Field”, 2006, *Publications of the Astronomical Society of Japan*, 58, 313

Ly, C., De Young, D. S., Bechtold, J., “The Discovery of Extended Thermal X-Ray Emission from PKS 2152-699: Evidence for a “Jet-Cloud” Interaction”, 2005, *The Astrophysical Journal*, 618, 609

Ly, C., Walker, R. C., Wrobel, J. M., “An Attempt to Probe the Radio Jet Collimation Regions in NGC 4278, NGC 4374 (M84), and NGC 6166”, 2004, The Astronomical Journal, 127, 119

Brotherton, M. S., Ly, C., Wills, B. J., Laurent-Muehleisen, S. A., van Breugel, W., Antonucci, R. R. J., “Multiband VLA Observations of the Faint Radio Core of 3CR 68.1”, 2002, The Astronomical Journal, 124, 1943

ABSTRACT OF THE DISSERTATION

**The Universe as Viewed from Star Forming
Galaxies over the Past Ten Billion Years**

by

Chun Ly

Doctor of Philosophy in Astronomy

University of California, Los Angeles, 2010

Professor Matthew A. Malkan, Chair

Star formation rate (SFR) measurements are one of the best observational tools for gaining insights on the structure evolution of the baryonic component in the universe. It is inherently linked to the mass assembly history of galaxies, the chemical enrichment of the interstellar medium, and energetic outflows from the death of massive stars (i.e., supernova).

SFRs can be estimated from observations that directly trace the recent formation of massive OB stars. These SFR indicators include H α λ 6563, forbidden optical nebular emission lines (e.g., [O II] λ 3727 and [O III] λ 5007), and the rest-frame ultra-violet (UV) continuum (1700–2500Å).

In this dissertation, the SFR density is determined over the past ten billion years using several different techniques that are sensitive towards identifying star-forming galaxies. These techniques are: narrow-band (NB) imaging, high- z broad-band photometric selection, and the selection of $z = 1 - 3$ galaxies with photometric redshift.

The NB method efficiently tunes towards nebular emission lines that are seen in star-forming galaxies by having the emission line redshifted into the NB filter.

SFR density measurements are derived using H α at four redshift intervals from $z = 0.07$ to $z = 0.81$. This required two complementary NB surveys targeting optical and near-infrared wavelengths. Constraints on the SFR density are also obtained between $z = 0.40$ and $z = 0.84$ with [O III], and between $z = 0.89$ and $z = 1.47$ with [O II]. Over 6000 line-emitting galaxies are identified at eleven different redshifts, and the combination of these measurements begins to show that the SFR density evolves rapidly over approximately eight billion years with a decline of about one order of magnitude from $z \sim 1.5$ to $z \sim 0.1$. The H α luminosity functions at $z \sim 0.1$, $z \sim 0.4$ and $z \sim 0.8$ are compared, and it appears that the decline in the SFR density is due to an evolution of the characteristic H α luminosity associated with the “knee” of the luminosity function. This indicates that the “typical” star-forming galaxies at $z \sim 0.8$ is producing stars at a rate that is approximately six times higher than in the typical star-forming galaxies in the local universe.

UV SFR measurements are then discussed for a large population of star-forming galaxies (hereafter Lyman break galaxies; LBGs) at $z \sim 2$ selected with a widely used method called the “Lyman break” technique. This sample is unique since it is the first of many surveys to extend such a technique into an unprobed era. This rest-frame UV study also shows a higher SFR density for when the universe was about three billion years old, consistent with the NB SFR density estimates.

To extend the sample of $z = 1 - 3$ galaxies, these LBGs are combined with galaxies identified by other photometric selection techniques. The different techniques are further investigated to understand how they dissect the multi-dimensional space of galaxies’ measured properties to determine selection biases of the techniques. A census of the photometric selection techniques is constructed

and a SFR density is derived for star-forming galaxies at $z = 1.5 - 2.6$. This census illustrates that these techniques are complementary, and that a significant fraction of galaxies at high- z are dusty. These dusty galaxies contribute to approximately half of the SFR density.

Finally, these SFR density measurements are combined and used to compare with predictions from numerical simulations. This comparison indicates that models cannot completely produce the evolution of the SFR density should the observational measurements be reliable. In particular, the factor of ten decline seen for $z \lesssim 1$ is not fully reproduced. A discussion of systematic issues that must be addressed in future studies (both observational and theoretical) is included, and future measurements at redshifts above $z = 3$ are discussed.

CHAPTER 1

Introduction

In the current paradigm for galaxy formation, it is believed that galaxy assembly is driven by “dark matter.” The growth of dark matter halos through gravitational instabilities provides seeds for which baryonic matter can collect to form galaxies. With this model, the latest N-body simulations (e.g., [Springel et al., 2005](#); [Boylan-Kolchin et al., 2009](#)), which begin with initial cosmological constraints (the most accurate and recent Λ CDM parameters are available in [Komatsu et al., 2010](#)), have predicted the dark matter power spectrum, the dark matter assembly rate, and the merger rate and their evolution over time. While these predictions are insightful, acquiring observational data to validate and improve upon the hierarchical model is difficult as dark matter are dissipationless. Furthermore, while dark matter is believed to be responsible for initiating the formation of galaxies, the observed properties of galaxies is tied to the baryonic component, which behaves differently compared to dark matter. As a result, there is a disconnect between the observed and simulated universe.

There are two solutions that have been developed to mitigate this problem. First, some theorists have taken a “semi-analytical approach” (for a review, see [Baugh, 2006](#)) where they artificially occupy the dark matter halos with galaxies. Included with this approach is the use of the latest prescriptions and sets of equations to account for many of the physical phenomena seen in galaxies (e.g., cooling, heating, feedback, and stellar population) to predict properties such as

colors, stellar masses, and star formation history. A major disadvantage of this method is the reliance on some observations to limit the degrees of freedom in their models. Some notable semi-analytical studies include Cole et al. (2000), Croton et al. (2006), and Somerville et al. (2008).

The second method involves hydrodynamical modelling of the gaseous component within dark matter halos (see e.g., Kereš et al., 2005; Nagamine et al., 2006; Dekel et al., 2009; Choi & Nagamine, 2009). This method also accounts for radiative transfer effects for the gas to dissipate energy, and is often considered more realistic since the gas is treated hydrodynamically. However, the complexity of the baryonic physics limits these hydrodynamical simulations to smaller cosmic volumes (by a factor of \sim 100 compared to N-body simulations). Nevertheless, these two methods should be seen as complementary.

On the observational side, one direct method for understanding galaxy evolution is through measurements of the star formation rates (SFRs). Since the timescale for massive¹ star formation is short (\lesssim 100 Myr), these measurements provide an indication of the instantaneous growth rate of galaxies. And by tracing the SFR density evolution, vital information about the structure evolution of the baryonic component in the universe can be obtained. This is through comparisons with predictions from either semi-analytical galaxy formation models and/or smooth particle hydrodynamic (SPH) simulations, as discussed previously.

The emphasis of my dissertation is focused on observational constraints on the cosmic star formation history, addressing some important and outstanding issues regarding such measurements, and comparing these measurements with theoretical predictions. The three techniques that I will use to (1) identify star-forming galaxies, (2) arrive at SFR density measurements, and (3) address the

¹The techniques developed to study star formation are currently sensitive to the high-mass stellar end.

following concerns are: narrow-band imaging, high- z broad-band photometric selection, and the selection of $z = 1 - 3$ galaxies with photometric redshift.

1.1 SFR Measurements and Outstanding Problems

While surveys of star-forming galaxies have existed for almost two decades, there are a couple issues that warrant attention so that SFR studies can be utilized as a better probe of galaxy evolution.

1.1.1 Calibrating SFR Indicators at High Redshifts

First, different SFR indicators have been developed such that observations can attain estimates of the SFR. The most common measurements are those of nebular emission lines (e.g., H α λ 6563, [O II] λ 3727, and [O III] λ 5007), the non-ionizing ultra-violet (UV) continuum between 1500Å and 2000Å, and the re-radiated dust emission in the far-infrared (10–100 μ m). A review detailing these and other methods can be found in [Kennicutt \(1998\)](#). However, since observational capabilities are greatest at optical wavelengths, any one of these SFR indicators has a limited redshift (z) coverage. For example, H α , [O III], and [O II] can only be used out to $z \approx 0.5$, $z \approx 0.9$, and $z \approx 1.5$, respectively. Likewise, the UV continuum enters the optical window between $z \approx 2$ and $z \approx 5$. This observational limitation proves problematic since the different SFR indicators suffer from systematic problems due to their dependence on stellar mass and metallicity, and are affected to different degrees by dust extinction (e.g., shorter wavelengths suffer from more dust obscuration).

These issues may explain the observed scatter of a factor of 2 seen in studies (e.g., [Hopkins, 2004](#)) that compile SFR measurements from many past work. As

it will be revealed later, this scatter is comparable to differences seen between theoretical models that attempt to predict the cosmic star formation history. Needless to say, these issues must be understood and first-order corrections must be developed to place tighter observational constraints.

A straight-forward solution that begins to tackle this problem is to span the largest redshift range possible with a single reliable SFR indicator. This indicator could then be used to “calibrate” other SFR indicators and remove any correlation that is seen with mass and metallicity. The latter would require that a large representative sample of galaxies have SFR estimates from different SFR diagnostics. H α has been considered one of the most reliable SFR indicators, since it is directly related to the number of ionizing photons produced from massive OB stars and suffers less dust attenuation by being redward of the UV continuum and oxygen emission lines.

H α will be used throughout Chapters 2 and 3. These chapters use the narrow-band (NB) technique to identify star-forming galaxies by tuning towards prominent nebular emission lines. The two greatest strengths of this technique are the ability to determine reliable redshifts at $\Delta z \lesssim 0.01$ (this is because the filters are typically 100–200Å) and to obtain calibrated emission line flux measurements. These are critical requirements for accurate SFR measurements. While deep multi-slit spectroscopic surveys also meet these requirements, the NB approach is 10 times more efficient since it operates in imaging mode.

In Chapter 2, I will discuss a multi-NB imaging survey at optical wavelengths that I led. This survey identifies galaxies between $z = 0.07$ and $z = 1.47$ when H α , [O III], and/or [O II] are redshifted into the filter bandpasses. This work used the deepest optical narrow-band data (to date) and probed approximately 8 Gyrs of look-back time. It has been entirely published in the *Astrophysical*

Journal (Ly et al., 2007). Chapter 3 will discuss another NB survey, but at near-infrared (NIR) wavelengths, providing H α SFR measurements at $z \approx 0.8$. When merged with the three H α measurements at $z \lesssim 0.4$ from Chapter 2, it yields constraints of the H α SFR density evolution over the latter half of the age of the universe. This has only been recently available (after circa 2007) due to accessibility to large NIR detectors.

I will discuss the ability to calibrate [O III] at $z \approx 0.4$ with simultaneous H α and [O III] measurements. Such calibration is crucial as [O III] measurements are affected by the evolution of the gas metallicity such that higher redshift measurements probe lower metallicity systems. In particular, the observed [O III]/H α ratio is expected to be higher, and we will show this in Chapter 2.

1.2 A Census of Star Formation at $z = 1 - 3$

Aside from the reliability of SFR indicators, there is a need for observations to attain a complete sample of star-forming galaxies. Ideally such census would span a large cosmic time, but that is unfeasible with current surveys. Instead, deriving a census at a particular epoch would be sufficient and would initiate future work to extend towards lower and higher redshifts. The era of greatest interest is arguably $z = 1 - 3$ where it appears that the average SFR density is highest (see e.g., Madau et al., 1998; Reddy et al., 2008; Ly et al., 2009), and is the epoch where typical galaxies at these redshifts appear most active and are assembling rapidly. Selection of galaxies at $z = 1 - 3$ through broad-band colors and photometric redshifts are discussed in Chapters 4 and 5.

1.2.1 Broad-band Photometric Selection

One method for selecting star-forming galaxies is through photometric selection. For example, star-forming galaxies have blue UV continuum, so a rest-frame UV selection, such as the Lyman break technique (Steidel et al., 1996) is capable of identifying galaxies at $z \sim 3$ with optical imaging. Likewise, other UV selection methods, such as the BX/BM method (Adelberger et al., 2004), can probe $z \sim 2$. However, there are some concerns with the UV selection techniques as they are more prone towards less dusty galaxies Reddy et al. (2005); Quadri et al. (2007). This raises the question that perhaps not all of the star formation has been counted. One solution is to use NIR photometric techniques, such as the BzK method (Daddi et al., 2004). This is able to identify massive dusty star-forming galaxies.

The selection of Lyman break galaxies (LBGs) at $z \sim 2$ and the SFR density deduced from the UV selected population is provided in Chapter 4. This work has been published in the *Astrophysical Journal* (Ly et al., 2009) and represents the first published study to identify LBGs at $z \sim 2$. In the past, limitations in the UV prevented observations for identifying a large number of $z \sim 2$ galaxies. This work extended a popular photometric technique into lower redshifts. I will then discuss in Chapter 5 a census of star-forming galaxies at $z \sim 1 - 3$ using multiple UV and NIR photometric selection techniques.

1.2.2 A Photometric Redshift Approach

While the above photometric techniques provide a “quick and dirty” solution for a census, high- z galaxies could potentially be missed by the criteria set forth in those selection. With pan-chromatic large surveys becoming more common, it is apparent that a photometric redshift survey encompassing star-forming galaxies

could yield a more complete census. Included in Chapter 5 will be the use of photometric redshifts to identify galaxies at $z \approx 1 - 3$. The samples derived from using photometric selection techniques will be compared to the photometric redshift sample to access the completeness of these techniques.

Finally in Chapter 6, I will combine SFR measurements described in each of the individual chapters and compare it to theoretical predictions. I will discuss the current agreements and disagreements of observations and theoretical predictions for the cosmic star formation history. I will raise potential problems that may explain such disagreements, discuss what future observations will hope to accomplish in tracing the cosmic star formation history. and what future observations and theoretical works will hope to accomplish.

1.3 Adopted Conventions

Throughout the dissertation, the concordance Λ CDM cosmology ($H_0 = 70 \text{ km s}^{-1} \text{ Mpc}^{-1}$ ($h_{70} = 1.0$; $h = H_0/100 \text{ km s}^{-1} \text{ Mpc}^{-1} = 0.70$), $\Omega_\Lambda = 0.7$, and $\Omega_M = 0.3$) is adopted, and all magnitudes (unless otherwise indicated) are reported on the AB system (Oke, 1974):

$$m_{\text{AB}} = -2.5 \log \left(\frac{f_\nu}{3630 \text{ Jy}} \right), \quad (1.1)$$

where f_ν is the flux density per frequency in $\text{erg s}^{-1} \text{ cm}^{-2} \text{ Hz}^{-1}$ and a Jansky (Jy) is $1 \times 10^{-23} \text{ erg s}^{-1} \text{ cm}^{-2} \text{ Hz}^{-1}$. In general, limiting magnitudes are provided as the 99.7% (3σ) confidence level, and aperture sizes are provided in diameter (denoted with a ϕ ; e.g., $2'' \phi$) unless otherwise indicated.

For SFR measurements, a Salpeter (1955) initial mass function (IMF) is adopted to convert the high-mass SFR to the total SFR. Recent studies (Davé, 2008; van Dokkum, 2008) have considered the possibility that the IMF evolves

with redshift, but such evidences have low significance. The data presented here cannot address any systematic evolution of the IMF, so no evolution is assumed.

CHAPTER 2

The Subaru Deep Field Narrow-band Survey: Measurements at Redshifts of 0.07 to 1.47

Over the past decade, deep spectroscopic surveys have utilized emission lines to measure the cosmic star-formation rate (SFR). Estimates of the SFR can be obtained from the H α emission line in star-forming galaxies (Kennicutt, 1983). However, H α is no longer visible (in optical spectrographs) beyond $z \sim 0.4$. To study the SFR at higher redshifts, one must obtain infrared spectroscopy of the H α line or detect bluer emission lines where optical spectrographs are used. Although the former has been successful (e.g., Malkan et al., 1995; Glazebrook et al., 1999; McCarthy et al., 1999; Yan et al., 1999; Hopkins et al., 2000; Moorwood et al., 2000; Tresse et al., 2002; Doherty et al., 2006; Rodriguez-Eugenio et al., 2006), difficulties, such as a bright background (for ground-based observations) and smaller areal coverage limit IR searches to small samples, mostly of the brightest galaxies.

The latter has been attempted by measuring the [O II] $\lambda\lambda 3726, 3729$. It has been used to determine the SFR out to $z = 1.6$ (Hogg et al., 1998; Hicks et al., 2002; Hippelein et al., 2003; Teplitz et al., 2003; Drozdovsky et al., 2005), but its measurements are more affected by internal extinction and metallicity uncertainties (Kennicutt, 1992; Kewley, Gellar, & Jansen, 2004). Studies have shown that the comoving SFR density increases by a factor of 10 from $z \sim 0$

to 1-1.5 and declines or flattens out at higher redshifts ([Hopkins, 2004](#)). The behavior above a redshift of 3 is not well known for two reasons: (*i*) the amount of UV extinction is questionable, and (*ii*) the shallowness of recent Lyman Break Galaxies studies at $z > 5$ has resulted in an extrapolation of the faint-end slope for a SFR estimate.

Since past studies identified galaxies and redshifts via spectra, the measured SFRs are biased toward the small selected sample of bright objects, and spectroscopy requires a greater demand of allocated telescope time, as opposed to the approach of using deep narrow-band (NB) imaging with large fields-of-view. The NB imaging method has proven to be quite effective in finding many emission line galaxies with the appropriate redshift for a strong line (e.g., Ly α , H α , [O II] $\lambda 3727$, H β , and [O III] $\lambda 5007$) to fall within the NB filter. For example, [Hu et al. \(2002\)](#), [Ajiki et al. \(2003\)](#), [Kodaira et al. \(2003\)](#), [Taniguchi et al. \(2003\)](#), [Hu et al. \(2004\)](#), [Kashikawa et al. \(2006\)](#), and [Shimasaku et al. \(2006\)](#) have confirmed candidate Ly α emitters (LAEs) at $z = 5.7$ and 6.6 with follow-up spectroscopy. These NB emitters (identified when their NB magnitude is substantially brighter than that of the broad-band continuum) provide an opportunity to study the cosmic evolution of star formation. [Fujita et al. \(2003\)](#), [Kodama et al. \(2004\)](#), and [Umeda et al. \(2004\)](#) have measured the H α luminosity function (the latter two are for clusters) at $z = 0.24$ or 0.40 by identifying NB emitters and then using their broad-band colors to distinguish a few hundred H α emitters from other line emitters. [Ajiki et al. \(2006\)](#) also examined the same field as [Fujita et al. \(2003\)](#) for other strong emission line galaxies such as [O III] and [O II]. Fabry-Perot (FP) interferometers have also been used to find emission line galaxies ([Jones & Bland-Hawthorn, 2001](#); [Hippelein et al., 2003](#); [Glazebrook et al., 2004](#)), but the comoving volume or limiting flux of past surveys is not comparable to that of the NB imaging technique, and their surveys currently lack broad-band colors. Other

work, such as COMBO-17 (Meisenheimer & Wolf, 2002) that uses intermediate-band filters is capable of selecting emission line galaxies, but these wider filters (compared to NBs) will only detect very strong line emitting galaxies.

In this paper, the luminosity function (LF) and SFR in almost a dozen redshift windows between $z = 0.07$ and 1.47 are presented from line-emitting galaxies in the Subaru Deep Field (SDF; Kashikawa et al., 2004). The approach of using broad-band colors to separate NB emitters will be considered. However, with spectra of some of our NB emitters, galaxies (with appropriate redshifts) from the Hawaii HDF-N (a deep spectroscopic survey), and multiple NB filters to cover two different lines at similar redshifts, the LF for line emitters other than the typical H α and Ly α can be studied. Broad-band (BB) multi-color selection of [O II] and [O III] emitters has yet to be done at these intermediate redshifts. The combination of deep, wide imaging with multiple broad- and narrow-band filters makes the SDF scientifically unique. In § 2.1, deep broad- and narrow-band imaging are presented. Selection criteria for different NB emitters are described and follow-up spectroscopy of the brightest line-emitting galaxies are also presented in § 2.1. Section 2.2 will discuss our methods of distinguishing different line emitters, derive emission line fluxes from NB photometry, calculate the luminosity function, and derive SFRs at 11 redshift windows. Comparisons with previous studies will be made in § 2.3, and a discussion of the evolution of the luminosity function and star formation rate density, and suggestions for future work are given in § 2.4. Concluding remarks are made in the final section.

2.1 Observations

2.1.1 Optical Imaging

Deep optical imaging of the SDF (centered at $13^{\text{h}}24^{\text{m}}38\overset{\text{s}}{.}9$, $+27^{\circ}29'25''$) has been obtained with Suprime-Cam on the 8.2-m Subaru Telescope (Kaifu, 1998; Iye et al., 2004). Five broad-band (B , V , R_{C} , i' , and z') and four narrow-band (NB704, NB711, NB816, and NB921⁹) images were obtained with a total integration time of 595, 340, 600, 801, 504, 198, 162, 600, and 899 minutes, respectively. The NB704 and NB711 images were part of a LAE study at $z \simeq 5$ taken in 2001 March-June and 2002 May before the SDF project began (Ouchi et al., 2003; Shimasaku et al., 2003, 2004). The remaining data were obtained as part of the SDF project. The limiting magnitudes (3σ with a $2''$ -aperture) for each $27' \times 34'$ image are (B) 28.45, (V) 27.74, (R_{C}) 27.80, (i') 27.43, (z') 26.62, (NB704) 26.67, (NB711) 25.99, (NB816) 26.63, and (NB921) 26.54. The correction for galactic reddening is small, $E(B - V) = 0.017$ (Schlegel, Finkbeiner, & Davis, 1998). Each image contains over 100,000 objects. After removing regions of low quality (the edges of the CCD and saturated regions around foreground stars), the effective field-of-view is about 868 sq. arcmin. Catalogs for each bandpass were constructed using Source Extractor v2.1.6 (SExtractor; Bertin & Arnouts, 1996).

This paper will only discuss low and intermediate redshift NB704, NB711, NB816, and NB921 emitters. High redshift LAEs in the SDF are discussed in Kodaira et al. (2003), Ouchi et al. (2003), Shimasaku et al. (2003, 2004), Taniguchi et al. (2005), Kashikawa et al. (2006), and Shimasaku et al. (2006).

⁹NB704, NB711, NB816, and NB921 are centered at 7046, 7126, 8150, and 9196Å with FWHM of 100, 73, 120, and 132Å, respectively.

2.1.1.1 NB704, NB711, NB816, and NB921 Line Emitters

BB-NB excess diagrams for the NB704, NB711, NB816, and NB921 catalogs are shown in Figures 2.1a-d for NB magnitudes up to the 3σ limiting magnitude. The NB704, NB711, NB816, and NB921 excesses are described by $Ri' - \text{NB704}$, $Ri' - \text{NB711}$, $i'z' - \text{NB816}$, and $z' - \text{NB921}$, respectively, where $Ri' = \frac{1}{2}(R_C + i')$ and $i'z' = 0.6i' + 0.4z'$. The limiting magnitude of Ri' is 27.62 and 27.11 for $i'z'$. Objects above the short-long dashed magenta lines in Figure 2.1a-d are fainter than 3σ of their broad-band flux (Ri' , $i'z'$, or z'). The median (i.e., featureless spectra) for the NB816 and NB921 excesses are 0.10 and -0.05 mag, respectively. NB line emitters are identified as points above the long-dashed blue (a minimum NB excess) and solid red lines in Figure 2.1. The solid red lines represent the 3σ excess: $\pm 3\sigma_{\text{BB-NB}} = -2.5 \log [1 \mp (f_{3\sigma NB}^2 + f_{3\sigma BB}^2)^{0.5} / f_{NB}]$, where the error $[f_{3\sigma NB}^2 + f_{3\sigma BB}^2]^{0.5}$ is shown in the upper right-hand corners of Figures 2.1a-d. The minimum NB excesses were chosen ‘by eye’ to be above the NB-BB scatter around NB of 23 mag.

These selection criteria yield 1135 NB704, 1068 NB711, 1916 NB816, and 2135 NB921 line emitters. These values are reduced to 1000, 986, 1563, and 1942 with good photometric errors ($\Delta m < 0.1$) for broad-band filters used in the color selections (see § 2.2.1.1-2.2.1.2). These line excess limits reach similar equivalent widths (see § 2.2.3) as Fujita et al. (2003) and Umeda et al. (2004).

2.1.2 Spectral Identification of NB Emitters

H α and [O III] NB emitters are the easiest to be identified in an optical spectrum. H α emitters can be confirmed from detection of other strong lines, [O III] and H β . And in cases (NB816 emitters) where the spectrum is truncated, the [N II] $\lambda\lambda 6548, 6583$ and [S II] $\lambda\lambda 6718, 6732$ doublet can be used. [O III] emitters

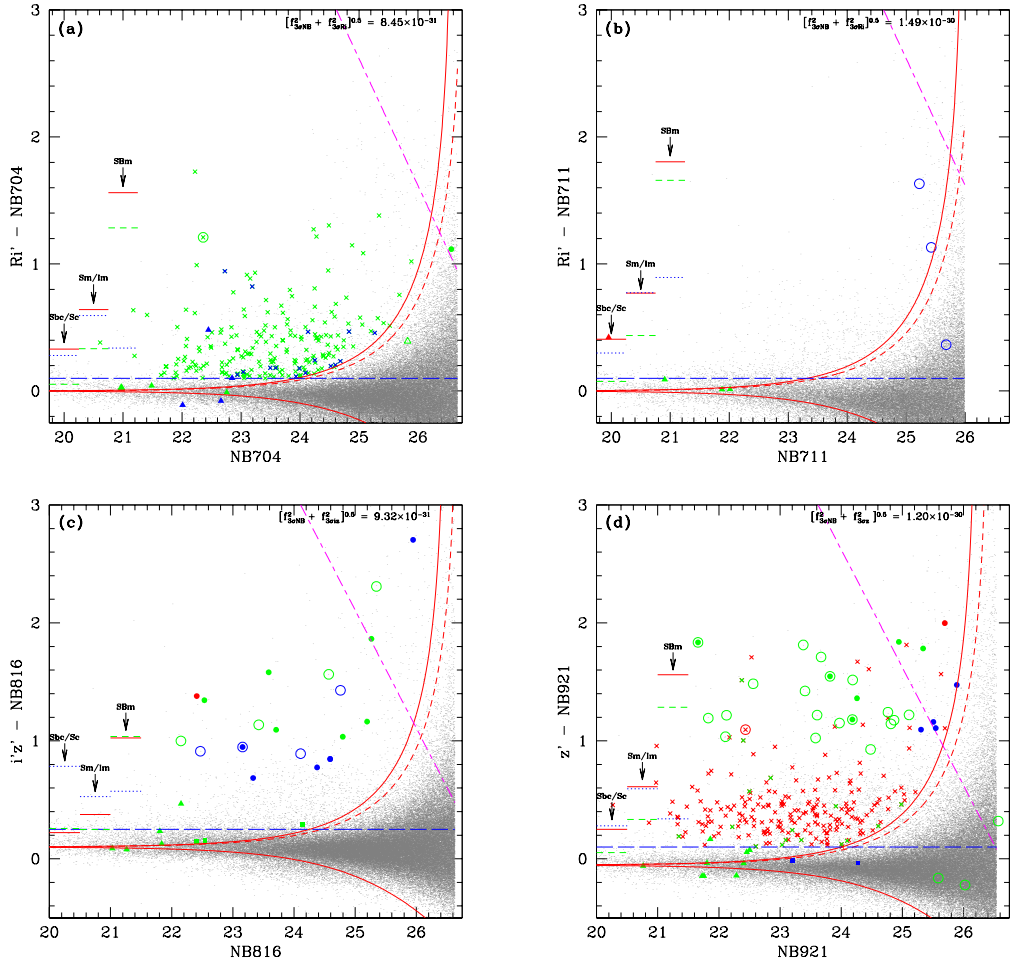


Figure 2.1 – NB excess plots for the (a) NB704, (b) NB711, (c) NB816, and (d) NB921 catalog. The abscissas show the NB magnitude with a $2''$ -aperture, and the ordinates show the line excess relative to the broad-band continuum. [O II], [O III]/H β , and H α emitters are identified as blue, green, and red, respectively in the electronic edition. Open circles are FOCAS sources, filled circles are DEIMOS targets, filled squares are serendipitous objects, crosses are NB704+921 emitters, and filled triangles are fortuitous sources. The solid and dashed lines (colored red in the electronic edition) are the excess of BB-NB for $\pm 3\sigma$ and 2.5σ , respectively. Long-dashed lines (colored blue in the electronic edition) represent an excess of (a) 0.10, (b) 0.10, (c) 0.25, and (d) 0.10 mag. Points above the short-long dashed lines (colored magenta in the electronic edition) have their broad-band continuum fainter than 3σ . Small horizontal lines on the left-hand side of the figures are the predicted excess for late type galaxies from the SDSS (Yip et al., 2004). Solid lines are for H α , short-dashed lines are for [O III], and dotted lines are for [O II]. The three columns from left to right are for Sbc/Sc, Sm/Im, and SBm galaxies.

are easily confirmed by the presence of its doublet feature, and H β for some objects. Also, for some NB921 [O III] emitters, the [O II] doublet appears on the blue side of the spectrum. Ly α and [O II] emitters are difficult to distinguish since the nearest lines are either weak ([Ne III] λ 3869, H δ , and H γ) or are AGN lines (C IV, [Ne III] λ 3869), and low spectral resolution cannot resolve the very close [O II] doublet (e.g., FOCAS; DEIMOS can resolve the doublet). However, Ly α appears asymmetric at high redshifts, and are undetected in B and V for NB704, NB711, and NB816 emitters, and B , V , R_C , and i' for NB921 emitters. Therefore, the asymmetry of the line and broad-band detection can be used to distinguish [O II] and Ly α ([Kashikawa et al., 2006](#); [Shimasaku et al., 2006](#)).

2.1.3 Previous Subaru/FOCAS Spectroscopy

Faint Object Camera and Spectrograph (FOCAS; [Kashikawa et al., 2002](#)) observations primarily targeting NB816 and NB921 emitters were made on 2002 June 7-10, 2003 June 5-8, and 2004 April 24-27. The description of these observations can be found in [Kodaira et al. \(2003\)](#), [Taniguchi et al. \(2005\)](#), [Kashikawa et al. \(2006\)](#), and [Shimasaku et al. \(2006\)](#). A total of 24 LAEs, 4 [O II], and 4 [O III] NB816 emitters were identified with FOCAS. For NB921 emitters, 11 LAEs, 19 [O III], and 1 H α were identified. These observations were intended to target LAEs, but a range in broad-band colors were allowed to determine the selection effects of a color-selected sample. The photometric and redshift information for non-LAEs are provided in Tables 2.1 and 2.2, and Figure 2.2 shows the spectrum of NB921 emitters with line fluxes (ordinate) plotted in $\text{erg s}^{-1} \text{cm}^{-2} \text{\AA}^{-1}$. The sky's spectrum is plotted at the top with arbitrary units. The spectra of NB816 emitters can be found in [Shimasaku et al. \(2006\)](#), so they are not reproduced. In addition, these NB emitters are plotted as open circles in Figure 2.1 and other

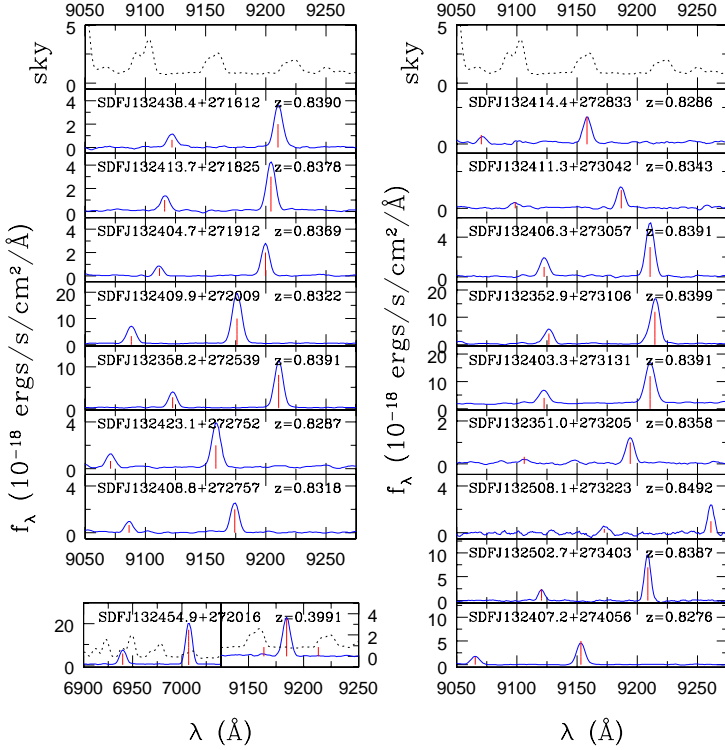


Figure 2.2 – Vertical lines (colored red in the electronic edition) identify the location of emission lines in the spectral window. For [O III] emitters, the lines are 4959Å and 5007Å. [O III] lines for the H α emitter are shown in the adjacent panel. The lines blue-ward and red-ward of H α are [N II] $\lambda\lambda$ 6548, 6583. The spectrum of the sky is shown in the top panels with arbitrary units and overlaid for the H α emitter as a dashed lines.

figures. The convention throughout this paper is that red, green, and blue points are H α , [O III]/H β , and [O II] emitters, respectively. Eight NB816 emitters and eight NB921 emitters remain unclear (either Ly α or [O II]).

Moreover, deeper broad-band observations have revealed that three NB711 emitters published in Shimasaku et al. (2003) appear to be [O II] emitters by detection in the B and V filters, but a chance projection of a foreground object cannot be ruled out. These sources are listed at the end of Tables 2.1 and 2.2.

Table 2.1. Photometric Properties of Spectroscopically Confirmed Narrow-Band Line-Emitting Galaxies

NB ID ^a	Name (SDFJ)	redshift	B	V	R_C	i'	z'
FOCAS NB816 emitters							
28247	132411.7+271531	1.1807	26.38	26.33	26.33	26.15	26.25
38133	132356.3+271726	1.1798	23.97	23.82	23.72	23.50	23.20
42561	132403.4+271817	0.6303	24.08	23.84	23.39	23.13	23.19
76702	132405.8+272537	1.1847 ^b	24.58	24.47	24.41	24.19	23.98
78892	132415.3+272559	0.6150	25.68	25.49	24.85	24.40	24.80
96705	132425.6+272947	0.6319	28.54	27.91	27.86	27.03	28.60
99588	132357.8+273030	0.6359	26.95	26.84	26.41	25.99	26.34
168136	132403.0+274435	1.1783	25.48	25.42	25.34	25.12	24.82
FOCAS NB921 emitters							
41910	132438.4+271612	0.8390	27.32	26.84	26.54	26.59	25.38
46399	132416.7+271655	0.8308 ^b	26.54	26.42	26.26	26.34	25.36
54902	132413.7+271825	0.8378	25.67	25.54	25.33	24.96	24.61
58816	132404.7+271912	0.8369	26.95	26.89	26.74	26.31	25.60
62897	132409.9+272009	0.8322	24.46	24.25	23.86	23.64	23.14
63322	132354.9+272016	0.3991	24.56	24.03	23.51	23.62	23.53
87190	132358.2+272539	0.8391	25.21	25.15	24.85	24.70	24.05
92017	132404.8+272645	0.8334 ^b	26.86	26.73	26.50	26.08	25.36
95258	132511.9+272731	0.8387 ^b	24.73	24.67	24.48	24.46	23.49
96981	132423.1+272752	0.8287	26.04	25.94	25.64	25.37	24.82
97394	132408.8+272757	0.8318	27.17	26.93	26.48	26.37	25.70
99909	132414.4+272833	0.8286	27.34	27.20	26.54	26.20	26.01
108717	132411.3+273042	0.8343	27.60	27.30	26.77	26.29	25.96
109516	132406.3+273057	0.8391	26.06	25.71	25.59	25.48	24.83
109948	132352.9+273106	0.8399	24.45	24.33	24.09	23.81	23.34
111896	132403.3+273131	0.8391	23.93	23.83	23.60	23.42	23.02
114783	132351.0+273205	0.8358	27.24	27.02	26.82	26.50	26.04
116106	132508.1+273223	0.8492	27.62	27.56	27.54	27.47	26.33
123068	132502.7+273403	0.8387	26.34	26.34	26.20	26.21	25.19
154431	132407.2+274056	0.8276	26.23	26.01	25.82	25.73	25.12
DEIMOS NB816 emitters							
29275	132517.9+271546	1.1818	25.84	25.37	24.87	24.35	23.52
31925	132515.6+271611	1.1813	26.37	26.08	25.88	25.62	25.17
34775	132508.1+271648	1.1830	27.90	27.34	26.57	25.56	24.55
56181	132525.9+272112	0.6197	27.52	27.39	26.77	26.22	26.56
59788	132510.2+272153	0.6283	28.05	(28.31)	27.20	26.79	(27.64)
68251	132340.7+272346	0.6347	25.81	25.57	25.06	24.76	24.87
70071	132434.9+272410	0.6229	24.55	24.40	24.02	23.76	24.06
110439	132524.7+273244	0.6293	25.95	25.81	25.35	24.98	25.44
122518	132513.5+273518	1.1735	>29.64	>28.93	>28.99	(28.33)	>27.81
136295	132505.5+273810	0.2438	24.21	23.96	23.69	23.72	23.90
165225	132453.4+274358	0.6373	26.93	26.69	26.08	25.81	25.87
DEIMOS NB921 emitters							
31248	132459.8+271423	1.4733	27.11	26.80	26.70	26.69	26.65
69400	132428.7+272136	0.3986	28.02	27.47	27.39	(27.98)	(27.69)
71165	132422.3+272202	1.4692	26.77	26.56	26.53	26.54	26.40
78567	132444.1+272344	0.8358	26.48	26.31	26.33	26.15	25.62
84040	132509.0+272455	0.8482	27.96	27.79	27.56	27.43	(27.12)
89013	132353.4+272602	0.8316	>29.64	>28.93	>28.99	(28.29)	26.78
128889	132520.5+273520	1.4771	>29.64	>28.93	(28.95)	27.67	26.67
134603	132507.4+273638	1.4513	>29.64	>28.93	>28.99	>28.62	(27.36)
Serendipitous Sources ^d							
59317	132510.3+272151	0.6750	25.22	25.09	24.61	24.41	24.49

Table 2.1 (cont'd)

NB ID ^a	Name (SDFJ)	redshift	B	V	R _C	i'	z'
67280	132515.2+272340	0.6300	24.43	23.94	23.14	22.78	22.58
104363	132505.8+273135	0.6382	25.59	24.46	23.39	22.73	22.26
41681	132415.8+271611	1.4920	25.44	25.29	24.93	24.67	24.24
132483	132507.8+273608	1.4328	24.53	24.31	23.95	23.64	23.19
Fortuitous Sources ^e							
13370	132517.3+271325	0.4306	22.45	21.65	21.10	20.89	20.58
18344	132456.2+271400	0.8224	24.29	23.71	23.18	22.57	22.14
30036	132455.4+271610	0.4570	24.02	23.33	22.83	22.66	22.47
39015	132520.5+271738	0.8242	26.09	24.39	23.30	22.30	21.61
40607	132524.6+271800	0.8306	25.88	24.31	23.26	22.29	21.58
57481	132452.2+272104	0.4498	22.62	21.99	21.57	21.48	21.31
58410	132520.4+272109	0.6375	23.69	23.46	22.87	22.64	22.59
59053	132517.8+272119	0.4658	23.88	22.88	22.09	21.69	21.22
60042	132420.9+272126	0.6360	23.79	23.22	22.49	22.13	21.90
69992	132416.2+272315	0.8352	23.49	23.15	22.77	22.28	22.03
80579	132414.7+272506	0.8978	23.63	23.37	23.13	22.72	22.51
93969	132507.1+272735	0.4676	24.64	23.41	22.30	21.75	21.31
104779	132521.1+272932	0.8984	23.91	23.53	23.24	22.66	22.37
104825	132523.0+272937	0.8983	24.69	23.33	22.39	21.41	20.70
106829	132520.6+272949	0.8988	24.02	23.43	22.94	22.22	21.77
120415	132523.6+273229	0.6236	24.66	23.36	22.29	21.52	21.09
134198	132511.1+273539	0.0842	21.18	20.69	20.47	20.29	20.18
139473	132523.6+273549	0.8487	24.21	23.80	23.43	22.85	22.58
169168	132500.7+274109	0.6871	23.72	23.21	22.57	22.08	21.79
27743 ^c	132410.8+271554	0.6316	24.46	23.09	22.10	21.32	20.81
FOCAS NB711 Emitters							
165413	132422.0+274016	0.9034	28.44	27.50	27.11	26.60	26.89
176956	132417.5+274221	0.9106	27.94	27.61	26.90	26.21	25.80
183380	132411.0+274331	0.9000	26.66	26.55	26.25	25.83	25.42

^aThe NB catalog number corresponds to the NB filter that the line emission is within. R_C-band ID's are provided for FOCAS NB711 emitters and fortuitous sources.

^bThese FOCAS objects were also observed with DEIMOS. The reported redshift is from the DEIMOS observation.

^cThis ID is for the i'-band catalog.

^dSerendipitous sources are secondary sources detected within the DEIMOS long slits and have the appropriate NB redshift.

^eFortuitous sources are lower priority targets for the DEIMOS observations with the appropriate NB redshift.

Table 2.2. Continuation of Table 2.1

NB ID ^a	NB704	NB711	NB816	NB921	[O II]	H β	[O III]	H α
FOCAS NB816 emitters								
28247	26.09	26.98	24.76	26.44	16.8
38133	23.76	23.78	22.47	23.30	71.7
42561	23.38	23.40	22.15	23.27	61.6	29.7	128	...
76702	24.46	24.60	23.16	24.11	109
78892	24.67	25.02	23.42	24.87	5.7	11.3	74.4	...
96705	(27.38)	(26.52)	25.35	27.50	5.6	...
99588	26.40	26.29	24.57	26.59	2.9	...	6.6	...
168136	25.28	25.82	24.11	24.82	15.0
FOCAS NB921 emitters								
41910	26.57	26.70	26.93	23.67	...	8.0	34.6	...
46399	26.17	26.49	26.85	23.82	7.9	16.2	82.3	...
54902	25.09	25.07	24.88	23.58	9.4	5.9	37.7	...
58816	26.75	24.04	...	4.0	23.3	...
62897	23.77	23.56	23.52	22.11	88.1	55.0	185	...
63322	22.36	23.74	23.76	22.44	...	30.8	161	31.6
87190	24.93	24.44	24.73	22.56	23.8	13.0	101	...
92017	26.28	25.99	26.11	24.18	5.1	14.0	71.9	...
95258	24.53	23.98	24.67	21.66	47.7	131	824	...
96981	25.44	25.23	25.32	23.61	9.8	...	36.8	...
97394	26.43	26.42	26.36	24.19	4.5	...	21.0	...
99909	26.37	26.03	26.30	24.76	2.0	...	11.9	...
108717	26.32	26.34	26.22	24.81	8.8	...
109516	25.52	25.31	25.44	23.41	1.2	8.9	48.0	...
109948	24.03	23.68	23.77	22.13	28.8	22.5	169	...
111896	23.62	23.29	23.42	21.83	58.7	28.1	158	...
114783	26.69	26.38	26.18	24.86	10.6	...
116106	>27.86	(26.88)	27.84	25.11	...	3.0	16.4	...
123068	26.77	26.02	26.08	23.38	...	10.2	66.4	...
154431	25.71	25.88	26.00	23.97	6.6	12.1	43.7	...
DEIMOS NB816 emitters								
29275	24.76	24.88	23.33	23.65	34.5
31925	26.25	25.79	24.59	25.38	17.3
34775	26.42	26.07	24.38	24.50	16.6
56181	(27.21)	(26.91)	25.20	26.82	9.7	...
59788	26.64	(26.59)	25.27	26.94	20.7	...
68251	25.19	24.71	23.71	24.88	19.5	13.8	71.0	...
70071	23.86	24.03	22.54	24.20	32.0	12.9	189	...
110439	25.24	25.23	23.52	25.41	...	12.9	33.3	...
122518	25.95	>27.73	7.5
136295	24.04	24.03	22.41	24.05	129	123
165225	26.28	25.94	24.80	25.88	9.4	...
DEIMOS NB921 emitters								
31248	(27.22)	>27.18	26.40	25.55	17.7
69400	26.57	(26.97)	(27.68)	25.69	...	6.7	1.1	25.8
71165	26.85	(26.59)	26.57	25.31	8.2
78567	26.25	26.02	26.36	24.26	...	7.0	27.7	...
84040	>27.86	27.39	(27.53)	25.34	38.8	...
89013	>27.18	24.94	...	3.0	18.3	...
128889	(27.18)	25.51	2.2
134603	>27.18	25.89	10.5
Serendipitous Sources ^d								
59317	24.56	24.57	24.15	24.67	24.1	18.1	57.4	...

Table 2.2 (cont'd)

NB ID ^a	NB704	NB711	NB816	NB921	[O II]	H β	[O III]	H α
67280	23.03	23.04	22.55	22.66	11.4
104363	23.10	23.14	22.40	22.28	...	9.1	31.8	...
41681	24.90	24.78	24.44	24.28	24.5
132483	23.80	23.83	23.48	23.20	8.9
Fortuitous Sources ^e								
13370	20.97	20.91	20.65	20.83	...	59.9	24.2	...
18344	22.80	22.84	22.27	22.29	38.5	34.8	77.2	...
30036	22.76	22.78	22.52	22.67	...	10.1	17.1	...
39015	23.12	22.90	21.82	21.76
40607	23.06	22.93	21.82	21.73
57481	21.48	21.53	21.37	21.45	...	58.9	86.3	...
58410	22.84	22.81	22.15	22.72	92.0	38.0	110	...
59053	21.95	21.88	21.41	21.36	...	39.1
60042	22.33	22.32	21.81	21.94	151	113	110	...
69992	22.52	22.45	22.10	21.86	171	103	143	...
80579	22.45	22.27	22.64	22.46	265	166
93969	21.99	22.01	21.48	21.39
104779	22.85	22.63	22.45	22.41	60.3
104825	22.01	21.93	21.05	20.76	24.9
106829	22.66	22.53	21.94	21.81	36.4
120415	21.96	21.85	21.26	21.12	...	-18.1
134198	20.43	19.96	20.17	20.29	422
139473	23.23	23.13	22.64	22.50	41.2	13.0	19.1	...
169168	22.31	22.26	21.84	21.85	23.6	21.2	6.2	...
27743 ^c	21.03	20.87
FOCAS NB711 Emitters								
165413	26.20	25.22	26.66	26.57	8.6
176956	27.05	25.43	26.21	26.02	6.0
183380	25.77	25.68	25.12	25.59	7.8

^aThe NB catalog number corresponds to the NB filter that the line emission is within. R_C -band ID's are provided for FOCAS NB711 emitters and fortuitous sources.

^dSerendipitous sources are secondary sources detected within the DEIMOS long slits and have the appropriate NB redshift.

^eFortuitous sources are lower priority targets for the DEIMOS observations with the appropriate NB redshift.

2.1.4 DEIMOS Spectroscopy of NB816 and NB921 Emitters

Deep Imaging Multi-Object Spectrograph (DEIMOS; [Faber et al., 2003](#)) observations were made on 2004 April 23 and 24 on Keck II. A total of four masks were used with an $830 \text{ lines mm}^{-1}$ grating and a GG495 order-cut filter. Each mask had an integration time of 7 - 9 kiloseconds, and had about 100 slits with widths of $1''.0$ (0.47\AA pix^{-1} , $R \sim 3600$ at 8500\AA). The typical seeing for these observations was $0''.5$ - $1''.0$. Standard stars BD $+28^\circ$ 4211 and Feige 110 ([Oke, 1990](#)) were observed for the flux calibration. The second mask was flux calibrated with BD $+28^\circ$ 4211, and the other three masks were calibrated with Feige 110. All DEIMOS observations were reduced in the standard manner with the spec2d pipeline. A total of 33 NB816 and 21 NB921 known line emitters (including LAEs) were targeted with DEIMOS. NB816 emitters were selected for having $i' - \text{NB816} \geq 1.0$ and $20.0 \leq \text{NB816} \leq 25.5$ (8.5σ), and NB921 emitters were selected for $z' - \text{NB921} \geq 1.0$ and $20.0 \leq \text{NB921} \leq 25.5$ (7.8σ). These criteria were used to identify the brightest line emitters in the sample.

Among the NB816 and NB921 line emitters that have been targeted, 4 [O II] $z = 1.47$, 4 [O II] $z = 1.19$, 3 [O III] $z = 0.84$, 6 [O III] $z = 0.63$, 1 H α $z = 0.40$, and 1 H α emitter at $z = 0.24$ have been *newly* identified. Their redshift and photometric information are also provided in Table [2.1](#) and [2.2](#). The flux-calibrated spectra of these sources are shown in Figure [2.3](#). For Figure [2.2](#) and [2.3](#), vertical red lines represent the location of emission lines at the given redshift. For [O II] emitters, the red lines are for a rest wavelength of 3726\AA and 3729\AA . While for [O III] emitters, the lines are 4959\AA and 5007\AA . In the case of the H α emitters, the bluer part (adjacent panel to the left) of the spectrum has been included to show the [O III] lines. Red lines near H α are the expected location of the [N II] doublet. The number of new LAEs at $z = 5.70 \pm 0.05$ and $z = 6.56$

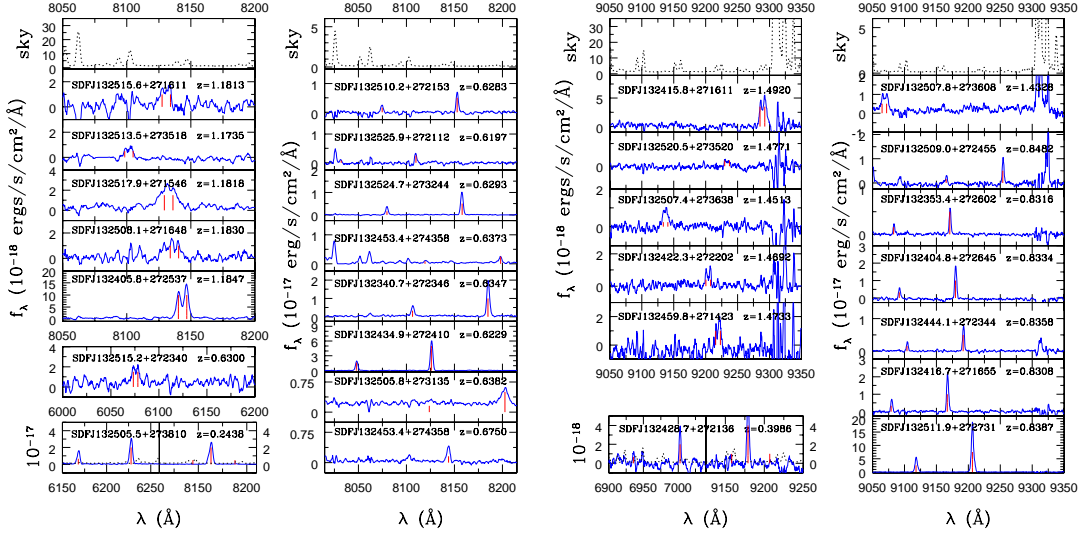


Figure 2.3 – NB816 emitters are shown on the *left*, and NB921 emitters are shown on the *right*. This includes serendipitous sources. Vertical grey lines (colored red in the electronic edition) identify the location of emission lines in the spectral window. For [O II] emitters, the lines are 3726Å and 3729Å, and 4959Å and 5007Å for [O III]. [O III] lines for H α emitters are shown in the adjacent panel. The lines blue-ward and red-ward of H α are [N II] $\lambda\lambda$ 6548, 6583. The spectrum of the sky is shown in the top panels with units of 10^{-18} and 10^{-17} $\text{erg s}^{-1} \text{cm}^{-2} \text{\AA}^{-1}$ for [O II] and [O III], respectively. For H α emitters, the sky’s spectrum is overlaid on the source’s as a dashed line. For the $z = 0.675$ galaxy at the bottom right of the left figure, the H β line is identified in the NB816 filter.

± 0.05 is 10 and 5, respectively. They are published in [Shimasaku et al. \(2006\)](#) and [Kashikawa et al. \(2006\)](#).

2.1.4.1 Spectroscopy of ‘Serendipitous’ and ‘Fortuitous’ Sources

Because of the long (up to 10'') DEIMOS slits, other galaxies falling within the slits are identified by the reduction pipeline as ‘serendipitous’. Moreover, other lower priority sources targeted with DEIMOS yield redshifts in the same range as those of the NB filters. These ‘fortuitous’ and serendipitous sources may not satisfy our NB excess selection criterion in § 2.1.1.1 or have any emission lines

Table 2.3. Summary of All 75 Spectra.

Redshift range (1)	Type (2)	FOCAS (3)	DEIMOS (4)	'S' (5)	'F' (6)	Total (7)
0.080 - 0.091	H α 711	0	0	0	1	1
0.233 - 0.251	H α 816	0	1	0	0	1
0.391 - 0.431	H α 921/[O III] 704	1	1	0	0	2
0.416 - 0.444	[O III] 711	0	0	0	1	1
0.616 - 0.656	[O III] 816	4	6	2	4	16
0.823 - 0.868	[O III] 921	19	3	0	5	27
0.439 - 0.460	H β 704	0	0	0	2	2
0.458 - 0.473	H β 711	0	0	0	2	2
0.664 - 0.689	H β 816	0	0	1	1	2
0.877 - 0.905	H β 921/[O II] 704	0	0	0	4	4
0.902 - 0.922	[O II] 711	3	0	0	0	3
1.171 - 1.203	[O II] 816	4	4	0	0	8
1.450 - 1.485	[O II] 921	0	4	2	0	6

Note. — Summary of different line emitters with spectroscopic confirmation. Col. (1) lists the redshift range, Col. (2) gives the emission line and the NB filter corresponding to the redshift, and Col. (3)-(6) list the number of sources that are FOCAS, DEIMOS, serendipitous ('S'), and fortuitous ('F'), respectively. The total number of sources for each redshift range is given in Col. (7).

(some are identified via absorption features), but they provide important information about the broad-band colors at these redshifts. There are five serendipitous sources with relevant redshifts: three $z \approx 0.83$ [O III] and two $z \approx 1.46$ [O II] that are included in this paper. They are plotted as filled squares in Figure 2.1 and subsequent figures, and are listed in Table 2.1 and 2.2. Twenty fortuitous sources are identified, and are included in Table 2.1 and 2.2. The spectra of the fortuitous sources are shown in Figure 2.4, and are identified in NB-excess, and two-color figures as filled triangles.

Therefore, the total (including serendipitous and fortuitous sources) number of spectra that will be used in our line classification scheme is 75. Table 2.3 summarizes the number of spectroscopically-identified sources within different redshift windows.

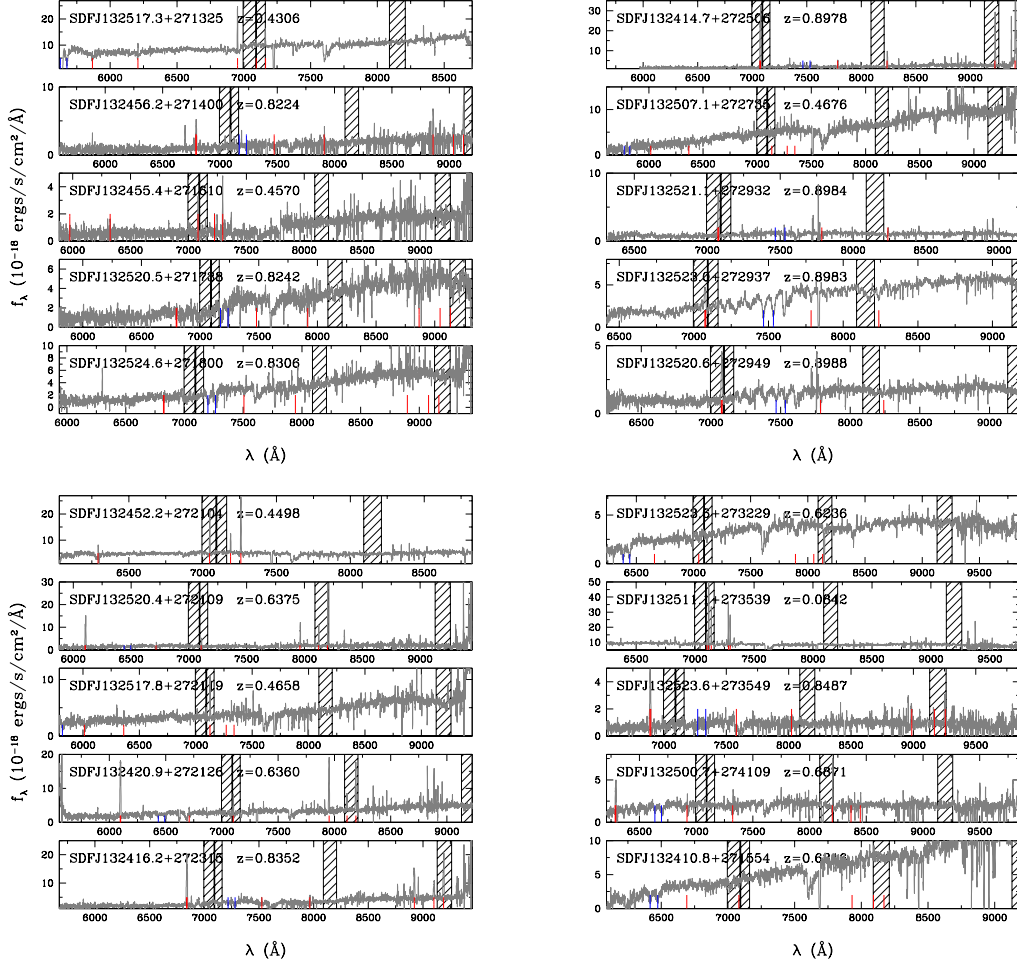


Figure 2.4 – The ordinates are given in 10^{-18} erg s $^{-1}$ cm $^{-2}$ Å $^{-1}$. Vertical lines (colored red in the electronic edition) identify the location of emission lines in the spectral window. They are from short to long wavelengths: [O II], H δ , H γ , H β , [O III] doublet, H α , [N II] doublet, and [S II] doublet. The blue lines (in the electronic edition) identify the location of Ca II K and H at 3933 and 3968Å. The FWHMs of the NB filters are shown by the shaded regions.

2.1.5 NB Excess Predictions from Sloan Digital Sky Survey

Mean spectra for six galaxy types (from early to late) were obtained from Yip et al. (2004) and were then redshifted for either H α , [O III], or [O II] to fall within the four NB filters and then convolved with the BB and NB filters. The spectra were averaged over 100 to 20000 Sloan Digital Sky Survey (SDSS) sources. This procedure tests whether or not typical galaxies detected in the SDSS are capable of being detected in the NB filters due to strong emission lines. The BB-NB excesses for the three latest types (Sbc/Sc, Sm/Im, and SBm) are shown as horizontal lines on the left-hand side of Figure 2.1a-d. The BB-NB excess method shows that the two latest types (Sm/Im and SBm) can easily be detected with NB filters due to their very strong emission lines, and Sbc/Sc can be detected in some cases. The Sm/Im and SBm galaxies make up 0.5% of the entire sample of Yip et al. (2004), and the Sbc/Sc sample consists of 23%. Thus at low redshift, for example, our NB imaging would detect about a quarter of the SDSS galaxies.

2.2 Results

Multiple possibilities exist for the identification of a detected emission line in a NB filter. Ly α , [O II] λ 3727, H β , [O III] $\lambda\lambda$ 4959, 5007, and H α are the strongest lines that most likely will be identified. The spectra of NB strong emitters show that they are either H α , [O III], or [O II]; neither of them are H β . Other objects (serendipitous and fortuitous) with H β in the filter have very low NB-BB excess. It is therefore assumed that these NB emitters are more likely to have [O III] rather than H β . The redshift range, comoving volume, and luminosity distance (d_L) are listed in Table 2.4 for all four NB filters.

Table 2.4. Redshift Ranges, Comoving Volumes, and Luminosity Distances

Line	Redshift range $z_1 \leq z \leq z_2$			
	NB704	NB711	NB816	NB921
Ly α	4.753-4.836	4.830-4.890	5.653-5.752	6.508-6.617
[O II] $\lambda 3727$	0.877-0.904	0.902-0.922	1.171-1.203	1.450-1.485
H β	0.439-0.460	0.458-0.473	0.664-0.689	0.878-0.905
[O III] $\lambda\lambda 4959, 5007$	0.397-0.417	0.416-0.430	0.616-0.640	0.823-0.850
H α	0.066-0.081	0.080-0.091	0.233-0.251	0.391-0.411
Comoving volume in $10^3 h_{70}^{-3}$ Mpc 3				
Ly α	198.57	142.70	214.13	214.52
[O II] $\lambda 3727$	46.59	35.46	70.88	88.48
H β	15.15	11.45	31.65	46.64
[O III] $\lambda\lambda 4959, 5007$	12.40	9.26	27.66	43.65
H α	0.43	0.42	4.71	12.11
Luminosity distance in h_{70}^{-1} Mpc				
Ly α	44407	45124	54406	64057
[O II] $\lambda 3727$	5726	5897	8167	10618
H β	2494	2604	4086	5736
[O III] $\lambda\lambda 4959, 5007$	2219	2322	3729	5302
H α	333	391	1213	2180

2.2.1 Broad-band Color Selection

Past studies (e.g., Fujita et al., 2003; Kodama et al., 2004; Umeda et al., 2004) that have used multi-color spectral energy distributions (SEDs) of NB emitters, relied on theoretical population synthesis models to identify photometric H α emitters. However, without spectra of a sample of bright galaxies, the identification of these emitters cannot be confirmed. Since spectra have been obtained for a few to over two dozen objects in each redshift bin, the multi-color classification of different ([O II] and [O III]) line emitters in this study is more reliable than previous studies. With five broad bandpasses, distinguishing different line emitters is more feasible in a multidimensional color space, as previous studies were limited to two or three broad bandpasses. Many of the colors that will be used rely on the Balmer break falling in a particular bandpass.

The NB704 filter provides the special advantage of determining the redshift of NB921 emitters into two possible intervals. This is almost equivalent to obtaining

a spectra, as a line-emitting galaxy in the NB704 and NB921 filters correspond to either a redshift of 0.397-0.411 or 0.878-0.904. The former occurs when the [O III] λ 5007 line falls within the NB704 filter, and the H α line is within the NB921 filter. The latter is for [O II] λ 3727 and H β (see Table 2.4). Coincidentally, the FOCAS spectra of an H α emitter (SDFJ132354.9+272016) is one of these NB704+921 line emitters, which shows that multiple NB filters can be used to select sources. The total number of NB704+921 line emitters is 212. As a comparison, other sets of filters were investigated. For NB704 and NB816, only 11 objects are emitters in both filters, and 7 objects for NB711 and NB816. NB816 and NB921 filters yielded 99 objects.

To better distinguish different line emitters, galaxies from the Hawaii HDF-N with known redshifts from either LRIS (Oke et al., 1995) or DEIMOS have been analyzed (Cowie et al., 2004). B , V , R_C , I_C , and z' photometry have been obtained by Capak et al. (2004) using Suprime-Cam. Currently, no transformation between I_C and i' exists for a sample of galaxies. However, SDSS studies¹⁰ of stars have shown that the transformation between the I_C and i' bandpasses is $I_C \approx i' - 0.4(i' - z')$. This formula is used to compute the i' magnitude for these Hawaii HDF-N galaxies. The number of sources within the NB704 and NB711 redshift intervals of 0.064 - 0.093 (H α), 0.395 - 0.475 ([O III] and H β), and 0.875 - 0.924 ([O II]) is 20, 200, 39, respectively. And the number of sources for NB816 and NB921 intervals of 0.231 - 0.253 (H α), 0.614 - 0.658 ([O III]), 0.662 - 0.691 (H β), 1.169 - 1.205 ([O II]), 0.389 - 0.413 (H α), 0.821 - 0.870 ([O III]), 0.876 - 0.904 (H β), and 1.448 - 1.487 ([O II]) is 19, 74, 58, 7, 46, 157, 21, and 8, respectively. Hawaii HDF-N galaxies are plotted as open squares in the two-color diagrams (see below) with the same color conventions used for the SDF spectroscopic sample. Also, there are two sources within the NASA/IPAC Extragalactic

¹⁰<http://www.sdss.org/dr4/algorithms/sdssUBVRITransform.html>.

Database (NED) at redshifts of 0.0718 and 0.45, which fall within the redshift windows. These sources are plotted as open triangles in the color-color diagrams. The SDSS spectra of Yip et al. (2004) have been redshifted and convolved with the broad-band filters to obtain the colors. They are overlayed as thick solid black lines on Figures 2.5 and 2.6. Because of the limited coverage (3500-7000Å) of these spectra, the desired colors could only be determined at $z = 0.07$ (NB704 and NB711 H α), 0.25 (NB816 H α), and 0.40 (NB704 and NB711 [O III]). There is good agreement between the SDSS predicted broad-band colors and those of the NB emitters.

For additional comparison, a stellar population model (Bruzual & Charlot, 2003) with constant star-formation is overlayed on these two-color diagrams. To correct the broad-band colors for strong nebular emission lines, we adopt the emission line ratios of Sm/Im galaxies from Yip et al. (2004). They are [O III]/H α +[N II] = 1.33, [O II]/H α +[N II] = 1.05, and H β /H α +[N II] = 0.43. The large [O III]/H α ratio is valid as a subsample of our data has a large ratio compared to local measurements (see § 2.2.6). Other lines (e.g., H γ , [S II] $\lambda\lambda$ 6718, 6732) while present in the spectrum do not affect the colors significantly compared to the strong emission of [O III], [O II], H β , and H α . Vectors are drawn on Figures 2.5-2.7 for H α +[N II] line strengths from 0 to 200Å EW. These vectors do pass through the majority of NB line emitters.

2.2.1.1 NB704 and NB711 Emitters

To distinguish NB704 and NB711 H α , [O III], or [O II] emitters, $V - R_C$ and $R_C - i'$ colors are plotted in Figure 2.5. [O III] emitters are selected by $V - R_C \geq 1.70(R_C - i')$ and $V - R_C \geq 0.82(R_C - i') + 0.26$. [O II] emitters are selected by $V - R_C \leq 1.70(R_C - i')$ and $V - R_C \leq 2.50(R_C - i') - 0.24$. The remaining

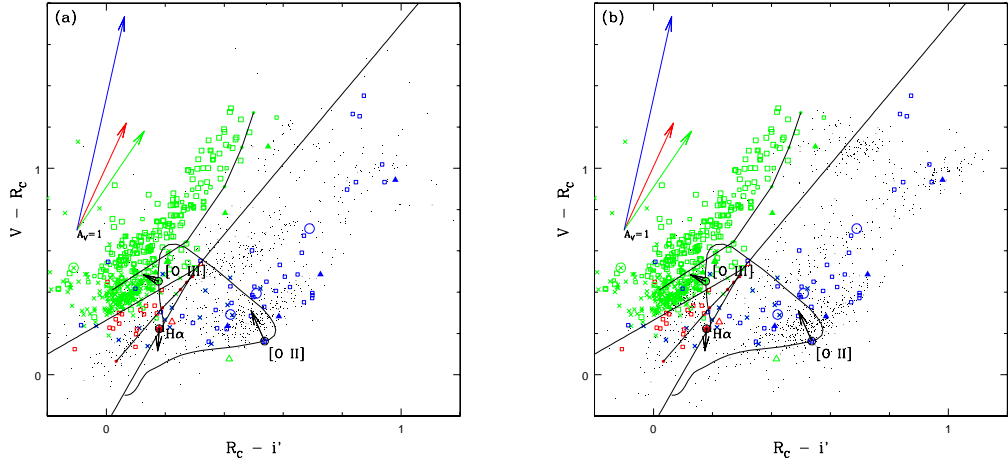


Figure 2.5 – Two-color diagrams in $V - R_C$ vs. $R_C - i'$ for (a) NB704 and (b) NB711 emitters. All spectroscopic NB704 and NB711 emitters are plotted on both diagrams. In the electronic edition, red points are $H\alpha$, blue points are $[O\text{ II}]$, and green points are $[O\text{ III}]$ and $H\beta$ emitters identified by FOCAS (open circles) and DEIMOS (filled circles). Open squares are galaxies from the Hawaii HDF-N, and triangles are fortuitous sources (filled) and from the NED database (open). NB704 and NB921 dual emitters are shown as crosses. The solid lines are $V - R_C = 1.70(R_C - i')$, $V - R_C = 0.82(R_C - i') + 0.26$, and $V - R_C = 2.5(R_C - i') - 0.24$. A theoretical model from [Bruzual & Charlot \(2003\)](#) with constant star-formation (without dust extinction) is shown by the solid black curve for $z = 0$ to 1.5 . Along this curve, the broad-band colors at specific redshifts of 0.07 , 0.40 , and 0.89 are shown by starred symbols with a circle surrounding it. Black vectors at these points indicate the direction that the colors follow with different emission line strengths. The vectors in the upper left-hand corner correspond to 1 magnitude of V extinction using the reddening curve of [Cardelli et al. \(1989\)](#). Filled pentagons and thick black lines represent the colors of [Yip et al. \(2004\)](#)'s spectra from early to late type SDSS galaxies for $z = 0.07$ and 0.40 .

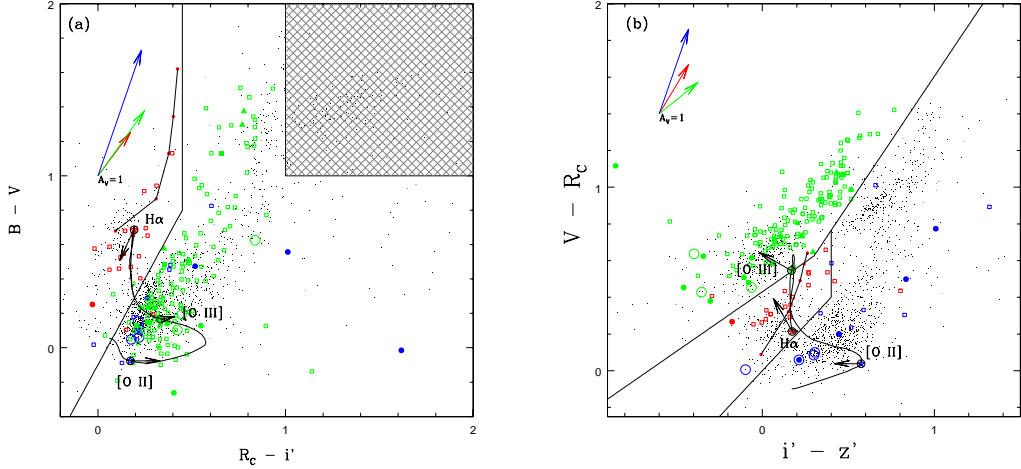


Figure 2.6 – Two-color diagrams in $B - V$ vs. $R_C - i'$ (a) and $V - R_C$ vs. $i' - z'$ (b) for NB816 emitters. Red points are $H\alpha$, blue points are $[O\text{ II}]$, and green points are $[O\text{ III}]$ and $H\beta$ emitters identified by FOCAS (open circles) or DEIMOS (filled circles). Open squares are galaxies from the Hawaii HDF-N, filled squares are serendipitous sources, and filled triangles are fortuitous sources. The solid lines in (a) are $B - V = 2.0(R_C - i') + 0.20$ and $R_C - i' = 0.45$, and in (b) $V - R_C = 0.65(i' - z') + 0.43$, $V - R_C = 1.4(i' - z') + 0.21$, $i' - z' = 0.40$, and $V - R_C = i' - z'$. A theoretical model from [Bruzual & Charlot \(2003\)](#) with constant star-formation (without dust extinction) is shown by the solid black curve for $z = 0$ to 1.5 . Along this curve, the broad-band colors at specific redshifts of 0.24 , 0.64 , and 1.20 are shown by starred symbols with a circle surrounding it. Black vectors at these points indicate the direction that the colors follow with different emission line strengths. The vectors in the upper left-hand corner correspond to 1 magnitude of V extinction using the reddening curve of [Cardelli et al. \(1989\)](#). Filled pentagons (red in the electronic edition) and thick black lines represent the colors of [Yip et al. \(2004\)](#)'s spectra from early to late for $z = 0.24$.

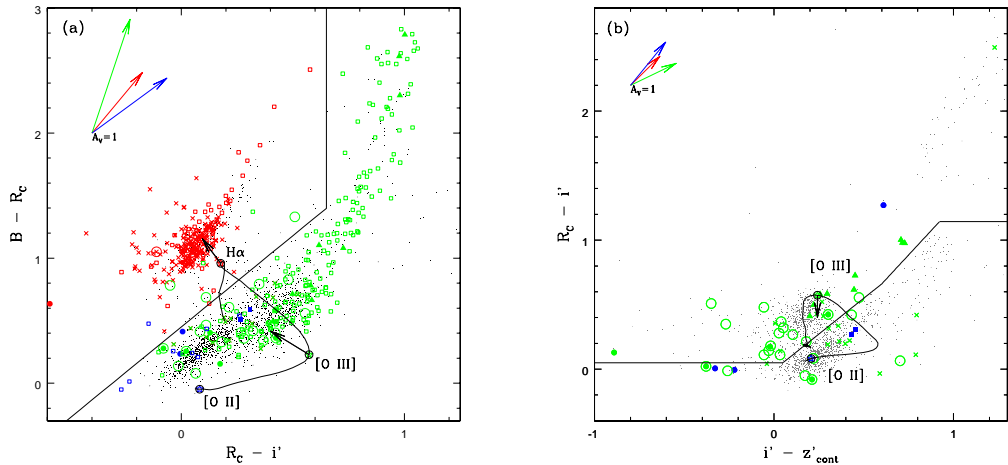


Figure 2.7 – Two-color diagrams in $B - R_C$ vs. $R_C - i'$ (a) and $R_C - i'$ vs. $i' - z'_{\text{cont}}$ (b) for NB921 emitters. In the electronic edition, red points are $\text{H}\alpha$, blue points are $[\text{O II}]$, and green points are $[\text{O III}]$ and $\text{H}\beta$ emitters identified by FOCAS (open circles) or DEIMOS (filled circles). Open squares are galaxies from the Hawaii HDF-N, filled squares are serendipitous sources, and filled triangles are fortuitous sources. NB704 and NB921 dual emitters are shown as crosses. The solid lines in (a) are $B - R_C = 1.46(R_C - i') + 0.58$, and $R_C - i' = 0.45$, and in (b) $R_C - i' = 0.05$, $R_C - i' = 1.11(i' - z'_{\text{cont}}) - 0.01$, $R_C - i' = 1.5(i' - z'_{\text{cont}}) - 0.24$, and $R_C - i' = 1.14$. A theoretical model from [Bruzual & Charlot \(2003\)](#) with constant star-formation (without dust extinction) is shown by the solid black curve for $z = 0$ to 1.5. Along this curve, the broad-band colors at specific redshifts of 0.40, 0.84, and 1.45 are shown by starred symbols with a circle surrounding it. Black vectors at these points indicate the direction that the colors follow with different emission line strengths. The vectors in the upper left-hand corner correspond to 1 magnitude of V extinction using the reddening curve of [Cardelli et al. \(1989\)](#).

sources are identified as H α . The total number of identified NB704 H α , [O III], and [O II] emitters is 120, 303, and 580, respectively, and 114, 158, and 713 for NB711 H α , [O III], and [O II] emitters.

The contamination rate—percentage for a type of source (e.g., [O III] or [O II]) to fall within another type’s selection criteria—can be determined from available spectra (including Hawaii HDF-N data). In the selection of H α , the contamination from [O II] is 5/46 (11%) and 3/208 (1%) for [O III] or H β emitters. For [O III], there is 4/46 (9%) contamination from [O II] and 1/22 (5%) from H α . Finally, for [O II], H α and [O III] or H β contribute 2/22 (9%) and 1/208 (< 1%) contamination, respectively.

2.2.1.2 NB816 Emitters

Figure 2.6a and b show $B - V$ vs. $R_C - i'$ and $V - R_C$ vs. $i' - z'$ for NB816 emitters. The first plot isolates H α emitters while the second plot primarily separates [O II] and [O III] emitters. H α emitters are identified by $B - V \geq 2(R_C - i') - 0.1$ and $R_C - i' < 0.45$. [O III] emitters are selected by $V - R_C \geq 0.65(i' - z') + 0.43$ and $V - R_C \geq 1.4(i' - z') + 0.21$ (solid black lines in Figure 2.6b). [O II] emitters are classified by $V - R_C \geq 1.4(i' - z') + 0.21$ and $i' - z' \geq 0.40$ or $V - R_C \leq i' - z'$. Sources within the shaded region of Figure 2.6a are “unknown” objects as no spectral identification is available in that area. Initially, these sources were thought to be [O II] emitters as their colors were $V - R_C \approx 0.9$ and $i' - z' \approx 0.6$, but this resulted in an excess ($N = 192$) of sources with line luminosities above L_* . Hypothetically, these objects may be [O III] emitters, therefore, two LFs (including and excluding the unknown sources) will be presented in § 2.2.3.2. The total number of NB816 line emitters identified as H α , [O III], and [O II] emitters is 205, 280 (472 including unknown NB816 emitters), and 831, respectively.

The contamination of [O II] and [O III] or H β line emitters into H α is 1/14 (7%) and 3/150 (2%). There is 2/20 (10%) contamination from H α into [O II] and zero contamination by [O III] or H β . And for [O III], a contamination of 1/20 (5%) from H α is found while [O II] contributes zero contamination.

2.2.1.3 NB921 Emitters

In Figure 2.7a, the $B - R_C$ and $R_C - i'$ colors for NB921 emitters are shown. Two $z = 0.40$ H α (red circles), and 196 NB704 and NB921 emitters at $z = 0.40$ are plotted as red crosses while 16 $z = 0.89$ NB704 and NB921 H β emitters are plotted as green crosses. The two types of NB704 and NB921 emitters are distinguished by their similarities in broad-band colors with galaxies that have been identified spectroscopically. H α NB921 emitters are identified for having $B - R_C \geq 1.46(R_C - i') + 0.58$ and $R_C - i' \leq 0.45$. In Figure 2.7b, NB921 emitters that are not identified as H α are plotted (as grey points) in $R_C - i'$ vs. $i' - z'_{\text{cont}}$, where z'_{cont} accounts for a brighter measurement in z' due to a bright emission line (see Equation 2.1 below). This correction will shift points bluer. The total number of NB921 H α , [O III], and [O II] emitters is 337, 655, and 899, respectively.

The amount of contamination of [O II] and [O III] or H β into our H α selection criteria are 1/12 (8%) and 5/209 (2%), respectively. And from the SDF spectroscopic sample, the contamination amount is 6/32 (19%) of [O III] or H β into [O II] and 1/5 (20%) of [O II] into [O III]. The [O II] NB921 contamination rate is higher due to small statistics. The low contamination rates for all four NB filters show that the method of determining H α , [O III], and [O II] is highly reliable.

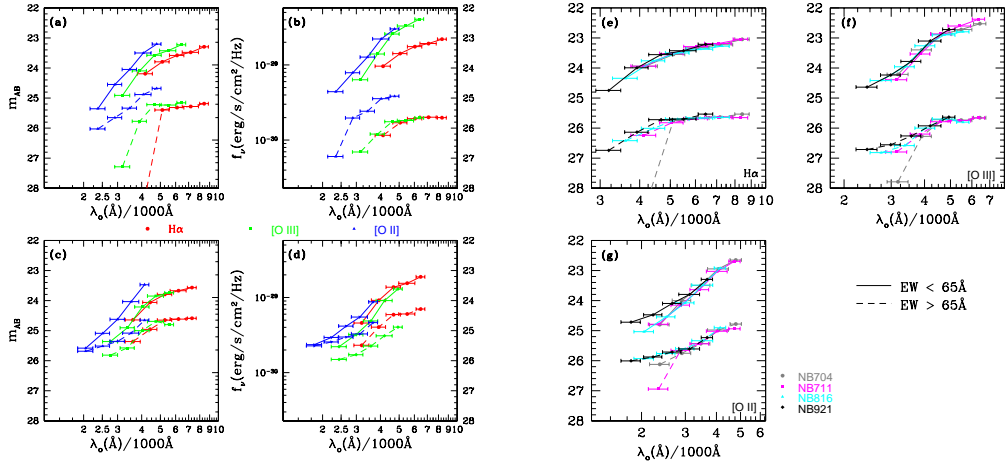


Figure 2.8 – Spectral energy distribution for (a) NB704, (b) NB711, (c) NB816, and (d) NB921 emitters. The outer ordinates give the AB magnitudes and the inner ones are flux densities in $\text{erg s}^{-1} \text{ cm}^{-2} \text{ Hz}^{-1}$. The rest wavelengths of the BB filters are given on the abscissas. In the electronic edition, red, green, and blue points correspond to H α (circles), [O III] (squares), and [O II] (triangles) line emitters. The solid and dashed lines correspond to low- and high-EWs, respectively. The division is made at observed EW of 65Å. The SEDs for H α , [O III], and [O II] emitters are compared in (e), (f), and (g), respectively, where vertical shifts are applied to overlap them. In (e)-(g), NB704, NB711, NB816, and NB921 emitters are given by grey circles, magenta squares, cyan triangles, and black diamonds, respectively in the electronic edition.

2.2.2 Averaged Spectral Energy Distributions

Based on the BB color selection, averaged rest-frame optical to UV SEDs are shown in Figure 2.8a-d for each type of line emitters (H α , [O III], and [O II]). SEDs of high and low observed equivalent widths (EWs) are provided where the division is made at 65Å (see § 2.2.3 for a description of determining EWs).

All high-EWs sources are bluer (flatter spectral index) compared to the low-EW sources. This is rather apparent for the [O II] emitters. This is not surprising as very high star-forming galaxies are expected to be blue. In addition, the NB816 high-EW [O III] SED appears to peak in the i' bandpass, which indicates that the

[O III] lines may be stronger relative to the continuum at $z = 0.64$. The H α SEDs show little differences among all four filters (i.e., redshifts from $z = 0.07$ to 0.4). A comparison of these SEDs with models used in photometric redshift algorithm (such as *hyperz*) and a more detail analysis of these SEDs will be discussed in a future paper.

2.2.3 The Luminosity Function

The total NB flux density (in units of $\text{erg s}^{-1} \text{ cm}^{-2} \text{ \AA}^{-1}$) can be defined as $f_{\text{NB}} = f_C + F_L/\Delta\text{NB}$, where f_C is the continuum flux density ($\text{erg s}^{-1} \text{ cm}^{-2} \text{ \AA}^{-1}$), F_L is the emission line flux ($\text{erg s}^{-1} \text{ cm}^{-2}$), and ΔNB is the width of the NB filter. The broad-band continuum flux density (f_{BB}) is $f_{Ri} = f_C + \epsilon_1 F_L/\Delta R$ (NB704 or NB711, $\epsilon_1 = 0.5$), $f_{iz} = f_C + \epsilon_2 F_L/\Delta i'$ (NB816, $\epsilon_2 = 0.6$), and $f_z = f_C + \epsilon_3 F_L/\Delta z'$ (NB921, $\epsilon_3 = 1.0$). Here, ϵ_i , the weight of a broad-band filter to determine the broad-band continuum, is introduced to maintain generality in the following equations. The widths are $\Delta\text{NB704} = 100\text{\AA}$, $\Delta\text{NB711} = 73\text{\AA}$, $\Delta\text{NB816} = 120\text{\AA}$, $\Delta\text{NB921} = 132\text{\AA}$, $\Delta R = 1124\text{\AA}$, $\Delta i' = 1489\text{\AA}$, and $\Delta z' = 955\text{\AA}$. Therefore the line flux, continuum flux density, and observed equivalent widths are

$$F_L = \Delta\text{NB} \frac{f_{\text{NB}} - f_{BB}}{1 - \epsilon(\Delta\text{NB}/\Delta BB)}, \quad (2.1)$$

$$f_C = \frac{f_{BB} - \epsilon f_{\text{NB}}(\Delta\text{NB}/\Delta BB)}{1 - \epsilon(\Delta\text{NB}/\Delta BB)}, \text{ and} \quad (2.2)$$

$$EW_{obs} = \frac{F_L}{f_C} = \Delta\text{NB} \left[\frac{f_{\text{NB}} - f_{BB}}{f_{BB} - \epsilon f_{\text{NB}}(\Delta\text{NB}/\Delta BB)} \right]. \quad (2.3)$$

The limiting line fluxes for NB704, NB711, NB816, and NB921 are 5.3, 6.5, 6.3, and $5.7 \times 10^{-18} \text{ erg s}^{-1} \text{ cm}^{-2}$, respectively. Fujita et al. (2003) reach a limiting line flux that is twice as bright as what is reported here for NB816 emitters. For a NB excess of 0.1 (NB704), 0.1 (NB711), 0.25 (NB816), and 0.1 mag (NB921),

the observed EW is 10, 7, 33, and 15Å, respectively. In Figure 2.9, line fluxes derived from photometry are compared to spectroscopic values, showing that the determination of line fluxes from photometry is accurate over a wide range of line fluxes. The *observed* LFs for H α , [O III], and [O II] are presented in § 2.2.3.1–2.2.3.3 follow by an analysis of the incompleteness of the sample.

2.2.3.1 H α Emitters

Since the NB filters include the [N II] doublet with the H α emission lines, these line flux measurements must be corrected. It is assumed that κ , the flux ratio of H α and the [N II] doublet (H α /[N II]), is 4.66. This is an average flux ratio from 17 DEIMOS spectra between $z = 0.08$ and 0.34 . Tresse & Maddox (1998), Yan et al. (1999), Iwamuro et al. (2000), and Fujita et al. (2003) used a flux ratio of 2.3, which is reported by Kennicutt (1992) and Gallego et al. (1997). In addition, the non-square shape of the NB filters must be accounted for, so a statistical correction of 28% is applied for all filters. Therefore the observed luminosity is $L_{\text{obs}}(\text{H}\alpha) = 4\pi d_L^2 F_L \frac{1}{1+1/\kappa} \times 1.28$. With these corrections, the luminosity function is constructed by

$$\Phi(\log L_i) = \frac{1}{\Delta \log L} \sum_j \frac{1}{V_i} \quad \text{with } |\log L_j - \log L_i| < \frac{1}{2} \Delta \log L. \quad (2.4)$$

The number of H α line emitting galaxies per Mpc³ per $\Delta \log L(\text{H}\alpha)$ is plotted in Figure 2.10 for (a) NB704 and NB711, (b) NB816, and (c) NB921 as small filled grey circles. The logarithmic bin size for H α is $\Delta \log L(\text{H}\alpha) = 0.4$. The comoving volume for each galaxy is corrected for the shape of the filter being triangular, which can be as high as 27% of the total accessible volume for the

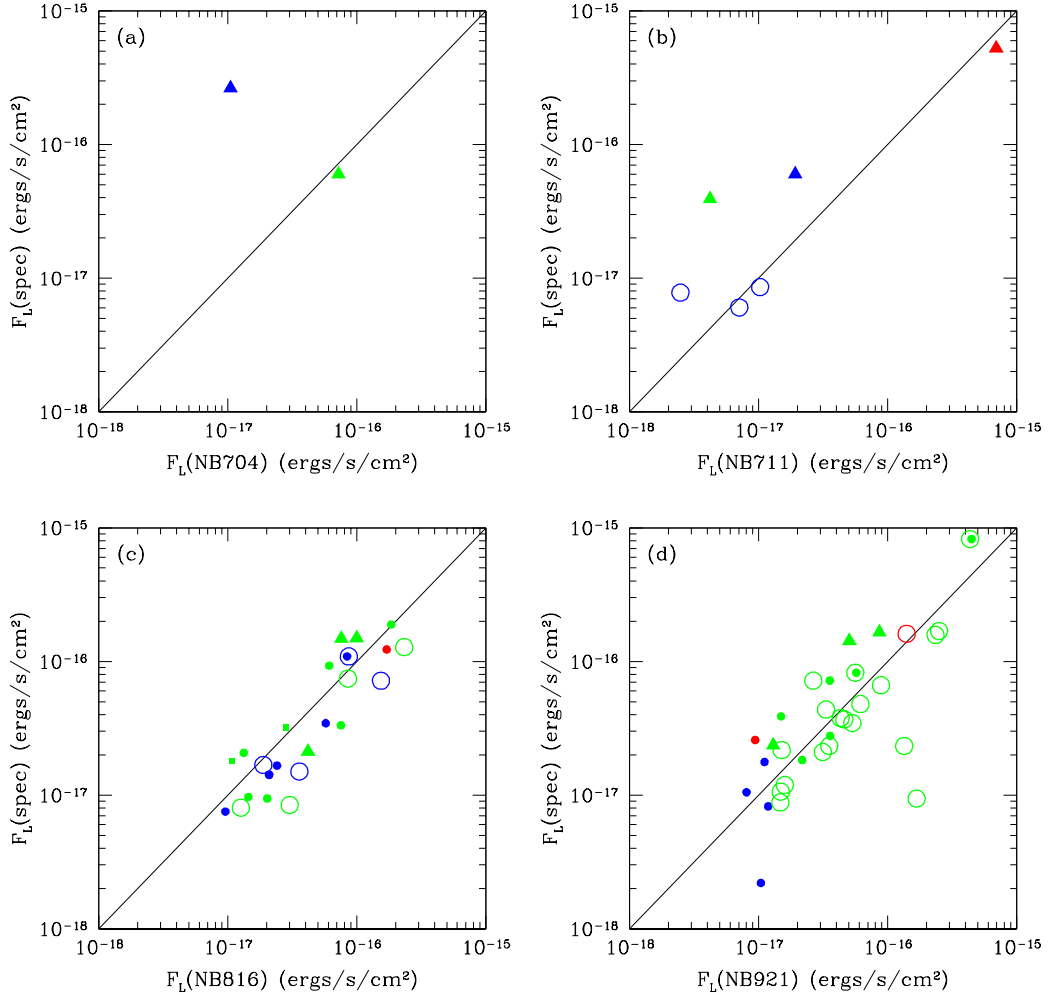


Figure 2.9 – (a) NB704, (b) NB711, (c) NB816, and (d) NB921 emitters. Line fluxes are given in $\text{erg s}^{-1} \text{cm}^{-2}$. In the electronic edition, red points are H α , blue points are [O II], and green points are [O III] and H β emitters identified by FOCAS (open circles) or DEIMOS (filled circles). Filled triangles and squares are fortuitous and serendipitous sources, respectively. The solid lines represent one-to-one correspondence.

faintest galaxies. The LFs are fitted to a Schechter profile (Schechter, 1976):

$$\Phi(L)dL = \phi_\star \left(\frac{L}{L_\star} \right)^\alpha \exp \left(-\frac{L}{L_\star} \right) \frac{dL}{L_\star}, \quad (2.5)$$

where $\Phi(\log L)d\log L = \Phi(L)dL$. The LF can be integrated to obtain the luminosity density $\mathcal{L} = \int_0^\infty dL L \Phi(L) = \phi_\star L_\star \Gamma(\alpha + 2)$ in $\text{ergs s}^{-1} \text{ Mpc}^{-3}$.

2.2.3.2 [O III] Emitters

Although the strongest [O III] line is located at 5007Å, the measured total line flux includes the 4959Å line for redshifts of 0.411-0.417, 0.430-0.431, 0.631-0.639, and 0.841-0.850. Assuming that $\frac{F_{5007}}{F_{4959}} = 3$, the corrected [O III] $\lambda 5007$ luminosity for redshifts when both lines are in the filter is $L_{\text{obs}}(\text{O III}) = 4\pi d_L^2 F_L \frac{3}{4} \times 1.28$. From the SDF spectroscopic sample (excluding fortuitous and serendipitous sources) of [O III] emitters, it is statistically estimated that 4/10 (NB816) and 2/22 (NB921) include both [O III] lines. If each NB filter is divided into 5Å bins, and the redshift distribution is uniform across the filter, then the fraction of detected line emitters where both lines are present is 6/24 (NB704), 1/15 (NB711), 8/24 (NB816), and 8/26 (NB921) must have their luminosity reduced by 25%. However, the non-square shape of the filters will lower the percentage for objects detected in these redshift intervals. Accounting for the filters' shape, the corrections are 21.2% (NB704), 3.3% (NB711), 23.3% (NB816), and 22.0% (NB921). It should be noted that these corrections should affect lower luminosity objects, but due to the degeneracy of line fluxes (truly faint versus off-center from \bar{z}), these corrections are applied regardless of their line flux.

The luminosity functions for [O III] are shown in Figure 2.11 for NB704 (a), NB711 (b), NB816 (c), and NB921 (d) as small filled grey circles. The LF are binned into $\Delta \log(\text{O III}) = 0.2$ except for the NB921 LF where 0.1 is used. The Schechter parameters for the [O III] NB816 LF including the unknown sources

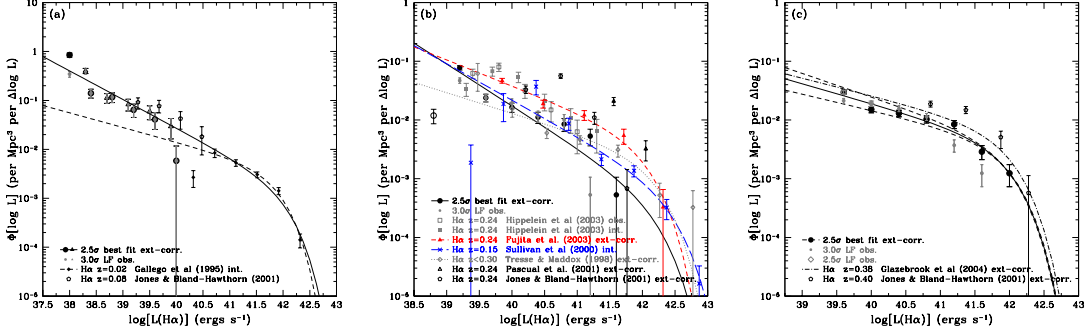


Figure 2.10 – (a) $z = 0.07 - 0.09$, (b) $z \approx 0.24 \pm 0.01$, and (c) $z \approx 0.40 \pm 0.01$. Ordinates are $\Phi[\log L]$ in units of Mpc^{-3} ($\Delta \log L$) $^{-1}$. Abscissas are $\log L(\text{H}\alpha)$ in ergs s^{-1} . The LFs of NB704, NB816, and NB921 are plotted as filled circles, and NB711 emitters are plotted as filled triangles in (a), where black and grey filled circles are for the 2.5σ extinction-corrected and 3σ observed sample, respectively. For NB921, the $\pm 1\sigma$ uncertainties in α are shown by the two thin short-dashed black lines, and the 2.5σ observed points are shown as open grey diamonds to illustrate the effect of incompleteness at the faint end. Open circles at the faint luminosity end are 2.5σ points excluded from the best fit given by the thick solid black lines. The luminosity functions from other studies are overlayed. Jones & Bland-Hawthorn (2001) at $z = 0.08, 0.24$, and 0.40 are shown as open pentagons, Gallego et al. (1995) as short-dashed black lines with open (observed) and filled (intrinsic) diamonds, $z = 0.24$ observed Hippelein et al. (2003) points are shown as open grey squares, and $z = 0.2 \pm 0.1$ Tresse & Maddox (1998) as filled grey diamonds and dotted line. In addition, Fujita et al. (2003) $z = 0.24$ is shown as a dashed line and filled triangles (colored red in the electronic edition), Sullivan et al. (2000) as a long-dashed line (colored blue in the electronic edition) with crosses, a dot - short-dashed black line for Glazebrook et al. (2004), and Pascual et al. (2005) as open triangles. All values have been converted to the common cosmology. Extinction-corrected values follow Equation 2.7 with the exception of Gallego et al. (1995), Tresse & Maddox (1998), Sullivan et al. (2000), and Hippelein et al. (2003) where their extinction-corrected LF are used.

are $\log L_\star = 41.69 \pm 0.08$, $\log \phi_\star = -2.16 \pm 0.07$, and $\alpha = -0.87 \pm 0.08$.

2.2.3.3 [O II] Emitters

Fortunately there are no strong lines near [O II] that fall within the NB filters, so the NB filter measures only the [O II] line and underlying continuum: $L_{\text{obs}}(\text{O II}) = 4\pi d_L^2 F_L \times 1.28$. The luminosity functions for [O II] are shown in Figure 2.12 as small filled grey circles. A bin size of $\Delta \log L(\text{O II}) = 0.1$ is used.

2.2.4 Completeness of the Luminosity Functions

One major question when constructing these luminosity functions is the completeness at the faint luminosity end. A common technique used to determine completeness is to distribute artificial sources on the images and then see what fraction of those are detected with SExtractor. Kashikawa et al. (2006) determined that the completeness for the SDF NB921 image used in this paper is about 50% at 26.0 mag. Since the depth of the other images is comparable to the NB921 or half a magnitude shallower, the completeness of these filters are given by adjusting the NB magnitude of 50% completeness based on the limiting magnitude of the images. This scaling implies that the magnitude for 50% completeness is 26.0 for NB704, 25.5 for NB711, and 26.1 for NB816. Using the number of NB emitters within a $\Delta \text{NB} = 0.25$ mag and the completeness curve as a function of magnitude (available at Kashikawa et al., 2004), the number of NB emitters missed due to incompleteness is 109 (NB704), 137 (NB711), 160 (NB816), and 214 (NB921).

As a consistency check, the amount of incompleteness can also be determined by loosening the 3σ BB-NB excess selection criteria to a depth of 2.5σ . The larger 2.5σ limits are shown as dashed red lines in Figure 2.1a-d. This threshold results

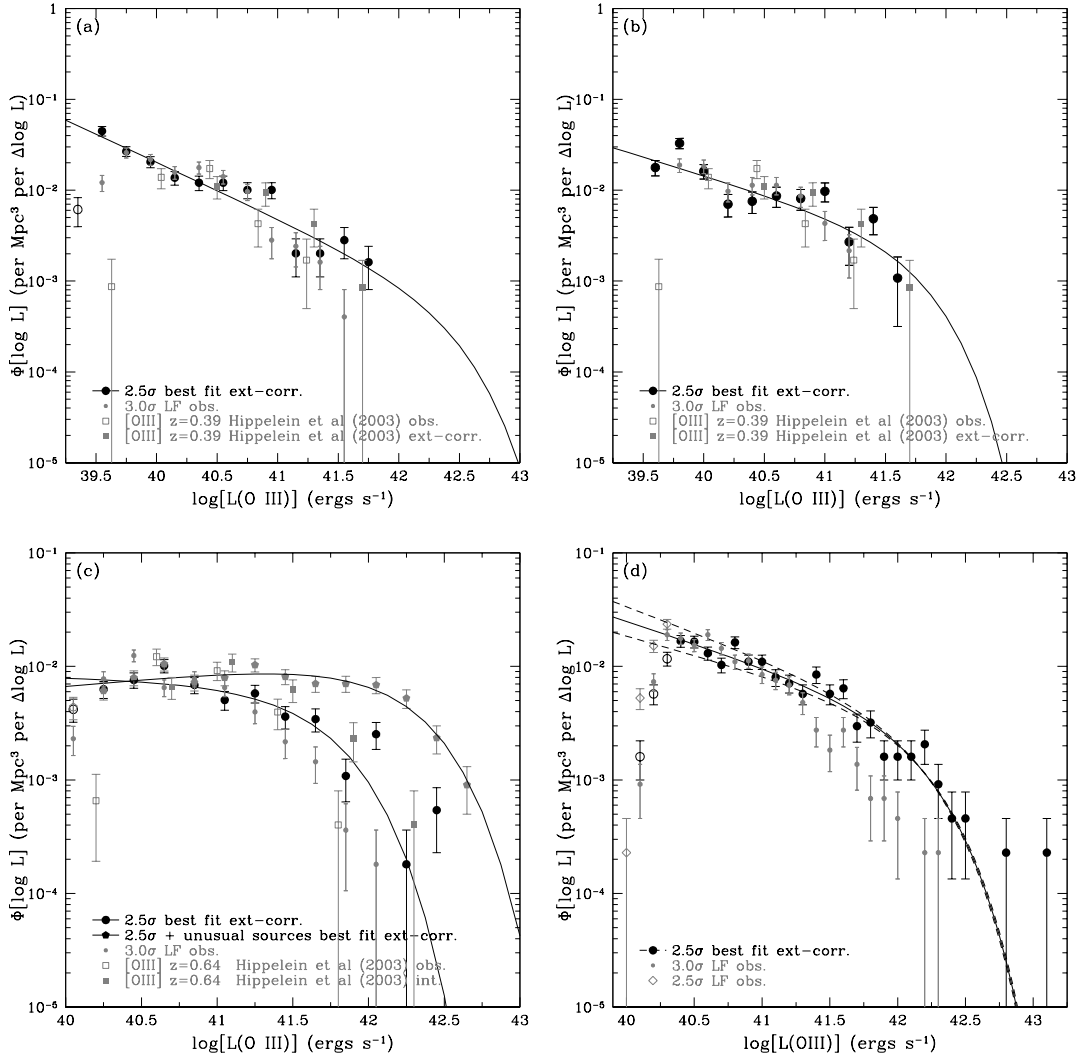


Figure 2.11 – (a) $z \approx 0.41 \pm 0.01$, (b) $z \approx 0.42 \pm 0.01$, (c) $z \approx 0.63 \pm 0.01$, and (d) $z \approx 0.84 \pm 0.01$. Ordinates are $\Phi[\log L]$ in units of $\text{Mpc}^{-3} (\Delta \log L)^{-1}$. Abscissas are $\log L(\text{O III})$ in ergs s^{-1} . The LFs of NB704, NB711, NB816, and NB921 are plotted as filled circles for the 2.5σ extinction-corrected (black) and 3σ observed (grey) sample. For NB921, the $\pm 1\sigma$ uncertainties in α are shown by the two thin short-dashed black lines, and the 2.5σ observed points are shown as open grey diamonds to illustrate the effect of incompleteness at the faint end. Open circles at the faint luminosity end are 2.5σ points excluded from the best fit given by the thick solid black lines. For NB816, the filled grey pentagons and solid line are the LF including the 192 unknown sources. The luminosity functions of Hippelein et al. (2003) at $z = 0.39 - 0.41$ and $0.63 - 0.65$ are shown as open (observed) and filled (extinction-corrected) grey squares.

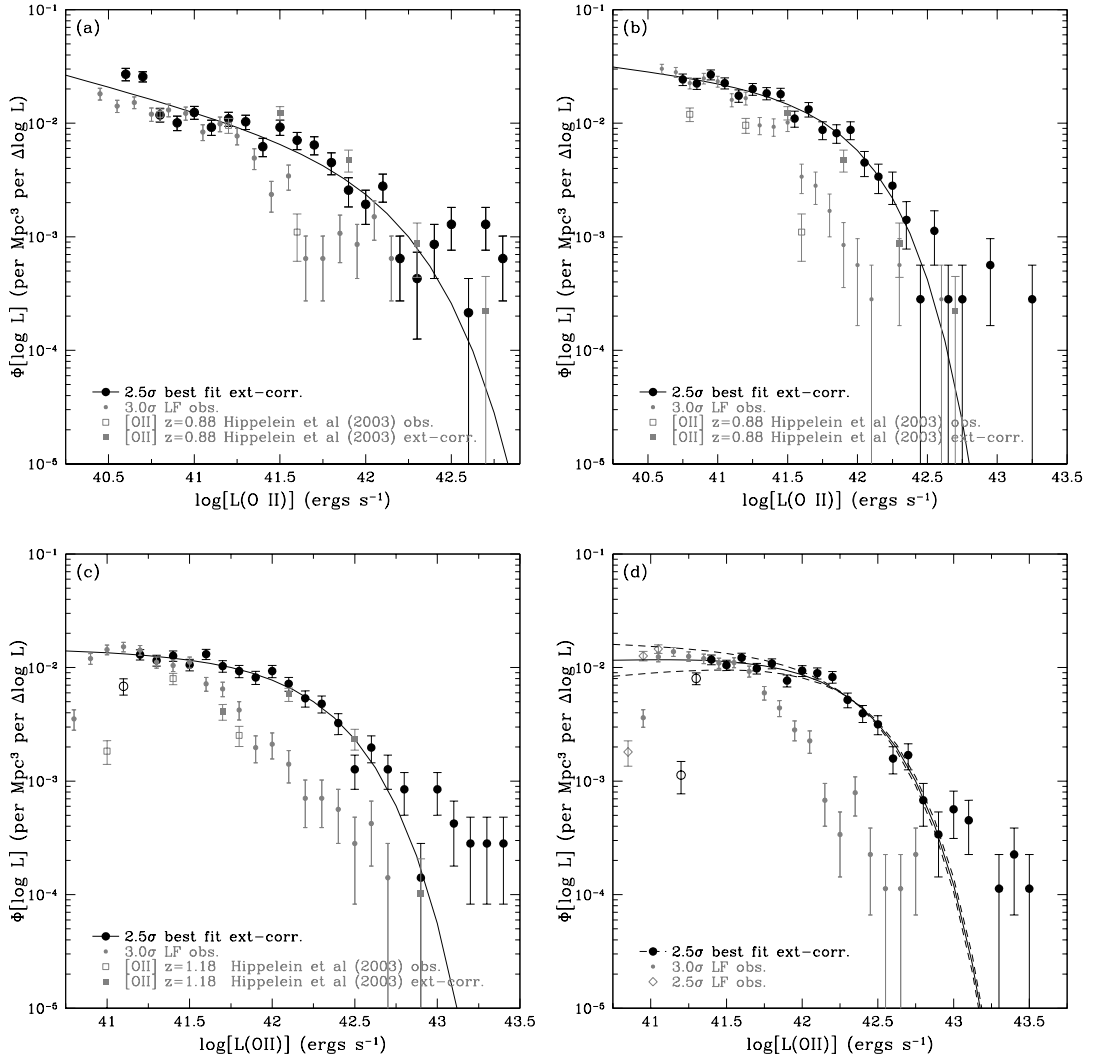


Figure 2.12 – (a) $z \approx 0.89 \pm 0.01$, (b) $z \approx 0.91 \pm 0.01$, (c) $z \approx 1.19 \pm 0.02$, and (d) $z \approx 1.47 \pm 0.02$. Ordinates are $\Phi[\log L]$ in units of $\text{Mpc}^{-3} (\Delta \log L)^{-1}$. Abscissas are $\log L(\text{O II})$ in ergs s^{-1} . The LFs for NB704, NB711, NB816, and NB921 are plotted as filled circles for the 2.5σ extinction-corrected (black) and 3σ observed (grey) sample. Open circles at the faint end are 2.5σ points excluded from the best fit given by the thick solid black lines. For NB921, the $\pm 1\sigma$ uncertainties in α are shown by the two thin short-dashed black lines, and the 2.5σ observed points are shown as open grey diamonds to illustrate the effect of incompleteness at the faint end. The luminosity functions of Hippelein et al. (2003) at $z = 0.87 - 0.89$ and $1.18 - 1.21$ are shown as open (observed) and filled (extinction-corrected) grey squares.

in detecting an additional 203, 188, 196, and 226 NB emitters for NB704, NB711, NB816, and NB921, respectively. Thus the 2.5σ method and the first method of artificial adding sources to the images yield similar results. For example, the NB816 and NB921 values are higher than method 1 by 22% and 6%, respectively. By extending the sample to 2.5σ , additional sources with an emission in the NB filter will be detected, but there will also be spurious detections. The predicted number of additional spurious detections based on Gaussian statistics is about 1%, which is rather optimistic. Even with 10% false detections, for example, this would mean that 20 sources are spurious (for each NB filter), but the remaining ~ 180 sources are real NB emitters. Only spectra of these faint emission lines can determine how many spurious sources exist at 2.5σ .

After re-identifying the NB emitters down to 2.5σ , the broad-band color classification described in § 2.2.1 are applied and the luminosity functions are then recalculated for each line emitter in all four NB filters. For the completeness-corrected Schechter fits provided in Table 2.5, this 2.5σ method is adopted as it shows the effects of incompleteness on the faint end slope. For the lowest luminosity bins (typically one to three, see Figures 2.10-2.12), the completeness of the H α 3σ sample as determined from this method is 52% (NB704, $\log L=38.0$), 67% (NB711, $\log L=37.9$ and 38.3), 59% (NB816, $\log L=39.2$), and 72% (NB921, $\log L=39.60$). For [O III], the completeness is 36% (NB704, $\log L=39.55$), 58% (NB711, $\log L=39.8$), 66% (NB816, $\log L=40.05$ and 40.25), and 62% (NB921, $\log L=40.1$, 40.2, and 40.3). Finally, the [O II] completeness is 68% (NB704, $\log L=40.45$), 51% (NB711, $\log L=40.5$), 54% (NB816, $\log L=40.8$ and 40.9), and 55% (NB921, $\log L=40.95$ and 41.05). These fits must be corrected for reddening to derive the star formation rate density.

2.2.5 Correcting for Dust Extinction

UV and optical measurements of the SFR are subject to significant dust obscuration. The amount of extinction can be estimated by comparing the observed and intrinsic Balmer decrements ($F_{H\alpha}/F_{H\beta}$), but this should be done for each individual galaxy. Generally, spectroscopy of all sources is not feasible, so to mitigate this problem, some studies apply a constant extinction throughout. For example, Fujita et al. (2003) and Pascual et al. (2005) adopted one magnitude of extinction for H α as determined by Kennicutt (1992). However, it has been apparent that more active star-forming galaxies suffer greater obscuration. In particular, Jansen et al. (2001) and Aragón-Salamanca et al. (2003) reveal that the Balmer-decrement derived color excess $E(B - V)$ depends on the M_B magnitude, and Hopkins et al. (2001) find a dependence of the color excess on the FIR luminosity. So far, observed SFRs have been reported.

To correct for extinction, three methods are considered. First, a standard $A_{H\alpha} = 1$ is applied. The second method utilizes available DEIMOS spectra. From 16 sources with redshift between 0.29 and 0.40, the average Balmer decrement after correcting for stellar absorption¹¹ is 4.38 ± 1.86 . The color excess can be determined from

$$E(B - V) = \frac{\log(R_{\text{obs}}/R_{\text{int}})}{0.4[k(\text{H}\beta) - k(\text{H}\alpha)]}, \quad (2.6)$$

where R_{obs} and R_{int} are the observed and intrinsic Balmer decrements. The latter is 2.86 for Case B recombination (Osterbrock, 1989). $k(\lambda) = A(\lambda)/E(B - V)$ is the reddening curve of Cardelli et al. (1989) with $k(\text{H}\beta) = 3.61$ and $k(\text{H}\alpha) = 2.54$. This corresponds to a color excess of $E(B - V) = 0.43 \pm 0.43$ or $A_{H\alpha} = 1.44 \pm 1.43$, which is reasonable compared to other studies that obtain $A_{H\alpha} = 0.5 - 1.8$ (Kennicutt, 1998, and references therein). The last method is the SFR-dependent

¹¹Following Kennicutt (1992), 5Å of stellar absorption is assumed for all objects.

correction of Hopkins et al. (2001):

$$\begin{aligned} \log SFR_{\text{obs}}(H\alpha) &= \log SFR_{\text{int}} - 2.360 \\ &\times \log \left[\frac{0.797 \log(SFR_{\text{int}}) + 3.786}{2.86} \right], \end{aligned} \quad (2.7)$$

where differences are due to cosmological corrections and using a Cardelli reddening curve rather than the Calzetti reddening curve (Hopkins, priv. comm). For [O II] and [O III] emitters, Equation 2.7 can be used so long as their luminosities are converted to H α prior to properly correcting for reddening. The conversions are given in § 2.2.6. The Schechter fits with the extinction correction of Equation 2.7 are provided in Table 2.6 and are shown in Figure 2.10-2.12 as filled black circles. For the H α NB711 LF, filled triangles are used to distinguish from the H α NB704 emitters. For [O III] measured in NB816, the extinction and completeness-corrected Schechter parameters including the unknown sources are $\log L_* = 42.23 \pm 0.07$, $\log \phi_* = -2.27 \pm 0.06$, and $\alpha = -0.88 \pm 0.05$. The first two methods of extinction corrections are also reported in this table.

2.2.6 The Star Formation Rate Density

The following conversions of luminosity to star-formation rate density $\dot{\rho}_{\text{SFR}}$ (in $M_\odot \text{ yr}^{-1} \text{ Mpc}^{-3}$) are assumed:

$$\dot{\rho}_{\text{SFR}}(\text{H}\alpha) = 7.9 \times 10^{-42} \mathcal{L}(\text{H}\alpha), \quad (2.8)$$

$$\dot{\rho}_{\text{SFR}}(\text{O II}) = (1.4 \pm 0.4) \times 10^{-41} \mathcal{L}(\text{OII}), \text{ and} \quad (2.9)$$

$$\dot{\rho}_{\text{SFR}}(\text{O III}) = (7.6 \pm 3.7) \times 10^{-42} \mathcal{L}(\text{OIII}), \quad (2.10)$$

where the H α and [O II] conversions are from Kennicutt (1998). The H α SFR conversion assumes a Salpeter initial mass function (IMF) with masses between 0.1 and 100 M_\odot . The [O II] conversion is from local emission line studies with an [O II]/H α = 0.57.

The conversion factor for [O III] is obtained from 196 NB704+NB921 emitters. Line fluxes for the two filters were obtained using Equation 2.1. A histogram plot of the [O III]-to-H α ratio is shown in Figure 2.13. This is compared with Hippelein et al. (2003)'s $z = 0.24$ and 0.64 [O III] emitters and the SDSS DR2 sample¹² (Brinchmann et al., 2004). These [O III] NB emitters have a larger [O III]/H α ratio compared with SDSS. This may be caused by a difference in the metallicity content between the two samples, and the selection requirement that both NB filters (NB704 and NB921) have an excess. The average and standard deviation for [O III] to H α +[N II] ratio are 0.86 and 0.42 . Correcting the NB921 line flux by the previous assumption that H α /[N II] = 4.66 , an [O III]/H α flux ratio of 1.05 ± 0.51 is used. This is similar to Teplitz et al. (2000), who fix this ratio to unity, and it is known to vary between 0.5 and 2 from Kobulnicky et al. (1999). In addition, the logarithm of the [O III]/H α ratio as a function of M_B^o is shown in Figure 2.13. The best fit is

$$\log \left[\frac{\text{O III}}{H\alpha} \right] = (0.073 \pm 0.013) M_B^o + 1.274 \pm 0.233, \quad (2.11)$$

which has less scatter and a higher [O III]-H α ratio compared to nearby star-forming galaxies of Jansen et al. (2000) and Moustakas & Kennicutt (2006). Although the [O III]-H α ratio is an average that allows for the determination of the SFR, a large dispersion in the ratio is found. A more appropriate calculation is to use the full histogram (see Figure 2.13) of [O III]-H α ratios known from 196 NB704+921 emitters. To use the histogram, a random integer between 1 and 196 is assigned for each [O III] emitter in all four NB filters. Each integer has a corresponding [O III]/H α value given from the sample of NB704+921 emitters. Then this ratio is used to convert from an [O III] LF to a H α LF for a SFR density. This method accounts for objects with low [O III]/H α , which will produce some

¹²The emission line catalogue can be found at http://www.mpa-garching.mpg.de/SDSS/DR2/Data/emission_lines.html.

luminous H α emission and hence an increase in L_* . Star formation rate densities for [O III] are reported using this method rather than integrating the [O III] LF.

For the remaining 16 NB704+921 emitters, which are believed to be [O II]+H β emitters based on BB colors, the [O II]/H β ratio is 0.51 ± 0.32 . This ratio is for seven emitters, as seven sources with line fluxes near the 3σ limit and two sources with [O II]/H β ratio of 5.2 and 8.7 are excluded.

In Table 2.6 the observed best fit Schechter parameters and the measured $\dot{\rho}_{\text{SFR}}$ for each redshift are summarized. The uncertainties in the Schechter parameters are determined using the non-linear least squares curve fitting package, MPFIT. These Schechter parameters are plotted as circles in Figure 2.14a, and the inferred SFR densities are plotted as circles in Figure 2.14b. Also plotted in Figure 2.14a as squares are measurements from Gallego et al. (1995, $z < 0.045$ H α), Hogg et al. (1998, $z < 1.5$ [O II]), Yan et al. (1999, $z = 1.3 \pm 0.6$ H α), Hopkins et al. (2000, $z = 1.25 \pm 0.55$ H α), Gallego et al. (2002, $z < 0.05$ [O II]), Tresse et al. (2002, $0.5 \leq z \leq 1.1$ H α), and Fujita et al. (2003, $z = 0.242 \pm 0.01$ H α). Extinction-corrected Schechter parameters (shown as filled squares) from Gallego et al. (1995), Tresse & Maddox (1998, $z = 0.2 \pm 0.1$ H α), Sullivan et al. (2000, $z < 0.3$ H α and [O II]), Tresse et al. (2002), Fujita et al. (2003), and Pérez-González et al. (2003, $z < 0.05$ H α) are provided in the upper panels. Also plotted are data points from Hippelein et al. (2003) for $z = 0.25 \pm 0.01$ H α , $z = 0.40 \pm 0.01$ and 0.64 ± 0.01 [O III], and 0.88 ± 0.01 and 1.19 ± 0.02 [O II]. All measurements have been converted from the published cosmology to the cosmology chosen in this paper.

For Figure 2.14b, SFR densities derived via integration of the luminosity function of previous surveys are included. In many cases, a LF is not available, and

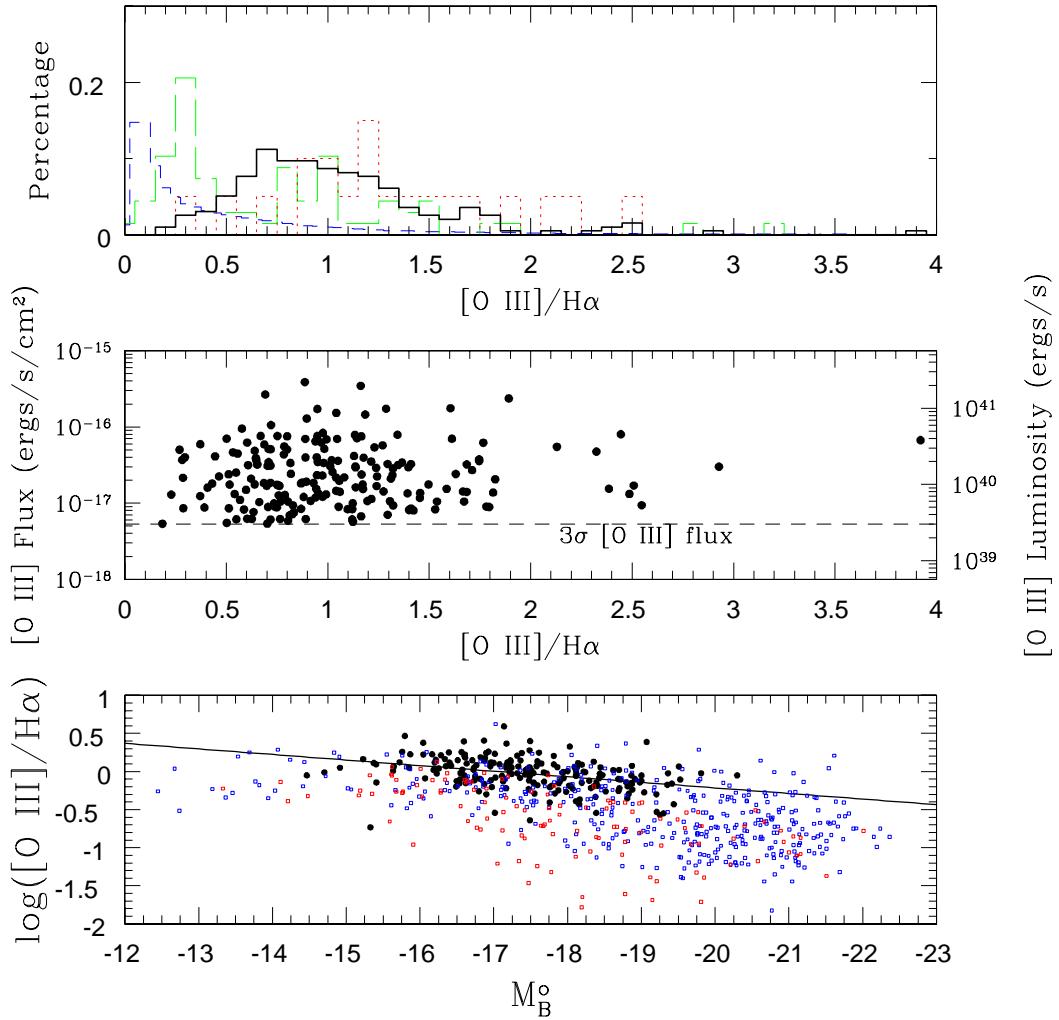


Figure 2.13 – The *top* diagram shows a solid black histogram for 196 $z \approx 0.40$ NB704+921 line emitters. The dotted and long-dashed histograms are from [Hippelein et al. \(2003\)](#) for 20 $z = 0.40$ and 68 $z = 0.25$ objects, respectively (colored red and green in the electronic edition). The SDSS DR2 histogram is shown as a short-dashed histogram (colored blue in the electronic edition). The *middle* figure shows the $[O\text{ III}]$ flux and luminosity as a function of the ratio. The *bottom* figure shows the logarithm of the ratio as a function of M_B° . In the electronic edition, the red and blue open squares are nearby star-forming galaxies from [Jansen et al. \(2000\)](#) and [Moustakas & Kennicutt \(2006\)](#), respectively. The best fit to the black points is given in Equation 2.11.

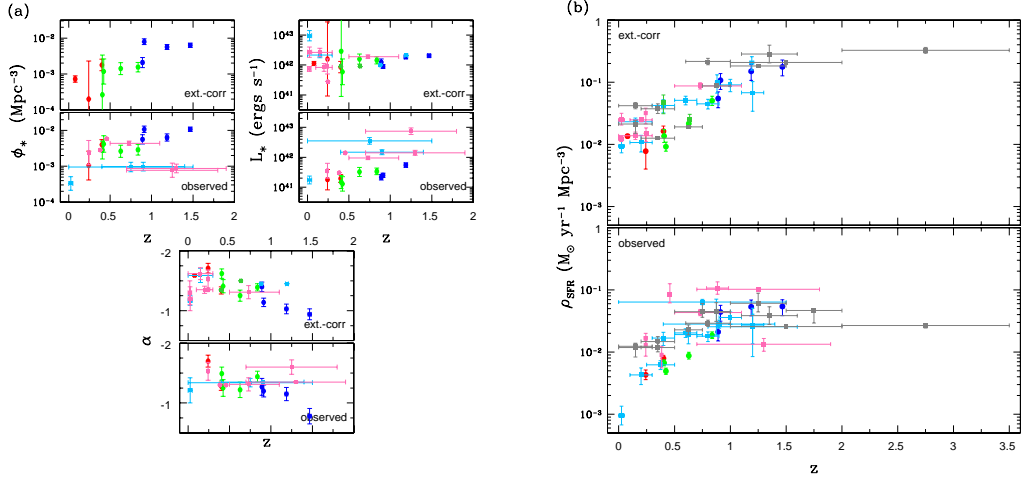


Figure 2.14 – NB emitters are shown as circles and squares represent previous emission line surveys: [O II] (light blue in the electronic edition) values are from Hammer et al. (1997), Hogg et al. (1998), Sullivan et al. (2000), Gallego et al. (2002), Hicks et al. (2002), and Teplitz et al. (2003). H α (pink in the electronic edition) points are from Gallego et al. (1995), Tresse & Maddox (1998), Glazebrook et al. (1999), Yan et al. (1999), Hopkins et al. (2000), Moorwood et al. (2000), Sullivan et al. (2000), Tresse et al. (2002), Fujita et al. (2003), Pérez-González et al. (2003), Glazebrook et al. (2004), and Pascual et al. (2005). [O III], [O III] (dark green in electronic edition), and H α data from Hippelein et al. (2003) are also included. Grey points are UV measurements from Cowie et al. (1999), Sullivan et al. (2000), Massarotti et al. (2001), and Wilson et al. (2002).

so these SFR densities are derived from a binned luminosity density. Additionally, studies that only report the luminosity density or SFR density are included. The H α $\dot{\rho}_{\text{SFR}}$ measurements are from Glazebrook et al. (1999) at $z = 0.89 \pm 0.1$, Glazebrook et al. (2004) for $z = 0.38$ and 0.46 , and Pascual et al. (2005) at $z = 0.24 \pm 0.01$. [O II] measurements from Hammer et al. (1997) at $z = 0.25$ - 0.50 , 0.50 - 0.75 , and 0.75 - 1.0 , Hogg et al. (1998) at $z = 0.2$, 0.4 , 0.6 , 0.8 , 1.0 , and 1.2 , and Hicks et al. (2002) at $z = 1.2 \pm 0.4$. Tables 2.7 and 2.8 summarizes the Schechter profiles and SFR densities for studies plotted in Figure 2.14a-b. UV-determined SFR densities from Lilly et al. (1996), Connolly et al. (1997), Treyer et al. (1998), Cowie et al. (1999), Sullivan et al. (2000), Massarotti et al. (2001), and Wilson et al. (2002) are shown as grey squares in Figure 2.14b. The conversion from the UV continuum between 1500 - 2800\AA to a star-formation rate is $\text{SFR}_{\text{UV}}(M_{\odot} \text{ yr}^{-1}) = 1.4 \times 10^{-28} L_{\nu}(\text{ergs s}^{-1} \text{ Hz}^{-1})$ (Kennicutt, 1998; Hopkins, 2004). Again a Salpeter IMF with masses between 0.1 and $100 M_{\odot}$ is assumed.

2.3 Comparison with Other Studies

2.3.1 H α Emitters

The LF reported here for $z \approx 0.07$ extends an order of magnitude fainter than Jones & Bland-Hawthorn (2001) and about two orders compared to Gallego et al. (1995), giving a better constraint on the faint end slope. The NB704 and NB711 H α LFs indicate that α is steeper by about 0.3 compared to Gallego et al. (1995); it is also steeper than that of Treyer et al. (2005) and Wyder et al. (2005). This effect makes little difference in the SFR density; however, it reveals that there are more low luminosity star-forming galaxies than previously predicted for $z \lesssim 0.1$. At similar luminosities, the NB704 and NB711 number densities agree with those

of [Jones & Bland-Hawthorn \(2001\)](#).

For $z \approx 0.24$, while many emission-line studies are available, there is still significant scatter in the resulting H α LFs. The H α NB816 LF is somewhat consistent with [Tresse & Maddox \(1998\)](#) and [Sullivan et al. \(2000\)](#) particularly the latter with a steep α : < -1.5 . However, the LFs of [Jones & Bland-Hawthorn \(2001\)](#), [Fujita et al. \(2003\)](#), [Hippelein et al. \(2003\)](#), and [Pascual et al. \(2005\)](#) have a higher number density by a factor of two or more. This is probably the result of cosmic variance as an estimate of the relative cosmic variance is significant: following [Somerville et al. \(2004\)](#), the bias b is about 0.7 for a comoving number density of 0.05 Mpc^{-3} and $\sigma_{\text{DM}} \approx 0.9$ for a volume of $4.7 \times 10^3 \text{ Mpc}^3$, therefore, $\sigma_v = b\sigma_{\text{DM}} \approx 0.6$.

The H α NB816 LF of [Fujita et al. \(2003\)](#) has twice as many line emitters per logarithmic bin than the NB816 emitters in this paper. But the $B - R_C$ and $R_C - I_C$ colors were examined for Hawaii HDF-N sources with NB816 redshifts, and a significant (about 50%) amount of contamination from [O III] into their H α selection criterion was found, which will certainly reduce their number densities. This can be seen in Figure 2.15, and indicates that using population synthesis models [as [Fujita et al. \(2003\)](#) have done] is not enough; spectroscopic identification is required to obtain a sample with low contamination. It should be pointed out that the selection criterion of [Fujita et al. \(2003\)](#) does distinguish [O II] from H α . At $z = 0.40$, [Jones & Bland-Hawthorn \(2001\)](#) report a higher density by about a factor of two. The estimate of the LF that [Glazebrook et al. \(2004\)](#) made with a small number of H α emitters is consistent with the H α NB921 LF.

The extinction-corrected H α SFR densities ($z < 0.5$) appear consistent with the H α surveys of [Gallego et al. \(1995\)](#), [Sullivan et al. \(2000\)](#), and [Hippelein et](#)

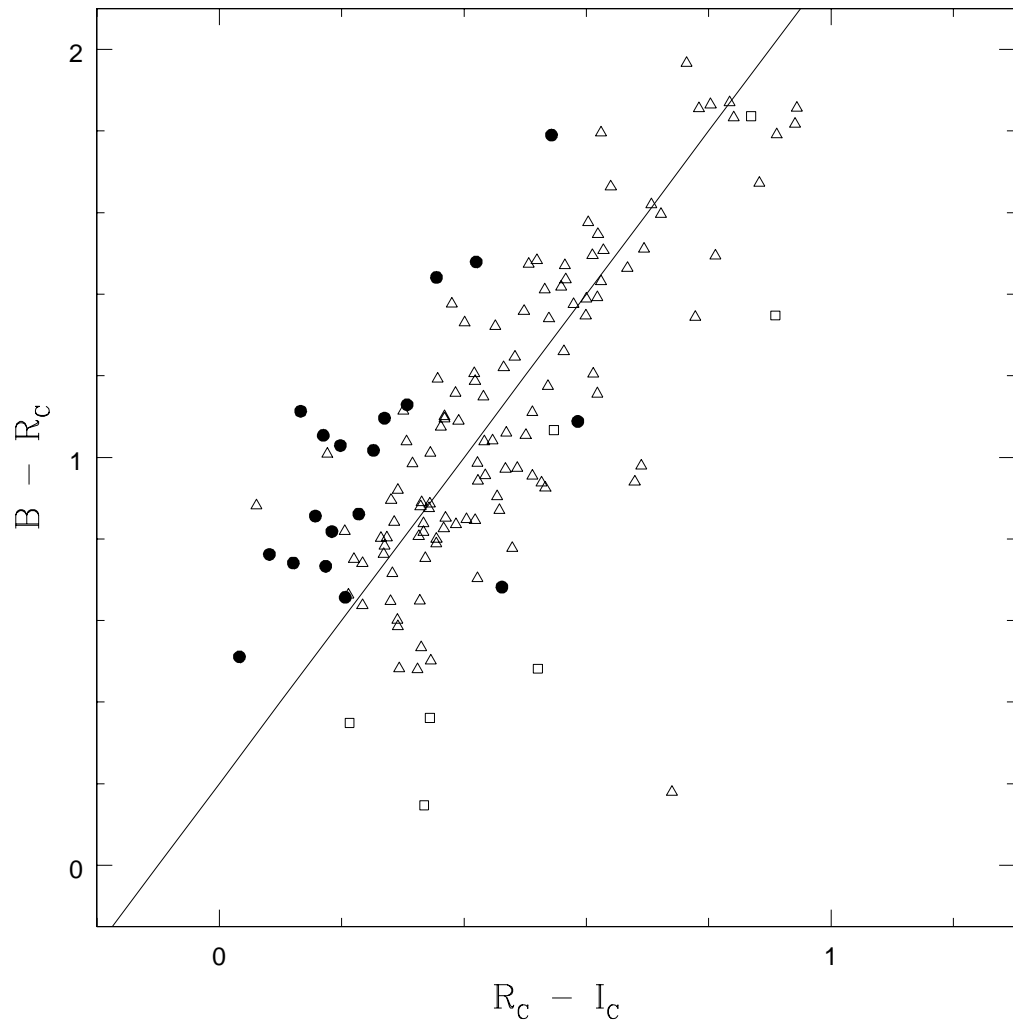


Figure 2.15 – $B - R_C$ and $R_C - I_C$ colors for Hawaii HDF-N galaxies with NB816 redshifts. Filled circles are $H\alpha$ ($z \approx 0.24$), open triangles are $[O\ III]$ or $H\beta$ ($z \approx 0.63$), and $[O\ II]$ are shown as open squares. The solid line is the selection criterion of [Fujita et al. \(2003\)](#): $B - R_C = 2(R_C - I_C) + 0.20$.

al. (2003), [O II] measurements from Hogg et al. (1998) and Gallego et al. (2002), and a UV measurement from Cowie et al. (1999). However, H α measurements from Fujita et al. (2003) and Pérez-González et al. (2003), [O III] from Hippelein et al. (2003), UV from Wilson et al. (2002), and [O II] from Sullivan et al. (2000) are twice as high. Assuming that each of these surveys do not have any systematic differences, cosmic variance can certainly explain a difference by a factor of two.

2.3.2 [O III] and [O II] Emitters

The Fabry-Perot interferometry technique employed by Hippelein et al. (2003) also selects similar redshift intervals with the exception of the NB921 emitters ($z = 0.84$ and 1.46). Figure 2.11a-c and 2.12a-c reveal good agreement between the observed LFs. The extinction-corrected LFs cannot be compared, as different reddening assumptions are used. The observed [O II] luminosity densities (or SFR densities since the same [O II]/H α ratio is used) for $z \approx 0.9$ to 1.5 agree with those of Hogg et al. (1998).

2.4 Discussion

2.4.1 Differences between NB704 and NB711 LFs

The LFs for H α at $z = 0.074$ and 0.086 show little differences. This could be coincidental given that cosmic variance is expected to be large in a small comoving volume. For [O III], the lower redshift LF shows a steeper faint end slope and has 351 versus 209 emitters. This can be the result of differences in the NB filter as the NB711 has a comoving volume that is smaller by 25%. For [O II], the density of NB711 emitters below a luminosity of $10^{41.5}$ ergs s $^{-1}$ is twice as high compared to NB704 emitters, and there is 818 versus 673 emitters. The

difference in number of line emitters cannot be explained by the smaller NB711 bandpass as more objects are seen in the NB711 filter. However, the difference can be attributed to cosmic variance.

2.4.2 Evolution of the LF and SFR Densities

In Figure 2.14a, a steep evolution in the number density ϕ_* is found while the luminosity L_* has a milder evolution. The comoving density and luminosity can be fitted with $\phi_* \propto (1+z)^P$ and $L_* \propto (1+z)^Q$ with $P = 3.85 \pm 0.95$ and $Q = 0.47 \pm 0.58$. This is contrary to Hopkins (2004) who reports $P = 0.15 \pm 0.60$ and $Q = 2.70 \pm 0.60$. In addition, the faint end slope α appears to flatten out at higher redshifts, evolving from -1.6 to -1.0 as z goes from 0.08 to 1.47 with $\alpha \propto (1.94 \pm 0.37) \log(1+z)$. The flattening at higher redshifts resembles the effects of incompleteness at the faint end. However, even with the completeness correction described in § 2.2.4, α still evolves toward a flatter slope at higher redshifts. Moreover, at the highest redshifts, α is well determined with several bins in the LF. One other possible concern is that [O III] and [O II] emitters were improperly identified, and resulted in a contamination at the faint end of the H α LF. The contamination reported from spectra indicated that less than 10% would be mis-identified, so this could not account completely for the steep faint end slope at low redshift. Gobasch et al. (2004, 2006) also see an evolution (although mild) in α from the blue and red band LFs of 5500 galaxies in the FORS Deep Field. However, Arnouts et al. (2005) and Wyder et al. (2005) find the converse with ultraviolet continuum measurements.

The integrated [O II] SFR densities at $z \sim 1$ are found to be 10 times higher than at $z < 0.5$ from the H α and [O III] NB emitters. While this is consistent with some studies, other studies report a SFR density that is twice as high for similar

redshifts. There is agreement between the extinction-corrected [O II] NB emitters with measurements above z of 0.75 from UV continuum and [O II] emission line surveys.

The [O III] SFR densities appear half as large as the H α and [O II] measurements. This is the result of not detecting sources with low [O III]/H α ratios, as these sources will be detected in the NB921 filter, but will be too faint for the NB704 filter. Figure 2.13 shows that local studies have found sources with [O III]/H α ratios as small as 0.03. Even if a small fraction of [O III] NB emitters have low [O III]/H α ratios, this can affect the LF enough to raise the SFR by an additional factor of two.

2.4.3 Future Work

The method described in this paper can be applied to other large fields. For example, deep NB816 imaging with Suprime-Cam of SSA22 (Hu et al., 2004) and around SDSSP J104433.04-012502.2 (Fujita et al., 2003; Ajiki et al., 2006) were intended to identify LAEs. The low- z NB emitter sample can be obtained from these fields at three additional redshifts of 0.24, 0.64, and 1.18. For SDSSP J104433.04, the previous work of Fujita et al. (2003) for $z \approx 0.24$ H α emitters can be improved by reducing contamination (see § 2.3.1). Also, imaging at the remaining three NB filters will significantly expand the sample with nine more redshift intervals. The results of these individual fields can be compared to the results presented for the SDF, and the effects of cosmic variance will be reduced when all NB emitters are combined together. Moreover, NB imaging of deep spectroscopic galaxy surveys (e.g., DEEP2) will (*i*) further improve these fields as this method provides the redshift of several hundred objects in the fields, (*ii*) provide existing spectra of NB emitters to further examine the NB technique, and

(*iii*) NB921 imaging of known DEEP2 galaxies with the redshifts of $z = 0.84$ and 1.47 would provide additional spectroscopic points to be overlayed on Figure 2.7b as the z'_{cont} is unknown without NB921 photometry.

2.5 Conclusion

Using four NB and five BB filters, one to two thousand NB line-emitters (for each filter) are photometrically identified. Considering the strongest emission lines ($\text{H}\alpha$, [O II], and [O III]), broad-band colors are used to distinguish them into twelve redshifts intervals (some of which overlap). With a large sample of NB emitters, an averaged rest-frame optical to UV SED is obtained for each redshift. The $\text{H}\alpha$ SEDs show little differences for all four redshifts. Generally, high-EW emitters appear bluer relative to the low-EW objects.

The luminosity functions are generated for eleven redshift windows between $z = 0.07$ and 1.47 . These luminosity functions are integrated to obtain a luminosity density, and converted to a measured star-formation rate density after correcting for extinction. The lowest redshifts covered by the NB704 and NB711 filters indicate a steep faint end slope. These NB emitters show that the SFR at $z \approx 1$ is ten times higher than $z \sim 0$ with a steep decline to $z \approx 0.4$. Moreover, the [O II] SFR is consistent with UV and other [O II] measurements. Below z of 0.5 , $\dot{\rho}_{\text{SFR}}$ measurements from $\text{H}\alpha$ and [O III] emitters are consistent with several studies; however, there appears to be a discrepancy in $\dot{\rho}_{\text{SFR}}$ by a factor of two or more from other studies. Cosmic variance may be imposed to explain the discrepancy.

Table 2.5. Schechter Fits and Inferred SFR Densities

z	N	Observed fit (completeness-corrected)				A = 0	$\log \dot{\rho}_{\text{SFR}}$ A = 1.0	$\log \dot{\rho}_{\text{SFR}}$ A = 1.44
		$\log \phi_{\star}$	$\log L_{\star}$	α	$\log \mathcal{L}$			
H α emitters								
0.07, 0.09	171, 147
0.24	259	-2.98 \pm 0.40	41.25 \pm 0.34	-1.70 \pm 0.10	38.74 \pm 0.08	-2.37	-1.97	-1.79
0.40	391	-2.40 \pm 0.14	41.29 \pm 0.13	-1.28 \pm 0.07	39.00 \pm 0.05	-2.10	-1.70	-1.53
[O III] emitters								
0.41	351	-2.55 \pm 0.25	41.17 \pm 0.22	-1.49 \pm 0.11	38.85 \pm 0.06	-2.17 ^a	-1.77	-1.59
0.42	209	-2.38 \pm 0.22	41.11 \pm 0.24	-1.25 \pm 0.13	38.81 \pm 0.09	-2.31 ^a	-1.91	-1.73
0.62	293	-2.58 \pm 0.17	41.51 \pm 0.15	-1.22 \pm 0.13	39.00 \pm 0.05	-2.06 ^a	-1.66	-1.48
0.83	662	-2.54 \pm 0.15	41.53 \pm 0.11	-1.44 \pm 0.09	39.19 \pm 0.03	-1.73 ^a	-1.33	-1.15
[O II] emitters								
0.89	673	-2.25 \pm 0.13	41.33 \pm 0.09	-1.27 \pm 0.14	39.18 \pm 0.03	-1.68	-1.28	-1.10
0.91	818	-1.97 \pm 0.09	41.40 \pm 0.07	-1.20 \pm 0.10	39.50 \pm 0.02	-1.36	-0.96	-0.78
1.18	894	-2.20 \pm 0.10	41.74 \pm 0.07	-1.15 \pm 0.11	39.58 \pm 0.02	-1.27	-0.87	-0.69
1.47	951	-1.97 \pm 0.06	41.60 \pm 0.05	-0.78 \pm 0.13	39.59 \pm 0.02	-1.27	-0.87	-0.69

^aThe [O III] $\log \dot{\rho}_{\text{SFR}}$ measurements do not use Equation 2.8, but follows the random integer approach described in § 2.2.6.

Table 2.6. Continuation of Table 2.5

z	N	Extinction-corrected fit				$\log \dot{\rho}_{\text{SFR}}$ Eq. 2.7
		$\log \phi_{\star}$	$\log L_{\star}$	α	$\log \mathcal{L}$	
H α emitters						
0.07, 0.09	171, 147	-3.14 \pm 0.09	42.05 \pm 0.07	-1.59 \pm 0.02	39.23 \pm 0.03	-1.87
0.24	259	-3.70 \pm 1.06	42.20 \pm 1.24	-1.71 \pm 0.08	38.99 \pm 0.29	-2.11
0.40	391	-2.75 \pm 0.16	41.93 \pm 0.19	-1.34 \pm 0.06	39.31 \pm 0.08	-1.79
[O III] emitters						
0.41	351	-3.58 \pm 1.11	42.46 \pm 1.51	-1.62 \pm 0.08	39.25 \pm 0.48	-1.87 ^a
0.42	209	-2.93 \pm 0.35	41.77 \pm 0.43	-1.41 \pm 0.11	39.02 \pm 0.17	-2.03 ^a
0.62	293	-2.51 \pm 0.11	41.70 \pm 0.10	-1.03 \pm 0.09	39.20 \pm 0.05	-1.66 ^a
0.83	662	-2.81 \pm 0.13	42.16 \pm 0.12	-1.39 \pm 0.06	39.51 \pm 0.04	-1.30 ^a
[O II] emitters						
0.89	673	-2.68 \pm 0.14	42.09 \pm 0.11	-1.40 \pm 0.08	39.59 \pm 0.03	-1.26
0.91	818	-2.10 \pm 0.08	41.95 \pm 0.06	-1.14 \pm 0.07	39.89 \pm 0.02	-0.97
1.18	894	-2.25 \pm 0.07	42.27 \pm 0.06	-1.03 \pm 0.08	40.03 \pm 0.02	-0.82
1.47	951	-2.20 \pm 0.06	42.31 \pm 0.05	-0.94 \pm 0.09	40.10 \pm 0.02	-0.75

^aThe [O III] $\log \dot{\rho}_{\text{SFR}}$ measurements do not use Equation 2.8, but follows the random integer approach described in § 2.2.6.

Table 2.7. Compilation of Emission-line Observed SFR Density Measurements

Reference	Estimator	Redshift	C_{L_\star}	C_{ϕ_\star}	$\log L_\star$	$\log \phi_\star$	α	$\dot{\rho}_{\text{SFR,obs}}^{\text{a}}$
Hammer et al. (1997)	[O II]	0.375±0.125	0.6880	1.5103	-2.20 ^{+0.07} _{-0.08}
		0.625±0.125	0.7801	1.2168	-1.72 ^{+0.11} _{-0.15}
		0.875±0.125	0.8538	1.0445	-1.35 ^{+0.20} _{-0.38}
Hogg et al. (1998)	[O II]	0.750±0.750	2.5650	0.2147	42.55±0.11	-3.02±0.13	-1.34±0.07	-1.20±0.04
		0.200±0.100	2.2799	0.2689	-2.37 ^{+0.11} _{-0.16}
		0.400±0.100	2.4363	0.2384	-1.77 ^{+0.09} _{-0.12}
		0.600±0.100	2.5280	0.2212	-1.69 ^{+0.06} _{-0.08}
		0.800±0.100	2.5725	0.2126	-1.75 ^{+0.07} _{-0.08}
		1.000±0.100	2.5839	0.2093	-1.44 ^{+0.09} _{-0.11}
Gallego et al. (2002)	[O II]	1.200±0.100	2.5731	0.2094	-1.57 ^{+0.18} _{-0.30}
		0.025±0.025	2.0940	0.3180	41.24±0.13	-3.48±0.19	-1.21±0.21	-3.02±0.15
		1.200±0.400	0.9279	0.9151	-1.59 ^{+0.30} _{-0.48}
		0.900±0.500	1.0000	1.0000	42.15±0.08	-3.06±0.12	-1.35	-1.55±0.06
		H α	0.885±0.099	0.8564	1.0394	-0.97±0.10
		H α	1.300±0.600	0.9468	0.8905	42.82	-2.82	-1.35
Hopkins et al. (2000)	H α	1.250±0.550	2.1095	0.2675	42.87±0.11	-3.11±0.20	-1.60±0.12	-1.00
		0.242±0.014	0.6305	1.8103	-1.77 ^{+0.08} _{-0.09}
Tresse et al. (2002)	H α	0.730 ^{+0.37} _{-0.23}	0.8131	1.0811	41.98±0.06	-2.36±0.06	-1.31±0.11	-1.37±0.050
Fujita et al. (2003)	H α	0.242±0.009	1.0000	1.0000	41.55±0.25	-2.62±0.34	-1.53±0.15	-1.90 ^{+0.08} _{-0.17}
Glazebrook et al. (2004)	H α	0.384±0.006	1.0000	1.0000	41.49	-2.55	-1.30	-2.05 ^{+0.14} _{-0.21}
		0.458±0.006	1.0000	1.0000	42.15	-2.23	-1.30	-1.07 ^{+0.17} _{-0.14}

^aThe luminosity density is obtained from the available binned data instead of integrating over all luminosities if no LF parameters are provided.

Note. — Col. (4) and (5) provide factors to convert L_\star (ergs s^{-1}) and ϕ_\star (Mpc^{-3}) to the common cosmology. Schechter parameters ($\log L_\star$, $\log \phi_\star$, and α), where available, are given in Col. (6)-(8) for observed measurements. Observed $\dot{\rho}_{\text{SFR}}$ (in $M_\odot \text{ yr}^{-1} \text{ Mpc}^{-3}$) is given in Col. (9).

Table 2.8. Compilation of Emission-line Extinction-Corrected SFR Density Measurements

Reference	Estimator	Redshift	C_{L_\star}	C_{ϕ_\star}	$\log L_\star$	$\log \phi_\star$	α	$\dot{\rho}_{\text{SFR,int}}^{\text{a}}$
Gallego et al. (2002)	[O II]	0.025±0.025	2.0940	0.3180	42.98±0.17	-4.21±0.16	-1.17±0.08	-2.03±0.110
Sullivan et al. (2000)	[O II]	0.150±0.150	2.3483	0.2351	42.33±0.09	-3.45±0.18	-1.59±0.12	-1.64±0.06
Hippelein et al. (2003)	[O II]	0.881±0.014	1.0000	1.0000	42.00	-2.36	-1.45	-1.00 ^{+0.12} _{-0.17}
		1.193±0.018	1.0000	1.0000	42.32	-2.36	-1.45	-0.68 ^{+0.09} _{-0.12}
Gallego et al. (1995)	H α	0.022±0.022	0.5219	2.5663	41.87±0.08	-2.79±0.20	-1.30±0.20	-1.91 ^{+0.04} _{-0.04}
Tresse & Maddox (1998)	H α	0.200±0.100	0.6110	1.8585	41.92±0.13	-2.56±0.09	-1.35±0.06	-1.61 ^{+0.03} _{-0.03}
Sullivan et al. (2000)	H α	0.150±0.150	2.3483	0.2351	42.42±0.14	-3.55±0.20	-1.62±0.10	-1.86±0.06
Tresse et al. (2002)	H α	0.730 ^{+0.37} _{-0.23}	0.8131	1.0811	42.28±0.06	-2.36±0.06	-1.31±0.11	-1.06±0.05
Fujita et al. (2003)	H α	0.242±0.009	1.0000	1.0000	41.95±0.25	-2.62±0.34	-1.53±0.15	-1.50 ^{+0.08} _{-0.17}
Hippelein et al. (2003)	H α	0.245±0.007	1.0000	1.0000	41.45	-2.32	-1.35	-1.83 ^{+0.10} _{-0.13}
Pérez-González et al. (2003)	H α	0.025±0.025	1.0000	1.0000	42.43±0.17	-3.00±0.20	-1.20±0.20	-1.61 ^{+0.11} _{-0.08}
Hippelein et al. (2003)	[O III]	0.401±0.011	1.0000	1.0000	41.95	-2.32	-1.35	-1.33 ^{+0.13} _{-0.18}
		0.636±0.010	1.0000	1.0000	41.95	-2.70	-1.50	-1.61 ^{+0.09} _{-0.11}

^aThe luminosity density is obtained from the available binned data instead of integrating over all luminosities if no LF parameters are provided.

Note. — Col. (4) and (5) provide factors to convert L_\star (ergs s^{-1}) and ϕ_\star (Mpc^{-3}) to the common cosmology. Schechter parameters ($\log L_\star$, $\log \phi_\star$, and α), where available, are given in Col. (6)-(8) for observed measurements. Observed $\dot{\rho}_{\text{SFR}}$ (in $M_\odot \text{ yr}^{-1} \text{ Mpc}^{-3}$) is given in Col. (9).

CHAPTER 3

H α Star Formation Rates at $z \approx 0.8$ from the NewH α Survey

The H α nebular emission line, a star formation rate (SFR) indicator valued for its direct physical connection to short-lived massive stars, has been widely used to measure the the SFRs of individual galaxies as well as the SFR density in the local universe ($z \sim 0.05$; Gallego et al. 1995, $z < 0.4$; e.g., Ly et al. 2007; Dale et al. 2008) universe. These measurements have shown that the SFR density was higher in the past than now. While it is logical to conduct H α surveys at even higher redshifts ($z > 0.5$) to trace the star formation history of the universe, such attempts have been difficult, as H α is redshifted into the near-IR where observational limitations (e.g., higher sky background, the inability to use CCDs) exist. While some have tried (e.g., Yan et al., 1999; Hopkins et al., 2000; Tresse et al., 2002), their resultant samples are small in size and area coverage, and are easily dominated by field-to-field fluctuations from the non-uniform distribution of galaxies. Thus, other SFR indicators (e.g, the UV continuum or other bluer emission lines), which are accessible in the optical, have been used. A decade of success has led to SFR density measurements in galaxies at redshifts as high as ≈ 6 (e.g., Steidel et al., 2003; Ly et al., 2007; Bouwens et al., 2007); however, the SFR indicators employed suffer from higher dust obscuration effects and dependence on metallicity, for example, and result in a scatter of a factor of a few in studying

the cosmic star formation history ([Hopkins, 2004](#)). It still remains that H α measurements at higher redshifts are needed as an additional constraint on the star formation history, and is one of the primary motivations for this chapter. In particular, it is useful to trace the cosmic star formation history throughout time with a single consistent tracer and be able to compare with the overall histories determined with different indicators.

In this study, we present H α luminosity functions and SFR densities at $z \approx 0.81$ (when the universe was half its age). The analysis is based on observations from the NewH α survey ([Lee et al., 2010](#)), which is conducted with the NOAO Extremely Wide-Field Infrared Imager (NEWFIRM; [Probst et al., 2004, 2008](#)) at the KPNO 4m telescope. NewH α has identified approximately four hundred H α emitting galaxies over 0.82 deg^2 with a narrow-band (NB; FWHM $\approx 110\text{\AA}$) filter centered at $1.187\mu\text{m}$ (hereafter NB1187). The general aspects and survey strategy of the NewH α survey are discussed in detail in [Lee et al. \(2010\)](#).

This chapter is outlined as follows. In § [3.1](#), we give an overview of the NewH α data that are used in our analysis. Also included is a discussion of the identification of NB1187 excess emitters and the follow-up optical spectroscopy that was obtained by the NewH α team. Section [3.2](#) discusses the empirical technique used to separate H α emitters from other NB1187 excess emitters, the accuracy of our photometric selection, and how emission-line fluxes and equivalent widths (EWs) are derived. In § [3.3](#), estimates of the survey’s completeness and the surveyed volume are presented, and § [3.4](#) presents the H α luminosity function (LF) and comoving SFR density at $z \sim 0.8$. Comparisons of these results with existing H α measurements are described in Section [3.5](#). We also provide a detailed comparison of the NewH α survey against other recent $z \sim 0.8$ narrow-band H α surveys, and explain how different choices in selection and lack of spectroscopic

data affect the final SFR density measurements. A discussion of our results and their implications for the evolution of typical galaxies at $z \sim 0.8$ is provided in Section 3.6. Future work is discussed in § 3.7, and we summarize this work in § 3.8.

3.1 The NewH α Survey

3.1.1 Near-IR Narrow-band Observations and Data Reduction

An overview of the NewH α survey is provided here. A complete description can be found in Lee et al. (2010). NEWFIRM J -band and NB1187 (centered at 11870Å with FWHM of 110Å) observations were obtained for 5 pointings in 2007 Dec, 2008 Sept, and 2008 Oct (see Table 3.1). The NB filter was designed to sample between the OH sky lines for greater depth. Three of the pointings are in the Subaru-XMM Deep Survey (SXDS; Furusawa et al., 2008, referred to as SXDS-N, SXDS-S, and SXDS-W), one pointing is in the Cosmic Evolution Survey¹ (COSMOS; Scoville et al., 2007), and a final pointing is located in SSA-22 (Cowie et al., 1996). These fields were chosen for the ancillary data that are available from other observatories (see Section 3.1.3 for further discussion). In this initial analysis, we present results for the SXDS and COSMOS pointings since the ancillary optical data for SSA-22 have less uniform coverage over our NEWFIRM field.

The FoV of the NEWFIRM detector is $27\rlap{.}'6 \times 27\rlap{.}'6$, and each pointing effectively covers ~ 700 arcmin 2 in size. The net integration time obtained in the NB1187 and J -band were 8.2-12.7 hours and 2.3-4.0 hours, respectively, with exposure times of 240 seconds and 60 seconds. This yielded 3σ limiting magnitude

¹Their public website can be found at <http://cosmos.astro.caltech.edu>.

depths of $\sim 23.8 - 24.0$ ($2'' \phi$). The sensitivity of the data was determined by placing ~ 5000 random apertures on the images. Pixels that were affected by the flux from a source, which is determined from an object mask from SExtractor, were excluded in the calculation. The seeing of the J (NB1187) data varied from $1''.0$ ($1''.1$) to $1''.6$ ($1''.9$) and observing conditions were mostly photometric, particularly during the 2008 observations. The total area utilized for our analyses is 0.82 deg^2 or a comoving volume of $9.12 \times 10^4 h_{70}^{-3} \text{ Mpc}^3$ ($2.72 \times 10^4 h_{70}^{-3} \text{ Mpc}^3$ per 0.25 deg^2).

Standard NIR reduction techniques were used to process the data. The procedure included a first-pass reduction to create a deep object mask. The object mask is then used to create flat-fields and sky images to enable subtraction of the sky background. Then the sky-subtracted images were used for the second-pass processing and creation of the final mosaics. One problem that these detectors suffer from is persistent flux from bright sources. We masked these false sources as follows. First we require that the telescope be dithered between frames by at least a few arcseconds to avoid persistent fluxes falling on genuine sources. Then the sky-subtracted images were used to generate reliable persistence masks by comparing the objects in a given image against the previous frames to identify affected pixels. The method that we developed to identify persistent sources flags roughly 95% of persistence sources that are seen “by eye.” The majority of the remaining 5% were faint enough that they did not appear in the mosaics after the stacking of a large number of frames.

The data reduction was performed with routines from the IRAF/NFEXTERN² package, using our own automated PyRAF-based pipeline, optimized for our NEWFIRM data.

²See the NOAO NEWFIRM page at <http://www.noao.edu/ets/newfirm/>.

Photometric and astrometric calibrations were done against $\sim 150 - 300$ 2MASS ([Skrutskie et al., 2006](#)) sources in each field. In general, the astrometry is good to within $0''.15 - 0''.20$ with negligible systematic offsets. It is assumed that there is no color-term correction between NB1187 and J for 2MASS sources (such corrections are small, ~ 0.05 mag). The accuracy of the zeropoint calibration is typically 0.05 mag and remains constant as a function of J /NB1187 magnitude and versus radius from the mosaic center to within the photometric scatter. Since 2MASS is on a Vega system, conversion to AB magnitudes was done by convolving the filter bandpasses with the Vega spectrum. The corrections that we determined are: $m(\text{AB}) - m(\text{Vega}) = 0.8676$ (NB1187) and 0.9528 (J).

3.1.2 Identification of Emission-Line Galaxy Candidates

To identify NB1187 excess emitters, first the PSF of the J -band and NB1187 mosaics are matched. This was done by stacking the postage stamps of point-like 2MASS sources (with no nearby objects) to generate the point spread function for each field in each waveband. After determining the FWHM, the mosaic with the higher resolution (typically the J -band) was then degraded to match the other (assuming a Gaussian kernel). As a sanity check, the PSF-matched J -band mosaics were scaled down (by the ratio of the filter bandpass widths) and then subtracted from the NB1187 mosaics. The residuals indicate that the image degradation process was done correctly.

SExtractor (SE, version 2.5.0; [Bertin & Arnouts, 1996](#)) was then run in dual-image mode with the NB1187 mosaic as the detection image. The broad-band minus narrow-band color is examined, and NB1187 excess emitters are identified if they meet the following two criteria. First, a minimum $J - \text{NB1187}$ color of

Table 3.1. Summary of NEWFIRM Imaging

Field	R.A., Dec (J2000)	Observation Dates	Filter	Int. time (hours)	FWHM (arcsec)	2'' ϕ AB Limiting Magnitude (3 σ)			
						SE	SW	NE	NW
COSMOS	10:01, +02:01	2007 Dec 4,5	<i>J</i>	2.30	1.20	23.808	23.917	23.933	23.929
		2007 Dec 2-5	NB	8.16	1.50	23.767	23.850	23.857	23.908
SSA-22	22:17, +00:19	2008 Sep 23,24,28, Oct 19	<i>J</i>	3.43	1.20	23.920	23.967	24.055	24.073
		2008 Sep 23,24,28, Oct 19-21	NB	11.53	1.15	23.935	24.051	24.071	24.087
SXDS-N	02:18, -04:38	2008 Sep 28,29, Oct 1,22,23	<i>J</i>	3.52	1.10	23.876	23.994	23.990	24.016
		2008 Sep 29, Oct 1,22,23	NB	8.47	1.20	23.773	23.938	23.902	23.977
SXDS-S	02:18, -05:15	2007 Dec 3-5	<i>J</i>	2.40	1.25	23.922	24.046	24.099	24.049
		2007 Dec 2-5	NB	10.28	1.60	23.743	23.816	23.911	23.925
SXDS-W	02:16, -04:57	2008 Sep 23-26,28, Oct 21,22	<i>J</i>	3.97	1.20	24.020	24.144	24.144	24.190
		2008 Sep 23-26,28, Oct 21,22	NB	12.67	1.15	23.876	23.959	24.057	24.026

at least 0.1 mag (for $2'' \phi$; observed $\text{EW} \approx 11\text{\AA}$) above the median or 0.15 mag (for $3'' \phi$; observed $\text{EW} \approx 18\text{\AA}$) is required. These minima were determined by examining the 3σ photometric scatter at the bright end. In general the 3σ scatter was smaller (0.07–0.09 mag for $2'' \phi$; 0.08–0.11 mag for $3'' \phi$) than 0.1 or 0.15 mag, so we adopted 0.1 and 0.15 mag for simplicity. Second, the excess must be detected above 3σ significance: $J - NB \geq -2.5 \log [1 \mp (f_{3\sigma NB}^2 + f_{3\sigma J}^2)^{0.5}/f_{NB}]$, where f refers to the flux density per unit frequency. This is illustrated in Figure 3.1 for the SXDS-S pointing. The selection that we have adopted here follows similar selection techniques of other NB surveys (e.g., Fujita et al., 2003; Shioya et al., 2008) and those presented in Chapter 2. Since each detector has a slightly different sensitivity,³ selection of NB1187 excess emitters is conducted on a per quadrant basis. The selection is applied for photometry in two apertures, $2''$ and $3'' \phi$, and the two NB1187 excess candidate lists are merged together. The use of a secondary aperture is such that the survey can also be sensitive to sources that have more diffuse extended nebular emission. The selection with a $3''$ aperture provided 20 – 34 sources that were not identified by the $2''$ selection in each NEWFIRM pointing. We find that these sources tend to have 50% lower EWs and emission-line fluxes.

The total number of NB1187 excess emitters is 1117 where 271, 242, 304, and 300 are found in COSMOS, SXDS-N, SXDS-S, and SXDS-W, respectively. This number excludes sources that were flagged as cosmic rays, bad pixels, reflection ghosts, stars, or persistence images from visual inspection in the narrow-band, J -band, and z' -band images. Of the 1117 sources, 944 were “secure” sources because they were detected in at least two filters. The difference of 173 sources is comparable to the 131 3σ outliers expected across all four fields. Eighty-nine

³One of the four NEWFIRM detectors is 0.2 mag less sensitive due to a different anti-reflection coating that was used.

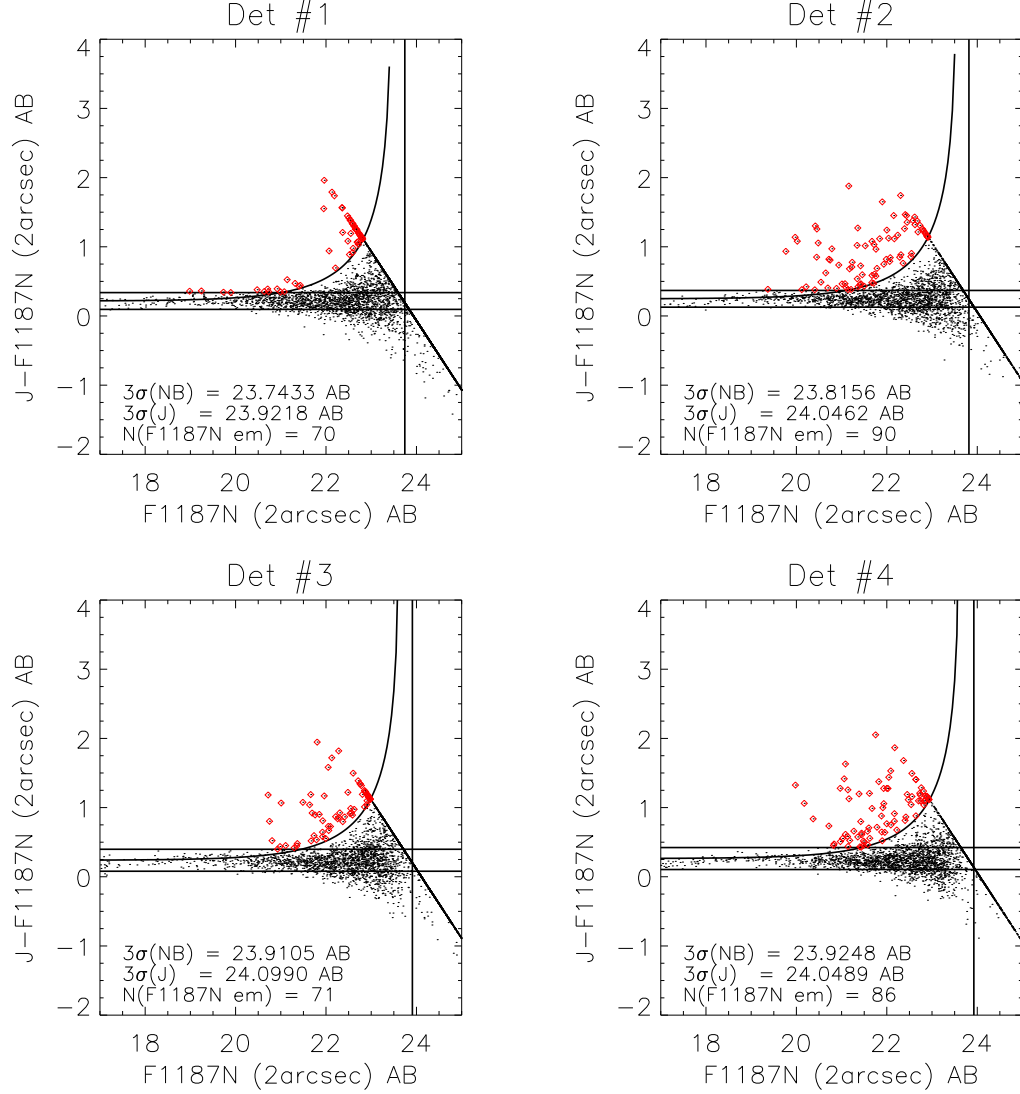


Figure 3.1 – NB1187 excess plots for the SXDS-S field using a $2''$ ϕ aperture. The abscissas show the NB1187 magnitude within a $2''$ aperture, and the ordinates show the $J - NB1187$ color. The solid black curves are the 3σ excess for $J - NB190$. The horizontal lines refer to the minimum $J - NB1187$ color of 0.1 mag above the mean. Red squares are the sources identified as NB1187 excess emitters. Selection is done based on the sensitivity in each detector.

Table 3.2. Summary of Photometric and Spectroscopic Samples

Field	Area	N_{NB1187}	$N_{H\alpha}$	N_{spec}	$N_{\text{spec}}(H\alpha)$
COSMOS	732.6	271	59	87 (32%)	29
SXDS-N	745.2	242	74	105 (43%)	42
SXDS-S	741.8	304	139	151 (50%)	109
SXDS-W	746.7	300	126	139 (46%)	89

Note. — Surveyed area provided in units of arcmin². N_{NB1187} refers to the number of non-spurious sources that meet the 3σ selection criteria.

per cent of the 944 sources have detections in all three bands while the rest are detected at z' but are too faint or marginally detected in the J . These numbers along with other aspects of the survey are provided in Table 3.2.

3.1.3 IMACS Spectroscopy

Spectroscopic follow-up is important for many reasons, such as (1) separating out other emission lines at different redshifts, (2) deriving gas metal abundances using the strong nebular emission lines that are present, (3) assessing the probability that spurious sources are scattered into our NB1187 selection, and (4) providing constraints on dust attenuation. Photometric redshifts are less reliable since they cannot distinguish [S II] $\lambda\lambda 6717, 6732$ at $z \approx 0.78$ from $H\alpha$ with typical $\Delta z_{\text{phot}} \gtrsim 0.05$ at $z \sim 1$. The spectroscopic follow-up of this project helps to address the [S II] issue, which other $z \sim 0.8$ surveys (e.g., Sobral et al., 2009) do not. This will be further discussed in § 3.2.2. We compare the standard empirical $H\alpha$ extinction corrections with preliminary results from the spectroscopy in Section 3.2.3. A detailed description of the data and attenuation properties of our $H\alpha$ candidates, as derived from these spectra, will be presented in Momcheva et al. (2010).

The spectroscopy was carried out with the Inamori Magellan Areal Camera

and Spectrograph (IMACS; Dressler et al., 2006) on the 6.5m Magellan I (Baade) telescope using the f/2 short camera. The majority of the observations utilized the red 300 lines mm⁻¹ grating and the WB6300 blocking filter. This gave us spectral coverage of 6300Å to 9600Å and 9Å spectral resolution with 1.5'' slits. Individual exposures were 20 or 30 minutes and total integration times added to 2 – 6.25 hours per mask. The fraction of NB1187 emitters targeted varies between 71% (SSA-22) and 91% (SXDS-S). We note that these fractions are lower in the final NB1187 samples. When we conducted our follow-up spectroscopy, we used an initial catalog produced with a different reduction package. The reduction systematically provided lower fluctuations in the background from the result of linear interpolation. The stack mosaics that we use now adopted an interpolation algorithm that does a better job of maintaining the true noise of the images. This difference resulted in 0.2–0.3 mag in the sensitivity, thus some of the spectroscopically targeted objects were missed in our final samples. There remains some on-going work to further understand why many of our previously spectroscopically targeted H α emitters are undetected, but since our spectra show that there are faint H α emitters that are missed, our SFR density measurements should be treated as a lower limit.

Spectroscopic redshifts were typically derived for more than 60% of the objects targeted. Table 3.2 summarizes this discussion. For almost all of the H α emitters at $z \sim 0.8$, we detected strong lines from [O II] and [O III], and for the bright sources, the higher level Balmer and Ca H and K absorption lines were also detected.

3.1.4 Public Ancillary Data

In addition to the NIR data, ground-based optical data, photometric redshift catalogs, and (where available) spectroscopic redshifts (z_{spec}) were included for these fields. For the SXDS pointings, $BVR_Ci'z'$ Suprime-Cam data⁴ (DR1 release; Furusawa et al., 2008) and proprietary z_{phot} and z_{spec} are used (H. Furusawa, private communication). For COSMOS, Suprime-Cam $BVr'i'z'$ imaging, z_{phot} from Ilbert et al. (2009), and publically available z_{spec} from the zCOSMOS (DR2; Lilly et al., 2007) and Magellan COSMOS (Trump et al., 2007) surveys are included. The sample sizes of the spectroscopic catalogs are 11975 for COSMOS and 4231 for SXDS, and among these, 2690 and 2386 fall in our COSMOS and SXDS surveyed regions, respectively. The zCOSMOS survey targeted $I < 22.5$ mag sources while the existing SXDS spectra were from several different instruments achieving different depths. The mean and 1σ of the magnitude distribution for the available SXDS z_{spec} catalog is $R_C = 21.7 \pm 2.0$ mag.

Since the spectroscopic surveys in these fields mostly targeted bright objects, where as our NB1187 excess emitters span a greater range of luminosities, the overlap with our candidate NB1187 excess emitters is small (63/944; 7%). Nevertheless, every spectroscopic redshift is important.

3.2 Selection of H α Emitters and Line Measurements

3.2.1 Selection of H α Emitters

Aside from H α , several possible emission lines can enter into the NB1187 filter, so the survey will also capture line-emitting galaxies at different redshifts. This includes [S III] $\lambda\lambda 9052, 9532$ at $z \approx 0.24$ and 0.30, H β at $z \sim 1.44$ or [O III] $\lambda 5007$

⁴Publically available at <http://step.mtk.nao.ac.jp/sxds/>.

at $z \approx 1.35$, and [O II] $\lambda 3727$ at $z \approx 2.2$. To identify H α emitters, a combination of spectroscopic redshifts (z_{spec}) and optical broad-band data are used. First, 43% of our NB1187 excess emitting galaxies have spectroscopic redshifts, and if their redshifts are such that H α would enter the NB1187 bandpass, then they were classified unambiguously as an H α emitting galaxy. For COSMOS, SXDS-N, SXDS-S, and SXDS-W, this approach immediately identified 29, 42, 109, and 89 H α emitters, respectively.

For the remaining NB1187 emitters that lack spectroscopic redshifts, NB1187 excess emitters with both z_{spec} information and optical data are used to define a set of empirical color selection. This is possible since the Balmer/4000Å break occurs at 6500Å for $z = 0.8$. In Figure 3.2, the $R_{\text{C}} - i'$ and $i' - z'$ colors are shown for SXDS NB1187 emitters. This illustrates that H α emitters can be cleanly separated from other interlopers. The broad-band selection criteria that we adopt for SXDS H α emitters without spec- z are:

$$R_{\text{C}} - i' \geq 0.3, R_{\text{C}} - i' \leq 1.05, \quad (3.1)$$

$$i' - z' \geq 0.0, \text{ and} \quad (3.2)$$

$$i' - z' \leq 0.35 \text{ or } R_{\text{C}} - i' \geq 1.375(i' - z') + 0.088. \quad (3.3)$$

Because the optical data of COSMOS are different from SXDS, COSMOS H α emitters with $r' - i' \geq 0.8$ are selected with $V - r' \leq 1.154(r' - i') - 0.375$ while those with $r' - i' < 0.8$ are selected by $B - V \leq 1.652(V - r') + 0.048$ and $V - r' \geq 0.1$ (see Figure 3.3).

The final numbers of H α emitters using z_{spec} and broad-band colors are 139 (SXDS-S), 126 (SXDS-W), 74 (SXDS-N), and 59 (COSMOS), which are also provided in Table 3.2. Comparing these numbers against the number of NB1187 excess emitters in each field, we find that the H α to NB1187 excess emitter ratio is between 22% and 46% (we discuss these variations in the context of expected

cosmic variance in § 3.4.1). According to photometric redshifts, the non-H α emitters were due to emission lines from [S II] ($\approx 10\%$), [O III]/H β ($\approx 42\%$), [O II] ($\approx 14\%$), and [S III] ($\approx 34\%$).

3.2.2 Comparison of Photometric Selection with Spectroscopic Redshifts

The selection of H α emitters benefits from targeted spectroscopy of our NB excess candidates. If the selection was conducted only with optical colors, we would find that a total of 341 (66) are H α emitters in the SXDS (COSMOS) fields. Nevertheless, spectroscopy would indicate that 37/341 (11%; SXDS) and 10/66 (15%; COSMOS) failed to have the appropriate redshift to be an H α emitter. The majority of these are due to [S II]. Moreover, there are 35/339 (SXDS) and 3/59 H α sources with colors that do not meet the above color selection. The majority of these sources in the SXDS fields have bluer $R_C - i'$ color. We also find that these sources have $J - \text{NB}1187$ excess of 1.13 mag compared to 0.75 mag for all H α emitters, which correspond to a median rest-frame H α +[N II] EWs of 135 \AA versus 69 \AA for the median of all H α emitters in our sample. This indicates that these sources have rather strong emission lines. If the [O II] emission line, which occurs in the R_C -band is also strong, it could explain the bluer colors of these sources. We discuss in § 5.3.1 that high emission-line EWs can have a strong affect on broad-band measurements that captures such emission lines. This can likely lead to less reliable photo- z estimates since the broad-band colors are $\approx 0.1\text{--}0.2$ mag off.

To summarize, on average, 12% of photometrically-selected H α emitters are not H α while 9.5% of the final H α sample have unusual colors. We confirm with our spectroscopic sample that color selection and photo- z simply cannot

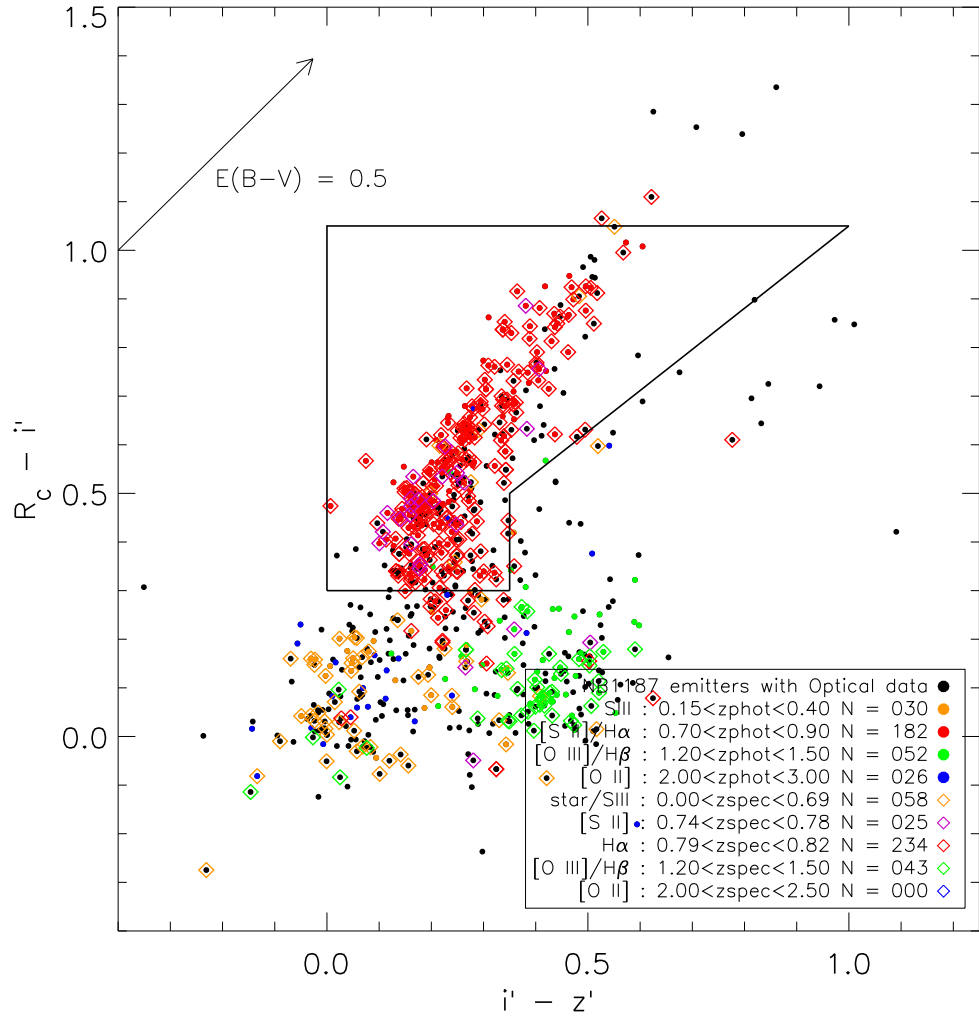


Figure 3.2 – $R_C - i'$ and $i' - z'$ colors for NB1187 excess emitters in the SXDS fields. A total of 704 points is plotted here. Objects with z_{spec} are indicated with diamonds while those with z_{phot} are represented as filled color circles. Their respective colors correspond to the redshift range as indicated in the lower right legend. The black lines correspond to the selection region as defined by Equations 3.1–3.3.

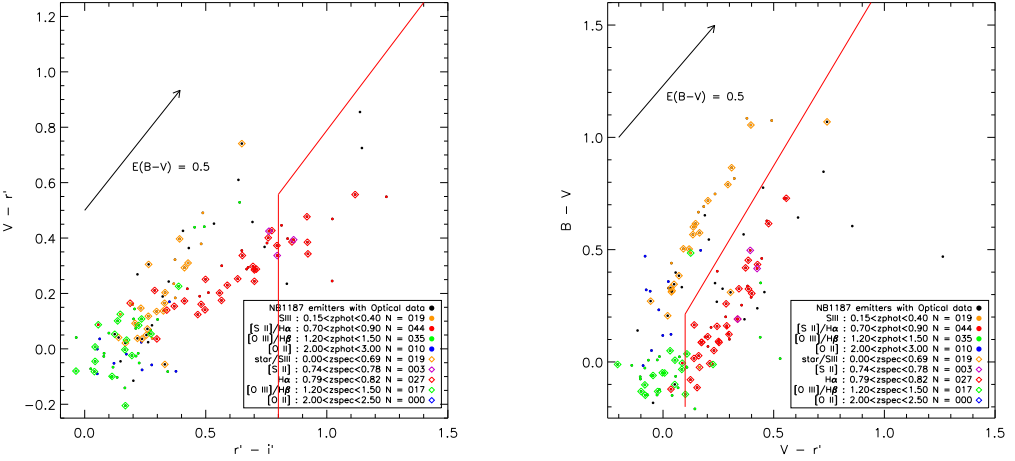


Figure 3.3 – $B - V$, $V - r'$, $r' - i'$, and $i' - z'$ colors for NB1187 excess emitters in the COSMOS field. The color and point style conventions follow those in Figure 3.2.

distinguish [S II] and H α . We find that among objects with optical data and spectroscopic information, 4% of these sources are [S II].

3.2.3 Deriving Emission-Line Flux and Luminosity Measurements

As discussed in § 2.2.3, broad- and narrow-band measurements can be utilized to determine emission-line properties. The flux densities ($\text{erg s}^{-1} \text{ cm}^{-2} \text{ \AA}^{-1}$) of the J -band and NB1187 observations can be written as: $f_{\text{NB}} = f_C + F_L/\Delta\text{NB}$ and $f_J = f_C + F_L/\Delta J$, where f_C is the continuum flux density, F_L is the emission line flux ($\text{erg s}^{-1} \text{ cm}^{-2}$), and ΔNB and ΔJ are the full width at half maximum of the NB (110Å) and J (1786Å) filters. Solving for F_L , the continuum flux, and the observed emission-line EW, we have:

$$F_L = \Delta\text{NB} \frac{f_{\text{NB}} - f_{\text{BB}}}{1 - (\Delta\text{NB}/\Delta\text{BB})}, \quad (3.4)$$

$$f_C = \frac{f_{\text{BB}} - f_{\text{NB}}(\Delta\text{NB}/\Delta\text{BB})}{1 - (\Delta\text{NB}/\Delta\text{BB})}, \text{ and} \quad (3.5)$$

$$EW_{\text{obs}} = \frac{F_L}{f_C} = \Delta\text{NB} \left[\frac{f_{\text{NB}} - f_{\text{BB}}}{f_{\text{BB}} - f_{\text{NB}}(\Delta\text{NB}/\Delta\text{BB})} \right]. \quad (3.6)$$

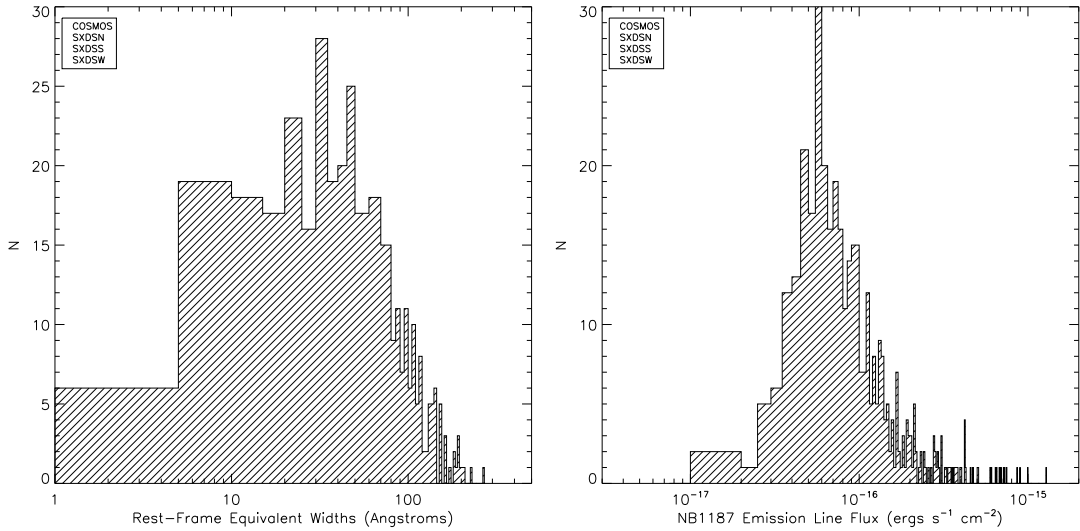


Figure 3.4 – Distribution of the rest-frame H α + [N II] EWs and emission-line fluxes for all identified H α emitters in the COSMOS and SXDS pointings. The emission-line fluxes have been corrected for [N II] contamination as described in § 3.2.3. We have applied a 9% statistical correction to the flux for the non-square shape of the NB filter (see § 3.3.2).

For the total line luminosity, we adopt a luminosity distance of $5095 h_{70}^{-1}$ Mpc ($z = 0.81$). The distributions of observed emission-line fluxes and EWs for H α emitters are illustrated in Figure 3.4, and the typical uncertainties associated with our measurements are provided as a function of magnitude in Table 3.3.

To determine the intrinsic total H α luminosity from the observed line luminosity, three corrections must be applied: [N II] contamination, dust attenuation, and aperture corrections.

[N II] contamination. The NB filter is wide enough for flux contribution from [N II] $\lambda 6548, 6583$.⁵ In the local universe, integrated spectroscopic surveys have found that the H α /[N II] flux ratio is 2.3 for typical L_* galaxies (Kennicutt, 1992; Gallego et al., 1997). This flux ratio, however, has been shown to increase with larger emission-line EW (see e.g., Villar et al., 2008) and with decreasing

⁵Hereafter, “[N II]” refers to both nitrogen nebular emission lines.

Table 3.3. Properties for Some H α Emitters

ID	RA	DEC	NB(3'')	J(3'')	EW _{rest}	F_L	z_{spec}	z_{phot}
S-S058	02:17:26.21	-5:15:27.02	20.77±0.04	21.74±0.07	103.87±14.0	26.38	...	0.79
S-S013	02:17:18.57	-5:22:15.73	21.95±0.11	23.24±0.28	173.65±81.8	10.41	0.810	0.74
S-S105	02:17:38.45	-5:06:47.99	21.59±0.07	22.77±0.18	145.97±44.9	13.93	0.796	...
S-S074	02:16:54.98	-5:13:43.67	20.96±0.04	21.68±0.07	64.24±10.0	18.03	0.805	0.75
S-S129	02:17:49.11	-5:03:53.36	20.44±0.02	20.78±0.03	23.99±3.1	16.02
S-S053	02:17:40.52	-5:16:09.08	21.22±0.06	21.53±0.06	22.04±6.7	7.37	...	0.78
S-S091	02:16:51.70	-5:10:44.72	21.82±0.09	22.57±0.15	70.00±23.9	8.55	0.809	0.79
S-S009	02:16:49.22	-5:23:06.17	20.92±0.04	21.49±0.05	46.99±7.7	15.86	...	0.76
S-S100	02:17:44.53	-5:09:09.67	20.31±0.02	20.75±0.03	33.43±3.3	22.60	...	0.74
S-S093	02:17:17.57	-5:10:15.10	21.02±0.04	21.44±0.05	31.49±6.3	11.30	0.798	1.00
S-W043	02:16:04.38	-5:01:21.59	22.25±0.13	22.86±0.19	51.72±26.4	4.92	0.800	0.77
S-W051	02:17:16.18	-5:00:00.35	20.31±0.02	21.12±0.04	78.27±6.9	36.04	...	0.74
S-W039	02:17:12.65	-5:02:16.17	21.50±0.07	22.07±0.10	47.58±13.3	9.40	0.806	0.37
S-W103	02:17:02.78	-4:48:39.19	21.57±0.06	22.04±0.09	36.05±10.4	7.43	0.797	0.74
S-W009	02:16:30.31	-5:07:59.26	20.51±0.03	21.00±0.03	38.63±4.3	20.70	0.806	0.83
S-W065	02:16:30.16	-4:58:40.25	21.57±0.07	21.95±0.08	27.15±9.3	6.15	...	0.57
S-W108	02:15:55.85	-4:47:33.11	21.57±0.06	22.42±0.12	83.59±20.5	11.63	0.799	...
S-W083	02:16:36.04	-4:55:05.38	22.27±0.12	23.43±0.31	140.02±75.4	7.31	0.806	...
S-W097	02:15:34.33	-4:52:22.93	20.78±0.03	21.33±0.04	44.15±5.7	17.39	0.801	...
S-W007	02:16:31.05	-5:08:43.44	20.60±0.03	21.77±0.07	143.54±18.5	34.39	0.805	0.74
S-N066	02:17:29.58	-4:23:13.32	21.94±0.09	22.96±0.22	113.14±45.5	9.29
S-N041	02:17:41.26	-4:32:38.96	22.56±0.16	>23.51	>100.25	>5.020	0.811	...
S-N057	02:17:31.84	-4:27:51.46	20.78±0.03	20.99±0.04	14.11±3.5	7.80
S-N044	02:17:25.47	-4:32:05.43	21.24±0.05	21.53±0.06	19.94±6.1	6.69
S-N004	02:18:50.10	-4:49:20.71	22.37±0.16	22.89±0.24	41.41±30.2	3.89	...	1.00
S-N072	02:18:18.40	-4:22:34.79	20.40±0.02	21.14±0.04	68.12±6.7	31.08
S-N003	02:17:35.53	-4:49:23.97	22.62±0.18	23.41±0.35	74.08±56.2	4.17	...	0.45
S-N016	02:18:11.57	-4:41:23.29	22.28±0.13	>23.47	>149.50	>7.41	0.808	...
S-N011	02:17:17.67	-4:45:18.79	20.78±0.03	21.42±0.05	54.55±7.6	19.56	0.796	0.80
S-N073	02:17:23.31	-4:22:33.40	20.80±0.03	20.99±0.04	12.63±3.5	6.99
C-006	10:01:18.87	01:49:36.41	20.59±0.03	21.95±0.11	193.58±33.0	37.71	0.811	0.78
C-031	10:01:06.78	02:01:43.23	20.57±0.03	21.15±0.05	47.09±6.0	21.90	0.798	0.85
C-043	10:01:09.99	02:10:01.44	22.14±0.13	23.35±0.36	151.10±92.4	8.41	0.798	...
C-040	10:01:16.88	02:06:36.04	21.76±0.09	22.68±0.19	94.36±35.5	10.19	0.814	0.81
C-031	10:01:06.78	02:01:43.23	20.57±0.03	21.15±0.05	47.09±6.0	21.90	0.798	0.85
C-021	10:01:03.11	01:53:31.22	21.90±0.10	22.63±0.18	66.17±27.5	7.71	...	0.81
C-039	10:01:26.22	02:05:46.34	20.88±0.04	22.02±0.10	138.03±24.8	26.24	0.813	0.83
C-036	10:01:59.86	02:02:41.98	21.67±0.08	22.47±0.16	76.43±25.8	10.20	...	0.74
C-040	10:01:16.88	02:06:36.04	21.76±0.09	22.68±0.19	94.36±35.5	10.19	0.814	0.81
C-032	10:01:49.99	02:01:48.05	22.50±0.18	>23.38	>88.34	>5.03	...	1.21

Note. — These sources were chosen randomly to illustrate the properties of H α emitters identified in the NewH α survey. ID of sources are abbreviated such that “S-” and “C-” correspond to SXDS and COSMOS fields with N, S, and W indicating the North, South, and West fields of SXDS. J2000 World coordinates are provided in hh:mm:ss and dd:mm:ss. EW_{rest} is the rest-frame EW of H α + [N II], and F_L is the emission line flux normalized to 1×10^{-17} erg s $^{-1}$ cm $^{-2}$. We defined non-detection in J by the 3σ limit for the appropriate detector.

B-band luminosities (Lee et al., 2009). Past H α surveys have often adopted a fixed correction of 2.3. In the SDF NB survey (see § 2.2.3.1), we adopted 4.66 based on optical spectroscopy. This is not surprising since the SDF H α emitters probed fainter luminosities, hence are more metal-poor and would have a lower contamination of [N II] flux in the NB filters. For this study, we follow Villar et al. (2008) and Sobral et al. (2009) of adopting an EW-dependent H α /[N II] flux ratio to be consistent.

This correction should be viewed as a “crude” estimate for [N II] contamination, but it is currently the best correction that accounts (to first order) the variation with galaxy types. This correction was constructed from thousands of $z \sim 0.1$ star-forming galaxies from the SDSS fourth data release. Villar et al. (2008) determined the mean of the distribution versus the rest-frame EW of H α + [N II] $\lambda 6583$, which is illustrated in Figure 3.5. We note that this correction for [N II] varies at the ≈ 0.2 dex level, which implies that estimates of the [N II]/H α ratio are unreliable for individual sources. However, this correction is more valid by looking at H α emitters “globally” to construct a luminosity function.

Also, our correction assumes that the [N II]/H α relation does not evolve with redshift. There could be a systematic offset in the [N II]/H α ratio for high- z galaxies, but no statistical high- z sample exists to argue for or against this. To first order, galaxies in the early universe are thought to be more metal-poor, so a lower [N II]/H α ratio is expected. This is partly accounted for through the EW of the emission lines. NIR multi-object spectroscopy will be needed to examine the H α /[N II] ratio for NB selected galaxies on a case-by-case basis. Assuming the Villar et al. (2008) [N II] correction, the H α /[N II] ratio varies from 1.85 to 7.97 with a median (average) of 2.64 (2.95) for our population of H α emitting galaxies.

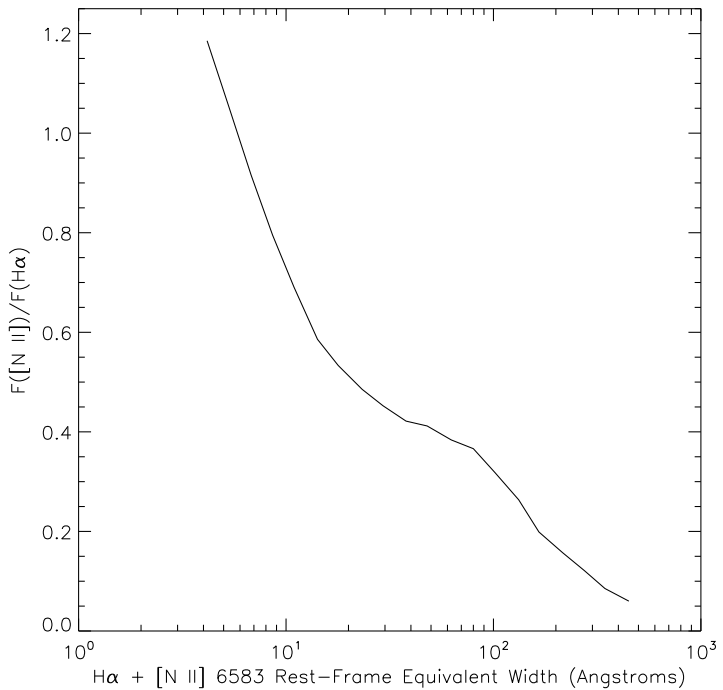


Figure 3.5 – The [N II] $\lambda 6583/\text{H}\alpha$ flux ratio against the rest-frame $\text{H}\alpha + \text{[N II]}$ $\lambda 6583$ EWs determined from SDSS spectra. This relation was derived in [Villar et al. \(2008\)](#) and is reproduced here.

Dust attenuation. To correct for dust attenuation, we adopt a luminosity-dependent extinction following Hopkins et al. (2001):

$$\log \text{SFR}_{\text{obs}}(H\alpha) = \log \text{SFR}_{\text{int}} - 2.360 \times \log \left[\frac{0.797 \log(SFR_{\text{int}}) + 3.786}{2.86} \right]. \quad (3.7)$$

This correction ($A[\text{H}\alpha]$) ranges from 0.30 to 1.86 mag with a median and average of 1.19 and 1.20 mag, respectively. These dust attenuation corrections were also adopted in Chapter 2 and often in other studies (e.g., Villar et al., 2008; Sobral et al., 2009; Dale et al., 2010). Equation 3.7 has roughly 0.2 dex scatter from $E(B - V)$ measurements. Much like the [N II] correction, these dust extinction corrections are more reliable when considering multiple sources of a given luminosity/SFR.

To show that this correction is reasonable, we compare it to those derived from Balmer decrements for a sub-sample of the objects contained in the spectroscopic follow-up survey (see § 3.1.3).⁶ Our sample consists of 27 objects with $H\beta$ and H_γ , and 15 objects with $H\beta$ and H_δ . Six objects are included in both samples. Note that we are still investigating slit losses and aperture corrections (discuss below) to use the $H\alpha/H\beta$ flux ratio. Since $H\beta$, H_γ , and H_δ are obtained from the same spectra, we assume that slit loss is the same for all three emission lines. We assume Case B recombination values for the intrinsic Balmer decrements, $H_\gamma/H\beta = 0.469$ and $H_\delta/H\beta = 0.260$, and adopt the Calzetti et al. (2000) law for dust extinction. From the two line ratios, we find mean (median $\pm 1\sigma$) values for the extinction at $H\alpha$ of $A(H\alpha) = 0.95$ (0.72 ± 1.08) and 0.89 (0.95 ± 0.51) mag, respectively. Comparing these values against those derived from the Hopkins et al. (2001) prescription based on the observed $H\alpha$ luminosity, we find good agreement in the mean values of $A(H\alpha)$ derived from both methods. A more detailed discussion is given in Momcheva et al. (2010).

⁶Iva Momcheva (Carnegie Observatories), for the NewH α team, did the following calculation.

Aperture corrections. The selection of these excess emitters was conducted in fixed photometric apertures. Since star-forming galaxies at $z \sim 0.8$ are extended (typically 8 kpc or $1''$ half light diameter; see e.g., [de Mello et al., 2006](#)), flux losses must be accounted for to determine the total SFRs for these galaxies. We measured growth curves for our H α emitters with aperture sizes from $2''.0$ to $10''.0$ ϕ . In most circumstances ($\sim 60 - 75\%$) the corrections are well behaved with a monotonic increase and then a plateau above $5'' \phi$ aperture. The aperture corrections for fainter sources suffer from more flux contamination from nearby sources and have more uncertain measurements with larger apertures. In the current analysis, we adopt median aperture corrections for each field. In the future, individual- and morphology-based corrections will be used. These corrections vary from field-to-field since the spatial resolution differs. The adopted corrections for *both* filters are a factor of 1.32, 1.19, 1.37, and 1.30 for COSMOS, SXDS-N, SXDS-S, and SXDS-W, respectively. These corrections are uncertain at the 9% level, which is smaller than the photometric uncertainties for our typical galaxies with $J = 23$ mag.

3.3 Completeness of the Survey

3.3.1 Monte Carlo Simulations

To account for the detection limits and photometric selection of NewH α survey, the completeness fraction, $\kappa(L)$, was derived for luminosity bins of 0.2 dex with Monte Carlo simulations.⁷ The simulations were performed by adding 1,000 artificial galaxies to each NEWFIRM mosaic, and comparing the number of artificial NB1187 excess emitting galaxies to the number detected. The galaxies were cre-

⁷These simulations were conducted by fellow NewH α collaborators, D. Dale and S. Staudaher (University of Wyoming).

ated using IRAF/`mkobjects` and physical parameters similar to those found in actual galaxies. The parameters included luminosities, H α EWs, semi-major to semi-minor axial ratios (between 0.15 and 1.0), the H α disk scale length (3.6 kpc; Dale et al., 1999), and extinction corrections.

The completeness of our survey is dependent on the underlying EW distribution of the population of galaxies. For the moment, we consider an H α EW distribution of late-type galaxies from a local census survey of star-forming galaxies (Lee et al., 2007). The distribution is described by a Gaussian with average $\log(\text{EW}/\text{\AA})$ of 1.52 dex and $\sigma[\log(\text{EW}/\text{\AA})]$ of 0.16 dex. We adopt this distribution since the median rest-frame EW of our galaxies is 54 \AA . We note that we are still investigating our completeness correction and how they behave with different adopted H α EW distributions. In general, the completeness correction will not significantly change (with future iterations) at high H α luminosities (i.e., the completeness is nearly one), so constraints on L_* and Φ_* of Schechter fits (described in § 3.4.1) are least affected. However, constraints on the faint-end slope may change when improvements are made to estimate the NewH α survey’s completeness.

H α extinction corrections also follow what was previously adopted in Section 3.2.3. After extracting sources in the same manner described in Section 3.2.1, the completeness, $\kappa(L)$, was calculated by dividing the number of simulated sources *detected*, $N(L)_{\text{obs}}$, by the number of simulated sources *created*, $N(L)_{\text{corr}}$:

$$N(L)_{\text{corr}} = \kappa(L)^{-1} N(L)_{\text{obs}}. \quad (3.8)$$

Each simulation was repeated at least 30 times using different seed numbers to increase the statistical accuracy of the results ($N \gtrsim 30,000$ per NEWFIRM pointing). We illustrate in Figure 3.6 the NewH α survey’s completeness as a function of H α luminosity for all four fields. The 50% completeness was found

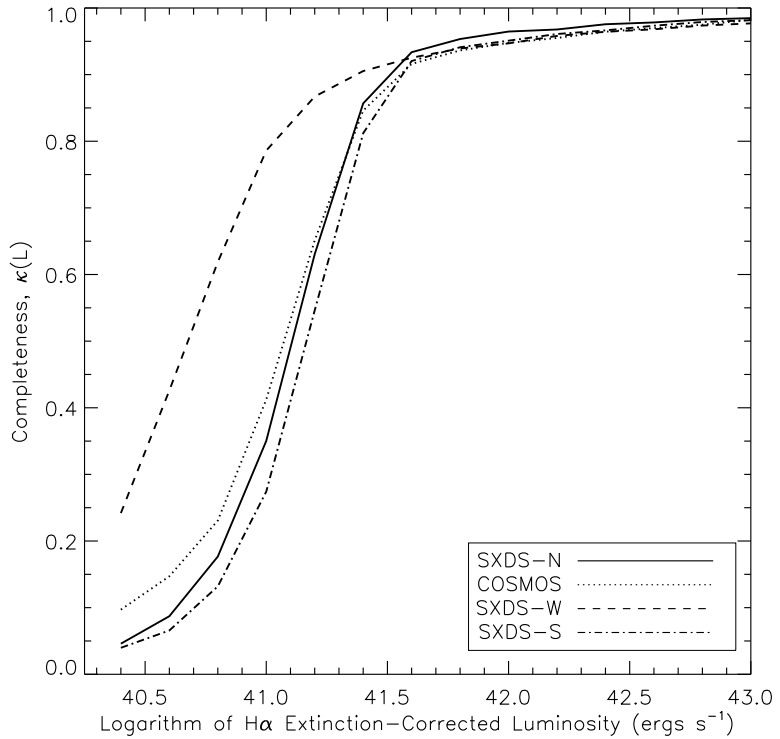


Figure 3.6 – The completeness correction $\kappa(L)$ derived from Monte Carlo simulations of our data. The line types denote different fields: COSMOS (dotted), SXDS-N (solid), SXDS-S (dot-dashed), and SXDS-W (dashed). The solid lines assume EW Gaussian distribution with averages of $\log(\text{EW}/\text{\AA}) = 1.52$ (see § 3.3.1). The higher completeness for SXDS-W is partly due to higher spatial resolution. We are still finalizing our determination of the survey’s completeness.

to be at extinction-corrected $\text{H}\alpha$ luminosities of 1.2×10^{41} (COSMOS), 1.5×10^{41} (SXDS-S), 1.3×10^{41} (SXDS-S), and $4.8 \times 10^{40} \text{ ergs s}^{-1}$ (SXDS-W). These numbers correspond to a SFR of 1.0, 1.2, 1.0, and $0.4 M_{\odot} \text{ yr}^{-1}$, respectively, when adopting the Kennicutt (1998) SFR- $\text{H}\alpha$ luminosity relation (see below). The MC simulation results are reported in Table 3.4. For bright luminosities the completeness reached an asymptotic value of ~ 0.98 due to source confusion.

3.3.2 Effective Volume

The volume for which the survey is capable of probing is determined simply by the shape of the NB filter. If this filter is a perfect square, then the same comoving volume is surveyed at all emission-line fluxes. However, for a non-square filter, a weak emission line can either result from the line falling in the wings of the NB filter profile or it is intrinsically weak but is located near the filter center. The net result is that a weak emission line is more likely to be detected near filter center, so a non-square filter reduces the effective volume at the faint end ([Ly et al., 2007](#)). The deviation of our filter from being square-like is 9% based on the area enclosed within $\Delta\lambda = \text{FWHM}$.

To determine the effective volume as a function of emission-line flux, we calculate the range in wavelengths such that an emission line is considered detectable within the NB filter. This emission line has an intrinsic S/N. We then place it at different wavelengths to determine what the degradation in the S/N would be due to lower throughput. We define that an emission line is undetectable below 3σ , and this criteria would yield the minimum and maximum NB wavelengths (hence redshift) that is observable for a particular S/N. The effective comoving volume per unit steradian would then be

$$\frac{V}{d\Omega} = \int_{z_1}^{z_2} dz \frac{dV}{dz d\Omega}, \text{ where} \quad (3.9)$$

$$\frac{dV}{dz d\Omega} = \frac{c}{H_0} \frac{D_M^2}{E(z)}, \quad (3.10)$$

$$E(z) \equiv \sqrt{\Omega_M(1+z)^3 + \Lambda_0}, \text{ and} \quad (3.11)$$

$$D_M = \frac{c}{H_0} \int_0^z \frac{dz'}{E(z')}. \quad (3.12)$$

Here, z_1 and z_2 refer to the minimum and maximum redshifts that the emission line is detectable. Note that these sets of equations assume a flat universe. The maximum surveyed volume ($V_{\text{eff}}/\Omega = 1.11 \times 10^5 \text{ Mpc}^3 \text{ deg}^{-2}$ or $\Delta\lambda = 110\text{\AA}$)

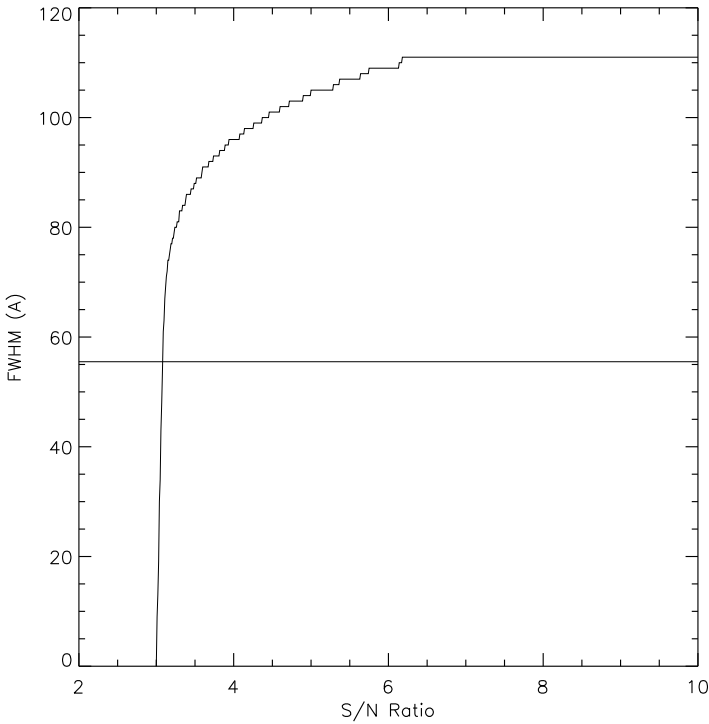


Figure 3.7 – The FWHM (in wavelength) of the survey volume versus S/N ratio. The horizontal line corresponds to 50% of the maximum effective volume, $V_{\text{eff}}/\Omega = 1.11 \times 10^5 \text{ Mpc}^3 \text{ deg}^{-2}$.

is observable for $\text{S/N} \geq 6.2$ and decreases to $V_{\text{eff}}/\Omega = 5.54 \times 10^4 \text{ Mpc}^3 \text{ deg}^{-2}$ ($\Delta\lambda = 55\text{\AA}$) at $\text{S/N} = 3.08$. This is illustrated in Figure 3.7.

3.4 Results

3.4.1 Luminosity Function and Star Formation Rate Densities

Figure 3.8 and Table 3.4 provide the (observed) H α luminosity function (LF) for this survey with and without completeness corrections. The EW-dependent [N II] correction, as discussed in § 3.2.3 has been adopted. Applying the necessary completeness corrections and adopting Hopkins et al. (2001) extinction correction,

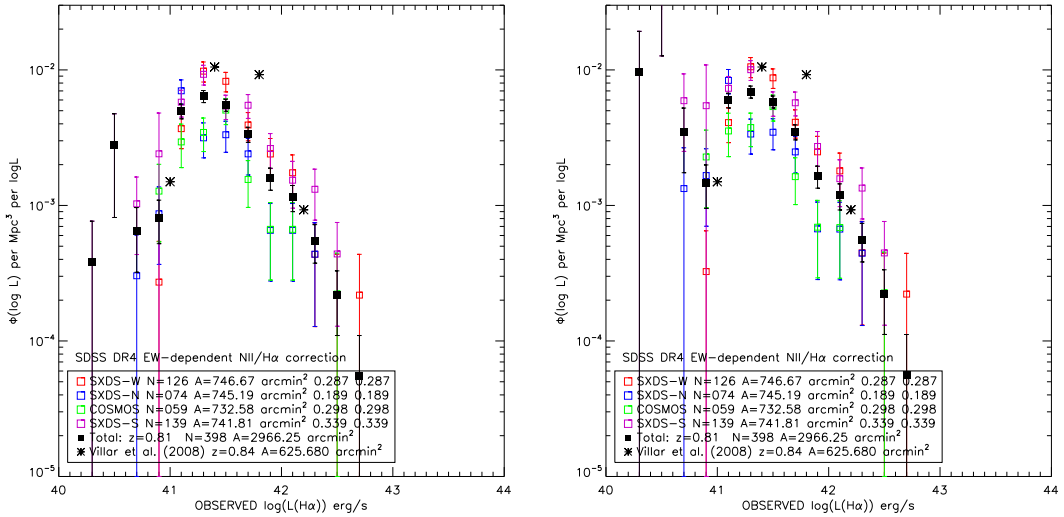


Figure 3.8 – The observed (i.e, no dust attenuation corrections have been applied) H α luminosity function before (left) and after (right) applying completeness correction. [N II] contamination, and aperture corrections have been included in both figures. The combined measurements from the four NewH α fields are shown as filled squares, where as open squares represent the individual pointings. Villar et al. (2008) measurements are shown as asterisks.

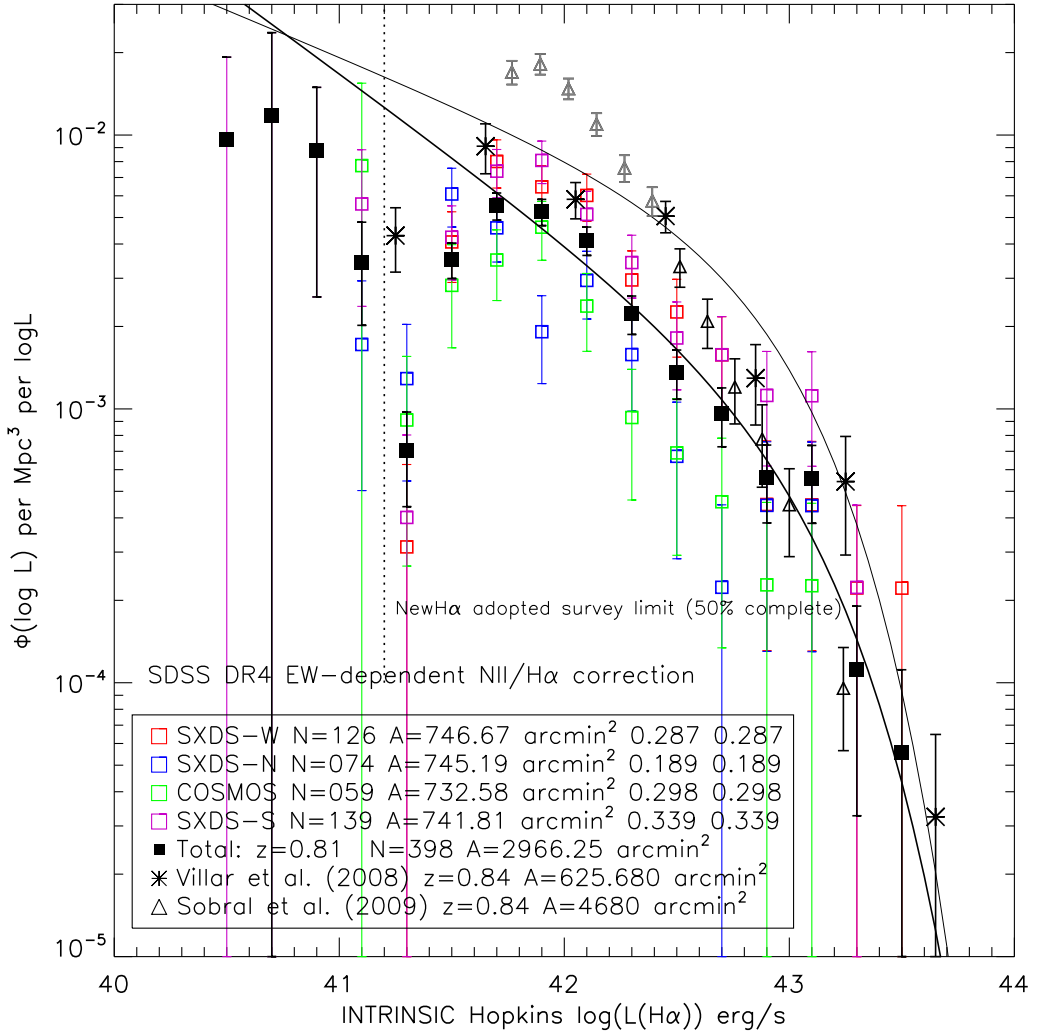


Figure 3.9 – The $\text{H}\alpha$ luminosity function corrected for dust extinction using the Hopkins et al. (2001) equation. The color and point-style conventions follow those in Figure 3.8. The solid black curve is the best-fitting Schechter function ($L_* = 10^{43.10 \pm 0.17} \text{ ergs s}^{-1}$, $\Phi_* = 10^{-3.40 \pm 0.13} \text{ Mpc}^{-3}$, and $\alpha = -1.6$). Measurements from Sobral et al. (2009) are overlayed as triangles. We discuss in § 3.5 the possibilities that their measurements below $\text{H}\alpha$ luminosity of $10^{42.4} \text{ ergs s}^{-1}$ could be affected by spurious source contamination. These measurements are marked in grey. For consistency, Sobral et al. (2009) measurements were adjusted to adopt the Hopkins et al. (2001) dust extinction equation instead of $A(\text{H}\alpha) = 1.0$ mag.

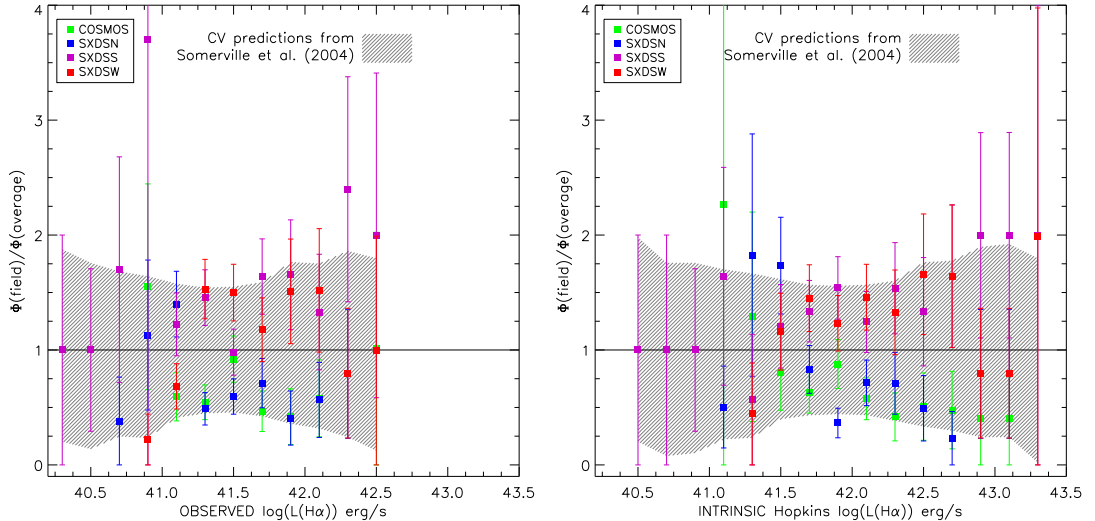


Figure 3.10 – The field-to-field fluctuations for four pointings. The x-axes show the observed (left) and extinction-corrected (right) H α luminosity while the y-axes show the number density of sources normalized to the average. Color convention of points follows those used in Figure 3.8. The shaded regions represent the 1σ variation predicted from the Λ CDM model of [Somerville et al. \(2004\)](#).

we have the H α LF presented in Figure 3.9 and Table 3.4. The binned luminosity function can be summed together to obtain a model-free H α luminosity density of $\mathcal{L} = 10^{39.94 \pm 0.10} \text{ ergs s}^{-1} \text{ Mpc}^{-3}$ as a lower limit.

The median variation of the number density relative to the average of all four fields is 50%, and we illustrate in Figure 3.10 the relative fluctuation of the four different pointings against the average. Using the predictions from [Somerville et al. \(2004\)](#), we find that the expected fluctuation (shaded region in Figure 3.10 for each pointing) is consistent with what is observed. The hourglass-like shape of expected amount of field-to-field fluctuations is due to (1) the stronger clustering of luminous galaxies, (2) the decrease of cosmic variance with number density, and (3) the small volume surveyed at low luminosities due to the weakness of emission lines. Thus, the minimum of field-to-field variations is around an observed H α luminosity of $3 \times 10^{41} \text{ ergs s}^{-1}$.

The LF is well represented by the Schechter function, as provided in Equation 2.5. In order to obtain the best-fitting parameters for a Schechter fit, a Monte Carlo simulation was performed to consider the full range of scatter in the extinction- and completeness-corrected H α LF. We ignored the six faintest luminosity bins as those suffer from lack of volume covered and incompleteness. Each datapoint was perturbed randomly 1×10^5 times following a Gaussian distribution with 1σ in Φ given by Poisson statistics. Each iteration is then fitted to obtain the Schechter parameters. Confidence contours for our best-fitting Schechter parameters (discussed below) are shown in Figure 3.11.

The NewH α survey is currently⁸ not sensitive enough to place *strong* constraints on the faint-end slope (α), so we have fixed it to $\alpha = -1.6$. This value has been adopted by others (Sobral et al., 2009), and are reasonable given what has been seen for the H α LF at $z < 0.5$ and the steep slope ($\alpha = -1.8$) in the rest-UV at $z \sim 2$ (Reddy et al., 2008). The resulting Schechter parameters are $L_\star = 10^{43.10 \pm 0.17}$ ergs s $^{-1}$ and $\Phi_\star = 10^{-3.40 \pm 0.13}$ Mpc $^{-3}$, which is shown against the binned H α LF in Figure 3.8. When we allow α to be free, we find: $L_\star = 10^{43.20 \pm 0.51}$ ergs s $^{-1}$, $\Phi_\star = 10^{-3.6 \pm 0.60}$ Mpc $^{-3}$, and $\alpha = -1.75 \pm 0.49$. It appears that the LF is steep at $z \sim 0.81$, indicating that galaxies below $0.2L_\star$ ($1L_\star$) contribute 70% (93%) to the total H α luminosity/SFR density.

The integral of the LF, $\int L\Phi dL$, yields a luminosity density (down to $L = 0$) of $\mathcal{L} = 10^{40.05 \pm 0.05}$ ergs s $^{-1}$ Mpc $^{-3}$ and $\mathcal{L} = 10^{40.16 \pm 0.85}$ ergs s $^{-1}$ Mpc $^{-3}$ for fixed and free α , respectively. For extinction-corrected luminosities above the survey limit⁹ ($L_{\text{lim}} = 1.6 \times 10^{41}$ ergs s $^{-1}$; $\text{SFR}_{\text{H}\alpha} \approx 1 \text{ M}_\odot \text{ yr}^{-1}$), we have $\mathcal{L} = 10^{39.90 \pm 0.05}$ ergs s $^{-1}$ Mpc $^{-3}$ ($\alpha = -1.6$).

⁸Future work with a higher resolution NIR camera will probe 3 – 5 times fainter than the current limiting depth of these NEWFIRM data.

⁹The survey limit is defined when completeness corrections is $\approx 50\%$ completeness.

Table 3.4. H α Luminosity Function at $z \sim 0.81$

L(H α)	COSMOS			SXDS-N		SXDS-S		SXDS-W		Total	
	Φ	$\kappa(L)$									
Raw number densities											
40.30	3.83 \pm 3.8	0.05	3.83 \pm 3.8	0.05	
40.50	27.81 \pm 19.7	0.11	27.81 \pm 19.7	0.11	
40.70	3.03 \pm 3.0	0.34	10.28 \pm 5.9	0.27	6.43 \pm 3.2	0.28	
40.90	12.75 \pm 7.4	0.70	8.69 \pm 5.0	0.69	24.04 \pm 24.0	0.62	2.72 \pm 2.7	0.88	8.08 \pm 2.9	0.70	
41.10	29.41 \pm 10.4	0.89	70.12 \pm 14.3	0.90	57.79 \pm 12.9	0.87	36.85 \pm 10.6	0.92	49.77 \pm 6.2	0.89	
41.30	34.56 \pm 9.6	0.93	31.54 \pm 9.1	0.95	92.76 \pm 15.5	0.94	97.92 \pm 16.6	0.94	63.91 \pm 6.5	0.94	
41.50	50.50 \pm 11.0	0.95	33.24 \pm 8.6	0.96	54.06 \pm 11.0	0.95	82.37 \pm 13.5	0.95	55.11 \pm 5.6	0.95	
41.70	15.54 \pm 5.9	0.96	24.01 \pm 7.2	0.97	54.82 \pm 11.0	0.96	39.21 \pm 9.2	0.96	33.45 \pm 4.3	0.96	
41.90	6.66 \pm 3.8	0.97	6.55 \pm 3.8	0.98	26.31 \pm 7.6	0.97	23.96 \pm 7.2	0.97	15.90 \pm 3.0	0.97	
42.10	6.66 \pm 3.8	0.97	6.55 \pm 3.8	0.98	15.35 \pm 5.8	0.98	17.43 \pm 6.2	0.97	11.52 \pm 2.5	0.98	
42.30	4.37 \pm 3.1	0.98	13.16 \pm 5.4	0.98	4.36 \pm 3.1	0.98	5.48 \pm 1.7	0.98	
42.50	2.22 \pm 2.2	0.98	4.39 \pm 3.1	0.98	2.18 \pm 2.2	0.98	2.19 \pm 1.1	0.98	
42.70	2.18 \pm 2.2	0.98	0.55 \pm 0.5	0.98	
Extinction and completeness-corrected number densities											
40.50	72.58 \pm 72.6	0.05	72.58 \pm 72.6	0.05	
40.70	78.60 \pm 78.6	0.10	78.60 \pm 78.6	0.10	
40.90	56.87 \pm 40.2	0.20	56.87 \pm 40.2	0.20	
41.10	59.96 \pm 60.0	0.53	12.27 \pm 8.7	0.49	37.44 \pm 21.6	0.41	23.74 \pm 9.7	0.45	
41.30	7.92 \pm 5.6	0.75	10.94 \pm 6.3	0.74	3.23 \pm 3.2	0.68	3.07 \pm 3.1	0.89	6.08 \pm 2.3	0.75	
41.50	27.13 \pm 11.1	0.88	58.28 \pm 14.1	0.90	39.70 \pm 12.0	0.87	40.26 \pm 11.6	0.92	33.73 \pm 5.0	0.89	
41.70	34.58 \pm 10.0	0.93	45.35 \pm 11.3	0.94	72.98 \pm 14.6	0.93	79.46 \pm 15.9	0.93	54.63 \pm 6.2	0.93	
41.90	45.79 \pm 11.1	0.94	19.02 \pm 6.7	0.96	80.36 \pm 14.2	0.95	64.41 \pm 12.6	0.94	52.20 \pm 5.7	0.95	
42.10	23.64 \pm 7.5	0.95	29.41 \pm 8.2	0.97	51.04 \pm 10.9	0.96	59.84 \pm 11.7	0.95	41.06 \pm 4.9	0.96	
42.30	9.25 \pm 4.6	0.96	15.73 \pm 5.9	0.97	34.13 \pm 8.8	0.96	29.46 \pm 8.2	0.96	22.19 \pm 3.6	0.96	
42.50	6.89 \pm 4.0	0.97	6.70 \pm 3.9	0.98	18.09 \pm 6.4	0.97	22.55 \pm 7.1	0.97	13.58 \pm 2.8	0.97	
42.70	4.57 \pm 3.2	0.97	2.23 \pm 2.2	0.98	15.72 \pm 5.9	0.98	15.71 \pm 5.9	0.97	9.57 \pm 2.3	0.97	
42.90	2.27 \pm 2.3	0.98	4.44 \pm 3.1	0.98	11.18 \pm 5.0	0.98	4.47 \pm 3.2	0.98	5.60 \pm 1.8	0.98	
43.10	2.26 \pm 2.3	0.98	4.43 \pm 3.1	0.98	11.16 \pm 5.0	0.98	4.45 \pm 3.1	0.98	5.58 \pm 1.8	0.98	
43.30	2.23 \pm 2.2	0.99	2.22 \pm 2.2	0.98	1.11 \pm 0.8	0.98	
43.50	2.21 \pm 2.2	0.98	0.56 \pm 0.6	0.98	

Note. — Observed (extinction-corrected) H α luminosities and raw (completeness-corrected) number densities (Φ) reported in the top (bottom) half of the table. Φ is normalized to $1 \times 10^{-4} h_{70}^{-3}$ Mpc $^{-3}$ dex $^{-1}$ and luminosities are given in ergs s $^{-1}$. $\kappa(L)$ refers to the completeness fraction defined in Section 3.3.1.

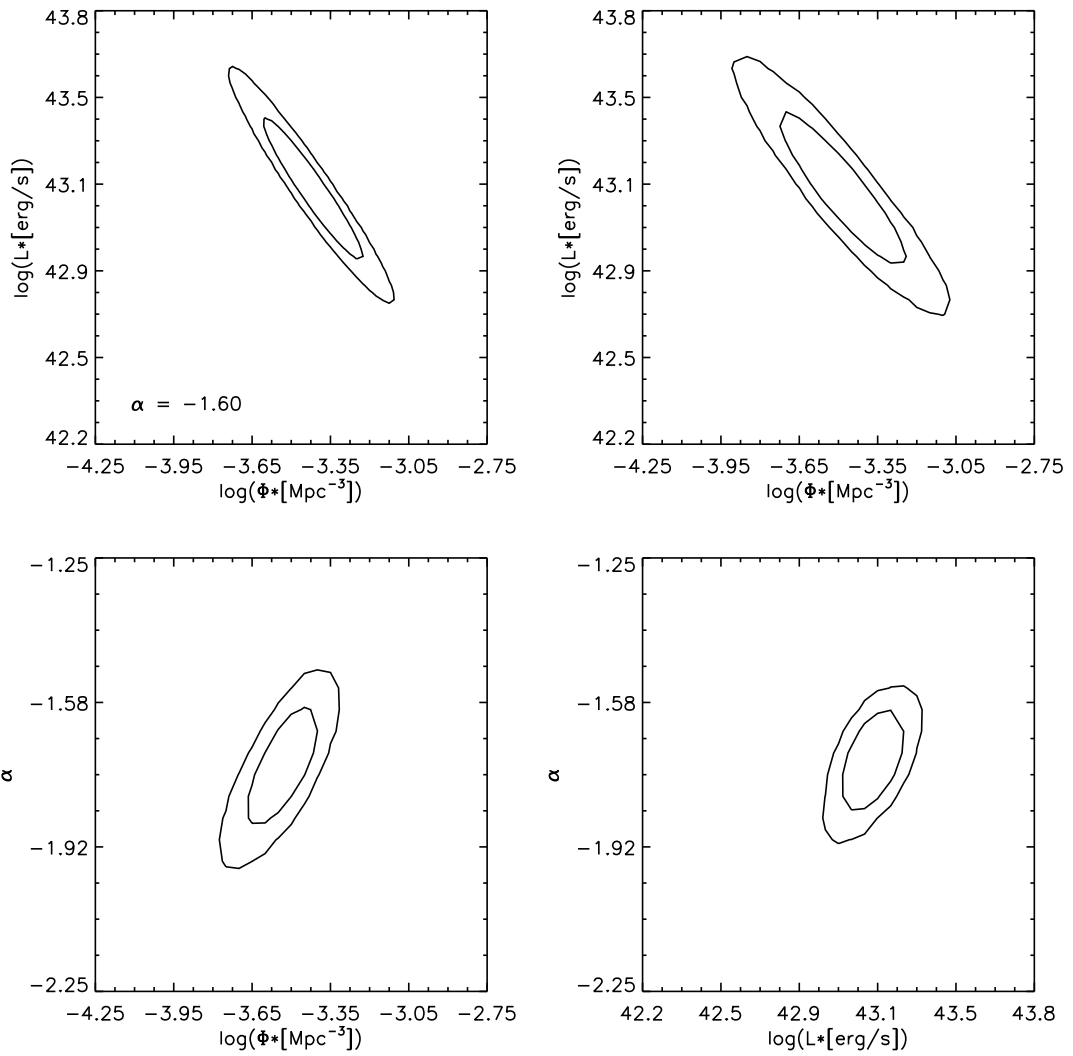


Figure 3.11 – Confidence contours at the 68% and 95% level for Φ_* , L_* , and α from a MC simulation of the H α LF with extinction, completeness, and [N II] contamination corrections. The faint-end slope is fixed to $\alpha = -1.6$ for the upper left panel and is free for the other three panels.

The transformation of the extinction-corrected H α luminosity density into a SFR density is given by $SFR(H\alpha) = 7.9 \times 10^{-42} L(H\alpha)$ where the SFR is provided in $M_\odot \text{ yr}^{-1}$ and the H α luminosity is given in ergs s^{-1} (Kennicutt, 1998). This conversion assumes a Salpeter IMF with minimum and maximum masses of $0.1M_\odot$ and $100M_\odot$ and solar metallicity. We determined that the H α SFR density is $\dot{\rho}_* = 10^{-1.06 \pm 0.05 \pm 0.17} M_\odot \text{ yr}^{-1} \text{ Mpc}^{-3}$ down to $L = 0$ and $\dot{\rho}_* = 10^{-1.20 \pm 0.05 \pm 0.18} M_\odot \text{ yr}^{-1} \text{ Mpc}^{-3}$ for $L > L_{\text{lim}}$, where the second set of errors are for cosmic variance estimated from Somerville et al. (2004). These calculations assume $\alpha = -1.6$. Compared to measurements at $z \lesssim 0.1$ (Gallego et al., 1995; Pérez-González et al., 2003; Brinchmann et al., 2004; Nakamura et al., 2004; Hanish et al., 2006; Ly et al., 2007; Westra et al., 2010), our H α SFR density at $z \sim 0.8$ is higher by a factor of 3 to 13.0 with a median of 6.5.

This H α SFR density estimate is generally believed to originate from star-forming galaxies and not AGN. Many NB surveys have tried to determine the AGN interloper fraction, but it is often difficult since deep x-ray and/or a wealth of spectroscopic information are needed. Villar et al. (2008) reported that Gallego et al. (1995) found 15% AGN contamination to the H α SFR density at $z \sim 0$. Villar et al. (2008) used X-ray data for a small (~ 50) sample of H α emitters at $z \sim 0.8$ and found $10\% \pm 3\%$ in SFR density. Sobral et al. (2009) looked at the spectra for a subset of $z \sim 0.8$ H α emitters and reported $15\% \pm 8\%$ in the SFR density. We have yet to examine more carefully the optical spectra that we have, so for this chapter, we adopt a 15% contamination in the SFR density. This reduces our total H α SFR density to $\dot{\rho}_* = 10^{-1.13 \pm 0.05 \pm 0.17} M_\odot \text{ yr}^{-1} \text{ Mpc}^{-3}$.

3.5 Comparisons with Other Near-Infrared H α Studies

Recently, two other independent groups have performed relatively wide-field near-IR NB imaging on 3-4 meter class telescopes to search for high- z emission line galaxies. [Villar et al. \(2008\)](#) first surveyed 626 arcmin 2 for H α emitting galaxies at $z \sim 0.84$. They identified 165 galaxies and obtained a extinction-corrected SFR density of $0.17 \text{ M}_\odot \text{ yr}^{-1} \text{ Mpc}^{-3}$. [Sobral et al. \(2009\)](#) surveyed a total of 1.3 deg 2 , identified 743 H α emitting galaxies at $z \sim 0.84$, and determined a SFR density of $0.15 \text{ M}_\odot \text{ yr}^{-1} \text{ Mpc}^{-3}$. NewH α covers almost 5 times more area than [Villar et al. \(2008\)](#). While [Sobral et al. \(2009\)](#) covers about 50% more area than we do, our survey is 0.6 dex deeper, so these two surveys should be considered complementary in terms of depth and volume surveyed. NewH α is currently the largest near-infrared H α NB survey with a depth of $1.6 \times 10^{41} \text{ ergs s}^{-1}$. The identification and selection of H α emitters are similar and different in several ways. We summarize them below and discuss the degree for which this might lead to differences in our measurements.

First, these surveys targeted slightly different redshifts using 1% NB filters centered on different wavelengths. However, we do not expect significant evolution from $z \sim 0.81$ to $z \sim 0.84$; corresponding to $\Delta t = 127 \text{ Myrs}$ at $\approx 6.5 \text{ Gyrs}$. [Villar et al. \(2008\)](#) reached an emission-line sensitivity which is comparable to ours while the sensitivity for [Sobral et al. \(2009\)](#) is roughly twice as poor. The main consequence in the different targeted redshift is that our survey is deeper because the custom filter used for the NewH α was designed to target a clean window in the OH airglow, which is not the case for the both these surveys.

We identify NB excess emitters as sources above 3σ with at least a $J - \text{NB1187}$ color of 0.1 mag or 0.15 mag depending on the aperture used for photometry. [Villar et al. \(2008\)](#) indicated that they selected sources at 2.5σ significance in a

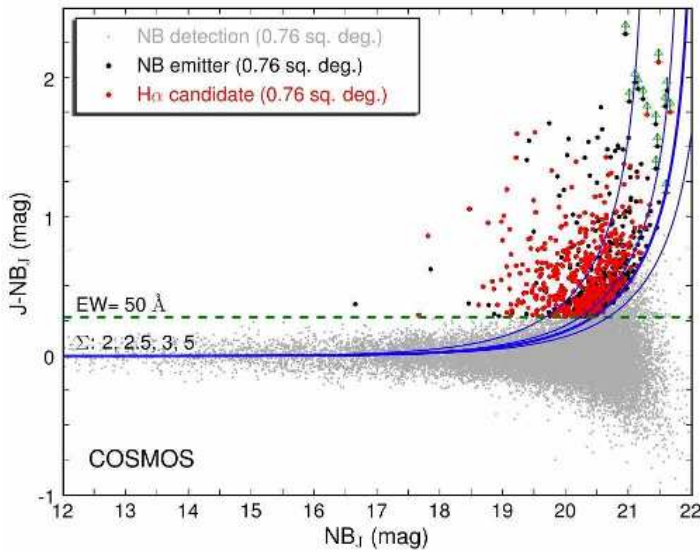


Figure 3.12 – The color-magnitude diagram used by Sobral et al. (2009) to select their NB_J excess emitters in their COSMOS pointings. This here is reproduced from Figure 2 of their paper. It appears that some of the sources selected as NB_J excess emitters is located within the scatter of photometric measurements, so there is a concern of potentially false sources (see text). Magnitudes used here are on a Vega system.

total of 10 apertures out to 5 times the FWHM with a minimum $J - NB$ color of 0.15 mag. We found that the inclusion of larger apertures for New $H\alpha$ only provided 10% more candidates than the $2''$ failed to catch. Larger apertures would only allow Villar et al. (2008) to identify bright and extended galaxies, which are often at lower redshifts. However, the 2.5σ limit would allow them to identify more faint NB excess candidates but potentially more spurious sources can enter into the selection. Sobral et al. (2009) also adopted 2.5σ for their candidates but only used a $3'' \phi$ selection with a minimum $J - NB$ color of 0.3 mag.

We note that in Figure 2 (reproduced here in Figure 3.12) of Sobral et al. (2009), it appears that many of their NB excess candidates are within the distribution of typical photometric scatter. This is apparent at bright magnitudes ($NB_J = 17 - 19$) where the 2.5 and 3σ distributions do not follow the photo-

metric scatter. Comparing this with Figure 3.1 and with Figure 1 of Villar et al. (2008), the 2.5 or 3σ fluctuations for $J - NB$ color *is* expected to encompass the observed scatter; however, this is not the case for Sobral et al. (2009). This raises a concern regarding the number of interlopers in their H α emitting sample. Since their data are unavailable to the public, it is difficult to understand the origin of this problem. The problem appears to begin at $NB_J = 19.75$ mag (Vega) and with a minimum of $J - NB_J = 0.3$ mag, the corresponding emission-line flux is 2×10^{-17} erg s $^{-1}$ cm $^{-2}$ or an H α extinction-corrected luminosity of 3×10^{42} ergs s $^{-1}$. We find that their number densities above this H α luminosity agree with the average of all four fields, but there is significant disagreement at the fainter end.

As another consistency check on the results presented here and in Sobral et al., we can estimate the expected number of H α emitters by using the surface density of [O III] emitters at $z \sim 0.84$ in the SDF (see Chapter 2). Sobral et al. (2009) reached an H α emission-line flux sensitivity of 1×10^{-16} erg s $^{-1}$ cm $^{-2}$. We have shown in § 2.2.6 that the observed [O III]/H α flux ratio is close to 1 and is well correlated with M_B for a large subset of NB excess emitters with [O III] and H α measurements in two different NB filters ($z \approx 0.4$). When we adopt the M_B -dependent [O III]/H α ratio and consider sources with estimated H α emission-line flux of 1×10^{-16} erg s $^{-1}$ cm $^{-2}$, we determine that there should be 60 $z \approx 0.84$ sources over 868 arcmin 2 (248 ± 32 deg $^{-2}$) in the SDF. This can be compared to 627 deg $^{-2}$ found by Sobral et al. (2009) in their COSMOS sample, and 500 deg $^{-2}$ for their UDS sample. In the present study we find a surface density of 230 deg $^{-2}$ for emitters with H α emission-line fluxes above 1×10^{-16} erg s $^{-1}$ cm $^{-2}$. It appears that the surface densities between NewH α and our estimates using the $z \sim 0.84$ [O III] emitters are consistent; however, the surface density found by Sobral et al. is 2–2.5 twice as high. Deep Suprime-Cam NB921 imaging has been

obtained over much of the UDS field. This would yield a sample of $z = 0.84$ [O III] emitters, and it would provide the ultimate and direct test as to whether their fainter candidates are indeed at $z \sim 0.84$ by using a dual narrow-band detection.

One may argue that the differences between the results of NewH α and Sobral et al. is cosmic variance, but estimates using the [Somerville et al. \(2004\)](#) model indicate that we expect $\sigma = 0.40$ for NewH α and $\sigma = 0.30$ for [Sobral et al. \(2009\)](#), so the combination of Poisson and field-to-field fluctuations can be ruled out at the 3σ confidence level.

After obtaining NB excess candidates, the selection of H α emitters is performed. Our survey uses a combination of spectroscopic redshifts and optical colors. The follow-up spectroscopy that we have provides unambiguous classification for 43% of our sources. It indicates that (on average) 12% of H α emitters could be misidentified and are $z \sim 0.75$ [S II] emitters. This estimate for [S II] contamination can easily change if a large-scale structure exists at $z \sim 0.75$. [Villar et al. \(2008\)](#) and [Sobral et al. \(2009\)](#) classified the majority of their sources by z_{phot} . These surveys have follow-up spectroscopy for 9% (138/1527; [Sobral et al., 2009](#)) and 48% (69/165; [Villar et al., 2008](#)). Note that [Villar et al. \(2008\)](#) only reported spectroscopy for their H α emitters rather than the full NB excess emitter sample, so this percentage can be lower. [Sobral et al. \(2009\)](#) did not report the size of the UDS spectroscopic sample that was used, thus the 9% is a lower limit on their spectroscopic completeness.

The LF of [Villar et al. \(2008\)](#) agrees with our NewH α results below a luminosity of 10^{42} ergs s $^{-1}$, but disagrees at the bright end by about +0.3 dex. The luminous end is poorly determined since their survey consists of three pointings (two in the Groth strip, one in GOODS-N) totaling less than 700 arcmin 2 . These individual pointings are significantly small and the Λ CDM model of [Somerville](#)

et al. (2004) estimate $\sigma = 0.50$ for the full Villar et al. (2008) sample and $\sigma = 0.65 - 0.70$ for each individual pointing, so the surface density from NewH α is consistent within the expected cosmic variance. The characteristic luminosity that Villar et al. (2008) determined ($L_\star = 10^{42.97 \pm 0.27}$ ergs s $^{-1}$) is similar to ours ($L_\star = 10^{43.10 \pm 0.17}$ ergs s $^{-1}$) while their normalization (Φ_\star) of the Schechter function is 0.6 ± 0.3 dex higher at the 2σ level, and the faint-end slope is shallower. These differences in Φ_\star and α is likely due to a higher number density from cosmic variance at the bright end, such that the knee is higher but the slope is less steep.

3.6 Discussion

In this section, we compare our H α SFR density measurements with those published in the literature. We have limited the sample to those measured using H α to limit systematic issues with other SFR indicators. The latest compilation of H α measurements was made by Dale et al. (2010). We compare in Figure 3.13 our SFR density measurements against those that have been published, which are summarized in Table 3.5. The dashed line is a fit determined by Dale et al. (2010) using several SFR density measurements where the NewH α measurement was not included in the fitting. It has the form of $\log \left(\frac{\rho_{\text{SFR}}}{M_\odot \text{ yr}^{-1}} \right) = -2.06 + 3.39 \log (1 + z)$. Our SFR density measurement with the removal of 15% for AGN contamination is near this line this line. This relation indicates that the H α SFR density increases by a factor of ≈ 10 per unit redshift at $z < 1.5$.

To understand this redshift evolution, we compare in Figure 3.14 the confidence contours of the Schechter parameters for measurements at $z = 0.07$, $z = 0.40$, and $z = 0.81$. The measurement at $z = 0.40$ utilized two comple-

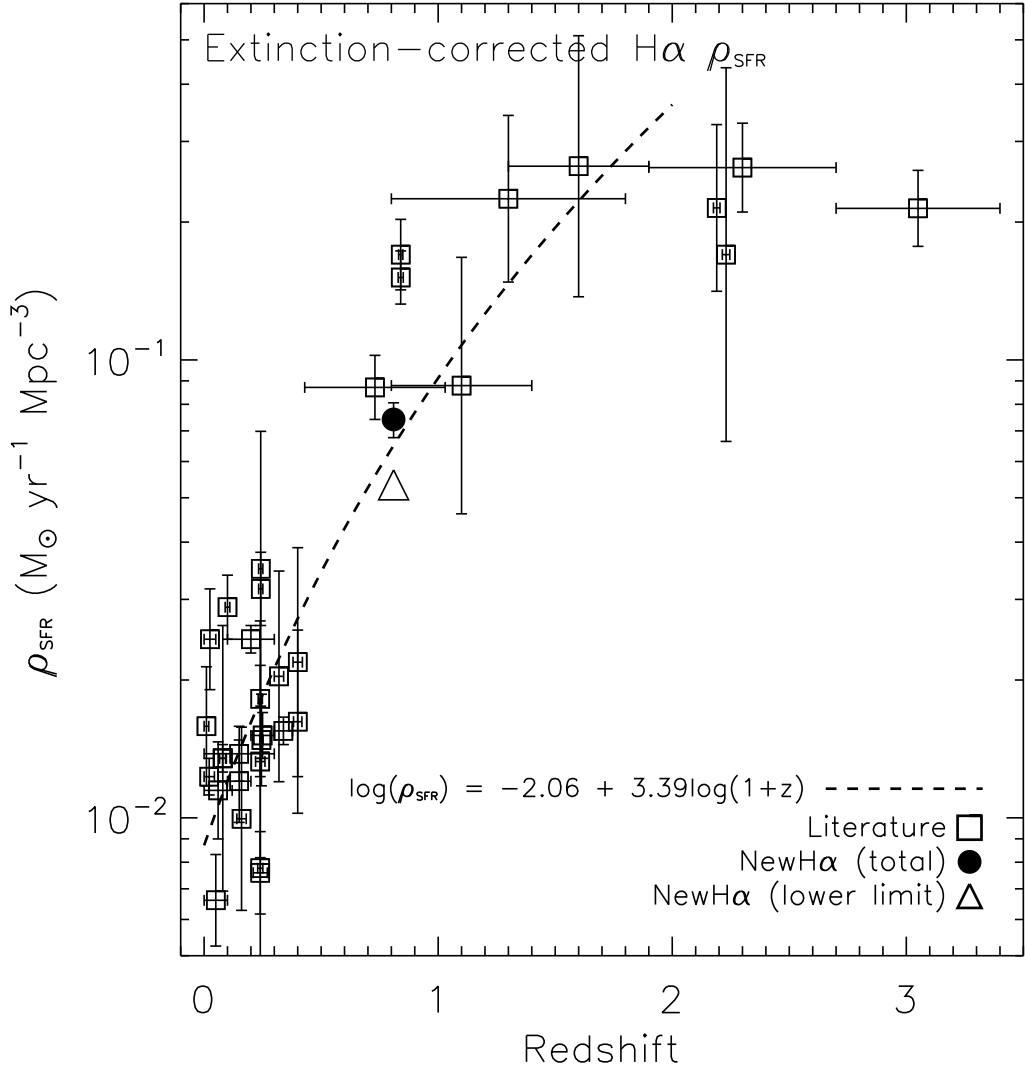


Figure 3.13 – The H α SFR density versus redshift. Open squares are 32 measurements from the literature (see § 3.6 and Table 3.5 for references) while NewH α measurements are shown as the filled circle ($\alpha = -1.6$, LF integrated to $L = 0$; field-to-field fluctuation estimates included) and as a triangle (above the survey limit). Our H α measurements have been systematically reduced by 15% to account for potential AGN contamination. The uncertainties in our “total” SFR density include an estimate of the amount of cosmic variance expected for our survey (see text) and the uncertainties in fitting the LF with a Schechter profile. The dashed line is the fit adopted by Dale et al. (2010) for $z < 2$ measurements (this fit excluded our measurement): $\log (\rho_{\text{SFR}} [M_{\odot} \text{ yr}^{-1}]) = -2.06 + 3.39 \log (1 + z)$.

mentary surveys: the SDF measurement discussed in Chapter 2 (extremely deep for 0.25 deg²) with those from the Wyoming Survey for H α (Dale et al., 2010, shallower sensitivity but covers 4 deg²). The combination of the two provides leverage over estimating the faint end slope and the characteristic luminosity, L_* . Likewise, $z < 0.1$ measurements from the SDF are combined with Gallego et al. (1995) for similar reasons. We find that the characteristic luminosity systematically increases by 1.05 dex (0.75 dex) from $z \sim 0.1$ ($z = 0.4$) to $z = 0.8$, but the normalization is lower by 0.25 dex at $z \sim 0.81$ than at $z \sim 0$. This indicates that the increase in the SFR density is a result of the idea that L_* galaxies at $z \sim 0.8$ are producing stars at a rate that is ≈ 10 times that of local L_* galaxies; however, they are underdense by a factor of ≈ 2 . The faint-end slope appears to be steeper compared to $z = 0.40$. If this holds with deeper H α surveys and after our final estimates of completeness, it would imply that low mass galaxies contribute more to the bulk of the star formation at higher redshifts.

3.7 Future Work

In this chapter, we discussed measurements of H α SFRs at $z \sim 0.81$. We hope to complete the NewH α survey with measurements at $z \sim 2.2$. We have already purchased, installed, and tested a 1% filter centered at 2.096 μm with NEWFIRM. One of five fields have been acquired in this NB filter. The completion of the survey at this redshift is expected to occur in late-2010 since previous data acquisition in 2009 were significantly affected by poor weather conditions. The goal is to detect ~ 300 H α emitters and probe SFRs down to $\sim 0.4L_*$ ($\sim 8 h_{70}^{-2} M_\odot \text{yr}^{-1}$). In addition, we hope to acquire deeper pointings at both redshifts using FourStar (Persson et al., 2008, expected science operations in late-2010) a new NIR camera for Magellan. The improvement in sensitivity is from a combination

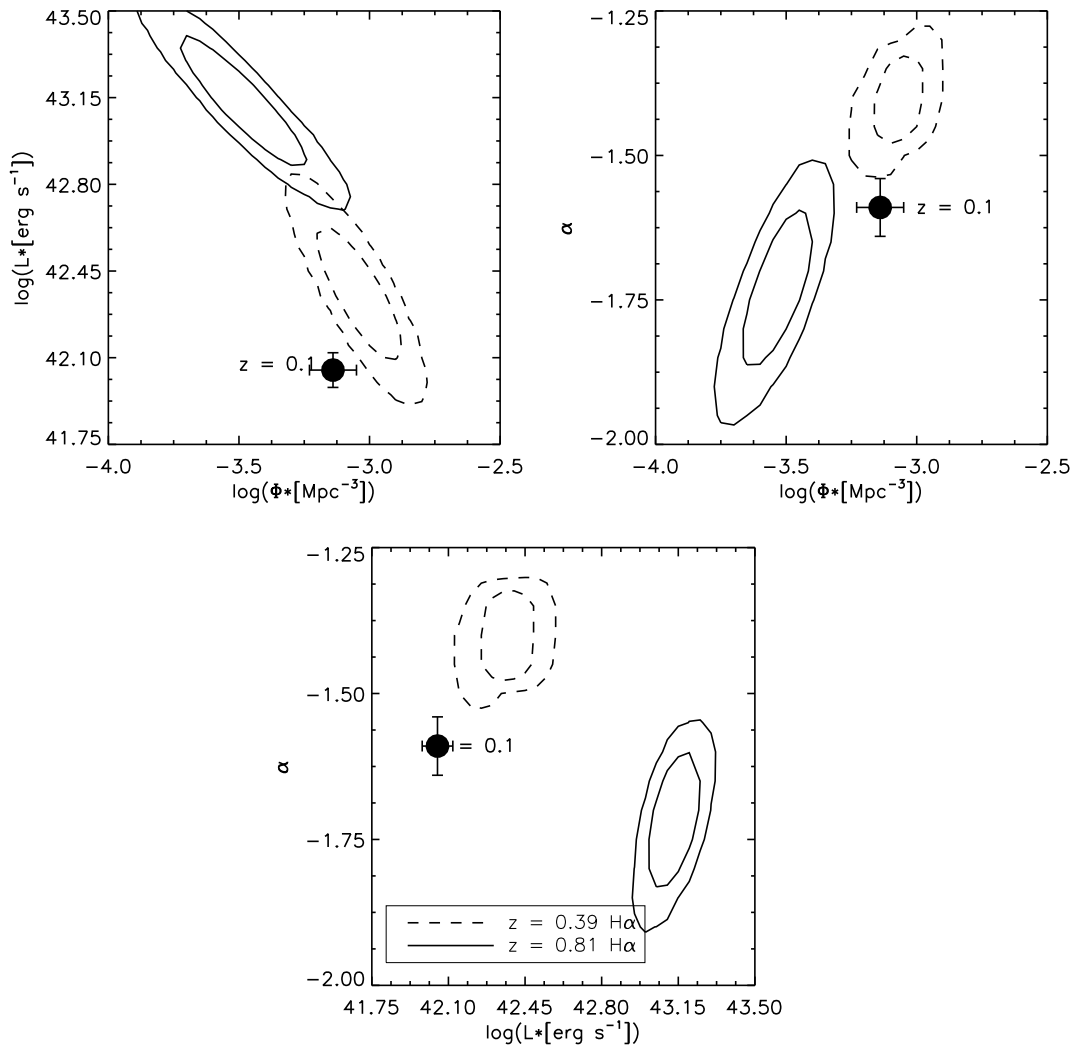


Figure 3.14 – Confidence contours for L_* , Φ_* , and α for $\text{H}\alpha$ measurements at $z \approx 0.1$ (black circle), $z = 0.39$ (dashed line), and $z = 0.81$ (solid line). The greatest difference is in L_* with it increasing by 0.4 dex.

Table 3.5. Compilation of H α SFR densities

References	z	Area	N	$\log(\rho_{\text{SFR}})^{\text{a}}$
Gallego et al. (1995)	0.022±0.022	471.4 deg 2	176	-1.91 ± 0.04
Tresse & Maddox (1998)	0.20±0.10	500 arcmin 2	138	-1.61 ± 0.03
Yan et al. (1999)	1.3±0.5	~ 85 arcmin 2	33	-0.574 ± 0.182
Sullivan et al. (2000)	0.15±0.15	...	216	-1.86 ± 0.06
Tresse et al. (2002)	0.73±0.30	...	30	-1.06 $^{+0.07}_{-0.08}$
Fujita et al. (2003)	0.242±0.009	706 arcmin 2	348	-1.50 $^{+0.08}_{-0.17}$ ^b
Hippelein et al. (2003)	0.245±0.007	407 arcmin 2	92	-1.83 $^{+0.10}_{-0.13}$
Pérez-González et al. (2003)	0.025±0.025	...	79	-1.61 $^{+0.11}_{-0.08}$
Brinchmann et al. (2004)	0.10±0.01	SDSS	...	-1.54 ± 0.07
Nakamura et al. (2004)	0.06±0.06	SDSS	1482	-1.94 $^{+0.106}_{-0.082}$
	0.079±0.013	-1.87 ± 0.03
Hanish et al. (2006)	0.06±0.06	SINGG	110	-1.80 $^{+0.13}_{-0.07}$
Ly et al. (2007)	0.08±0.015	868 arcmin 2	318	-1.87 ± 0.29 ^c
	0.24±0.011	868 arcmin 2	259	-2.11 ± 0.24 ^c
	0.40±0.018	868 arcmin 2	391	-1.79 ± 0.20 ^c
Geach et al. (2008)	2.23±0.016	0.60 deg 2	55	-0.77 $^{+0.408}_{-0.23}$
Morioka et al. (2008)	0.242±0.009	875 arcmin 2 + SDSS	575	-1.456 $^{+0.30}_{-0.174}$
Shioya et al. (2008)	0.24±0.009	5540 arcmin 2	980	-1.74 $^{+0.17}_{-0.097}$
Villar et al. (2008)	0.84±0.009	625 arcmin 2	165	-0.77 ± 0.077
Westra & Jones (2008)	0.24±0.03	1771 arcmin 2	707	-2.12 $^{+0.09}_{-0.12}$
Shim et al. (2009)	1.1±0.3	~ 104 arcmin 2	35	-1.056 ± 0.28
	1.6±0.3	~ 104 arcmin 2	45	-0.577 ± 0.285
Sobral et al. (2009)	0.84±0.011	1.3 deg 2	743	-0.82 ± 0.058 ^d
Dale et al. (2010)	0.16±0.02	~4 deg 2	214	-2.002 ± 0.20
	0.24±0.02	~4 deg 2	424	-1.877 ± 0.21
	0.32±0.02	~4 deg 2	438	-1.691 ± 0.23
	0.40±0.02	~4 deg 2	91	-1.660 ± 0.25
Hayes et al. (2010)	2.19±0.014	56 arcmin 2	55	-0.668 ± 0.182
Westra et al. (2010)	0.05±0.05	4 deg 2	322	-2.18 ± 0.10
	0.15±0.05	4 deg 2	1127	-1.92 ± 0.09
	0.25±0.05	4 deg 2	1268	-1.82 ± 0.05
	0.34±0.04	4 deg 2	848	-1.81 ± 0.03
NewH α (total)	0.809±0.008	0.82 deg 2	398	-1.18 ± 0.18 ^c
NewH α ($L \geq L_{\text{lim}}$)	0.809±0.008	0.82 deg 2	352	-1.33 ± 0.18 ^c

^a ρ_{SFR} in units of $M_{\odot} \text{ yr}^{-1} \text{ Mpc}^{-3}$. Corrections for dust extinction have been included.

^b See § 2.3.1 for discussion of potentially 50% contamination, which was not accounted.

^c Estimates for cosmic variance are included within the uncertainties.

^d See § 3.5 for discussion of possible systematic contamination from false NB excess emitting sources.

of the larger collecting area (6.5 m versus 4 m) and sub-arcsecond seeing from a better site. It will yield more accurate constraints on the faint-end slope, which is currently poorly constrained at $z \gtrsim 1$.

We presented in this chapter, results from four of our five NEWFIRM pointings. The H α sample for the last field (SSA-22) will be published with those presented here later this year. This will extend the NewH α survey to 1 deg 2 and will provide better estimates in fitting the H α LF.

This work has only investigated the sample of H α emitters. We hope to construct the emission-line LF for [O III] emitters at $z \sim 1.4$ with a statistically large enough sample. Such measurements would allow us to extend [O III] LF above $z = 1$. The sample will certainly probe the bright end, but that may be sufficient to look at evolution in the knee of the LF between $z \approx 0.84$ and $z \approx 1.4$.

We have proposed for follow-up NIR spectroscopy in late-2010 with FMOS. This will provide more reliable and appropriate [N II] flux contamination determination for our population of star-forming galaxies. With our optical spectroscopy, we will probe the full suite of rest-frame optical emission lines, to place constraints on gas metallicities, dust extinction corrections, and AGN activity at $z \sim 1$.

3.8 Conclusions

We have conducted a wide-area search for star-forming galaxies using the NB technique in the near-infrared. This study is the first of NB H α near-infrared surveys to probe down to an extinction-corrected H α luminosity of 1.6×10^{41} ergs s $^{-1}$ (SFR of $\approx 1 M_\odot$ yr $^{-1}$) with an area coverage of 0.82 deg 2 . We have identified 1117 NB excess emitters, and 398 are classified as H α emission-line galaxies at $z \sim 0.81$ over 0.82 deg 2 . The classification utilized a large spectroscopic sample

providing unambiguous determination of redshifts for 43% of the sample. These spectra were also used to calibrate the multi-color selection of the remaining H α emitters without spectroscopic follow-up.

We constructed the extinction- and completeness-corrected H α luminosity function. Corrections for [N II] flux contamination and the effective surveyed volume, which is dependent on the line flux, were included. The LF is well described by a Schechter function with $L_\star = 10^{43.10 \pm 0.17}$ ergs s $^{-1}$ and $\Phi_\star = 10^{-3.40 \pm 0.13}$ Mpc $^{-3}$ (adopting $\alpha = -1.6$). Allowing the faint-end slope to be free, we determined $L_\star = 10^{43.20 \pm 0.51}$ ergs s $^{-1}$, $\Phi_\star = 10^{-3.6 \pm 0.60}$ Mpc $^{-3}$, and $\alpha = -1.75 \pm 0.49$. We derived a SFR density of $\dot{\rho}_\star = 10^{-1.20 \pm 0.05 \pm 0.18}$ M $_\odot$ yr $^{-1}$ Mpc $^{-3}$ above our survey limit and $\dot{\rho}_\star = 10^{-1.13 \pm 0.05 \pm 0.17}$ M $_\odot$ yr $^{-1}$ Mpc $^{-3}$ when the LF is integrated to $L = 0$ and we account for 15% AGN contamination. The latter is (on average) 5 times higher than $z \sim 0$ measurements. We determined that the characteristic H α luminosity is systematically higher at $z \sim 0.81$ by 0.75 and 1.05 dex compared to $z = 0.40$ and $z \sim 0.1$ estimates; however, the normalization of the LF at $z \sim 0.8$ is a factor of 2 lower compared to $z \sim 0$. This implies that the cause of the redshift evolution in the H α SFR density can be attributed to the idea that typical galaxies at $z \sim 0.8$ are forming stars at a rate that is ≈ 10 times more rapid than the typical galaxies seen locally but with a factor of 2 lower number density.

This study illustrates that H α can be extended to high redshift, and with more sensitive detectors and large field coverage in the near future, H α measurements for thousands of galaxies out to $z \sim 3$ will be possible. One of the greatest strengths of emission-line surveys is the ability to have redshifts as accurate as $1\%/(1+z)$. This opens up the possibility that such surveys could place constraints on the equation of state of dark energy ([Geach et al., 2010](#)). These emission-line

surveys provides significant efficiency in obtaining redshifts, thus complementing future large spectroscopic surveys with the same goal in mind.

The greatest limitation for ground-based NIR surveys is the OH background, which explains the dearth of H α measurements at $z = 0.5 - 0.8$ and in the H -band window ($z \sim 1.5$). The new *Hubble*/WFC3 IR camera will be able to fill these uncovered epochs by using a grism (much like the work of [Yan et al., 1999](#); [Shim et al., 2009](#)), but with deeper and wider observations. Such a survey (Malkan et al., in preparation) has begun, and it will yield H α SFRs at $z = 0.25 - 1.6$ as well as other emission lines (e.g., [O II] and [O III]) out to $z \approx 4$ to probe a significant fraction of the early universe. Finally, this field will benefit from multi-object NIR spectrographs. Several spectrographs, such as Keck/MOSFIRE, Subaru/FMOS, and Gemini/FLAMINGOS-2 are nearing completion or in operation, and detailed study of the metallicity and dynamics (through studying the emission line profiles) of typical galaxies at $z \sim 1$ will be possible with a statistically large sample.

CHAPTER 4

Lyman Break Galaxies at $z \approx 1.8 - 2.8$

Over the past decade, the number of Lyman break galaxies (LBGs; for a review, see [Giavalisco, 2002](#)) identified at $z \sim 3 - 6$ has grown rapidly from deep, wide-field optical imaging surveys (e.g., [Steidel et al., 1999](#); [Bouwens et al., 2006](#); [Yoshida et al., 2006](#)). Follow-up spectroscopy on large telescopes has shown that this method (called the Lyman break technique or the “drop-out” method) is efficient at identifying high- z star-forming galaxies. Furthermore, these studies have measured the cosmic star-formation history (SFH) at $z > 3$, which is key for understanding galaxy evolution. It indicates that the star-formation rate (SFR) density is 10 or more times higher in the past than at $z \sim 0$.

Extending the Lyman break technique to $z < 3$ requires deep, wide-field UV imaging from space, which is difficult. In addition, [O II] (the bluest optical nebular emission line) is redshifted into the near-infrared (NIR) for $z \gtrsim 1.5$ where high background and lower sensitivity limit surveys to small samples (e.g., [Malkan et al., 1996](#); [Moorwood et al., 2000](#); [van der Werf et al., 2000](#); [Erb et al., 2003](#)). The combination of these observational limitations has made it difficult to probe $z \approx 1.5 - 2.5$.

One solution to the problem is the ‘BX’ method developed by [Adelberger et al. \(2004\)](#). This technique identifies blue galaxies that are detected in U , but show a moderately red $U - G$ color when the Lyman continuum break begins to enter into the U -band at $z \sim 2$.

Other methods have used NIR imaging to identify galaxies at $z = 1 - 3$ via the Balmer/4000Å break. For example, selection of objects with $J - K > 2.3$ (Vega) has yielded “distant red galaxies” at $z \sim 2 - 3$ (van Dokkum et al., 2004), and the ‘ BzK ’ method has found passive and star-forming (dusty and less dusty) galaxies at $z \approx 1.5 - 2.5$ (Daddi et al., 2004; Hayashi et al., 2007). The completeness of these methods is not as well understood as UV-selected techniques, since limited spectra have been obtained.

In this paper, the Lyman break technique is extended down to $z \sim 1.8$ with wide-field, deep NUV imaging of the Subaru Deep Field (SDF) with the Galaxy Evolution Explorer (*GALEx*; Martin et al., 2005). This survey has the advantage of sampling a large contiguous area, which allows for large scale structure studies (to be discussed in future work), an accurate measurement of a large portion of the luminosity function, and determining if the SFH peaks at $z \sim 2$.

In § 4.1, the photometric and spectroscopic observations are described. Section 4.2 presents the color selection criteria to produce a photometric sample of NUV -dropouts, which are objects undetected or very faint in the NUV , but present in the optical. The removal of foreground stars and low- z galaxy contaminants, and the sample completeness are discussed in § 4.3. In § 4.4, the observed UV luminosity function (LF) is constructed from ~ 7100 NUV -dropouts in the SDF, and the comoving star-formation rate (SFR) density at $z = 1.8 - 2.8$ is determined. Comparisons of these results with previous surveys are described in § 4.5, and a discussion is provided in § 4.6. A description of objects with unusual spectral properties is provided in Appendix A.

4.1 Observations

This section describes the deep *NUV* data obtained (§ 4.1.1), followed by the spectroscopic observations (§ 4.1.2 and 4.1.4) from Keck, Subaru, and MMT (Multiple Mirror Telescope). An objective method for obtaining redshifts, cross-correlating spectra with templates, is presented (§ 4.1.3) and confirms that most *NUV*-dropouts are at $z \sim 2$. These spectra are later used in § 4.2.2 to define the final empirical selection criteria for $z \sim 2$ LBGs. A summary of the success rate for finding $z \sim 2$ galaxies as *NUV*-dropouts is included.

4.1.1 *GALEX/NUV Imaging of the SDF*

The SDF was imaged with *GALEX* in the *NUV* ($1750 - 2750\text{\AA}$) between 2005 March 10 and 2007 May 29 (GI1-065) with a total integration time of 138176 seconds. A total of 37802 objects are detected in the full *NUV* image down to a depth of ≈ 27.0 mag (3σ , $7.5''$ diameter aperture). The *GALEX*-SDF photometric catalog will be presented in future work. For now, objects undetected or faint ($NUV > 25.5$) in the *NUV* are discussed.

The *NUV* image did not require mosaicking to cover the SDF, since the *GALEX* field-of-view (FOV) is larger and the center of the SDF is located at $(+3.87'', +3.72'')$ from the center of the *NUV* image. The *NUV* spatial resolution (FWHM) is $5.25''$, and was found to vary by no more than 6% across the region of interest (Morrissey et al., 2007).

4.1.2 Follow-up Spectroscopy

4.1.2.1 Keck/LRIS

When objects for Keck spectroscopy were selected, the *NUV* observations had accumulated 79598 seconds. Although the selection criteria and photometric catalog are revised later in this paper, a brief description of the original selection is provided, since it is the basis for the Keck sample. An *initial NUV-dropout* catalog (hereafter ver. 1) of sources with $NUV - B > 1.5$ and $B - V < 0.5$ was obtained. No aperture correction was applied to the $7.5''$ aperture *NUV* flux and the $2''$ aperture was used for optical photometry. These differ from the final selection discussed in § 4.2.2. The *NUV* 3σ limiting magnitude for the ver. 1 catalog is 27.0 within a $3.39''$ radius aperture. Postage stamps (see Figure 4.1) were examined for follow-up targets to ensure that they are indeed *NUV*-dropouts.

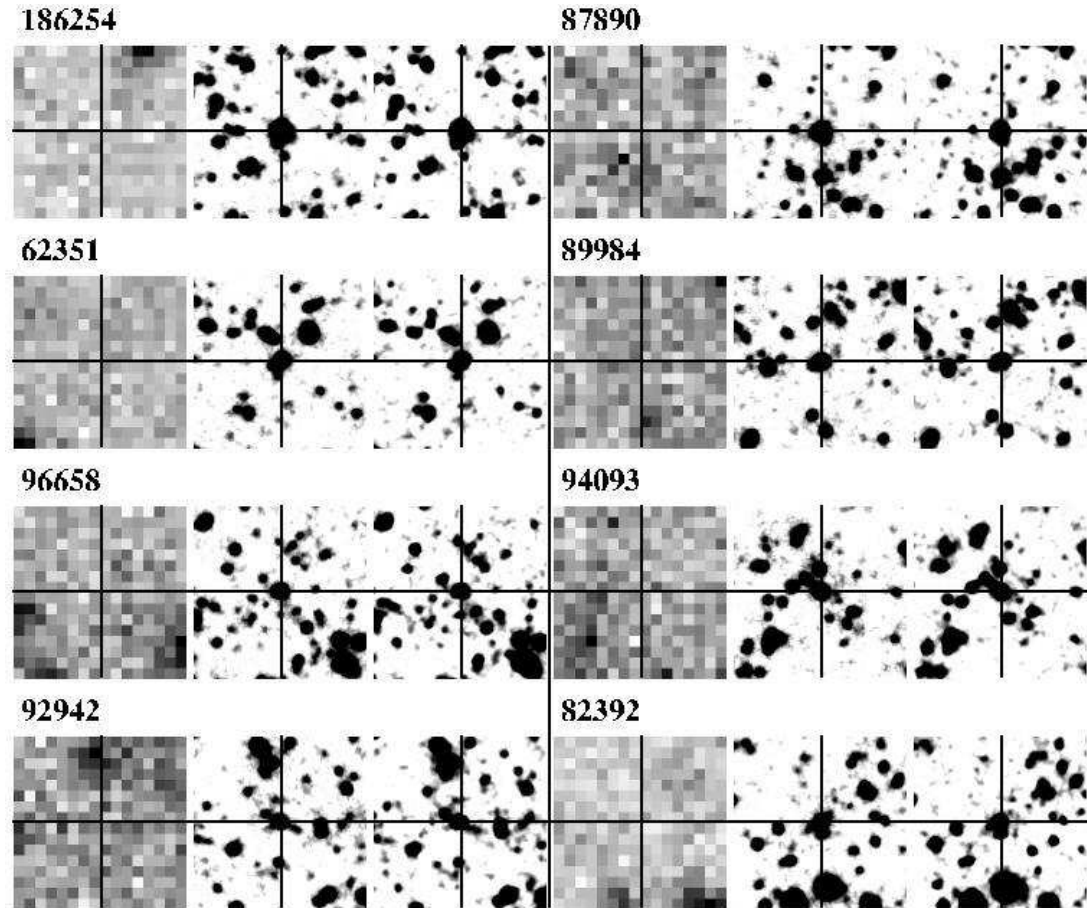


Figure 4.1 – From left to right is *NUV*, *B*, and *V*. Each image is $24''$ on a side and reveals that optical sources do not have a *NUV* counterpart. Photometric and spectroscopic information are provided in Table 4.1.

Table 4.1. Properties of Spectroscopically Targeted NUV -dropouts and BzKs

B -band ID ^a	Name (SDF)	$NUV - B$	$B - V$	NUV	B	V	R_C	i'	z'
With emission lines									
179350L	>2.662	0.078	>27.121	24.459	24.366	24.379	24.430	24.500	
170087L	>2.562	0.128	>27.126	24.564	24.498	23.991	23.880	23.859	
62056L	>2.991	0.107	>27.165	24.174	24.161	24.103	24.182	24.263	
60962L	>2.896	0.136	>27.164	24.268	24.110	23.993	23.917	23.527	
96658L	>2.605	0.282	>27.158	24.553	24.310	24.193	24.220	24.485	
87890L	>3.597	0.278	>27.161	23.564	23.334	23.298	23.335	23.362	
92076L	>2.666	0.239	>27.143	24.477	24.256	24.130	24.115	24.184	
89984L	>3.386	0.246	>27.169	23.783	23.567	23.516	23.436	23.309	
94093L	>3.248	0.129	>27.165	23.917	23.770	23.693	23.674	23.705	
82392L	>2.941	0.196	>27.166	24.225	24.037	24.025	24.084	24.054	
139014M	2.110	0.238	26.131	24.021	23.863	23.569	23.283	23.109	
140830M	>2.816	0.100	>27.158	24.342	24.264	24.024	23.821	23.390	
142813M	>2.552	0.124	>27.160	24.608	24.420	24.401	24.194	23.647	
143960M	>2.421	0.347	>27.161	24.740	24.436	24.393	23.965	23.682	
166380M	>2.994	0.356	>27.278	24.284	23.951	23.870	23.745	23.532	
166078M	>3.332	0.530	>27.138	23.806	23.290	23.081	22.884	22.628	
158464M	0.597	0.193	>25.235	24.638	24.485	24.162	23.887	23.513	
170958M	>1.136	0.495	>27.121	25.985	25.489	25.079	24.912	24.690	
171558M	0.094	0.248	>25.145	25.051	24.842	24.675	24.304	23.936	
188586M	1.535	0.309	25.720	24.185	24.102	23.725	23.328	22.886	
78625H	2.625	-0.162	25.171	22.546	22.704	22.225	22.211	22.153	
175584H	2.405	0.223	25.284	22.879	22.643	22.341	22.084	21.723	
169311H	>3.838	0.429	>27.142	23.304	22.949	22.847	22.890	22.875	
144397H	3.621	0.421	26.231	22.970	22.541	22.386	22.336	22.326	
133660H	2.646	0.175	25.785	23.139	22.970	23.009	22.673	22.609	
Absorption line systems									
186254L	>4.032	0.203	>27.145	23.113	22.910	22.833	22.727	22.560	
62351L	>3.213	0.221	>27.179	23.966	23.750	23.712	23.610	23.462	
144516H	1.915	0.291	25.014	23.099	22.804	22.638	22.243	21.955	
182284H	3.560	0.288	26.004	22.444	22.198	21.962	21.774	21.384	
$Z < 1.5$ interlopers and stars									
179764L	1.421	0.183	25.673	24.252	24.054	23.970	23.602	23.391	
63771L	>2.767	0.331	>27.163	24.396	24.058	23.832	23.383	22.922	
68765L	>1.561	0.256	>27.183	25.622	25.336	24.711	24.401	24.404	
48542L	1.725	0.138	26.109	24.384	24.191	23.904	23.680	23.361	
104403L	1.544	0.326	26.110	24.566	24.294	24.102	23.752	23.580	
136893M	>2.666	0.346	>27.157	24.491	24.145	23.700	23.300	22.769	
137114M	1.751	0.245	25.626	23.875	23.669	23.348	23.064	22.504	
163292M	1.098	0.295	26.278	25.180	24.875	24.544	24.263	23.777	
191435M	0.673	0.119	23.899	23.226	23.100	22.959	22.788	22.427	
145511H	3.258	0.148	25.944	22.686	22.539	22.337	22.176	21.765	
71239L	>3.984	0.623	>27.183	23.199	22.574	22.301	22.175	22.088	
66611L	>4.863	0.532	>27.178	22.315	21.783	21.581	21.485	21.440	
86900L	>4.206	0.616	>27.161	22.955	22.341	22.131	22.060	22.033	
149720H	3.621	0.367	26.215	22.594	22.227	22.094	22.061	22.048	
178741H	1.760	0.266	24.286	22.526	22.262	22.268	22.338	22.432	
Ambiguous NUV -dropouts									
185177L	>3.181	0.128	>27.145	23.964	23.837	23.703	23.630	23.286	
165834L	>4.227	0.181	>27.147	22.920	22.762	22.728	22.649	22.607	
56764L	>2.591	0.159	>27.171	24.580	24.320	24.317	24.346	24.192	
80830L	>2.522	0.226	>27.148	24.626	24.414	24.380	24.360	24.351	
96927L	>3.255	0.190	>27.162	23.907	23.707	23.621	23.537	23.384	

Table 4.1 (cont'd)

<i>B</i> -band ID ^a	Name (SDF)	<i>NUV</i> − <i>B</i>	<i>B</i> − <i>V</i>	<i>NUV</i>	<i>B</i>	<i>V</i>	<i>R</i> _C	<i>i'</i>	<i>z'</i>
92942L	>2.638	0.198	>27.160	24.522	24.253	24.280	24.260	24.236	
169090L	>3.154	0.164	>27.137	23.983	23.798	23.660	23.461	23.223	
86765L	>2.404	0.571	>27.176	24.772	24.215	24.078	24.025	23.759	
137763H	2.547	0.102	25.458	22.911	22.821	22.798	22.801	22.522	
92150H	3.903	0.498	26.516	22.613	22.117	21.934	21.864	21.855	
176626H	4.172	0.482	26.852	22.680	22.201	21.972	21.896	21.837	
166856H	>4.160	0.305	>27.286	23.126	22.820	22.625	22.469	22.137	
146434H	1.864	0.091	24.721	22.857	22.755	22.676	22.630	22.470	
183911H	2.367	0.157	25.361	22.994	22.821	22.562	22.396	22.043	
78733H	4.126	0.367	27.164	23.038	22.683	22.586	22.567	22.575	
66488H	>4.595	0.447	>27.165	22.570	22.126	21.960	21.897	21.833	
190498H	3.652	0.409	26.211	22.559	22.148	21.999	21.969	21.930	
190947H	>4.344	0.212	>27.140	22.796	22.597	22.423	22.259	22.081	
153628H	>4.563	0.457	>27.268	22.705	22.243	22.066	21.993	21.962	
Undetected <i>NUV</i> -dropouts									
174747L	1.951	0.247	26.332	24.381	24.184	24.080	24.028	23.969	
182447L	>2.603	0.385	>27.105	24.502	24.126	23.642	23.192	22.584	
180088L	>2.720	0.129	>27.120	24.400	24.262	24.198	24.040	23.766	
172253L	>2.911	0.224	>27.120	24.209	24.017	23.970	23.960	23.853	
184387L	>2.362	0.173	>27.137	24.775	24.606	24.275	24.109	23.586	
63360L	>2.353	0.443	>27.167	24.814	24.275	23.840	23.600	23.346	
113109L	>2.478	0.209	>27.158	24.680	24.417	24.408	24.252	24.298	
94367L	>3.386	0.246	>27.169	23.783	23.567	23.516	23.436	23.309	

Note. — Identified sources are based on an $R > 3.0$ criterion (exceptions are AGNs, stars, and those with emission lines). Col. (1) is the *B*-band catalog ID, Col. (2) is the J2000 coordinates, and magnitudes and colors are given in Cols. (3) to (10). The cross-correlated redshifts and R -values from `xcsao` are provided in Cols. (11) and (12). The template yielding the highest R -value is given in Col. (13), where 1–4 correspond to the four spectra of Steidel et al. (2003) from strongest Ly α absorption to emission, and 5 and 6 refer to the Shapley et al. (2003) composite and cB58 spectra, respectively. ‘7’ corresponds to the rest-frame NUV spectra from Savaglio et al. (2004), and ‘AGN’ refers to a SDSS QSO template. For interlopers, the six SDSS composite spectra presented in Yip et al. (2004) correspond to [1] to [6] from strongest absorption-line to strongest emission-line systems. [7], [8], and [9] correspond to the RVSAO templates “femtemp”, “EA”, and “eatemp”, respectively. For objects with Ly α emission, the line flux (in units of 10^{-18} ergs s $^{-1}$ cm $^{-2}$) and rest-frame EWs (in units of Å) are given in Cols. (14) and (15), respectively. These were measured using the `splot` routine.

^aThe character following the ID number corresponds to the spectrograph used: ‘H’=Hectospec, ‘L’=LRIS, ‘M’=MOIRCS.

^bValues in superscript correspond to other templates, which yielded similar cross-correlated velocities with $R \geq 2.5$.

^cAs discussed in § A, this source shows an unusual Ly α profile, so the reported flux and rest-frame EW excluded the blue excess by deblending in IRAF `splot`.

^dThe values reported here correspond to the best cross-correlated results, but may be wrong due to the low S/N of the spectra.

Table 4.2. Continuation of Table 4.1

B-band ID ^a	Name (SDF)	redshift	R	Temp. ^b	F(Ly α)	EW _o (Ly α)
With emission lines						
179350L	132431.8+274214.28	2.0387	9.72	4 ⁵	157	5.38
170087L	132428.6+274037.95	2.2992	12.29	4 ⁵	80.4	58.20
62056L	132452.9+272128.50	2.6903	34.21	4 ^{3,5}	66.4 ^c	37.12 ^c
60962L	132436.7+272118.67	1.9098	3.06	4 ^{3,5}	20.3	7.14
96658L	132521.5+272730.24	2.5639	3.99	5 ^{3,4}	9.5	5.21
87890L	132520.3+272559.22	2.5747	9.84	2 ^{3,4,5}	28.9	5.56
92076L	132507.6+272303.44	2.1720	3.93	3 ^{2,5}	13.4	6.52
89984L	132506.8+272620.75	2.0894	3.30	2 ¹	5.6	4.11
94093L	132457.7+272703.10	2.0025	6.87	5 ^{2,3,4}	56.9	20.71
82392L	132454.4+272503.97	2.6527	28.57	4 ^{2,3,5}	112	45.56
139014M	132417.5+273512.63	1.750
140830M	132422.4+273530.21	1.504
142813M	132414.8+273552.41	2.018
143960M	132425.5+273603.42	1.872
166380M	132410.4+273958.51	2.013
166078M	132418.2+273954.46	2.044
158464M	132419.6+273842.92	1.506
170958M	132415.8+274043.52	1.710
171558M	132409.1+274052.82	1.796
188586M	132417.8+274405.52	1.719
78625H	132343.4+272426.33	1.6755	2.30	AGN
175584H	132504.3+274147.60	2.3902	2.69	4 ³
169311H	132440.0+274040.27	2.6693	6.72	3 ^{1,2,4,5}
144397H	132422.5+273612.47	2.6421	2.60	1
133660H	132507.0+273413.84	1.9345	2.52	AGN
Absorption line systems						
186254L	132442.0+274334.89	1.7550	3.15	6 ²
62351L	132447.2+272135.84	1.7921	6.61	6 ^{1,2}
144516H	132350.8+273614.52	1.7488	5.79	5 ⁶
182284H	132348.4+274301.74	1.5926	3.22	7 ⁶
$Z < 1.5$ interlopers and stars						
179764L	132442.6+274220.19	1.0139	9.32	[7] ^{4,5,6}
63771L	132452.9+272147.91	1.0965	10.37	[7] ^{4,5}
68765L	132444.4+272237.13	0.6898	6.29	[5] ^{4,6,7}
48542L	132434.6+271901.63	1.4220	3.77	[7] ^{4,5}
104403L	132508.4+272853.98	0.9921	10.22	[7] ^{4,5,6}
136893M	132424.1+273447.28	1.479
137114M	132416.4+273455.52	1.174
163292M	132423.2+273923.57	1.498
191435M	132422.3+274421.71	1.250
145511H	132429.9+273635.92	1.4729	2.82	7
71239L	132453.1+272307.35	-0.0008	6.32	[2] ^{1,3}
66611L	132446.5+272218.81	-0.0018	9.96	[2] ^{1,3}
86900L	132511.5+272303.44	-0.0015	4.65	[1] ^{2,3}
149720H	132407.7+273704.83	0.0006	3.81	[9]
178741H	132515.4+274212.36	0.0002	1.87	[8]
Ambiguous NUV -dropouts						
185177L	132442.7+274319.52	2.6739 ^d	2.28	3
165834L	132431.0+273954.97	2.1348 ^d	2.41	1,6
56764L	132449.4+272029.14	0.2473 ^d	2.49	[1]
80830L	132503.3+272445.16	2.0855 ^d	2.22	[6]
96927L	132523.0+272734.22	2.6436 ^d	2.98	1 ⁶

Table 4.2 (cont'd)

<i>B</i> -band ID ^a	Name (SDF)	redshift	<i>R</i>	Temp. ^b	F(Ly α)	EW _o (Ly α)
92942L	132515.7+272653.97	1.0713 2.1863 ^d 0.9496	2.68 2.64 2.44	[3] 6 [3]
169090L	132420.8+274025.74	0.0932 ^d	2.51	[2] ^{1,3}
86765L	132453.3+272545.01	0.4717 ^d	2.55	[1] ^{2,3}
137763H	132406.1+273502.82	0.1367 ^d	1.89	[8]
92150H	132505.3+272646.15
176626H	132352.4+274152.41	1.6906 ^d	2.64	6
166856H	132442.1+274005.24	0.0071 ^d	2.39	[1]
146434H	132524.8+273631.59	2.1028 ^d	2.29	6
183911H	132439.6+274311.57	2.0213 ^d	2.97	5
78733H	132346.4+272426.09	1.8112 ^d	2.15	7
66488H	132520.4+272220.46	2.4233 ^d	2.89	5
190498H	132516.9+274417.26	2.3434 ^d 0.8932	2.84 2.79	6 [3]
190947H	132346.0+274419.92	1.7273 ^d 0.9612	2.89 2.38	3 [3]
153628H	132514.5+273743.52	0.0551 ^d	2.63	[2]
Undetected <i>NUV</i> -dropouts						
174747L	132436.7+274129.12
182447L	132429.1+274249.80
180088L	132421.6+274223.22
172253L	132414.3+274100.26
184387L	132414.6+274308.58
63360L	132433.2+272142.21
113109L	132514.6+273028.10
94367L	132459.1+272709.00

Note. — See Table 4.1.

The Keck Low Resolution Imaging and Spectrograph (LRIS; [Oke et al., 1995](#)) was used to target candidate LBGs in multi-slit mode on 2007 January 23–25. The total integration times were either 3400, 3600, or 4833 seconds, and 36 *NUV*-dropouts were targeted within 3 slitmasks. A dichroic beam splitter was used with the 600 lines mm⁻¹ grism blazed at 4000Å and the 400 lines mm⁻¹ grating blazed at 8500Å, yielding blue (red) spectral coverage of 3500 – 5300Å (6600 – 9000Å), although the coverages varied with location along the dispersion axis. The slits were 4'' to 8'' in length and 1'' in width, yielding spectral resolution of \approx 0.9Å at 4300Å and \approx 1.2Å at 8000Å.

Standard methods for reducing optical spectra were followed in PyRAF where an IRAF script, developed by K. Adelberger to reduce LRIS data, was used. When reducing the blue spectra, dome flat-fields were not used due to the known LRIS ghosting problem. Other LRIS users have avoided flat-fielding their blue spectra, since the CCD response is mostly flat (D. Stern, priv. comm).

HgNe arc-lamps were used for wavelength calibration of the blue side while OH sky-lines were used for the red side. Typical wavelength RMS was less than 0.1Å. For flux calibration, long-slit spectra of BD+26 2606 ([Oke & Gunn, 1983](#)) were obtained following the last observation for each night.

In the first mask, three of five alignment stars had coordinates that were randomly off by as much as 1'' from the true coordinates. These stars were taken from the USNO catalog, whereas the better alignment stars were from the 2MASS catalog with a few tenths of an arcsecond offsets. This hindered accurate alignment, and resulted in a lower success rate of detection: the first mask had 7 of 12 *NUV*-dropouts that were *not* identified, while the other two masks had 2/10 and 3/14.

4.1.2.2 MMT/Hectospec

Spectra of *NUV*-dropouts from the final photometric catalog were obtained with the multifiber optical spectrograph Hectospec (Fabricant et al., 2005) on the 6.5m MMT on 2008 March 13 and April 10, 11, and 14. Compared to Keck/LRIS, MMT/Hectospec has a smaller collecting area and lower throughput in the blue, so fewer detections were anticipated. Therefore, observations were restricted to bright ($V_{\text{auto}} = 22.0 - 23.0$) sources, which used 21 of 943 fibers from four configurations. Each source was observed in four, six, or seven 20-minute exposures using the 270 mm^{-1} grating. This yielded a spectral coverage of $4000 - 9000 \text{\AA}$ with 6\AA resolution. The spectra were wavelength calibrated, and sky-subtracted using the standard Hectospec reduction pipeline (Fabricant et al., 2005). A more detailed discussion of these observations is deferred to a forthcoming paper (Ly et al. 2008, in prep.).

4.1.3 Spectroscopic Identification of Sources

The IRAF task, `xcsao` from the RVSAO package (Kurtz & Mink, 1998, ver. 2.5.0), was used to cross-correlate with six UV spectral templates of LBGs. For cases with Ly α in emission, the composite of 811 LBGs from Shapley et al. (2003) and the two top quartile bins (in Ly α equivalent width) of Steidel et al. (2003) were used. For sources lacking Ly α emission (i.e., pure absorption-line systems), the spectra of MS 1512-cB58 (hereafter ‘cB58’) from Pettini et al. (2000), and the two lowest quartile bins of Steidel et al. (2003) were used.

When no blue features were present, the red end of the spectrum was examined. An object could still be at $z > 1.5$, but at a low enough redshift for Ly α to be shortward of the spectral window. In this case, rest-frame NUV features, such as Fe II and Mg II, are available. Savaglio et al. (2004) provided a

composite rest-frame NUV spectrum of 13 star-forming galaxies at $1.3 < z < 2$. For objects below $z \approx 1.5$, optical features are available to determine redshift. The composite SDSS spectra (3500 – 7000Å coverage) from Yip et al. (2004) and those provided with RVSAO (3000 – 7000Å) are used for low- z cases. Note that in computing redshifts, several different initial guesses were made to determine the global peak of the cross-correlation. In most cases, the solutions converged to the same redshift when the initial guesses are very different. The exceptions are classified as ‘ambiguous’.

Where spectra had poor S/N, although a redshift was obtained for the source, the reliability of identification (as given by `xcsao`’s R -value) was low ($R = 2–3$). An objective test, which was performed to determine what R -values are reliable, was to remove the Ly α emission from those spectra and templates, and then re-run `xcsao` to see what R -values are obtained based on absorption line features in the spectra. Among 10 cases (from LRIS spectroscopy), 6 were reconfirmed at a similar redshift ($\Delta z = 2.4 \times 10^{-4} – 1.5 \times 10^{-3}$)¹¹ with R -values of 2.30–7.07. This test indicates that a threshold of $R = 2.5$ is reasonable for defining whether the redshift of a source (lacking emission lines) was determined. This cut is further supported by Kurtz & Mink (1998), who found that the success of determining redshifts at $R = 2.5 – 3$ is $\sim 90\%$. However, to obtain more reliable redshifts, a more stricter $R = 3.0$ threshold is adopted. If a $R = 2.5$ threshold is adopted, then seven sources with $R = 2.5 – 3$ (ID 86765, 92942, 96927, 153628, 169090, 190498, and 190947) are re-classified as ‘identified’. These redshifts are marginally significant: a few to several absorption features coincide with the expected UV lines for the best-fit redshifts of ~ 2 , but a few additional absorption lines are not evident in the low S/N data. Statistics presented below are provided

¹¹This is lower, but still consistent with differences between emission and absorption redshifts of 650 km s^{-1} for LBGs (Shapley et al., 2003).

for both adopted R -value cuts.

While some sources are classified ambiguous, it is likely that they could be at high- z . For example, 185177 (classified as ambiguous) could be a LBG, since it shows a weak emission line at $\sim 4500\text{\AA}$ ($z \sim 2.7$ if Ly α) and a few absorption lines. This source, statistics ($\sim 50\%$ successful identification for $R = 2.0 - 2.5$) from [Kurtz & Mink \(1998\)](#), and NUV-78625 (with $R = 2.3$ but identified ‘by eye’ to be a $z \approx 1.6$ AGN) suggest that while a cut is placed at $R = 2.5$ or $R = 3.0$, it could be that some solutions with $R = 2.0 - 3.0$ are correctly identified. An $R = 3.0$ ($R = 2.5$) typically corresponds to a peak of ~ 0.25 (~ 0.2) in the cross correlation spectra, which is typically 3σ ($2 - 3\sigma$) above the RMS in the cross-correlation (see Figure 4.2).

4.1.3.1 LRIS Results

12 (14 with $R \geq 2.5$) LBGs are found at $1.7 \lesssim z \lesssim 2.7$ out of 36 attempts. Among those, 10 show Ly α in emission, while 2 (4 with $R \geq 2.5$) are identified purely by UV absorption lines. Their spectra are shown in Figures 4.3 and 4.4, and Table 4.1 summarizes their photometric and spectroscopic properties. Contamination was found from 3 stars and 5 (7 with $R \geq 2.5$) low- z galaxies (shown in Figure 4.5), corresponding to a 60% success rate (58% if $R > 2.5$ is adopted). Four sources showed a single emission line, which is believed to be [O III] at $z \sim 1 - 1.5$, one source showed [O II], H β , and [O III] at $z \sim 0.7$, and two sources with absorption lines have $R \sim 2.5$ results with $z \sim 0.1$ and ~ 0.5 (these would be “ambiguous” with the $R \geq 3.0$ criterion). The success of identifying $z \sim 2$ LBGs improves with different color selection criteria that remove most interlopers (see § 4.2.2).

Of the remaining 16 spectra (12 with $R > 2.5$ cut), 8 (4 with $R > 2.5$ cut)

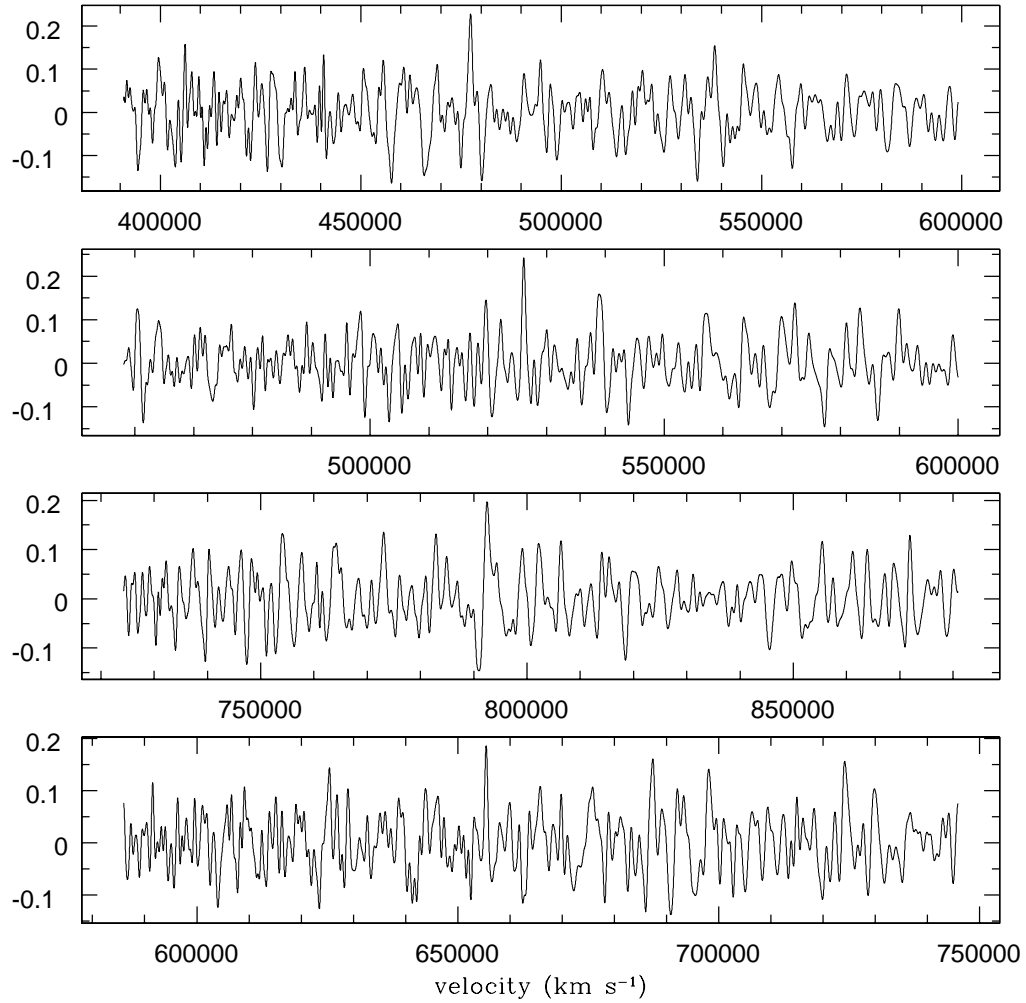


Figure 4.2 – These are of targets with $R = 2.5 - 3.2$ and lack an emission line. From top to bottom shows *NUV-dropout* ID 182284, 186254, 96927, and 92942. The top two have R -values of $\gtrsim 3.1$ and are identified as LBGs while the latter two have $R = 2.6 - 3.0$ and are classified as ambiguous. The peak near the center of the plots represents the strongest peak in the cross-correlation.

were detected, but the S/N of the spectra was too low, and the other 8 were undetected. These objects were unsuccessful due to the short integration time of about one hour and their faintness (average V magnitude of 24.2).

It is worthwhile to indicate that the fraction of LRIS spectra with Ly α emission is high (83%). In comparison, [Shapley et al. \(2003\)](#) reported that 68% of their $z \sim 3$ spectroscopic sample contained Ly α in emission. If the fraction of LBGs with Ly α emission does not increase from $z \sim 3$ to $z \sim 2$, it would imply that 5 $z \sim 2$ galaxies would not show Ly α in emission. Considering the difficulties with detecting Ly α in absorption with relatively short integration times, the above 83% is not surprising, and suggests that most of the $z > 1.5$ ambiguous LRIS redshifts listed in Table 4.1 are correct.

4.1.3.2 Hectospec Results

Among 21 spectra, 7 objects (2 are AGNs) are identified ($R > 3.0$; 9 if $R > 2.5$) at $z > 1.5$, 2 objects are stars, 1 (2 with $R > 2.5$) is a $z < 1.5$ interloper, and 11 are ambiguous (8 if $R > 2.5$ is adopted). These MMT spectra are shown in Figures 4.6–4.8, and their properties are listed in Table 4.1.

The spectrum of a $R_C \sim 22$ $z \sim 1.6$ LBG detected the Fe II and Mg II absorption lines, which indicates that MMT is sensitive enough to detect luminous LBGs. In fact, since the surface density of bright LBGs is low, slitmask instruments are not ideal for the bright end. However, the entire SDF can be observed with Hectospec, so all ~ 150 $V_{\text{auto}} < 23.0$ objects can be simultaneously observed.

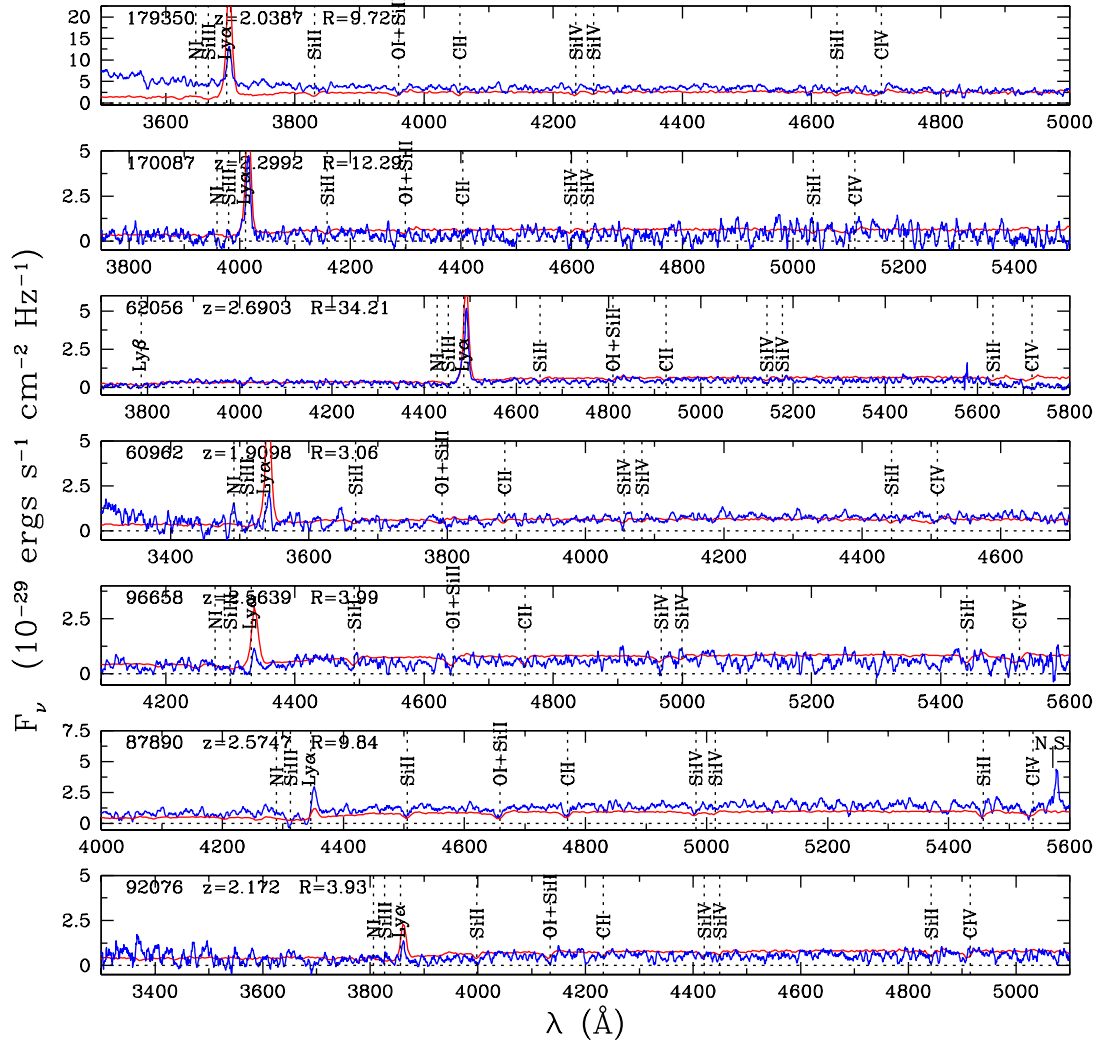


Figure 4.3 – Most of the LBGs with Ly α emission are shown here with the remaining in Figure 4.4. Overlayed on these spectra is the composite template (shown as grey) with the highest R -value (see Table 4.1) from cross-correlation. Note that these overlayed templates are intended to show the location of spectral features, and is not meant to compare the flux and/or the spectral index differences between the spectra and the templates. The ID number, redshifts, and R -values are shown in the upper left-hand corner of each panel.

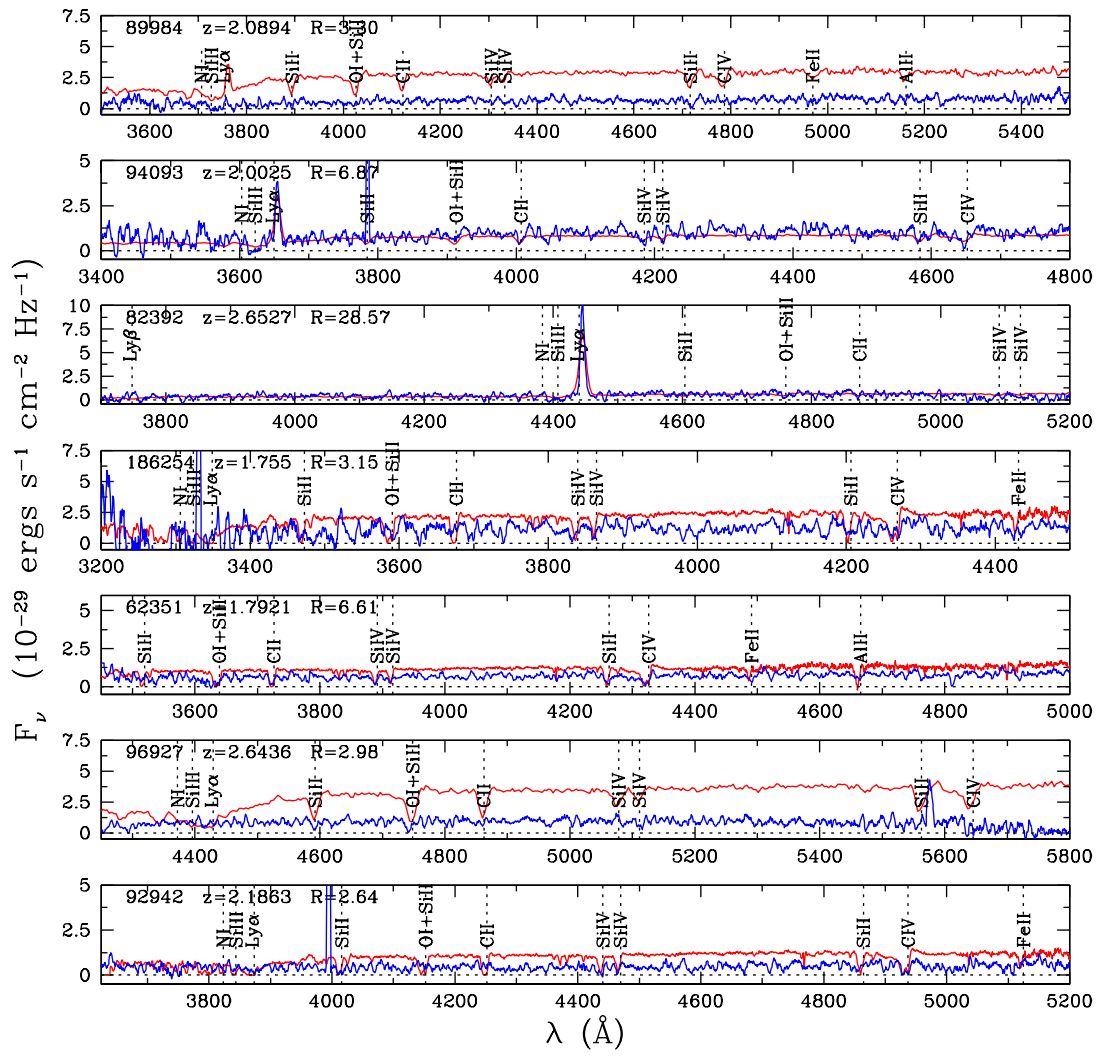


Figure 4.4 – The strong line seen in the spectrum of 96927 at $\sim 5570\text{\AA}$ is a sky subtraction artifact, and cosmic rays are seen in the spectra of 94093 (at 3780\AA), 186254 (at 3325\AA), and 92942 (at 3990\AA). These features are removed in the cross-correlation process.

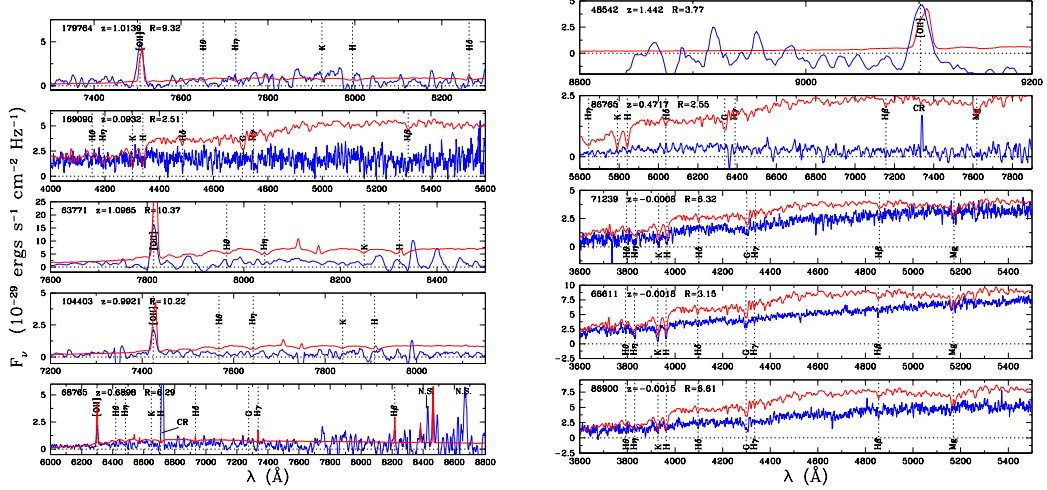


Figure 4.5 – This shows the $z < 1.5$ interlopers and galactic stars.

4.1.4 Additional Spectra with Subaru/MOIRCS

The *BzK* technique, which identifies galaxies with a wide range (old and young, dusty and unreddened) of properties, could include objects that would also be classified as *NUV*-dropouts. As a check, cross-matching of spectroscopically identified star-forming *BzK*'s with the *GALEX*-SDF photometric catalog was performed. Spectra of *BzK*s were obtained on 2007 May 3–4 with Subaru using the Multi-Object Infrared Camera and Spectrograph (MOIRCS; Ichikawa et al., 2006). 44 sources were targeted and 15 were identified by the presence of H α and [N II] or [O II], [O III] and H β emission. One of the 15 was not in the *B*-band catalog. Among the 14 objects, 7 are also classified as *NUV*-dropouts and were not previously identified (i.e., LRIS or Hectospec targets). This included 5 galaxies at $z > 1.5$ and 2 at $z = 1 - 1.5$. Their properties are included in Table 4.1. Among the 7 *BzK*s that did *not* meet the *NUV*-dropout criteria, 2 are below $z = 1.5$ and the other five are at high- z . For two of the high- z *BzK*s, one was below the $NUV - B = 1.75$ cut because it is faint ($V > 25.3$), thus not considered a *NUV*-dropout, and the other missed the $B - V = 0.5$ selection by having

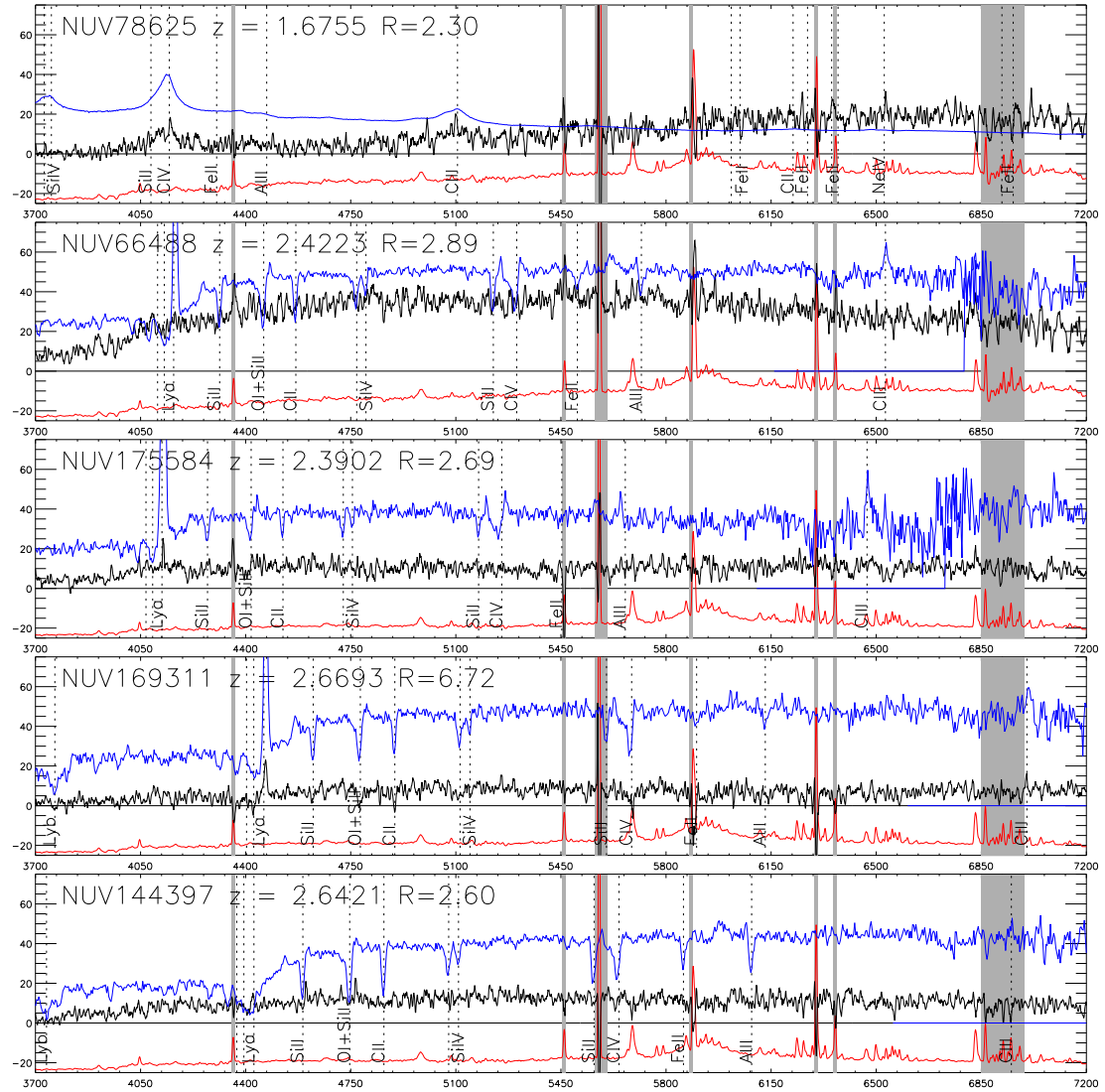


Figure 4.6 – These are Hectospec observations of LBGs in the final photometric catalog. The cross-correlation template and the typical sky spectrum are shown above and below the spectrum of the source, respectively.

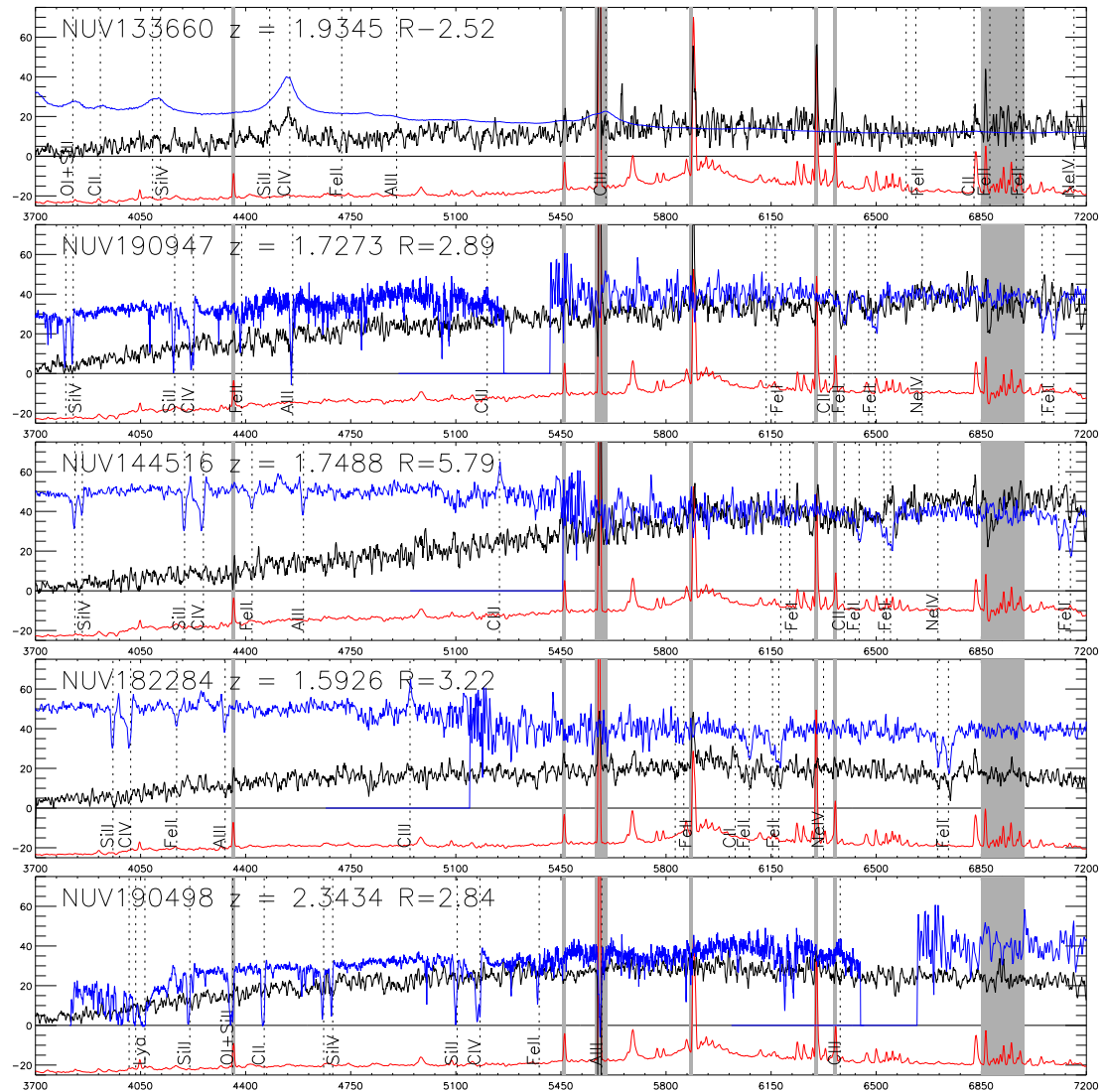


Figure 4.7 – Continuation of Figure 4.6.

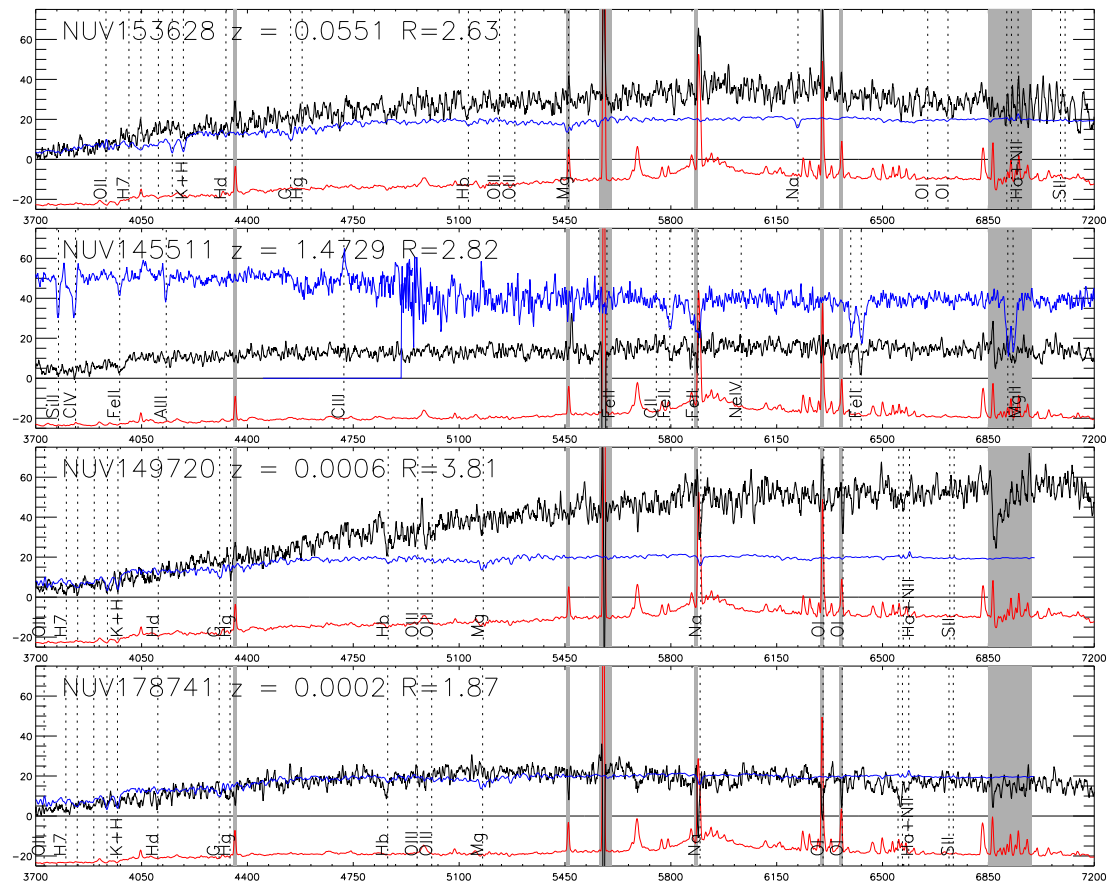


Figure 4.8 – This shows the low- z interlopers and galactic stars.

$B - V = 0.53$.¹² The other three sources have low- z neighboring sources that are detected in the *NUV*, which influences the *NUV* photometry to be brighter. The cause of confusion is due to the poor resolution of *GALEX*, which is discussed further in § 4.3.3. The details of these observations and their results are deferred to Hayashi et al. (2008).

4.1.5 Summary of Observations

In order to probe $1.5 < z < 3$ with the Lyman break technique, deep (>100 ks) *GALEX/NUV* imaging was obtained. Spectroscopic observations from Keck and MMT independently confirm that most *NUV*-dropouts (with their UV continuum detected spectroscopically) are found to be at $1.5 < z < 2.7$.

A summary of the number of LBGs, stars, and low- z interlopers identified spectroscopically is provided in Table 4.2. Among the spectra targeting *NUV*-dropouts (i.e., excluding MOIRCS spectra), 53% (30/57) were identified, and among those, 63% are at $z > 1.5$. Including seven objects with $R = 2.5 - 3.0$, the percentages are 65% and 62%, respectively. These statistics are improved with the final selection criteria discussed in § 4.2.2.

4.2 Photometric Selection of *NUV*-dropouts

This section describes the *NUV* and optical photometric catalogs (§ 4.2.1) and the methods for merging the two catalogs. Then in § 4.2.2, ~ 8000 *NUV*-dropouts are empirically identified with the spectroscopic sample to refine the selection criteria.

¹²If the selection criteria were modified to include this object, no low- z interlopers or stars would have contaminated the criteria. However, a $B - V \leq 0.5$ is still adopted for simplicity.

Table 4.3. Summary of Spectroscopic Observations

Instrument	Total	LBGs [AGNs]	$z \leq 1.5$	stars	Ambiguous	Undet.
LRIS	36 (28) {4}	12 {2}	5 (1) {2}	3 (0)	8 (7) {-4}	8 (8)
Hectospec	21 (20) {3}	7 [2] {2}	1 (1) {1}	2 (1)	11 (11) {-3}	0 (0)
MOIRCS	44	10 (5)	4 (2)	0
Total	101	29 (24) [2] {4}	10 (4) {3}	5 (1)	19 (18) {-7}	8 (8)

Note. — Sources with $z > 1.5$ are classified as “LBG”. Values in square brackets are those that appear to be AGNs, and those in parentheses meet the final selection criteria in § 4.3.2. Values in curly brackets represent LBGs that are reclassified as “identified” if a lower ($R = 2.5$) threshold is adopted rather than a $R = 3.0$ cut. None of the LBGs and AGNs was missed by the final selection criteria.

4.2.1 Revised *NUV* Photometric Catalogs

Prior to any measurements, an offset ($\Delta\alpha = -0.39''$, $\Delta\delta = -0.18''$) in the *NUV* image coordinates was applied to improve the astrometry for alignment with Suprime-Cam data. The scatter in the astrometric corrections was found to be $\sigma_{\Delta\alpha}=0.39''$ and $\sigma_{\Delta\delta}=0.33''$. This only results in a 0.01 mag correction for *NUV* measurements, and is therefore neglected.

The coordinates of ~ 100000 SDF *B*-band sources with $B_{\text{auto}} < 27.5$ were used to measure *NUV* fluxes within a $3.39''$ (2.26 pixels) radius aperture with the IRAF/DAOPHOT task, `phot`. For objects with *NUV* photometry below the 3σ background limit, the 3σ value is used. This limit is determined from the mode in an annulus with inner and outer radii of $22.5''$ and $37.5''$ (i.e., an area of 1200 pixels), respectively. For sources detected in the *NUV*, a point-source aperture correction of a factor of ≈ 1.83 is applied to obtain the “total” *NUV* flux. This correction was determined from the point spread function (PSF) of 21 isolated sources distributed across the image. The *NUV* catalog is then merged with the *B*-band catalog from SExtractor (SE; [Bertin & Arnouts, 1996](#)) that contains $BVR_{\text{C}}i'z'$ photometry.

Throughout this paper, “total” magnitudes from the Suprime-Cam images are given by SE `mag_auto`, since the corrections between B -band Kron and the $5''$ diameter magnitudes were no greater than 0.03 mag for isolated ($5''$ radius), point-like (SE `class_star` ≥ 0.8) targets.

The merged catalog was also corrected for galactic extinction based on the Cardelli et al. (1989) extinction law. For the SDF, they are: $A(NUV) = 0.137$, $A(B) = 0.067$, $A(V) = 0.052$, $A(R_C) = 0.043$, $A(i') = 0.033$, and $A(z') = 0.025$. Since the Galactic extinction for the SDF is low, the amount of variation in $A(NUV)$ is no more than 0.02, so all NUV magnitudes are corrected by the same value.

4.2.2 Broad-band Color Selection

Using the sample of spectroscopically confirmed $z > 1.5$ LBGs, low- z interlopers, and stars, the color selection is optimized to minimize the number of interlopers while maximizing the number of confirmed LBGs. In Figure 4.9, known LBGs are identified in the $NUV - B$ versus $B - V$ diagram, where the $NUV - B$ color is given by the “total” magnitude and the $B - V$ is the color within a $2''$ aperture. The latter was chosen because of the higher S/N compared to larger apertures. The final empirical selection criteria for the LBG sample are:

$$NUV - B \geq 1.75, \quad (4.1)$$

$$B - V \leq 0.50, \quad \text{and} \quad (4.2)$$

$$NUV - B \geq 2.4(B - V) + 1.15, \quad (4.3)$$

which yielded 7964 NUV -dropouts with $21.90 \leq V \leq 25.30$. Among the Hectospec and LRIS spectra, these selection criteria included all spectroscopic LBGs and excluded 4/5 stars and 4/6 (4/9 with $R > 2.5$) interlopers. Therefore, the

fraction of NUV -dropouts that are confirmed to be LBGs with the new selection criteria is 86% (the $R = 2.5$ cut implies 79%). Note that while the B -band catalog was used (since the B filter is closer in wavelength to the NUV), the final magnitude selection was in V , to compare with the rest-frame wavelength ($\approx 1700\text{\AA}$) of $z \sim 3$ LBGs in the R -band.

To summarize, a NUV -optical catalog was created, and it was combined with spectroscopic redshifts to select 7964 NUV -dropouts with $NUV - B \geq 1.75$, $B - V \leq 0.50$, $NUV - B \geq 2.4(B - V) + 1.15$, and $21.90 \leq V \leq 25.30$. The spectroscopic sample indicates that 14% of NUV -dropouts are definite $z \leq 1.5$ interlopers.

4.3 Contamination and Completeness Estimates

Prior to constructing a normalized luminosity function, contaminating sources that are not LBGs must be removed statistically. Section 4.3.1 discusses how foreground stars are identified and removed, which was found to be a 4–11% correction. Section 4.3.2 describes the method for estimating low- z contamination, and this yielded a correction of $34\% \pm 17\%$. These reductions are applied to the number of NUV -dropouts to obtain the surface density of $z \sim 2$ LBGs. Monte Carlo (MC) realizations of the data, to estimate the completeness and the effective volume of the survey, are described in § 4.3.3. The latter reveals that the survey samples $z \approx 1.8 - 2.8$.

4.3.1 Removal of Foreground Stars

The Gunn & Stryker (1983) stellar track passes above the NUV -dropout selection criteria box (as shown in Figure 4.9). This poses a problem, as objects that are

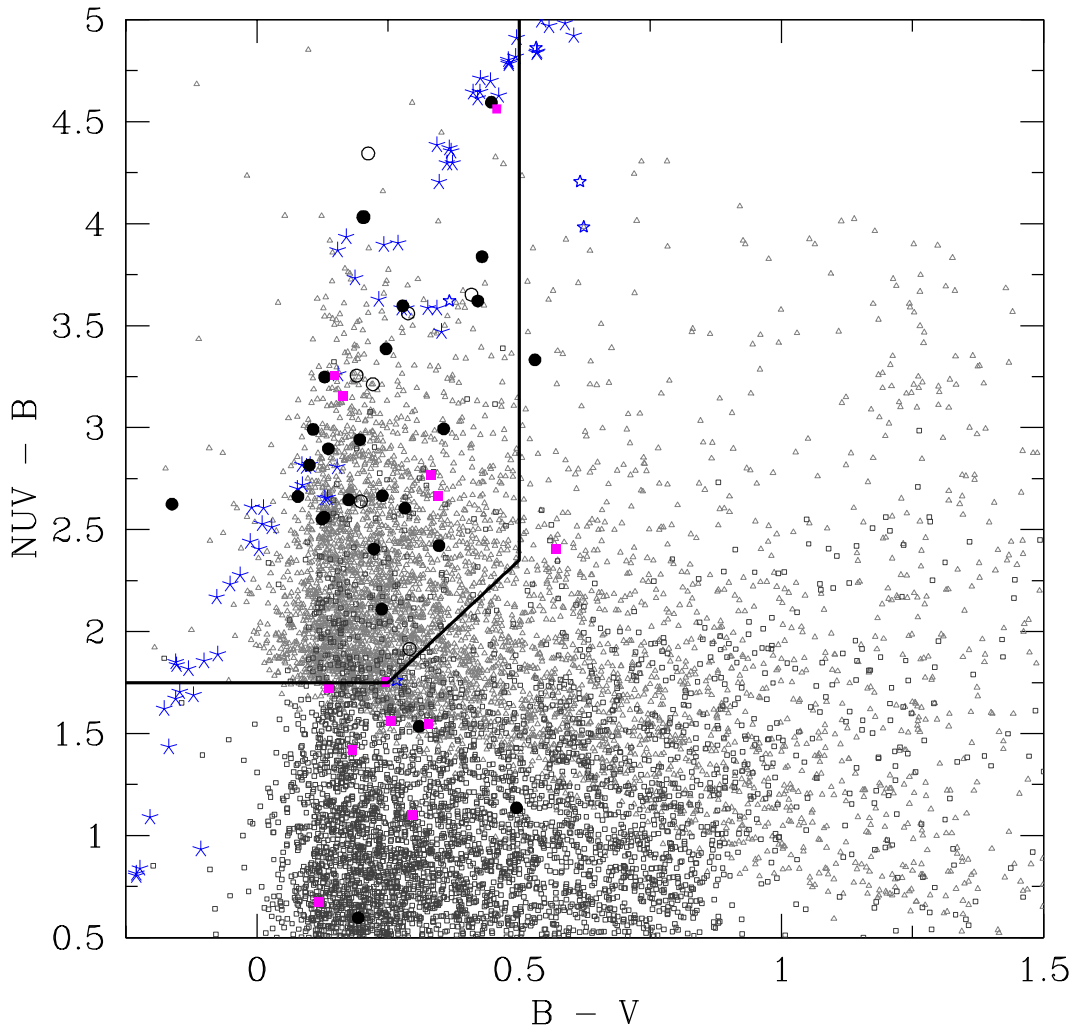


Figure 4.9 – A total of $\sim 33,000$ sources are represented here, but only one-third are plotted, for clarity. Sources undetected (at the 3σ level) in the NUV are shown as grey unfilled triangles while the detected sources are indicated as dark grey unfilled squares. Filled (unfilled) circles correspond to sources that have been confirmed as LBGs with (without) emission lines. Low- z interlopers are shown as filled squares while stars are shown as unfilled stars. Skeletal stars represent Gunn-Stryker stars.

undetected in the *NUV* can be faint foreground stars. A simple cut to eliminate bright objects is not sufficient, because faint halo stars exist in the SDF (as shown later). To reduce stellar contamination, additional photometric information from the SExtractor $BVR_{\text{c}}i'z'$ catalogs is used. The approach of creating a “clean” sample of point-like sources, as performed by [Richmond \(2005\)](#), is followed. He used the `class_star` parameter and the difference (δ) between the $2''$ and $3''$ aperture magnitudes for each optical image. A ‘1’ is assigned when the `class_star` value is $0.90 - 1.00$ or $0.10 < \delta < 0.18$, and ‘0’ otherwise for each filter. The highest score is 10 [$(1+1) \times 5$], which $2623 V_{\text{auto}} = 21.9 - 26.0$ objects satisfied, and is referred to as “perfect” point-like or “rank 10” object. These rank 10 objects will be used to define the stellar locus, since contamination from galaxies is less of a problem for the most point-like sample. Then objects with lower ranks that fall close to the stellar locus will also be considered as stars after the locus has been defined. Unfortunately, distant galaxies can also appear point-like, and must be distinguished from stars. This is done by comparing their broad-band optical colors relative to the stellar locus. Figure 4.10 shows the $B - V$, $V - R_{\text{C}}$, and $R_{\text{C}} - z'$ colors used in [Richmond \(2005\)](#) for the “clean” sample. The stellar locus is defined by the solid black lines using brighter ($V \leq 23.0$) sources. Figure 4.10 shows differences in the colors between the stellar locus defined for point-like SDF stars and those of Gunn-Stryker stars. [Richmond \(2005\)](#) states that this is due to metallicity, as the SDF and Gunn-Stryker stars are selected from the halo and the disk of the Galaxy, respectively.

For each object in the clean sample, the $V - R_{\text{C}}$ color is used to predict the $B - V$ and $R_{\text{C}} - z'$ colors along the stellar locus (denoted by ‘S.L.’ in the subscript of the colors below). These values are then compared to the observed colors to determine the magnitude deviation from the stellar locus, $\Delta = -[(B - V)_{\text{obs}} - (B - V)_{\text{S.L.}}] + [(R_{\text{C}} - z')_{\text{obs}} - (R_{\text{C}} - z')_{\text{S.L.}}]$. Therefore, an

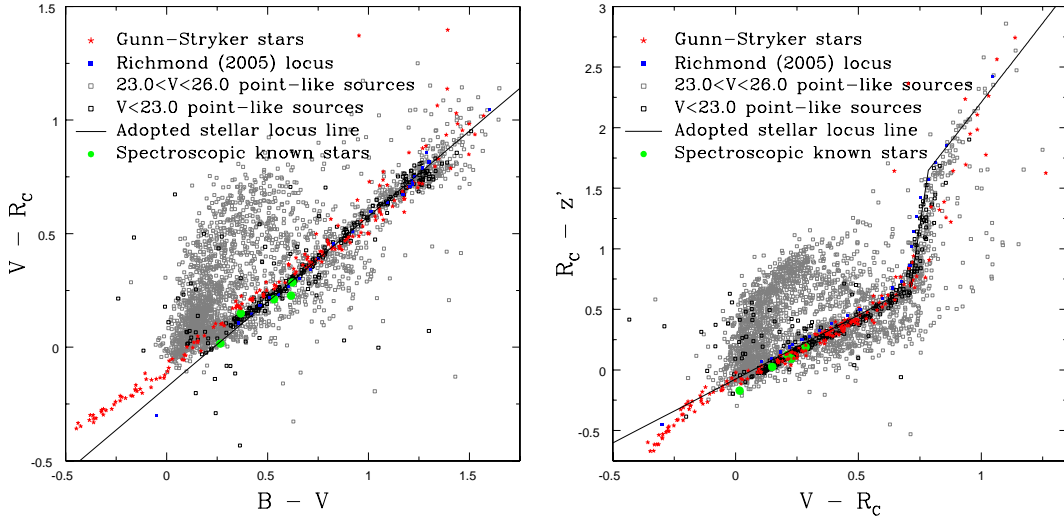


Figure 4.10 – Grey (small) and black (large) squares represent sources brighter than $V_{\text{auto}} = 26.0$ and 23.0, respectively. The Gunn-Stryker stars are shown as stars, and the SDF stellar locus of [Richmond \(2005\)](#) is shown as filled squares. The solid lines define the stellar locus for calculating Δ (see § 4.3.1). The five sources that have been spectroscopically identified to be stars are shown as filled green circles.

object with $\Delta \approx 0$ mag is classified as a star. This method is similar to what is done in [Richmond \(2005\)](#), where an object is considered a star if it is located within the stellar locus “tube” in multi-color space. This approach provides stellar contamination at faint magnitudes, which is difficult spectroscopically ([Steidel et al., 2003](#)). A histogram showing the distribution of Δ in Fig. 4.11a reveals two peaks: at $\Delta \approx 0$ and 0.8 mag. The comparison of Δ versus the V -band magnitude is shown in Fig. 4.11b, and a source is identified as a star if it falls within the selection criteria shown by the solid lines in this figure. A total of 1431 stars $V \leq 26.0$ are identified, while the remaining 1192 sources are classified as galaxies. The surface density as a function of magnitude for the identified stars agrees with predictions made by [Robin et al. \(2003\)](#) and other surface density measurements near the galactic pole. When the *NUV*-dropout selection criteria

are applied¹³, these numbers are reduced to 336 stars (i.e., a 4% contamination for the *NUV*-dropout sample) and 230 galaxies with $21.9 \leq V_{\text{auto}} \leq 25.3$.

Sources that are ranked 7–9 are also considered and were classified as a star or a galaxy using the above approach. Of those that met the *NUV*-dropout criteria, 535 and 252 have the colors of stars and galaxies, respectively. Thus, the photometric sample of *NUV*-dropouts contains 7093 objects after statistically removing 871 stars (11% of the *NUV*-dropout) that are ranked 7–10. The reasons for only considering objects with a rank of 7 or greater are (1) the stellar contamination does not significantly increase by including rank 6 or rank 5 objects (i.e., another 128 rank 6 stars or 1.5% and 143 rank 5 stars or 1.8%), and (2) comparison of the surface density of rank 7–10 stars with expectations from models showed evidence for possible contamination from galaxies at the faint end ($V > 24.0$; A. Robin, priv. comm.), and the problem will worsen with rank 5 and 6 objects included. As it will be apparent later in this paper, stellar contamination is small and not expected to significantly alter any discussion of differences seen in the luminosity function. A hard upper limit by considering objects of rank 1 and above as stars would imply an additional (rank 1 to 6) stellar contamination of 14.5%.

Among the 5 sources spectroscopically determined to be stars, 3 of them (71239, 66611, and 149720) are classified as stars with the Δ method, and the other two stars (86900 and 178741) fall outside the Δ selection criteria. Among the known LBGs, 8 are rank 8–10 and 3 (166380, 78625, and 133660) are classified as *not* being stars. Since the spectroscopic sample of rank 10 objects is small, additional spectra will be required to further optimize the Δ technique. However, the spectroscopic sample (presented in this paper) indicates that 3–7%

¹³The $B - V$ and $NUV - B$ color cuts limit the stellar sample to spectral types between A0 and G8.

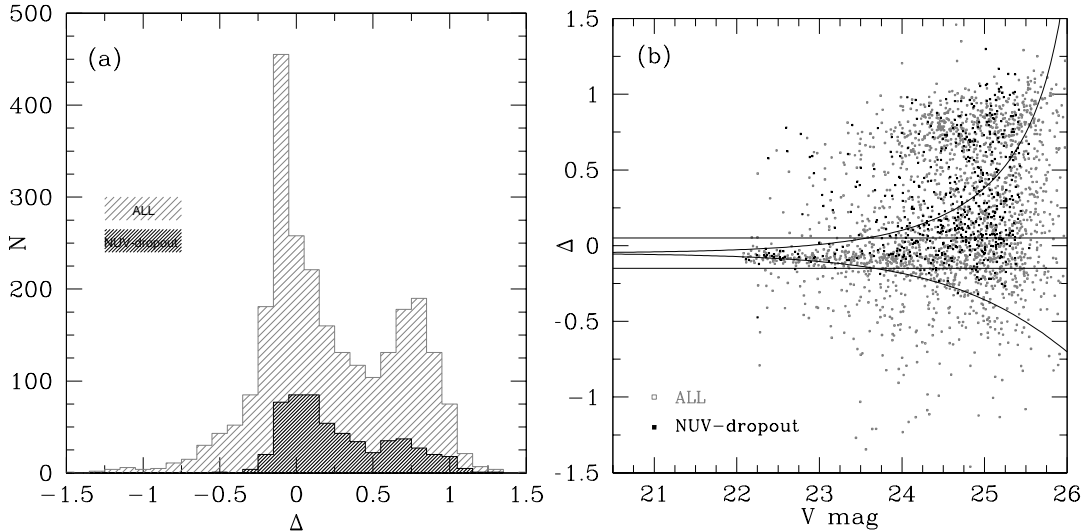


Figure 4.11 – A histogram of Δ is shown in (a) while (b) plots Δ versus V -band Kron magnitude. The grey histogram and squares are for *all* point-like sources while those that satisfy the *NUV*-dropout selection criteria are represented in black. The selection of foreground stars is given by the solid lines in (b). The horizontal solid lines represent a minimum Δ at the bright end while the two solid curves are the $\pm 3\sigma$ criteria for Δ , as given by $-2.5 \log [1 \mp (f_{3\sigma B}^2 + f_{3\sigma V}^2 + f_{3\sigma R_C}^2 + f_{3\sigma z'}^2)^{0.5}/f_V]$. Here f_X is the flux density in the X filter.

of *NUV*-dropouts are stars, which is consistent with the 4–11% derived with the Δ method.

4.3.2 Contamination from $z < 1.5$ Interlopers

One of the biggest concerns in any survey targeting a particular redshift range is contamination from other redshifts. The spectroscopic sample of *NUV*-dropouts shows that 5% are definite $z < 1.5$ galaxies. This number increases to an upper value of 51% if the ambiguous *NUV*-dropouts (that meet the color selection criteria) are all assumed to be low- z interlopers. However, it is unlikely that all unidentified *NUV*-dropouts are low- z , since LBGs without Ly α emission in their

spectra¹⁴ are likely missed. A secondary independent approach for estimating low- z contamination, which is adopted later in this paper, is by using a sample of $z < 1.5$ emission-line galaxies identified with narrow-band (NB) filters. Since a detailed description of this sample is provided in Ly et al. (2007), only a summary is given below:

A total of 5260 NB emitters are identified from their excess fluxes in the NB704, NB711, NB816, or NB921 filter either due to H α , [O III], or [O II] emission line in 12 redshift windows (some overlapping) at $0.07 \lesssim z \lesssim 1.47$. These galaxies have emission line equivalent widths and fluxes as small as 20Å (observed) and a few $\times 10^{-18}$ erg s $^{-1}$ cm $^{-2}$, and are as faint as $V = 25.5 - 26.0$. Cross-matching was performed with the *NUV*-dropout sample, which yielded 487 NB emitters as *NUV*-dropouts. The redshift and V -band magnitude distributions are shown in Figure 4.12. Note that most of the contaminating sources are at $1.0 < z < 1.5$, consistent with the spectroscopic sample.

Since this sample represents a fraction of the $0.07 \lesssim z \lesssim 1.5$ redshift range, the above results must be interpolated for redshifts in between the NB redshifts. It is assumed that emission-line galaxies exist at all redshifts, and possess similar properties and number densities to the NB emitters. One caveat of this approach is that blue galaxies that do *not* possess nebular emission lines, may meet the *NUV*-dropout selection.¹⁵ The statistics of such objects are not well known, since spectroscopic surveys are biased toward emission line galaxies, due to ease of identification. Therefore, these contamination estimates are treated as lower limits. A further discussion of this approach is provided in § 4.6.

Using the redshift distribution shown in Figure 4.12, the number of objects per comoving volume ($N/\Delta V$) is computed at each NB redshift window. For redshifts

¹⁴Either because they do not possess Ly α in emission or they are at too low of a redshift for Ly α to be observed.

¹⁵Red galaxies are excluded by the $B - V < 0.5$ criterion.

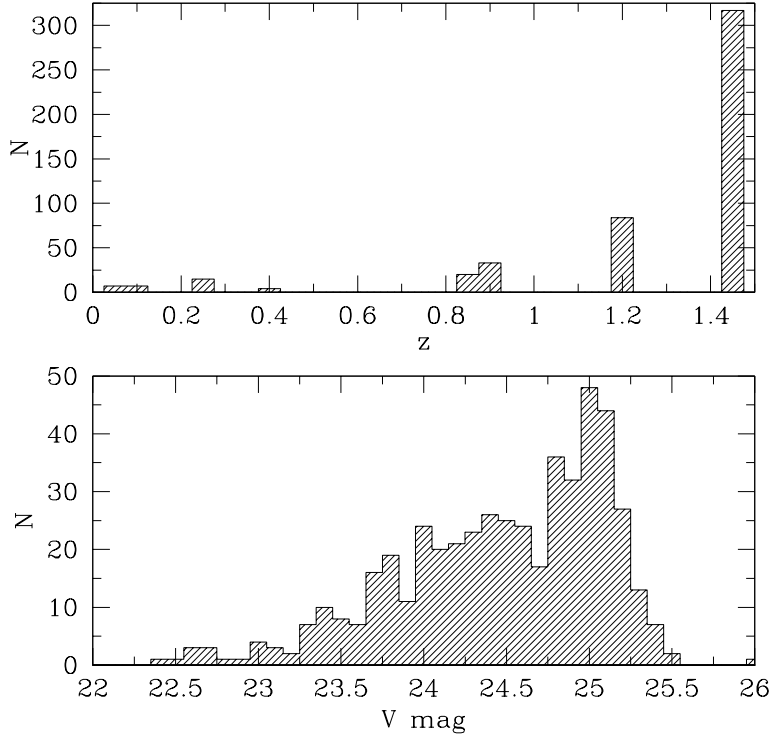


Figure 4.12 – Redshift (top) and V -band magnitude (bottom) distributions of 487 NB emitters that meet the NUV -dropout criteria. Note that the redshift bins are made larger to clearly show the histogram.

not included by the NB filters, a linear interpolation is assumed. Integrating over the volume from $z = 0.08$ to $z = 1.5$ yields the total number of interlopers to be 2490 ± 1260 , which corresponds to a contamination fraction of $f_{\text{contam}} = 0.34 \pm 0.17$. The error on f_{contam} is from Poissonian statistics for each redshift bin, and are added in quadrature during the interpolation step for other redshifts. This is also determined as a function of magnitude (hereafter the “mag.-dep.” correction), since the redshift distribution will differ between the bright and faint ends. The f_{contam} (V -band magnitude range) values are 0.39 ± 0.20 (22.9 – 23.3), 0.40 ± 0.21 (23.3 – 23.7), 0.37 ± 0.21 (23.7 – 24.1), 0.31 ± 0.16 (24.1 – 24.5), 0.27 ± 0.14 (24.5 – 24.9), and 0.39 ± 0.19 (24.9 – 25.3).

4.3.3 Modelling Completeness and Effective Volume

In order to obtain an accurate LF for *NUV*-dropouts, the completeness of the sample must be quantified. This is accomplished with MC simulations to calculate $P(m, z)$, which is the probability that a galaxy of apparent V -band magnitude m and at redshift z will be detected in the image, and will meet the *NUV*-dropout color selection criteria. The effective comoving volume per solid area is then given by

$$\frac{V_{\text{eff}}(m)}{\Omega} = \int dz P(m, z) \frac{dV(z)}{dz} \frac{1}{\Omega}, \quad (4.4)$$

where $dV/dz/\Omega$ is the differential comoving volume per dz per solid area at redshift z . Dividing the number of *NUV*-dropouts for each apparent magnitude bin by V_{eff} will yield the LF. This approach accounts for color selection biases, limitations (e.g., the depth and spatial resolution) of the images (Steidel et al., 1999), and choice of apertures for “total” magnitude.

In order to determine $P(m, z)$, a spectral synthesis model was first constructed from GALAXEV (Bruzual & Charlot, 2003) by assuming a constant SFR with a Salpeter initial mass function (IMF), solar metallicity, an age of 1 Gyr, and a redshift between $z = 1.0$ and $z = 3.8$ with $\Delta z = 0.1$ increments. The model was reddened by assuming an extinction law following Calzetti et al. (2000) with $E(B - V) = 0.0 - 0.4$ (0.1 increments) and modified by accounting for IGM absorption following Madau (1995). The latter was chosen over other IGM models (e.g., Bershady et al., 1999) for consistency with previous LBG studies. This model is nearly identical to that of Steidel et al. (1999).

Figure 4.13 shows the redshift evolution of the $NUV - B$ and $B - V$ colors for this model. These models were scaled to apparent magnitudes of $V = 22.0 - 25.5$ in increments of 0.25. These 2175 ($29 \times 15 \times 5$) artificial galaxies are randomly distributed across the *NUV*, *B*, and *V* images with the appropriate spatial res-

olution (assumed to be point-like) and noise contribution with the IRAF tasks `mkobject` (for optical images) and `addstar` (using the empirical *NUV* PSF). Because of the poor spatial resolution of *GALEx*, each iteration of 435 sources (for a given $E[B - V]$ value) was divided into three sub-iterations to avoid source confusion among the mock galaxies. The artificial galaxies were then detected in the same manner as real sources. This process was repeated 100 times. Note that 21% of artificial sources did not meet the *NUV*-dropout criteria (see e.g., Figure 4.14), as they were confused with one or more nearby sources detected in the *NUV*. This serves as an estimate for incompleteness due to confusion, and is accounted for in the final LF. These results are consistent with MOIRCS spectra that finds that 14 – 29% of BzKs with $z \geq 1.5$ was missed by *NUV*-dropout selection criteria with nearby objects affecting the *NUV* flux. In addition, this simulation also revealed that among all mock LBGs with $z \leq 1.5$, 30% were photometrically scattered into the selection criteria of *NUV*-dropouts, which is consistent with the 34% low- z contamination fraction predicted in § 4.3.2.

Figure 4.14 shows $P(m, z)$ as a function of magnitude for $E(B - V) = 0.1$, 0.2, and $0.0 - 0.4$. The latter is determined from a weighted average where the $E(B - V)$ distribution from Steidel et al. (1999) is used for weighting each completeness distribution. This corresponds to an average $E(B - V) \sim 0.15$. The adopted comoving volume uses the weighted-average results. Table 4.3 provides the effective comoving volume per arcmin², the average redshift, the FWHM and standard deviation of the redshift distribution for subsets of apparent magnitudes.

4.3.4 Summary of Survey Completeness and Contamination

Using optical photometry, 871 foreground stars (i.e., a 11% correction) were identified and excluded to yield 7093 candidate LBGs. Then $z < 1.5$ star-forming

Table 4.4. LBG Effective Volume Estimates

V mag	z_{avg}	σ_z	$FWHM(z)$	$V_{\text{eff}}/d\Omega$	z_{avg}	σ_z	$FWHM(z)$	$V_{\text{eff}}/d\Omega$
$E(B - V) = 0.0$								
22.0-22.5	2.422	0.312	1.860–2.962	2.93	2.313	0.318	1.757–2.860	2.89
22.5-23.0	2.420	0.312	1.865–2.961	2.67	2.304	0.323	1.746–2.859	2.67
23.0-23.5	2.418	0.317	1.862–2.962	2.36	2.304	0.328	1.738–2.864	2.40
23.5-24.0	2.401	0.333	1.831–2.969	2.12	2.290	0.339	1.717–2.863	2.20
24.0-24.5	2.379	0.361	1.772–2.974	2.14	2.261	0.355	1.645–2.846	2.10
24.5-25.0	2.312	0.369	1.680–2.910	2.14	2.199	0.349	1.575–2.774	2.02
25.0-25.5	2.220	0.352	1.603–2.788	1.80	2.133	0.325	1.569–2.659	1.44
$E(B - V) = 0.2$								
22.0-22.5	2.150	0.304	1.627–2.667	2.69	2.074	0.290	1.563–2.569	2.41
22.5-23.0	2.148	0.307	1.613–2.668	2.48	2.079	0.287	1.573–2.567	2.16
23.0-23.5	2.146	0.312	1.592–2.664	2.23	2.088	0.291	1.573–2.574	1.88
23.5-24.0	2.166	0.320	1.585–2.682	1.97	2.077	0.295	1.567–2.572	1.79
24.0-24.5	2.157	0.331	1.570–2.684	1.93	2.060	0.293	1.559–2.559	1.77
24.5-25.0	2.104	0.314	1.561–2.631	1.81	2.002	0.279	1.557–2.422	1.29
25.0-25.5	2.043	0.292	1.560–2.487	1.01	1.898	0.266	1.550–2.004	0.35
$E(B - V) = 0.4$								
22.0-22.5	1.956	0.236	1.553–2.359	1.78	2.278	0.333	1.752–2.837	2.79
22.5-23.0	1.952	0.233	1.559–2.352	1.57	2.274	0.335	1.740–2.834	2.56
23.0-23.5	1.957	0.230	1.562–2.350	1.40	2.273	0.338	1.741–2.832	2.28
23.5-24.0	1.952	0.232	1.557–2.349	1.34	2.268	0.345	1.711–2.839	2.07
24.0-24.5	1.934	0.235	1.553–2.313	1.28	2.248	0.360	1.610–2.834	2.02
24.5-25.0	1.887	0.237	2.131–2.243	0.56	2.194	0.354	1.574–2.762	1.91
25.0-25.5	1.967	0.334	1.962–2.062	0.08	2.139	0.336	1.571–2.652	1.30
$E(B - V) = 0.0 – 0.4$								

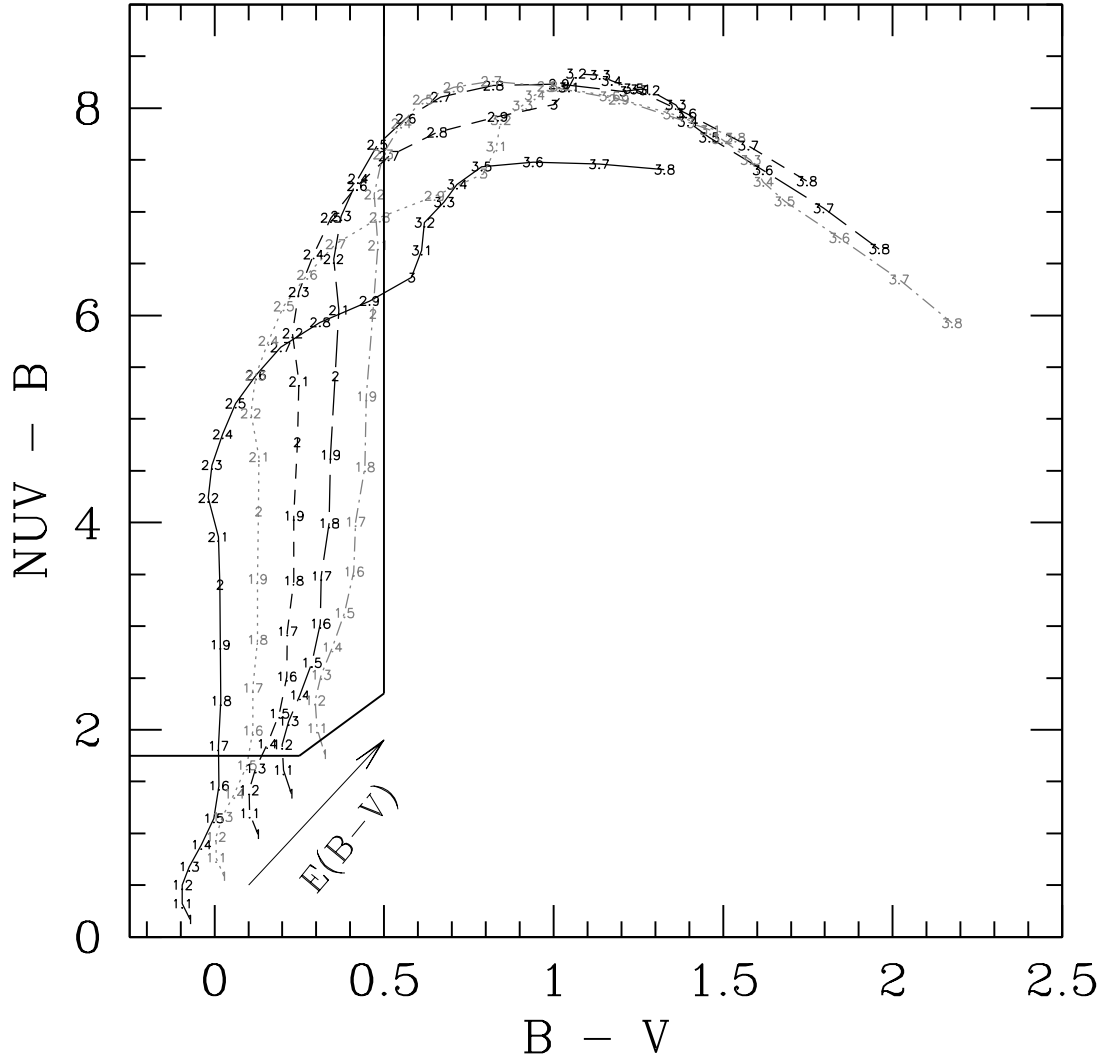


Figure 4.13 – The solid, dotted, short-dashed, long-dashed, and dot short-dashed lines correspond to the spectral synthesis model described in § 4.3.3 with $E(B - V) = 0.0, 0.1, 0.2, 0.3$, and 0.4 , respectively. The thick solid black lines represent the selection criteria in § 4.2.2.

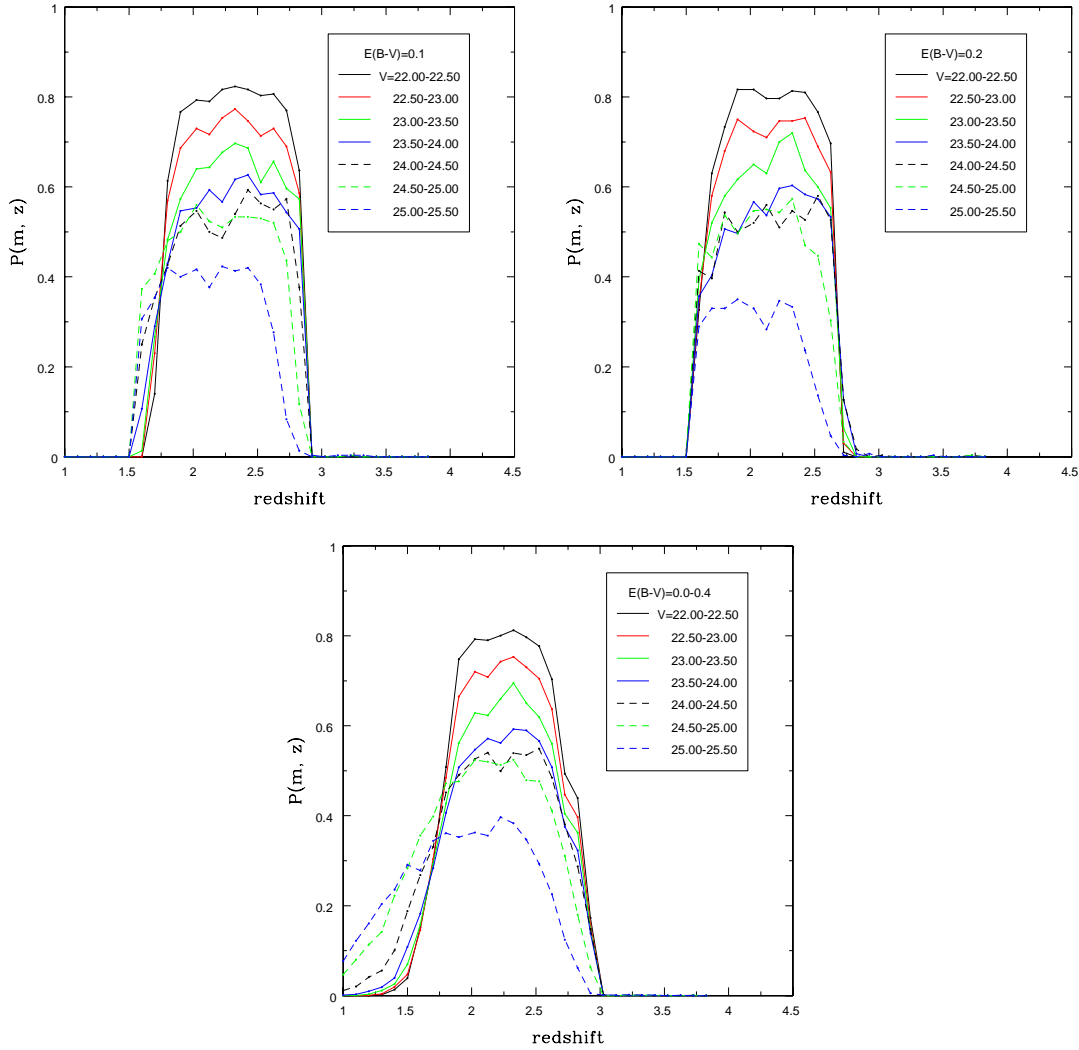


Figure 4.14 – Estimates of completeness of the Monte Carlos simulation. From left to right is the result for $E(B - V) = 0.1$, 0.2 , and $0.0 - 0.4$ (a weighted average assuming the $E(B - V)$ distribution of [Steidel et al., 1999](#)).

galaxies, identified with NB filters, were cross-matched with the *NUV*-dropout sample to determine the contamination fraction of galaxies at $z < 1.5$. Redshifts missed by the NB filters were accounted for by interpolating the number density between NB redshifts, and this yielded 2490 ± 1260 interlopers, or a contamination fraction of 0.34 ± 0.17 .

To determine the survey completeness, the V_{eff} was simulated. This consisted of generating spectral synthesis models of star-forming galaxies, and then adding artificial sources with modelled broad-band colors to the images. Objects were then detected and selected as *NUV*-dropouts in the same manner as the final photometric catalog. These MC simulations predict that the survey selects galaxies at $z \sim 2.28 \pm 0.33$ (FWHM of $z = 1.8 - 2.8$), and has a maximum comoving volume of $2.8 \times 10^3 h_{70}^{-3} \text{ Mpc}^3 \text{ arcmin}^{-2}$.

4.4 Results

This section provides the key measurements for this survey: a $z \sim 2$ rest-frame UV luminosity function for LBGs (§ 4.4.1), and by integrating this luminosity function, the luminosity and SFR densities are determined (§ 4.4.2).

4.4.1 The 1700Å UV Luminosity Function

To construct a luminosity function, a conversion from apparent to absolute magnitude is needed. The distance modulus is $m_{1700} - M_{1700} \approx 45.0$, where it is assumed that all the sources are at $z \approx 2.28$ and the K-correction term has been neglected, since it is no more than 0.08 mag. The luminosity function is given by

$$\Phi(M_{1700}) = \frac{1}{\Delta m} \frac{N_{\text{raw}}(1 - f_{\text{contam}})}{V_{\text{eff}}(M_{1700})}, \quad (4.5)$$

where N_{raw} is the raw number of *NUV*-dropouts within a magnitude bin ($\Delta m = 0.2$), $V_{\text{eff}}(M_{1700})$ is the effective comoving volume described in § 4.3.3, and f_{contam} is the fraction of *NUV*-dropouts that are at $z < 1.5$ (see § 4.3.2). The photometric LF is shown in Figure 4.15. For the mag.-dep. f_{contam} case, the adopted correction factor for $V \leq 22.9$ is $f_{\text{contam}} = 0.34$ (the average over all magnitudes).

Converting the Schechter (1976) formula into absolute magnitude, the LF is fitted with the form:

$$\Phi(M_{1700})dM_{1700} = \frac{2}{5} \ln(10)\phi^*x^{\alpha+1} \exp[-x]dM_{1700}, \quad (4.6)$$

where $x \equiv 10^{-0.4(M_{1700} - M_{1700}^*)}$. In order to obtain the best fit, a MC simulation was performed to consider the full range of scatter in the LF. Each datapoint was perturbed randomly 5×10^5 times following a Gaussian distribution with 1σ given by the uncertainties in Φ . Each iteration is then fitted to obtain the Schechter parameters. This yielded for the mag.-dep. f_{contam} case: $M_{1700}^* = -20.50 \pm 0.79$, $\log \phi^* = -2.25 \pm 0.46$, and $\alpha = -1.05 \pm 1.11$ as the best fit with 1σ *correlated* errors. Since these Schechter parameters are based on lower limits of low- z contamination (see § 4.3.2), they imply an upper limit on ϕ^* . This luminosity function is plotted onto Figure 4.15 as the solid black line, and the confidence contours are shown in Figure 4.16. With the faint-end slope fixed to $\alpha = -1.60$ (Steidel et al., 1999) and -1.84 (Reddy et al., 2008), the MC simulations yielded $(M_{1700}^*, \log \phi^*)$ of $(-20.95 \pm 0.29, -2.50 \pm 0.17)$ and $(-21.30 \pm 0.35, -2.75 \pm 0.21)$, respectively.

4.4.2 The Luminosity and Star-Formation Rate Densities

The LF is integrated down to $M_{1700} = -20.11$ —the magnitude where incompleteness is a problem—to obtain a comoving *observed* specific luminosity density (LD) of $\log \mathcal{L}_{\text{lim}} = 26.28 \pm 0.69$ erg s $^{-1}$ Hz $^{-1}$ Mpc $^{-3}$ at 1700Å. The con-

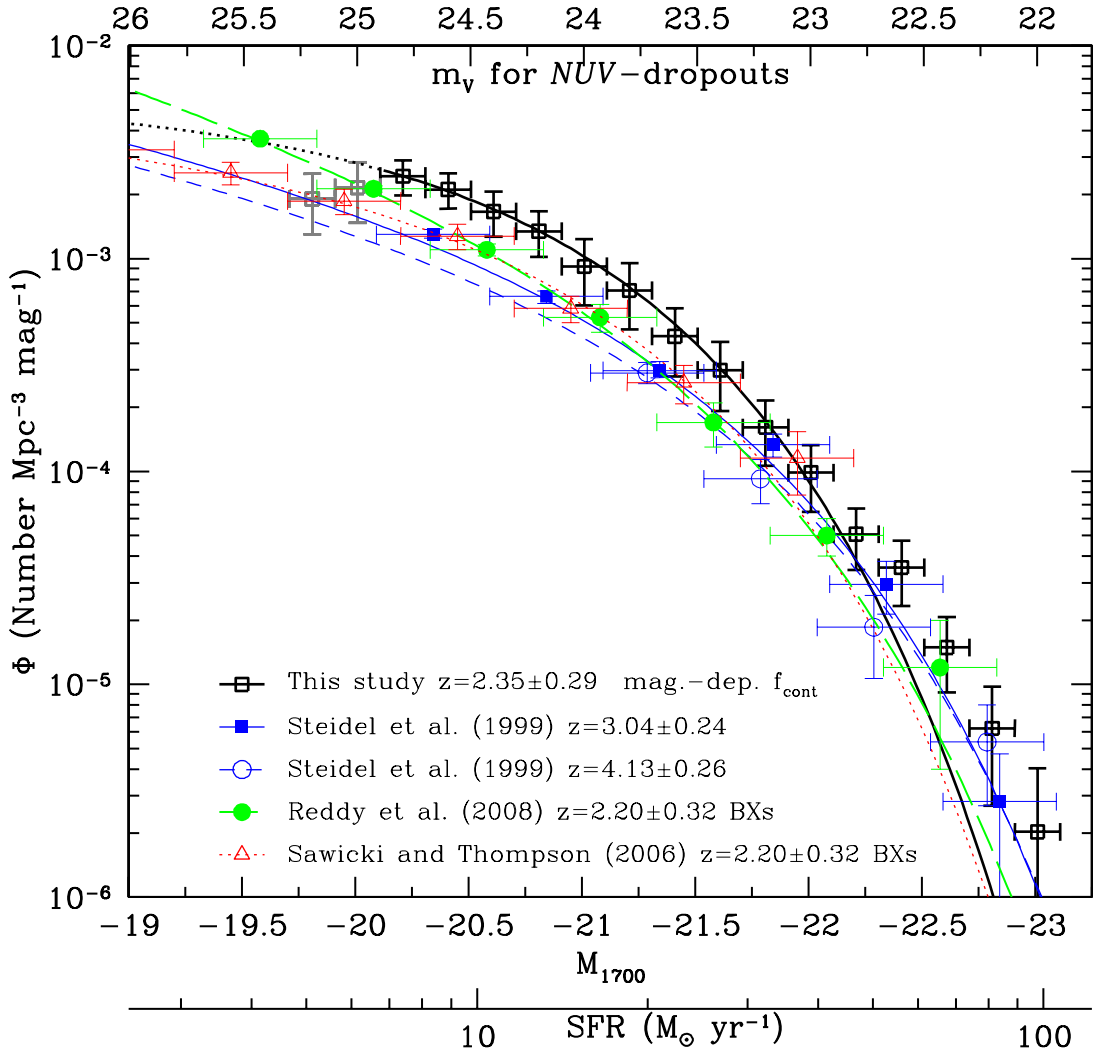


Figure 4.15 – The LF of this work is shown by the thick black solid curve with unfilled squares. Grey points are those excluded from the MC fit. Steidel et al. (1999) measurements are shown as filled squares with solid thin curve ($z \sim 3$) and opened circles with short-dashed thin curve ($z \sim 4$). Reddy et al. (2008) BX results are shown as filled circles with long-dashed line, and Sawicki & Thompson (2006a) is represented by unfilled triangles and dotted line. Corrections to a common cosmology were made for Steidel et al. (1999) measurements, and SFR conversion follows Kennicutt (1998).

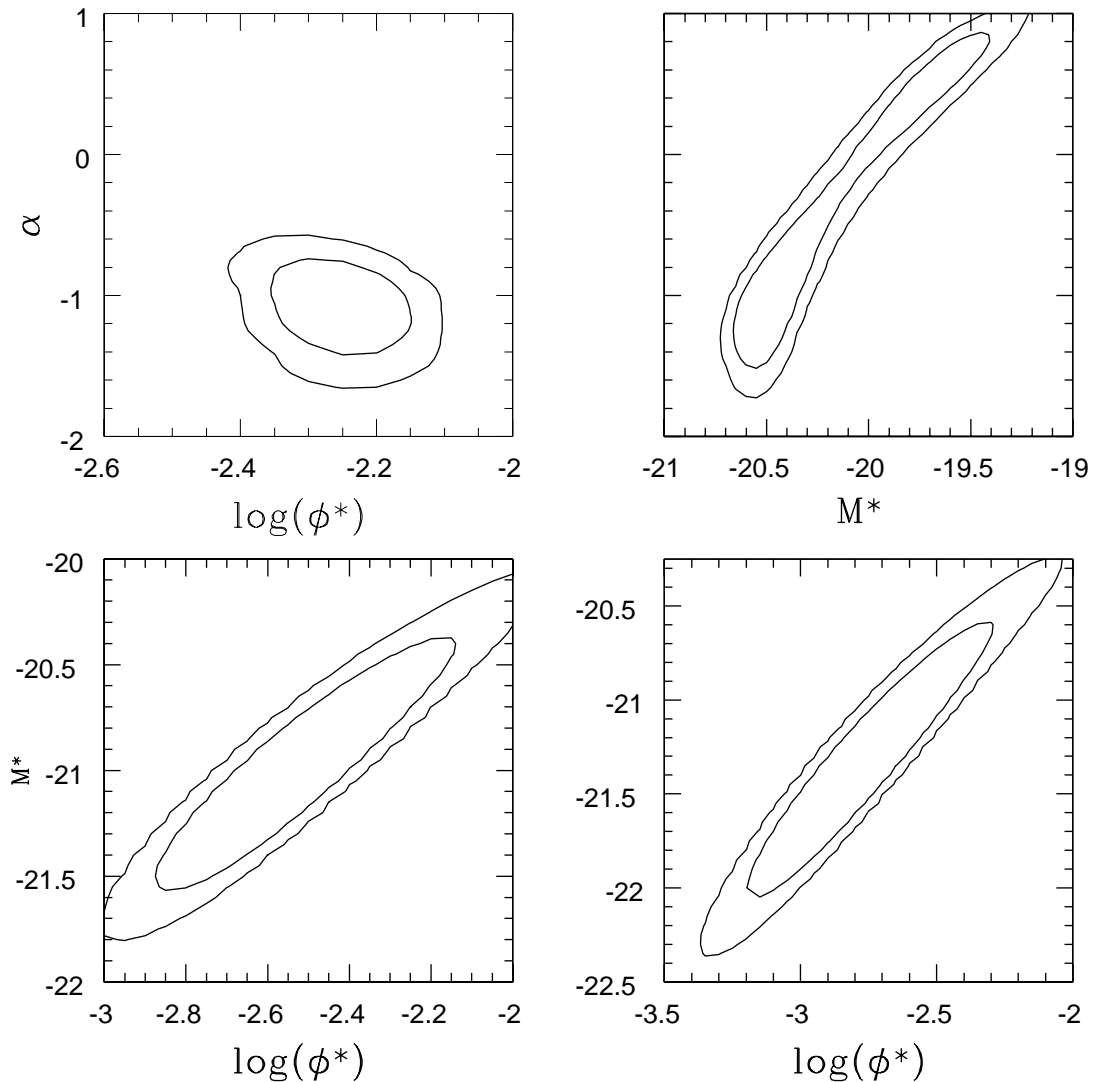


Figure 4.16 – (Top) The mag.-dep. correction where the faint-end slope is a free parameter. The vertical axes show α while the horizontal axes show $\log(\phi^*)$ (left) and M^* (right). (Bottom) M^* vs. $\log(\phi^*)$ for $\alpha = -1.6$ (left) and $\alpha = -1.84$ (right). The inner and outer contours represent 68% and 95% confidence levels.

version between the SFR and specific luminosity for 1500–2800Å is $\text{SFR}_{\text{UV}}(M_{\odot} \text{ yr}^{-1}) = 1.4 \times 10^{-28} L_{\nu}(\text{erg s}^{-1} \text{ Hz}^{-1})$, where a Salpeter IMF with masses from $0.1 - 100 M_{\odot}$ is assumed (Kennicutt, 1998). Therefore, the extinction- (adopted $E[B - V] = 0.15$ and Calzetti law) and completeness-corrected SFR density of $z \sim 2$ LBGs is $\log \dot{\rho}_{\text{star}} = -0.99 \pm 0.69 M_{\odot} \text{ yr}^{-1} \text{ Mpc}^{-3}$. Using the Madau et al. (1998) conversion would decrease the SFR by $\sim 10\%$. Integrating to $L = 0.1 L_{z=3}^*$, where $L_{z=3}^*$ is L^* at $z \sim 3$ ($M_{z=3}^* = -21.07$, Steidel et al., 1999), yields $\log \mathcal{L} = 26.52 \pm 0.68 \text{ erg s}^{-1} \text{ Hz}^{-1} \text{ Mpc}^{-3}$ or an extinction-corrected SFR density of $\log \dot{\rho}_{\text{star}} = -0.75 \pm 0.68 M_{\odot} \text{ yr}^{-1} \text{ Mpc}^{-3}$.¹⁶

4.4.3 Summary of Results

A UV luminosity function was constructed and yielded a best Schechter fit of $M_{1700}^* = -20.50 \pm 0.79$, $\log \phi^* = -2.25 \pm 0.46$, and $\alpha = -1.05 \pm 1.11$ for $z \sim 2$ LBGs. The UV specific luminosity density, above the survey limit, is $\log \mathcal{L}_{\text{lim}} = 26.28 \pm 0.68 \text{ erg s}^{-1} \text{ Hz}^{-1} \text{ Mpc}^{-3}$. Correcting for dust extinction, this corresponds to a SFR density of $\log \dot{\rho}_{\text{star}} = -0.99 \pm 0.68 M_{\odot} \text{ yr}^{-1} \text{ Mpc}^{-3}$.

4.5 Comparisons with other Studies

Comparisons in the UV specific luminosity densities, LFs, and Schechter parameters can be made with previous studies. First, a comparison is made between the $z \sim 2$ LBG LF with $z \sim 2$ BX and $z \sim 3$ LBG LFs. Then a discussion of the redshift evolution in the UV luminosity density and LF (parameterized in the Schechter form) is given in § 4.5.2.

The results are summarized in Figures 4.15, 4.18, and 4.19 and Table 4.4. For

¹⁶The above numbers are upper limits if the low- z contamination fraction is higher than estimates described in § 4.3.2.

completeness, three different UV specific luminosity densities are reported by integrating the LF down to: (1) $0.1L_{z=3}^*$; (2) L_{lim} , the limiting depth of the survey; and (3) $L = 0$. The latter is the least confident, as it requires extrapolating the LF to the faint-end, where in most studies, it is not well determined.

Table 4.5. Compilation of UV Luminosity Functions

Reference	z	N	Area	λ_{rest}	C_E	C_L	C_Φ	$\log \phi_*$	M_*	α
Bouwens et al. (2006)	5.90±0.30	506	344.2	1350	1.51	1.000	1.000	-2.69 ^{+0.15} _{-0.21}	-20.25±0.20	-1.73 ^{+0.21} _{-0.20}
Bouwens et al. (2007)	3.80±0.35	4671	347	1600	2.692	1.000	1.000	-2.89 ^{+0.06} _{-0.07}	-20.98±0.10	-1.73±0.05
	5.00±0.35	1416	367	1600	1.995	1.000	1.000	-3.00 ^{+0.11} _{-0.16}	-20.64±0.13	-1.66±0.09
	5.90±0.30	627	396	1350	1.51	1.000	1.000	-2.85 ^{+0.16} _{-0.15}	-20.24±0.19	-1.74±0.16
Burgarella et al. (2007)	1.10±0.20	420	947	1800	3.651	1.000	1.000
Foucaud et al. (2003)	3.20 ^{+0.02} _{-0.30}	1294	1700	1900	...	1.000	1.000
Giavalisco et al. (2004)	3.78±0.34	1115	316	1500	7.48	1.000	1.000	-1.60 ^f
	4.92±0.33	275	316	1500	7.48	1.000	1.000	-1.60 ^f
	5.74±0.36	122	316	1500	7.48	1.000	1.000	-1.60 ^f
Hildebrandt et al. (2007)	2.96±0.24	14283	9.99	1650	3.88	1.000	1.000	-3.29±0.08 ^e	-22.43±0.11 ^e	-1.60 ^g
Iwata et al. (2007)	4.80±0.40	853	1290	1500	7.48	1.000	1.000	-3.39 ^{+0.23} _{-0.53}	-21.23±0.30	-1.45 ^{+0.38} _{-0.32}
Madau et al. (1996)	2.75±0.75	69	4.65	1620	3.23	1.108	0.712
	4.00±0.50	14	4.65	1630	3.23	1.170	0.662
Massarotti et al. (2001)	1.50±0.50	315	5.31	1500	8.10	0.980	0.844
	2.75±0.75	232	5.31	1500	12.17	1.108	0.712
	4.00±0.50	54	5.31	1500	12.00	1.170	0.662
Paltani et al. (2007)	3.50±0.50	113	1720	1700	3.80	1.000	1.000	-2.91 ^{+0.14} _{-0.22}	-21.49±0.19	-1.40 ^f
Reddy et al. (2008)	2.20±0.32	10007	1925.8	1700	3.796	1.000	1.000	-2.76 ^{+0.13} _{-0.20}	-20.97±0.23	-1.84±0.11
Sawicki & Thompson (2006a,b)	2.20±0.32	2417	169	1700	5-15	1.000	1.000	-2.52 ^{+0.20} _{-0.26}	-20.60 ^{+0.38} _{-0.44}	-1.20 ^{+0.24} _{-0.22}
	2.96±0.26	1481	169	1700	5-15	1.000	1.000	-2.77 ^{+0.13} _{-0.09}	-20.90 ^{+0.22} _{-0.14}	-1.43 ^{+0.17} _{-0.09}
	4.13±0.26	427	169	1700	5-15	1.000	1.000	-3.07 ^{+0.21} _{-0.33}	-21.00 ^{+0.40} _{-0.46}	-1.26 ^{+0.40} _{-0.36}
Shimasaku et al. (2005)	5.90±0.30	12	767	1425	4.358	1.000	1.000
Shim et al. (2007)	3.20±0.14	1088	9468	1550	3.964	1.000	1.000	-2.81 ^e	-20.69 ^e	-0.83 ^f
Steidel et al. (1999)	2.96±0.26	1270	1046	1700	3.796	1.126	0.693	-2.86	-21.07±0.15	-1.60±0.13
	4.13±0.26	207	828	1700	3.796	1.175	0.658	-2.97	-21.11	-1.60 ^f
Wadadekar et al. (2006)	2.75±0.75	125	5.67	1850	4.70	0.862	1.249
Yoshida et al. (2006)	4.00±0.30	3808	875	1500	3.381	1.000	1.000	-2.84 ^{+0.11} _{-0.12}	-21.14 ^{+0.14} _{-0.15}	-1.82±0.09
	4.70±0.30	539	875	1500	3.381	1.000	1.000	-2.91 ^{+0.13} _{-0.11}	-20.72 ^{+0.16} _{-0.14}	-1.82 ^f
This work	2.28±0.33	7093	857.5	1700	3.796	1.000	1.000	-2.25±0.46	-20.50±0.79	-1.05±1.11
								-2.50±0.17	-20.95 ^{+0.43} _{-0.29}	-1.60 ^f
								-2.75±0.21	-21.30±0.35	-1.84 ^f

Note. — Cols. (1) through (5) list the reference, the redshift, the sample size, the area (arcmin^2), and the rest-wavelength of measurements (Å). Dust extinction correction is provided in Col. (6), and corrections to a common cosmology for luminosity and number density are shown in Cols. (7) and (8). Schechter LF parameters are listed in Cols. (9)-(11) in units of Mpc^{-3} for number density.

^eThese values were not reported in the paper, but was obtained by fitting their LF with data provided in the paper or by the authors. For Shim et al. (2007), the results are not well constrained given the limited number of degrees of freedom.

^fThis value was kept fixed, while the other Schechter parameters were fitted.

Table 4.6. Compilation of UV Luminosity Densities

Reference	$\log \mathcal{L}_{\text{obs}}$		
	$L \geq 0.1L_{z=3}$	$L \geq L_{\text{lim}}$	$L \geq 0$
Bouwens et al. (2006)	26.047	$26.224^{+0.10}_{-0.13}$	26.567
Bouwens et al. (2007)	26.276	26.503 ± 0.05	26.668
	25.952	26.161 ± 0.06	26.313
	25.885	26.100 ± 0.08	26.421
Burgarella et al. (2007)	...	$25.738^{+0.08}_{-0.10}$...
Foucaud et al. (2003)
Giavalisco et al. (2004)	...	26.212 ± 0.07	...
	...	26.017 ± 0.14	...
	...	26.061 ± 0.19	...
Hildebrandt et al. (2007)	26.362	26.097	26.492
Iwata et al. (2007)	$25.841^{+0.06}_{-0.04}$	25.679	$25.995^{+0.23}_{-0.09}$
Madau et al. (1996)	...	<26.101	...
	...	<25.588	...
Massarotti et al. (2001)	...	26.240 ± 0.19	...
	...	26.259 ± 0.19	...
	...	25.889 ± 0.24	...
Paltani et al. (2007)	$26.093^{+0.16}_{-0.26}$...	$26.499^{+0.09}_{-0.12}$
Reddy et al. (2008)	$26.439^{+0.06}_{-0.07}$	26.256	27.030
Sawicki & Thompson (2006a,b)	26.320 ± 0.02	26.314	26.424 ± 0.03
	26.257 ± 0.01	26.303	26.422 ± 0.03
	25.969 ± 0.03	25.965 ± 0.03	26.061 ± 0.07
Shimasaku et al. (2005)	...	$24.447^{+0.11}_{-0.15}$...
Shim et al. (2007)	26.027	25.578	26.067
Steidel et al. (1999)	26.462	26.193	26.711
	26.397	25.734	26.640
Wadadekar et al. (2006)	26.518
Yoshida et al. (2006)	$26.450^{+0.06}_{-0.07}$	26.343 ± 0.02	26.968
	26.138 ± 0.24	$25.645^{+0.03}_{-0.05}$	26.726
This work	26.519 ± 0.68	26.276 ± 0.68	26.601 ± 0.92
	26.601 ± 0.07	26.293 ± 0.07	26.864 ± 0.07
	26.633 ± 0.08	26.305 ± 0.08	27.172 ± 0.08

Note. — Cols. (1) through (5) list the reference, the redshift, the sample size, the area (arcmin^2), and the rest-wavelength of measurements (\AA). Dust extinction correction is provided in Col. (6), and corrections to a common cosmology for luminosity and number density are shown in Cols. (7) and (8). Schechter LF parameters are listed in Cols. (9)-(11) in units of Mpc^{-3} for number density.

^eThese values were not reported in the paper, but was obtained by fitting their LF with data provided in the paper or by the authors. For Shim et al. (2007), the results are not well constrained given the limited number of degrees of freedom.

^fThis value was kept fixed, while the other Schechter parameters were fitted.

4.5.1 UV-selected Studies at $z \sim 2 - 3$

In Figure 4.15, the $z \sim 2$ LBG LF at the bright end is similar to those of LBGs from Steidel et al. (1999) and BX galaxies from Sawicki & Thompson (2006a) and Reddy et al. (2008); however, the faint end is systematically higher. This is illustrated in Figure 4.17 where the ratios between the binned $z \sim 2$ UV LF and the fitted Schechter forms of Steidel et al. (1999) and Reddy et al. (2008) are shown. When excluding the four brightest and two faintest bins, the *NUV*-dropout LF is a factor of 1.7 ± 0.1 with respect to $z \sim 3$ LBGs of Steidel et al. (1999) and $z \sim 2$ BX galaxies of Reddy et al. (2008) and Sawicki & Thompson (2006a). The hard upper limit for stellar contamination (see § 4.3.1) would reduce this discrepancy to a factor of 1.4 ± 0.1 . There appears to be a trend that the ratio to Reddy et al. (2008) LF increases towards brighter magnitudes. This is caused by the differences in the shape of the two LFs, particularly the faint-end slope. The increase in the ratio is less noticeable when compared to Steidel et al. (1999), which has a shallower faint-end slope. Since the LFs of Sawicki & Thompson (2006a) and Reddy et al. (2008) are similar, the comparison of any results between the *NUV*-dropout and the BX selections will be made directly against Reddy et al. (2008).

All 11 points are $1 - 3\sigma$ from a ratio of 1. It has been assumed in this comparison that the amount of dust extinction does not evolve from $z \sim 3$ to $z \sim 2$. Evidence supporting this assumption is: in order for the *intrinsic* LBG LFs at $z \sim 2$ and 3 to be consistent, the population of LBGs at $z \sim 2$ would have to be relatively *less* reddened by $\Delta E(B - V) = 0.06$ (i.e., $E[B - V] = 0.09$ assuming a Calzetti extinction law). However, the stellar synthesis models, described previously, indicate that $E(B - V) = 0.1$ star-forming galaxies are expected to have observed $B - V \sim 0.1$, and only 15% of *NUV*-dropouts have

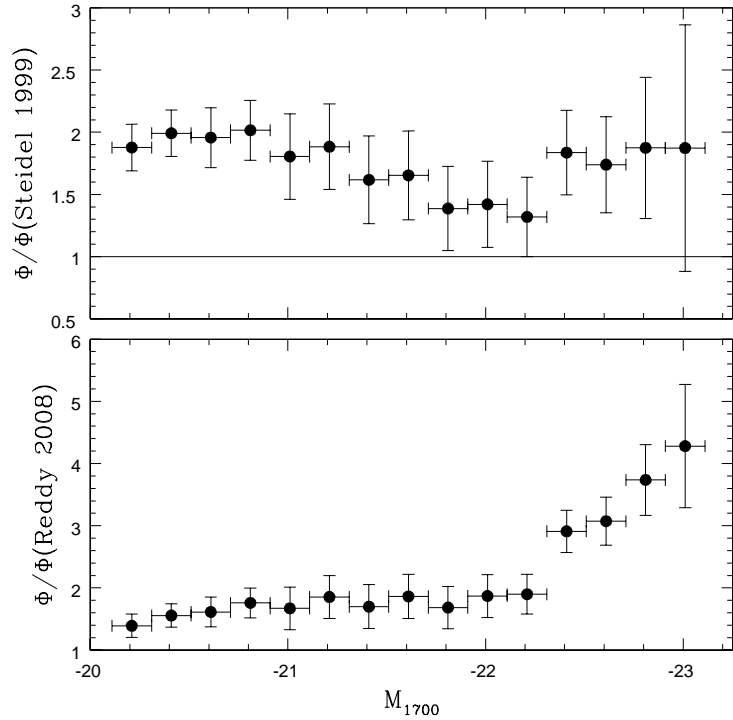


Figure 4.17 – The ratios of the $z \sim 2$ LBG LF to the Schechter fits of Steidel et al. (1999) LF and Reddy et al. (2008) are shown in the top and bottom panels, respectively. On average, the $z \sim 2$ LBG LF is a factor of 1.7 ± 0.1 higher than these studies.

$B - V \leq 0.1$. This result implies that dust evolution is unlikely to be the cause for the discrepancy seen in the LFs.

To compare the luminosity densities, the binned LF is summed. This is superior to integrating the Schechter form of the LF as (1) no assumptions are made between individual LF values and for the faint-end, and (2) the results do not suffer from the problem that Schechter parameters are affected by small fluctuations at the bright- and faint-ends. The logarithm of the binned luminosity densities for $-22.91 < M_{1700} < -20.11$ are 26.27 ± 0.16 (this work), 26.02 ± 0.04 (Steidel et al., 1999), and $26.08 \pm 0.07 \text{ erg s}^{-1} \text{ Hz}^{-1} \text{ Mpc}^{-3}$ (Reddy et al., 2008), which implies that the $z \sim 2$ LBG UV luminosity density is 0.25 ± 0.16 dex higher

than the other two studies at the 85% confidence level.

Since the low- z contamination fraction is the largest contributor to the errors, more follow-up spectroscopy will reduce uncertainties on the LF. This will either confirm or deny with greater statistical significance that the luminosity density and LF of $z \sim 2$ LBGs are higher than the $z \sim 3$ LBGs and $z \sim 2$ BXs.

4.5.2 Evolution in the UV Luminosity Function and Density

The Schechter LF parameters, listed in Table 4.4, are plotted as a function of redshift in Figure 4.18. There appears to be a systematic trend that M^* is less negative (i.e., a fainter L^*) by ≈ 1 mag at higher redshifts for surveys with $\alpha \leq -1.35$. No systematic evolution is seen for ϕ^* , given the measurement uncertainties. Limited information are available on the faint-end slope, so no analysis on its redshift evolution is provided. It is often difficult to compare Schechter parameters, since they are correlated, and without confidence contours for the fits of each study, the apparent evolution could be insignificant. A more robust measurement is the product ($\phi^* \times L^*$), which is related to the luminosity density.

The observed LDs, integrated to $0.1L_{z=3}^*$, show a slight increase of ≈ 0.5 dex from $z \sim 6$ to $z \sim 3$. However, the two other luminosity densities appear to be flat, given the scatter in the measurements of $\approx 0.5 - 1.0$ dex. A comparison between $z \sim 2$ and $z \sim 5$ studies reveal a factor of $3 - 6$ higher luminosity density at $z \sim 2$. The extinction-corrected results for $L_{\text{lim}} = 0$ and $L_{\text{lim}} = 0.1L_{z=3}^*$ show a factor of 10 increase from $z \sim 6$ [Bouwens et al. \(2007\)](#)'s measurement to $z \sim 2$. [Bouwens et al. \(2007\)](#) assumed a lower dust extinction correction. If an average $E(B - V) = 0.15$ with a Calzetti law is adopted, the rise in the extinction-corrected luminosity density is ≈ 3 .

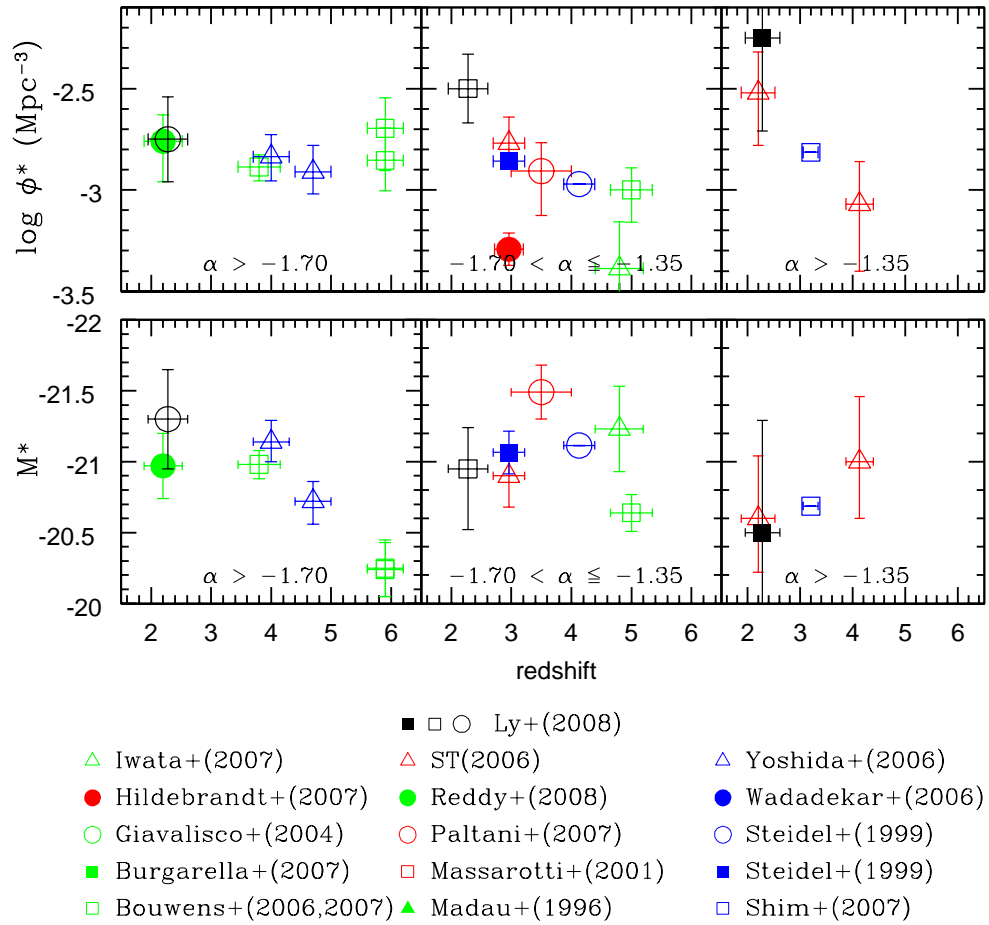


Figure 4.18 – Top and bottom show the the normalization (ϕ^*), and the “knee” of the UV LF (M^*), respectively. Measurements are grouped according to α : ≤ -1.70 , between -1.70 and -1.35 , and > -1.35 . This NUV-dropout work is shown as black filled square ($\alpha = -1.05$). The color and symbol conventions for studies in Figure 4.15 are identical for this figure. In the legend, Sawicki & Thompson (2006a) is abbreviated as “ST(2006).” Some points are not shown here but have luminosity density measurements presented in Figure 4.19.

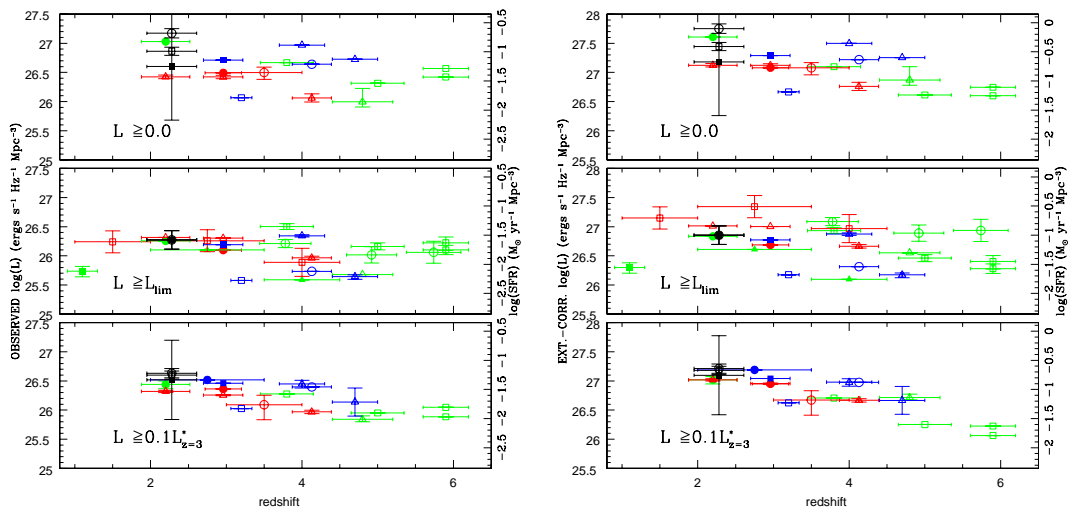


Figure 4.19 – The observed (*left*) and extinction-corrected (*right*) UV specific luminosity densities as a function of redshift. The luminosity function is integrated to three different limits: $L = 0$ (top panel), $L = L_{\text{lim}}$ (the survey's limit; middle panel), and $L = 0.1L_{z=3}^*$. The color and point-type schemes are the same as Figure 4.18. The SFR densities are shown on the right axes following Kennicutt (1998) conversion. For the $z \sim 2$ LBG luminosity density integrated to $L = L_{\text{lim}}$, only one value is shown, since all the fits with different α are almost identical.

4.6 Discussion

In this section, the discrepancy between the UV LF of this study and two BX studies, shown in § 4.5.1, is examined. Three possible explanations are considered:

1. Underestimating low- z contamination. To estimate contamination, a large sample of $z \lesssim 1.5$ NB emitters was cross-matched with the *NUV*-dropout sample. This method indicated that $34\% \pm 17\%$ of *NUV*-dropouts are at $z < 1.5$. However, it is possible that star-forming galaxies at $z = 1 - 1.5$ could be missed by the NB technique, but still be identified as *NUV*-dropouts. This would imply that the contamination rate was underestimated. To shift the *NUV*-dropout LF to agree with Reddy et al. (2008) and Sawicki & Thompson (2006a) would require that the contamination fraction be more than 60%. However, the spectroscopic sample has yielded a large number of genuine LBGs and a similar low- z contamination (at least 21% and at most 38%). If the large (60%) contamination rate is adopted, it would imply that only 15 of 40 spectra (LRIS and Hectospec) are at $z > 1.5$, which is argued against at the 93% confidence level (98% with $R = 2.5$ threshold), since 24 LBGs (1.6 times as many) have been identified. Furthermore, the LRIS and Hectospec observations independently yielded similar low contamination fractions, and the MC simulation (that involved adding artificial LBGs to the images) independently suggested 30% contamination from $z \leq 1.5$.

2. Underestimating the comoving effective volume. The second possibility is that V_{eff} was underestimated, as the spectral synthesis model may not completely represent the galaxies in this sample, and misses $z \sim 1 - 1.5$ galaxies. However, a comparison between a top-hat $P(m, z)$ from $z = 1.7 - 2.7$ versus $z = 1.4 - 2.7$ ($z = 1.0 - 2.7$) would only decrease number densities by $\approx 20\%$ (37%). Note that the latter value is consistent with f_{contam} .

3. Differences between LBG and BX galaxies selection. This study uses the Lyman break technique while other studies used the ‘BX’ method to identify $z \sim 2$ galaxies. Because of differences in photometric selection, it is possible that the galaxy population identified by one method does not match the other, but instead, only a fraction of BX galaxies are also LBGs and vice versa. This argument is supported by the higher surface density of LBGs compared to BXs over 2.5 mag, as shown in Figure 4.20a. However, their redshift distributions, as shown in Figure 4.20b, are very similar.

This scenario would imply that there is an increase in the LF and number density of LBGs from $z \sim 3$ to $z \sim 2$, indicating that the comoving SFR density peaks at $z \sim 2$, since there is a decline towards $z \sim 0$ from UV studies (see Hopkins, 2004, and references therein). However, it might be possible that the selection ($NUV - B - V$) of $z \sim 2$ LBGs could include more galaxies than the U_nGR color selection used to find $z \sim 3$ LBGs. Although no reason exists to believe that $z \sim 3$ LBG selection is more incomplete than at $z \sim 2$ (nor is there any evidence for such systematic incompleteness for $z > 4$ LBGs), it is difficult to rule out this possibility for certain. But if so, then the SFR density might not evolve. In addition, the conclusion that $z \sim 2$ is the peak in star-formation is based on UV selection techniques, which are less sensitive at identifying dusty ($E[B - V] > 0.4$) star-forming galaxies. However, spectroscopic surveys have revealed that the sub-mm galaxy population peaks at $z \approx 2.2$ (Chapman et al., 2005), which further supports the above statement that $z \sim 2$ is the epoch of peak star-formation.

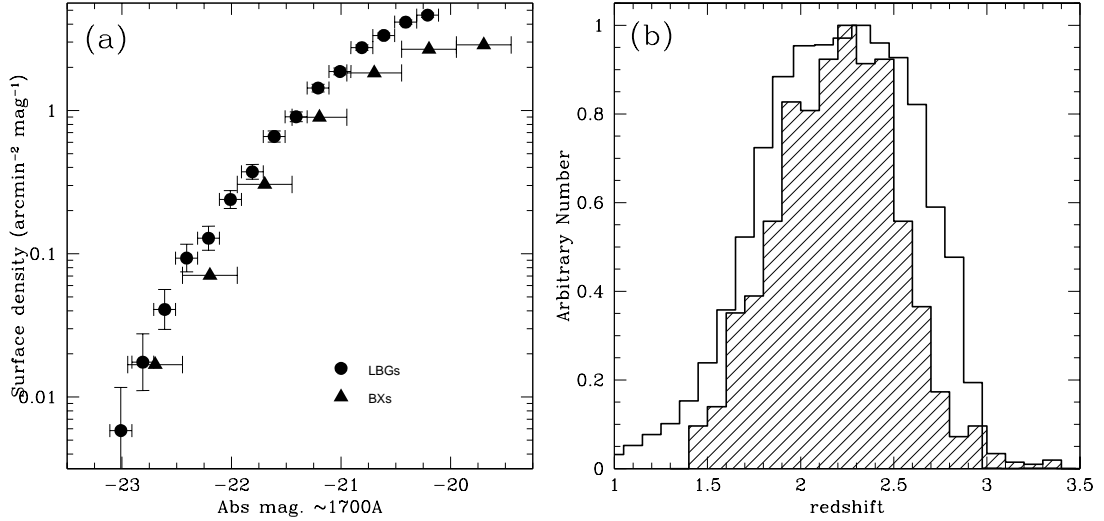


Figure 4.20 – In (a), the surface densities of LBGs and BXs are shown as circles and triangles, respectively. Both studies have stellar and low- z contamination corrections applied. This figure reveals that the LBG surface density is systematically higher than the BX's. The redshift distributions are shown in (b). The shaded (unshaded) histogram corresponds to BXs (LBGs). For the BX, the redshift distribution is obtained from Reddy et al. (2008) spectroscopic sample, while the LBG is determined from the MC simulations described in § 4.3 for all magnitudes. The similarities in redshifts surveyed by both studies and the higher surface density of LBGs indicate that the BX technique misses a fraction of LBGs.

4.7 Conclusions

By combining deep *GALEX/NUV* and optical Suprime-Cam imaging for the Subaru Deep Field, a large sample of LBGs at $z \sim 2$ has been identified as *NUV*-dropouts. This extends the popular Lyman break technique into the redshift desert, which was previously difficult due to the lack of deep and wide-field UV imaging from space. The key results of this paper are:

1. Follow-up spectroscopy was obtained, and 63% of identified galaxies are at $z = 1.6 - 2.7$. This confirms that most *NUV*-dropouts are LBGs. In addition, MMT/Hectospec will complement Keck/LRIS by efficiently completing a spectroscopic survey of the bright end of the LF.
2. Selecting objects with $NUV - B \geq 1.75$, $B - V \leq 0.5$, and $NUV - B \geq 2.4(B - V) + 1.15$ yielded 7964 *NUV*-dropouts with $V = 21.9 - 25.3$. The spectroscopic sample implied that 50–86% of *NUV*-dropouts are LBGs.
3. Using broad-band optical colors and stellar classification, 871 foreground stars have been identified and removed from the photometric sample. This corresponds to a 4 – 11% correction to the *NUV*-dropout surface density, which is consistent with the 3 – 7% from limited spectra of stars presented in this paper.
4. In addition, low- z contamination was determined using a photometric sample of NB emitters at $z \lesssim 1.47$. This novel technique indicated that the contamination fraction is (at least) on average $34\% \pm 17\%$, which is consistent with the spectroscopic samples and predictions from MC simulations of the survey.
5. After removing the foreground stars and low- z interlopers, MC simulations were performed to estimate the effective comoving volume of the survey.

The UV luminosity function was constructed and fitted with a Schechter profile with $M_{1700}^* = -20.50 \pm 0.79$, $\log \phi^* = -2.25 \pm 0.46$, and $\alpha = -1.05 \pm 1.11$.

6. A compilation of LF and SFR measurements for UV-selected galaxies is made, and there appears to be an increase in the luminosity density: a factor of 3–6 (3–10) increase from $z \sim 5$ ($z \sim 6$) to $z \sim 2$.
7. Comparisons between *NUV*-dropouts with LBGs at $z \sim 3$ (Steidel et al., 1999) and BXs at $z \sim 2$ (Sawicki & Thompson, 2006a; Reddy et al., 2008) reveal that the LF is 1.7 ± 0.1 (1.4 ± 0.1 if the hard upper limit of stellar contamination is adopted) times higher than these studies. The summed luminosity density for $z \sim 2$ LBGs is 1.8 times higher at 85% confidence (i.e., 0.25 ± 0.16 dex).
8. Three explanations were considered for the discrepancy with $z \sim 2$ BX studies. The possibility of underestimating low- z contamination is unlikely, since optical spectroscopy argues against the possibility of a high (60%) contamination fraction at the 93% confidence. Second, even extending the redshift range to increase the comoving volume is not sufficient to resolve the discrepancy. The final possibility, which cannot be ruled out, is that a direct comparison between BX-selected galaxies and LBG is not valid, since the selection criteria differ. It is likely that the BX method may be missing some LBGs. This argument is supported by the similar redshift distribution of BXs and LBGs, but the consistently higher surface density of LBGs over 2.5 mag.
9. If the latter holds with future reduction of low- z contamination uncertainties via spectroscopy, then the SFR density at $z \sim 2$ is higher than $z \gtrsim 3$ and $z \lesssim 1.5$ measurements obtained via UV selection. Combined with sub-mm results (Chapman et al., 2005), it indicates that $z \sim 2$ is the epoch

where galaxy star-formation peaks.

CHAPTER 5

A Census of Star-Forming Galaxies at $z = 1 - 3$

The use of photometric selection techniques to identify galaxies at desired redshifts has grown with the advent of large telescopes with wide-field detectors. These methods require imaging in only a few broad-band filters to isolate spectral features, such as the Lyman continuum and Balmer/4000Å breaks.

At optical wavelengths, the Balmer/4000Å break is well sampled below $z \approx 1$, and the Lyman continuum break succeeds at identifying Lyman break galaxies (LBGs) at $z = 3 - 7$ (e.g., Steidel et al., 1999; Bouwens et al., 2006; Yoshida et al., 2006). The net result is the historical inability to identify galaxies at $z \approx 1 - 3$, often referred to as the “redshift desert.”

The extension of the Lyman break technique to lower redshift requires deep NUV imaging, which has only been recently available with the *GALEX* satellite (see Chapter 4). Prior to this, different techniques were developed including the BX and BM techniques (Adelberger et al., 2004; Steidel et al., 2004), the BzK method (Daddi et al., 2004), and the selection of “distant red galaxies” (DRGs; Franx et al., 2003; van Dokkum et al., 2004). However, each technique suffers from its own selection bias. For example, UV techniques (e.g., LBG, BX) often identify young star-forming galaxies with comparably low dust extinction, while IR techniques (e.g., BzK, DRG) select more massive dusty galaxies.

In this chapter, all $z = 1 - 3$ photometric selection techniques are utilized in

the SDF to identify \sim 19000 galaxies for a complete census of optical and near-infrared (NIR) selected star-forming galaxies in this redshift epoch. This survey, compared to previous work (Reddy et al., 2005; Quadri et al., 2007; Grazian et al., 2007), has a larger galaxy sample from a factor of 2 – 10 times more area coverage and additional photometric selection techniques. In addition to these photometric techniques, a census derived from a photometric redshift ($\text{photo-}z$) is included.

This chapter is outlined as follows. The observations spanning wavelengths from 1500Å to $2\mu\text{m}$ are described in § 5.1. Section 5.2 presents the technique used to merge the multi-wavelength data together, which accounts for differences in the spatial resolution across different wave-bands. Section 5.3 discusses the method for determining photometric redshift (z_{phot}) and the modelling of the spectral energy distribution (SED) for the $z = 1 - 3$ galaxies. In § 5.4, the different photometric techniques used and individual sample properties are presented. Section 5.5 discusses the selection effects of one technique against another, and presents a comparison of photometric selection techniques to a z_{phot} -selected sample. We also compare our work against past surveys that examined this issue. The discussion of our results and suggestions for future high- z surveys are provided in § 5.6, while § 5.7 discusses future improvements. Conclusions from this $z = 1 - 3$ census are summarized in § 5.8.

5.1 Subaru Deep Field Multi-Wavelength Observations

In this section, imaging in each waveband is described. A summary of the properties (depth, spatial resolution, sample sizes) of these data is provided in Table 5.1, while the spatial coverage of the SDF with the different datasets is shown in Figure 5.1. In most circumstances the data are described in previous chapters, so

Table 5.1. Summary of SDF Multi-Wavelength Data

Filter	$\lambda_{\text{cen}}^{\text{a}}$	$\lambda_{\text{FWHM}}^{\text{a}}$	$m_{\text{lim}}^{\text{b}}$	FWHM ('')	N(3 σ) ^c	N(5 σ) ^c	Aper. Corr. ^d
<i>FUV</i>	1533	209	26.841	~4.5	13895 (16859)	6592 (8016)	1.454
<i>NUV</i>	2284	697	27.151	~5.0	47845 (57668)	30271 (36470)	1.707
<i>U</i>	3634	750	26.842	1.49	34926 (42379)	24124 (29257)	1.164
<i>B</i>	4438	687	28.621	1.01	88703 (107935)	74836 (91017)	1.192
<i>V</i>	5463	885	27.893	1.11	75522 (92182)	62341 (76025)	1.178
<i>R_C</i>	6515	1100	28.083	1.11	90452 (110151)	76773 (93466)	1.173
<i>i'</i>	7659	1419	27.757	1.11	82308 (100245)	69666 (84902)	1.168
<i>z'</i>	9020	956	26.825	0.96	57163 (69778)	46767 (57017)	1.181
<i>z_b</i>	8842	620	26.361	0.91	47067 (57551)	36289 (44405)	1.175
<i>z_r</i>	9841	1000	25.501	0.91	28989 (35276)	21853 (26571)	1.274
<i>IA598</i>	6007	303	26.789	0.91	47764 (58322)	34987 (42724)	1.262
<i>IA679</i>	6780	340	27.393	0.96	72221 (87969)	57672 (70361)	1.214
<i>J</i>	12492	1799	23.449	1.27	16694 (19985)	9637 (11713)	1.214
<i>H</i>	16186	5700	22.883	1.18	10662 (12691)	5684 (6949)	1.208
<i>K</i>	22035	2995	24.227	0.81	24788	17415	1.371

^aFilter's center and FWHM are in units of Å.

^bLimiting magnitudes are defined as 3 σ with a 3'' ϕ (*U*, *J*, and *H*), 6''.8 ϕ (*FUV* and *NUV*), or 2'' ϕ (remaining wave-bands) aperture.

^cFirst values exclude sources in the *K*-band low sensitivity region while those in parentheses include sources in this region.

^dCorrections of aperture fluxes to total source flux assuming a point source. These are determined within the same aperture as m_{lim} .

detailed discussions are omitted.

5.1.1 Subaru/Suprime-Cam Data

The *BVR_Ci'z'* observations are the deepest data obtained to date from Suprime-Cam.¹ The limiting magnitudes in a 2'' ϕ aperture were re-determined with more rigorous masking of pixels affected by object flux and are $\approx 0.1 - 0.2$ mag deeper than those quoted in § 2.1. They range from 26.8 to 28.6 mag.

In addition to these data, Suprime-Cam imaging in four intermediate-band filters, IA598, IA679, *z_b*, and *z_r* are also available. Studies (e.g.; Meisenheimer & Wolf, 2002; Ilbert et al., 2009; van Dokkum et al., 2009) using intermediate-band

¹These data are publically available at <http://step.mtk.nao.ac.jp/sdf/data/>.

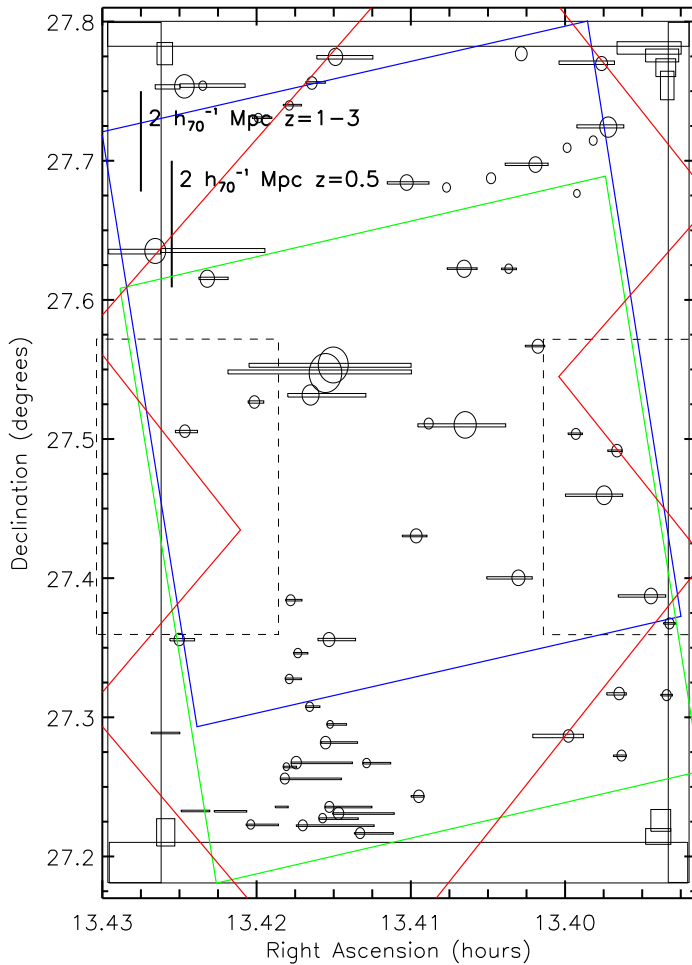


Figure 5.1 – The sky coverage of SDF data described in § 5.1. Masked regions for the Suprime-Cam data are shown with the solid black rectangles and circles. The dashed lines correspond to the regions of lower K -band sensitivity. The area coverage is 870.4 arcmin 2 prior to excluding the dashed-line regions and is 718.7 arcmin 2 . *GALEX* covers a region larger than what is illustrated here, given its 1° field-of-view. NEWFIRM and MOSAIC data have coverage over the entire SDF region. *Spitzer* 1 kilosecond coverage is illustrated with the blue (3.6 and 5.8 μ m), green (4.5 and 8.0 μ m), and red (24 μ m) squares. Deeper (\sim 10 kiloseconds) data have been recently acquired but does not provide as uniform of an area coverage. See § 5.7 for further discussion of *Spitzer* data. The angular size for $2 h_{70}^{-1}$ Mpc is shown by the thick bars at $z = 0.5$ and $z = 1 - 3$.

filters have found improvements to photo- z estimates, as they are able to identify the location of spectral break more accurately. Thus they are included in our photometric redshift and SED modelling analyses. The z_b and z_r observations were obtained in 2003 and 2004, and are described in [Shimasaku et al. \(2005\)](#). The net integrations are 85 and 600 min for z_b and z_r , which give a limiting magnitude of 26.4 and 25.5 mag in a $2'' \phi$ aperture, respectively. The IA598 and IA679 observations were obtained in 2007, and are described in [Nagao et al. \(2008\)](#). Their depths 26.8 and 27.4 mag ($2'' \phi$ aperture), respectively.

5.1.2 UKIRT/WFCAM Data

K -band data for this survey were acquired with Wide-Field Camera (WFCAM; [Casali et al., 2007](#)) on the United Kingdom Infrared Telescope (UKIRT) on 2005 April 14–15 and 2007 March 5–6. Because the field-of-view (FoV) of WFCAM is split into four $13'6 \times 13'6$ images separated by $12'8$, four pointings were required to cover the whole SDF optical image. The total exposure time for each pointing is 294–300 minutes, except for one pointing of 15 minutes. We ignore the less sensitive regions, so 80% of the SDF optical coverage has uniform K -band data down to the deepest sensitivity (see Fig. 5.1). Previous results using a subset of this data were presented in [Hayashi et al. \(2007\)](#). The data were reduced following standard NIR reduction procedures in IRAF. Photometry and astrometry were carried out using 2MASS objects in the field. The final K -band data reaches a depth of $K = 23.5$ mag (5σ , $2'' \phi$).

5.1.3 Mayall/MOSAIC Data

U -band data were obtained from the KPNO Mayall 4-meter telescope with the Mosaic-1 Imager (with a FoV of $36'$; [Muller et al., 1998](#)) on 2007 Apr 18 and

19. Observing conditions were dark (new moon) with minimal cloud coverage. A series of 25 min exposures was obtained to accumulate 47.4 ks. A standard dithering pattern was followed to provide more uniform imaging across the CCD gaps of about $10''$.

The MSCRED IRAF (version 2.12.2) package was used to reduce the data and produced final mosaic images with a pixel scale of $0''.258$ and an average weighted seeing of $1''.5$ FWHM. The reduction steps followed closely the procedures outlined for the reduction of the NOAO Deep Wide-Field Survey MOSAIC data.

While several [Landolt \(1992\)](#) standard star fields were observed, Landolt's U -band filter differs significantly from the MOSAIC/ U , which makes it difficult to photometrically calibrate the data. Instead, 102 Sloan Digital Sky Survey (SDSS) stars distributed uniformly across the 8 Mosaic-1 CCDs with $u' \lesssim 21$ mag were used. This approach requires a transformation between SDSS u' and MOSAIC/ U , which is obtained by convolving the spectrum of 175 Gunn-Stryker stars with the total system throughput at these wavebands. These stars span $B - V = -0.2$ to 0.8 , and show that the $B - V$ color term is smaller than the scatter ($1\sigma = 0.06$ mag) in the data and that the $U - u'$ color has 0.05 mag scatter. The limiting magnitude within a $3'' \phi$ aperture is 26.8 AB.

5.1.4 *GALEX/NUV* and *FUV* Data

The *GALEX* satellite provides simultaneous *FUV* and *NUV* imaging with a pixel scale of $1''.5$ and a FoV of 1.2° , which encompasses the entire SDF. A total of 161225² seconds (80851 seconds) was obtained in the *NUV*-band (*FUV*-band). The data were processed through the *GALEX* reduction pipeline and stacked accordingly. The spatial resolution and limiting magnitude (within a $3''.39$ radius

²This is deeper than what was used in Chapter 4.

aperture) is $4\farcs5$ and 26.8 mag for the *FUV* and $5\farcs0$ and 27.15 mag for the *NUV*. A fortunate advantage for the *FUV* data is the low sky background (29.35 mag arcsec $^{-2}$).

5.1.5 Mayall/NEWFIRM Data

J-band and *H*-band observations were obtained from NEWFIRM on 2008 May 10–12. Exposures of 60 (*J*) and 20 or 30 (*H*) seconds were taken with a simple five-point dithering pattern to image across the detector gaps ($\approx 35''$ in size) and to avoid latent images of bright sources on the same source. A total of 27.5 ks and 5.5ks were acquired in *J* and *H*. While cloud coverage was minimal, the conditions were non-photometric, and the effective exposure time was approximately 9ks. These NEWFIRM data followed the same reduction procedure that is described in § 3.1.2. The limiting magnitude was determined to be 23.4 mag in a $3'' \phi$ aperture, and the seeing is $\approx 1\farcs2$ (*H*) and $1\farcs3$ (*J*).

5.2 Synthesizing Multi-band Data

A key requirement of this survey is to merge the full multi-wavelength data. However, the spatial resolution varies by a factor of a few for the different instruments, which introduces systematic problems, such as source confusion. For the optical and NIR data, Figure 5.2 illustrates the point spread function from stacking the images of 11 – 24 stars that are bright, unsaturated, and isolated. Simply degrading the best data ($\sim 1''$) to match the poorest resolution ($4 - 5''$ for *GALEX* data) would only hamper the identification of faint galaxies, most of which are at high redshift.

A solution to this problem is a hybrid approach of (1) degrading high-resolution

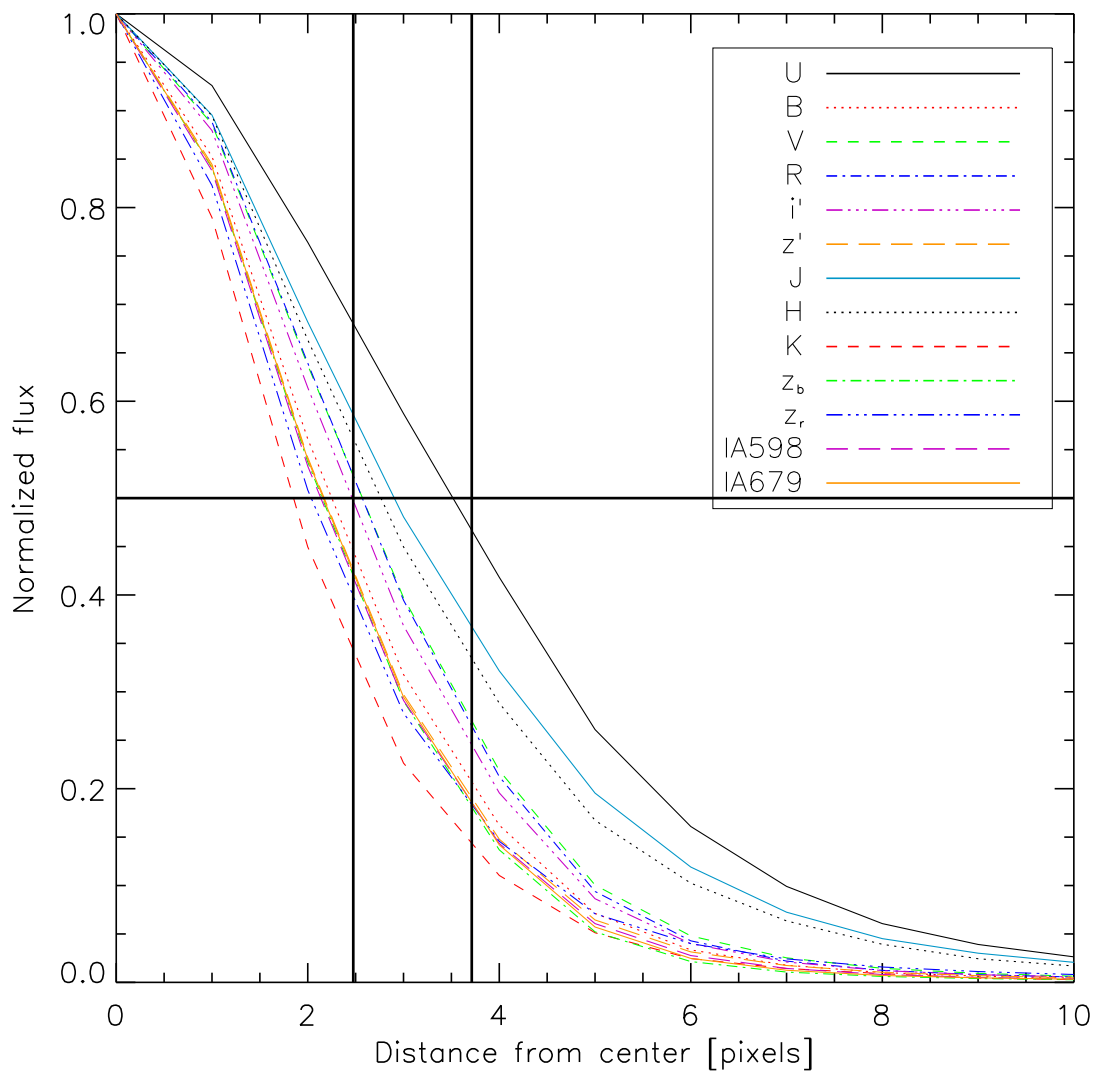


Figure 5.2 – The PSF for the $UBVR_{\text{C}}i'z'z_rJHK$, IA598, and IA679 images. The two vertical lines correspond to $1''.0$ and $1''.5$. The pixel scale is $0''.202$.

images to match a “baseline” spatial resolution that is not significantly different, and (2) using aperture corrections. This method would not greatly compromise sensitivity, and the aperture corrections are reliable, since this work mostly probes compact galaxies (they are faint and at high- z).

We begin by creating an ultra-deep image where multiple broad-band data are combined. This image will then be used to define detected sources (for the photo- z catalogs and the photometrically-selected samples) when running SExtractor in “dual-image” mode. The similarities of the spatial resolution for $BVR_{\text{C}}i'z'z_bz_rK$, IA598, and IA679 allow us to degrade these images to a 1''.1 (hereafter psf-matched). The inclusion of K implies that this ultra-deep mosaic is simultaneously sensitive towards optically- and NIR-selected galaxies. To stack these images, we follow the technique outlined by [Szalay et al. \(1999\)](#). This method adopts a χ^2 weighting approach by determining the probability that a given pixel imaged in N bands is sampling a source or sky. For broad-band image i , the determined mean (μ_i) is removed and then the image is scaled by the sky fluctuation (σ_i):

$$g_i = \frac{f_i - \mu_i}{\sigma_i}, \quad (5.1)$$

where f_i is the measurement (this can be in data numbers, electrons, or fluxes) in image i , and g_i can be viewed as the signal-to-noise ratio for a given pixel. The mean and dispersion that we adopted are provided in Table 5.1. With the psf-matched images normalized to their respective random fluctuation, the ultra-deep image could be statistically defined as the sum of the squares: $y = \sum_{i=1}^N g_i^2$ with $N = 10$. There is a small discrepancy between the y distribution for the ultra-deep image and the predicted probability distribution in the direction that the former peaks at lower y . This is potentially due to sky subtraction for individual images, and the problem is seen at low-S/N values. Since all of the galaxies that

we use in our analyses have high significance (they are bright in multiple bands), this effect is minor. We will pursue a more rigorous understanding of the problem later.

With this ultra-deep χ^2 image, a total of 243964 sources are detected with a minimum of 5 pixels above a $\sqrt{y} = 3.5$, of which 211594 are in the unmasked regions shown in Figure 5.1. This sample is further reduced to 174837 by excluding the region that is poorly sampled at K -band.

This is the largest photometric catalog for the SDF that contains $BVR_{\text{C}}i'z'K$, z_b , z_r , IA598, and IA679. The photometric fluxes are measured in $2''$ aperture with SExtractor, and are corrected for aperture losses that are provided in Table 5.1. To illustrate the advantages of using the multi-band detection method, we compare in Figure 5.3 the number counts in the K -band.

The spatial resolution of the FUV -, NUV -, U -, J -, and H -band images is significantly poorer. We adopt different aperture measurements, and then correct them for their respective loss of flux for a point-like source. U , J , and H used a $3'' \phi$ aperture with measurements from SExtractor while the $GALEX$ bands used a $6''.8 \phi$ aperture. For the $GALEX$ data, we did not match the images to the Suprime-Cam pixel scale. Instead, we used DAOPHOT to measure the fluxes at known positions, which follows the identical procedure discussed in Chapter 4.

One of the biggest concerns for the FUV and NUV is source confusion, given their poor PSF. The best solution is PSF-fitting and removal. This would consist of two stages: fitting and removing the brighter sources with the PSF, and then for faint sources, aperture photometry can be done on the image with the sources removed. Due to time constraints, we take a simpler approach to identify and flag $GALEX$ measurements that are affected by confusion.

First, we consider a set of source positions. We decide if the central position

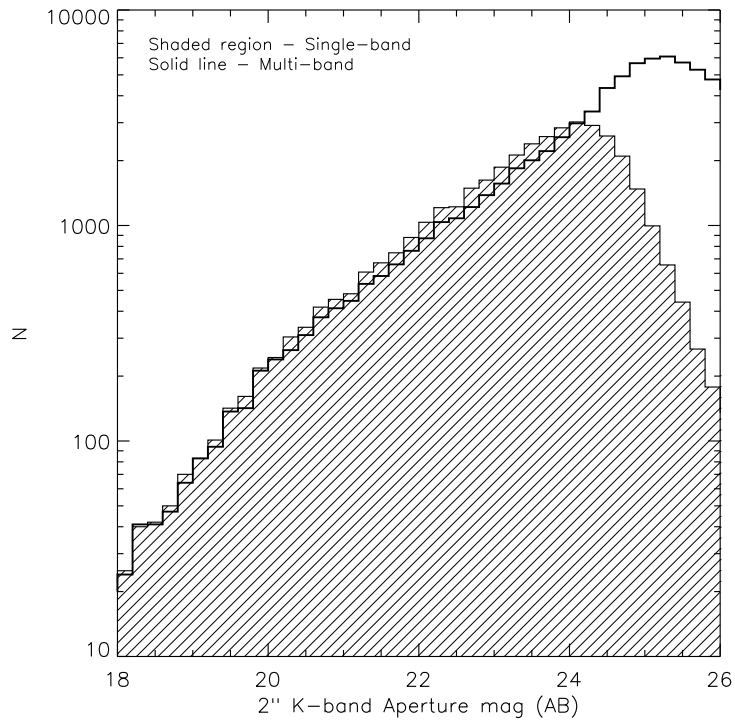


Figure 5.3 – The distribution of K -band $2'' \phi$ magnitude. Sources extracted using only the K -band are shown by the shaded region while the thick black line shows the sources selected from the synthesis of multiple bands. Combining data from multiple wavebands allow for us to identify more K -faint galaxies.

for a source should be flagged as being associated with an object detection using an object mask image. For the situation where the central position gives the null result, we ask how many pixels (N_{pix}) in a $6''8$ aperture have an object flag. If N_{pix} is at least 4, we then flag its measurements as “confusion affected.” With this approach, 13192 (*FUV*) and 31967 (*NUV*) of 243964 measurements were flagged as confusion-affected. For photo- z and SED modelling that are discussed in § 5.3, measurements in these wavebands are ignored for confusion-affected sources.

5.2.1 The Identification of Stars

To identify foreground stars we use two techniques. First, stars can be easily identified in the NIR, since this measures the Rayleigh-Jeans tail, and forms a stellar locus in color space distinct from galaxies. Studies that have selected BzK galaxies also distinguish stars by their $z' - K$ colors (see e.g., Quadri et al., 2007). For sources detected in the K -band, we classify stars with $z' - K \leq 0.455(B - z') - 0.773$ and $z' - K \leq 0.235(B - z') - 0.279$. This method classified 1603 K -band sources over 718.7 arcmin².

For sources that are undetected in K (or lack K data), we use the technique (called the Δ method) that is described in § 4.3.1. The idea is to first consider potential candidates as stars based on how close they are to being point-like. They were given a number between 0 and 10 to rank how point-like they are (10 being most point-like). However, unresolved galaxies might also be very compact. Therefore, to distinguish these galaxies from stars, we then calculate their deviation from the stellar locus in the $B - V$, $V - R_C$, and $R_C - z'$ colors. This deviation (Δ) from the locus in a multi-color space is certainly affected by photometric scatter for faint sources, so we limit stellar identification with the Δ method to $V = 25.0$. Δ values for 67185 sources are illustrated in Figure 5.4a,

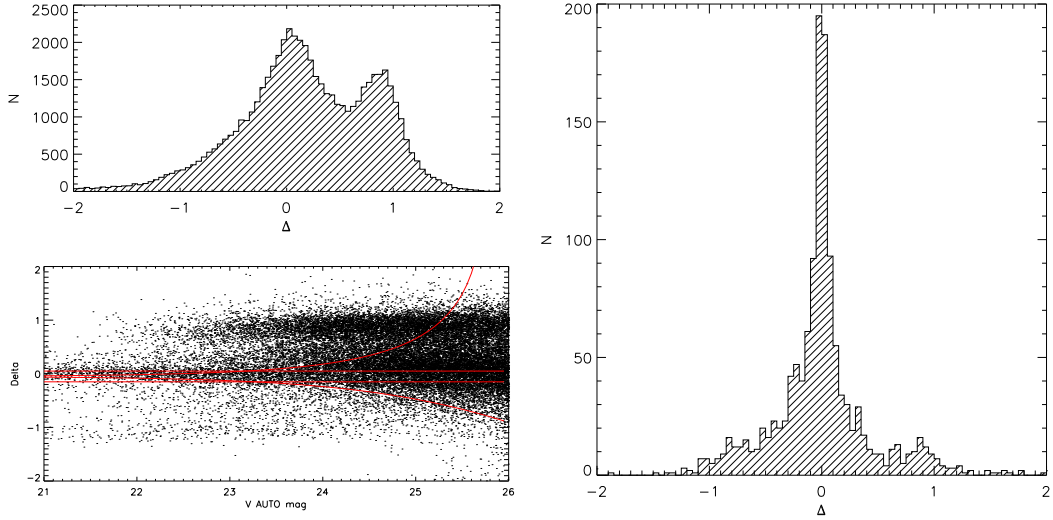


Figure 5.4 – The deviation (Δ) in magnitudes from the stellar locus in a 3-color space. (a) Distribution of Δ is shown for 67185 with point-like rank of 4 – 10 in the top panel and against V in the bottom panel. The red curves correspond to the $\pm 3\sigma$ fluctuations expected from a combination of the B , V , R_C , and z' depth. (b) The distribution of Δ for 1603 K -band selected stellar sources based on their $B - z'$ and $z' - K$ colors. This shows the majority of stellar sources have $\Delta \approx 0$.

and show a strong peak at $\Delta \approx 0$ (the secondary peak is for low- z galaxies). One of the best tests of this method is to compare with the sample identified from $B - z'$ and $z' - K$ colors. The distribution of Δ for the 1603 K -band selected stars is plotted in Figure 5.4b and supports the Δ method. Among the K -band stellar sources, 82% (1315/1603) of them have point-like rank values of 4 and higher, with the majority (1017/1603) at 5. Thus, we classify K -band undetected sources with rank values of 4 and higher, $V < 25.0$, and Δ values within 3σ of the expected fluctuations in Δ -magnitude relation as stellar sources. This yielded 1167 additional sources as stars for a total of 2770 stellar sources. We removed these stellar sources from our full catalog and report stellar contamination for individual galaxy selection samples below.

5.3 Photometric Redshifts and SED Modelling

5.3.1 Photometric Redshifts

For this survey, the number of spectroscopic redshifts is limited ($N \sim 1000$), so well-calibrated photometric redshifts are used. These z_{phot} are determined from 15 bands, FUV , NUV , $UBVR_Ci'z'z_bz_rJHK$, IA598, and IA679, using the Easy and Accurate z_{phot} from Yale (EAZY; [Brammer et al., 2008](#)) package. This photo- z code has the following advantages: (1) it is easy to use and fast, (2) it handles input measurements in fluxes rather than magnitudes, which is crucial for non-detections (see below), (3) it can easily ignore certain wavebands where data should be excluded (e.g., sources in the less sensitive K -band regions), (4) the full redshift probability distribution, $P(z)$, for an individual galaxy is determined, and (5) it has been well-calibrated against existing optical to NIR data, to $\sigma_z/(1+z) \approx 0.03$.

Where a source is below the 1σ detection threshold in a given wave-band, the 0.5σ flux value is adopted with measurement uncertainties of 0.5σ . This value has the aperture correction included, to represent a total upper 1σ limit flux. We have considered different criteria for detection/non-detection by also adopting 2σ and 3σ thresholds, but found that the accuracy of photometric redshift (see below for mathematical definition) improved by as much as a factor of 2 when adopting a 1σ threshold. We concluded that for high- z galaxies, the UV flux is extremely sensitive to redshift and a $z \sim 2$ galaxy with $R \sim 25$ is expected to be well below the 2 or 3σ threshold. Therefore, a 1σ threshold is more appropriate. Throughout the paper, redshift distribution is described by $N(z)$, which uses the peak of the probability redshift distribution $P(z)$. We have compared $N(z)$ for a subset of galaxies at high redshift to the distribution made by adding the full

redshift distribution for each galaxy. We find that the two distributions agree to within $\Delta z = 0.1$, indicating that using the peak of $P(z)$ provides a good first-order solution.

Illustrated in Figure 5.3.1 is a comparison of photometric and spectroscopic redshifts for 420 sources using FUV , NUV , $UBVR_Ci'z'z_bz_rJK$, IA598, and IA679 (15 bands). The spectroscopy was obtain with several instruments from Subaru, MMT, and Keck. The inclusion of the NUV improved photo- z accuracy by 17% compared to $UBVR_Ci'z'z_bz_rJK$, IA598, and IA679. H -band and FUV measurements provided a further $\sim 10\%$ improvement. This illustrates that photometric redshifts derived from 15 bands yield accuracy of 2.4% out to $z \approx 1.8$.

Another analysis that supports the accuracy of the photo- z sample is a comparison with sources identified with narrow-band filters (see Chapter 2). Among 5029 NB excess emitters between $z = 0.24$ and $z = 1.47$, 4568 have photo- z estimates. This is a factor of 10 gain over the number of spectra that we had previously used to compare z_{phot} with z_{spec} . We estimate the median z_{phot} and find good to reasonable agreement: $z_{\text{phot}} = 0.24 \pm 0.03$ for $z \approx 0.24$ $H\alpha$ emitters, $z_{\text{phot}} = 0.37 \pm 0.01$ for $z \approx 0.40$ $H\alpha$ emitters, $z_{\text{phot}} = 0.37 \pm 0.01$ for $z \approx 0.40$ [O III] emitters, $z_{\text{phot}} = 0.43 \approx 0.05$ for $z \approx 0.42$ [O III] emitters, $z_{\text{phot}} = 0.60 \pm 0.02$ for $z \approx 0.63$ [O III] emitters, $z_{\text{phot}} = 0.76 \pm 0.02$ for $z \approx 0.84$ [O III] emitters, $z_{\text{phot}} = 0.78 \pm 0.09$ for $z \approx 0.89$ [O II] emitters, $z_{\text{phot}} = 0.83 \pm 0.08$ for $z \approx 0.91$ [O II] emitters, $z_{\text{phot}} = 1.05 \pm 0.29$ for $z \approx 1.18$ [O II] emitters, and $z_{\text{phot}} = 1.51 \pm 0.14$ for $z \approx 1.47$ [O II] emitters. These photo- z were derived without the inclusion of narrow-band data, which strongly support (1) our ability (in Chapter 2) to distinguish $H\alpha$, [O III], and [O II] emitters using simple two-color selection, and (2) the z_{phot} derived for SDF galaxies are reliable. The offsets seen for the higher redshift samples can be due to a couple of reasons. For example, extremely strong

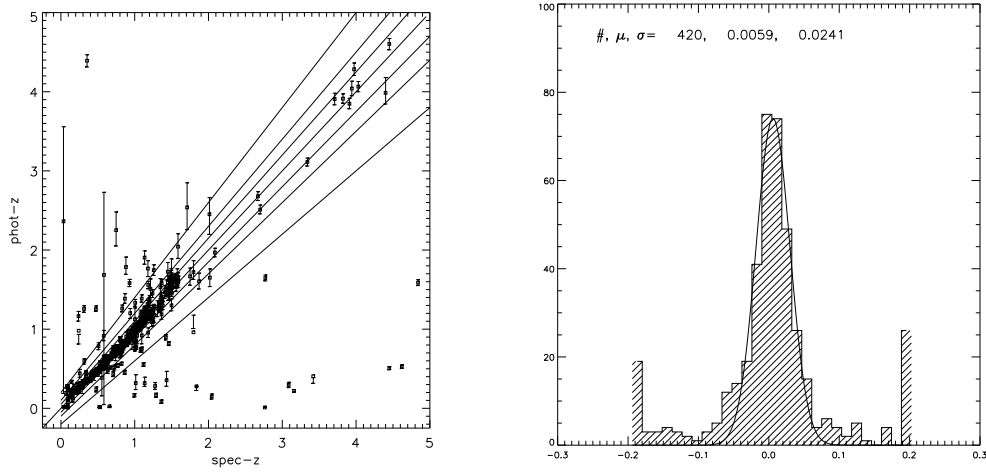


Figure 5.5 – Comparison of photometric and spectroscopic redshifts. A total of 420 spectroscopic sources have association with the 5BK3 σ . The photometric redshifts are derived from 15-band photometry and show accuracy of $(z_{\text{phot}} - z_{\text{spec}})/(1 + z_{\text{spec}}) = 0.024$ with a negligible (less than 1%) systematic offset. We find similar results using a smaller sample that have 5 σ detection in K.

emission lines can affect the broad-band magnitude, thus producing poorer fits (Ilbert et al., 2009). A similar problem is seen for the photo- z used in Chapter 3, with a systematic offset towards lower redshift when compared against spec- z . The future inclusion of NB data could mitigate this problem in the SDF sample.

Another illustration of the reliability of the z_{phot} is shown in Figure 5.3.1, where half of the upper 68% minus the lower 68% confidences in redshift are shown versus photometric redshift. We refer to this as $\Delta z_{68} \equiv \frac{(z_{+68} - z_{-68})/2}{1+z_{\text{phot}}}$ and use it as an indicator of photometric redshift accuracy. As expected, $z \approx 1.8 - 2.8$ suffers from larger photometric redshift errors due to lower sensitivity in the NIR, and in most cases, non detection in the rest-UV wave-bands. The median and standard deviation of Δz_{68} are reported in Table 5.2 and are shown in Figure 5.3.1 in red.

We did a control test of excluding K -band measurements (our deepest NIR

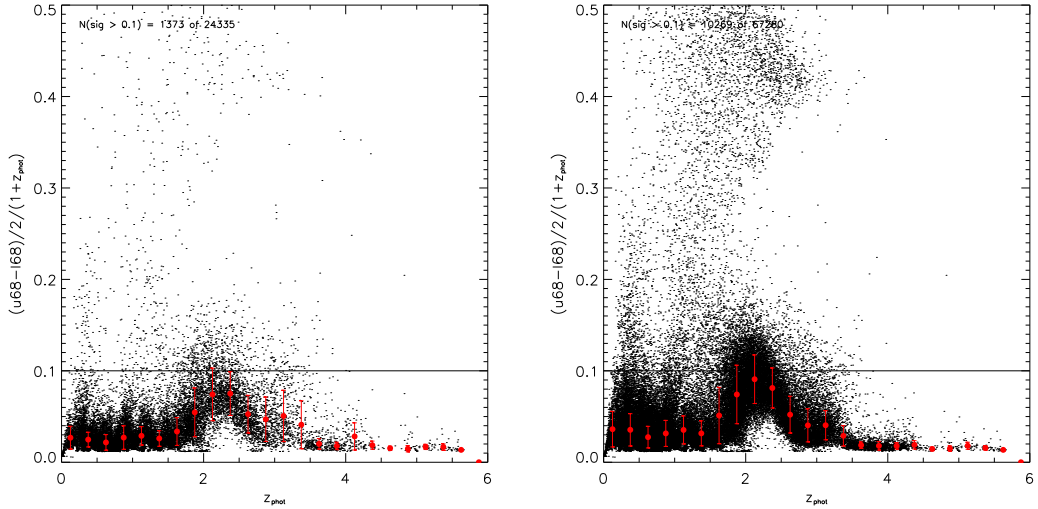


Figure 5.6 – An illustration of the photometric redshift uncertainties for the 5BK3 σ (left) and 5B5 σ (right) samples. The x -axes show the best-fitting z_{phot} while y -axes show Δz_{68} , the half-width of $P(z)$ at the 68% confidence level normalized by $1+z_{\text{phot}}$. The horizontal lines correspond to the adopted 10% accuracy per $(1+z_{\text{phot}})$ that is adopted to exclude less accurate photo- z estimates.

data) for a set of 24,000 K -band galaxies detected at 3σ in at least 5 bands. We find that the z_{phot} errors are significantly worse by 20% (mostly at $z > 1$) , that the number of outliers (see below) doubles, and the greatest ($\Delta z_{\text{phot}} \approx 0.4$) systematic offsets occur at $z_{\text{phot}} = 1.3 - 2.2$ (see Fig. 5.7). However, for the majority (76%) of sources, the photometric redshift without K is good to within $\Delta z = \pm 0.05$, particularly at $z_{\text{phot}} < 1.2$. Therefore, we generate two photo- z samples consisting of bright sources with K -band data and those that lack it. The first sample requires a minimum of 5-band detection at the 3σ limit (hereafter 5BK3 σ) with one of the bands being K . The second sample consists of at least 5-band detection (without any K restrictions) at the 5σ level (hereafter 5B5 σ). These samples are 22853 and 64691 in size (after stellar removal). Of course, not all of these sources are detected in all 15 bands since high- z sources would be undetected in some bands, such as the NUV . To illustrate, we summarize for

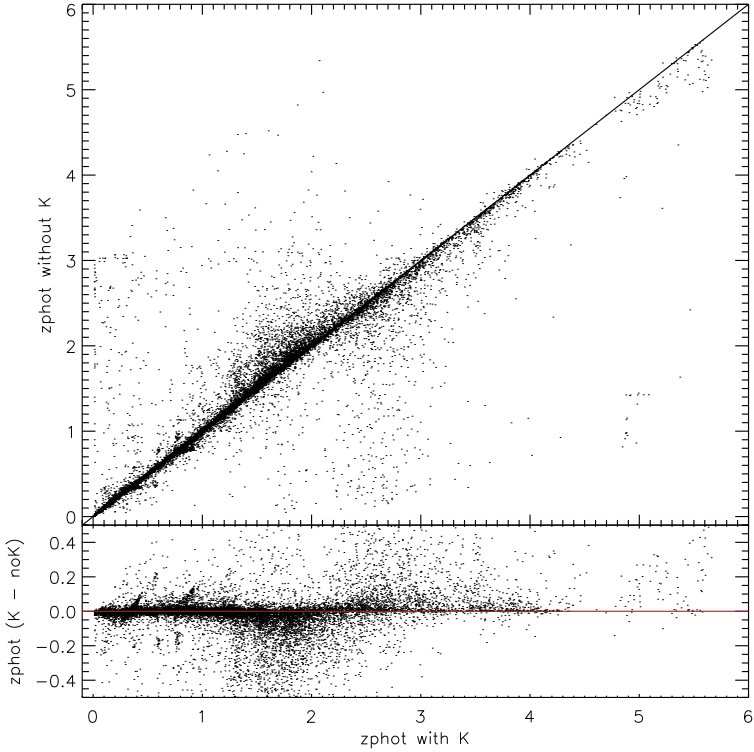


Figure 5.7 – A comparison of z_{phot} with and without K measurements for sources that are detected in the K -band. This shows good agreement over most redshift except for $z = 1.3 - 2.2$.

the 5BK3 σ sample, the mixture of detections that we have across all 15 bands in Table B.1.

We exclude photo- z measurements that are unreliable at the 10% level based on Δz_{68} . This yielded a total sample of 54724 sources. Note that some of the sources in the 5BK3 σ sample are not in the 5B5 σ catalog given the difference in their sensitivity criteria (3 versus 5 σ). The photo- z distribution for both catalogs are illustrated in Figure 5.8 where 24230 sources are identified to be at $z_{\text{phot}} = 1 - 3$ while 26303 are located below $z = 1$ and 4191 are above $z = 3$. We will return later to this sample in § 5.5.4, when we discuss a census derived from photometric selection techniques.

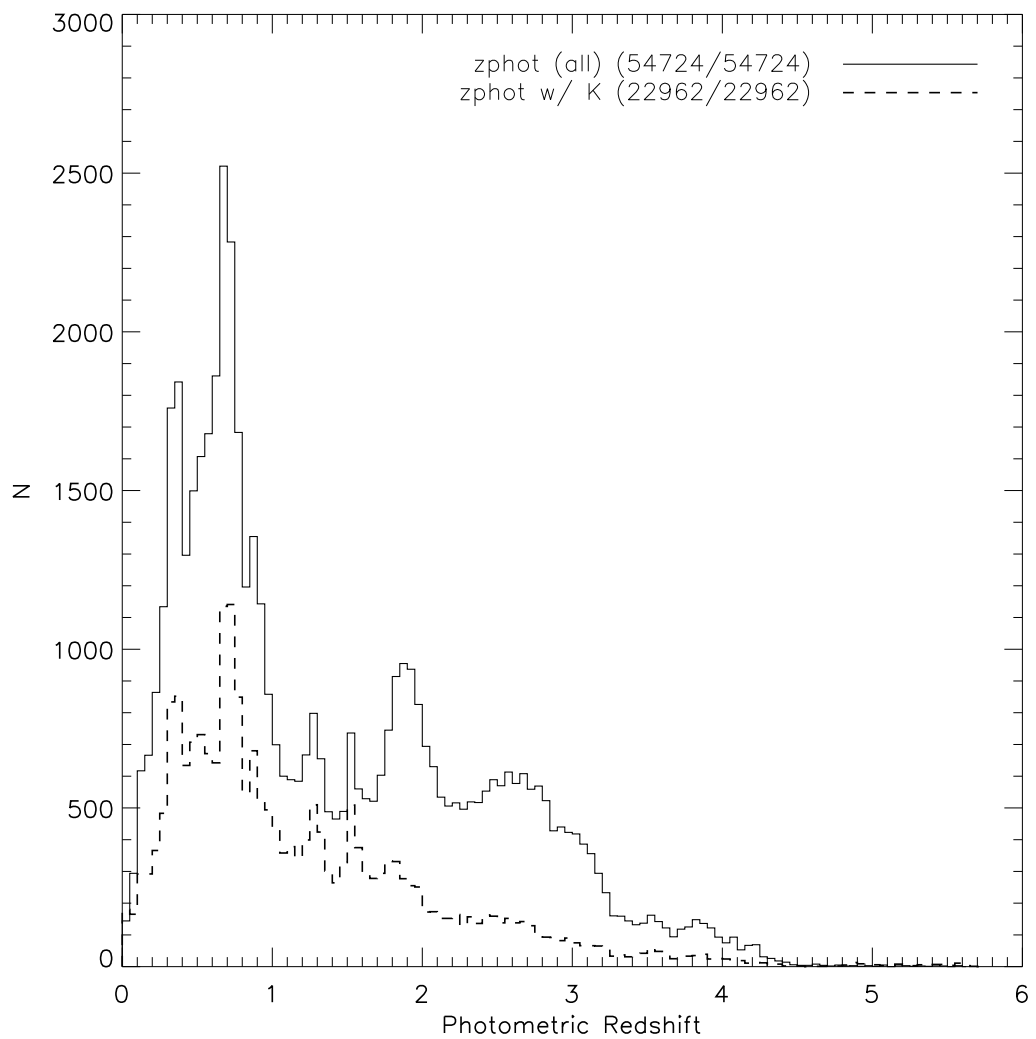


Figure 5.8 – The z_{phot} distribution for the combination of the 5BK3 σ and 5B5 σ samples (solid line) and only the 5BK3 σ sample (dashed line). Sources classified as stars were removed and we excluded objects with $\Delta z_{68} > 0.1$.

Table 5.2. Summary of Photometric Redshift Uncertainties

z	5BK3 σ			5B5 σ		
	N	Median ^a	σ ^b	N	Median ^a	σ ^b
0.00–0.25	1313	0.027	0.012	3181	0.036	0.019
0.25–0.50	3583	0.025	0.008	8764	0.035	0.018
0.50–0.75	4343	0.022	0.009	10426	0.027	0.012
0.75–1.00	3123	0.027	0.013	6732	0.032	0.014
1.00–1.25	1979	0.029	0.010	3563	0.035	0.015
1.25–1.50	1912	0.026	0.009	3306	0.032	0.014
1.50–1.75	1818	0.034	0.015	3581	0.051	0.031
1.75–2.00	1597	0.055	0.027	5772	0.074	0.032
2.00–2.25	1000	0.074	0.029	4693	0.091	0.027
2.25–2.50	886	0.075	0.024	3410	0.081	0.022
2.50–2.75	756	0.053	0.021	3173	0.052	0.020
2.75–3.00	498	0.047	0.024	2536	0.040	0.018
3.00–3.25	354	0.051	0.028	1734	0.040	0.016
3.25–3.50	202	0.041	0.026	762	0.029	0.011
3.50–3.75	213	0.020	0.006	631	0.019	0.003
3.75–4.00	160	0.018	0.004	612	0.018	0.005
4.00–4.25	90	0.028	0.015	359	0.018	0.004
4.25–4.50	30	0.019	0.004	115	0.019	0.005
4.50–4.75	4	0.015	0.002	26	0.015	0.002
4.75–5.00	40	0.015	0.003	43	0.015	0.003
5.00–5.25	25	0.017	0.003	35	0.018	0.004
5.25–5.50	27	0.017	0.004	27	0.016	0.002
5.50–5.75	22	0.014	0.001	21	0.014	0.001

^aThe median value of the 68% photometric redshift uncertainty: $\Delta z_{68} \equiv (z_{+68} - z_{-68})/2/(1 + z_{\text{phot}})$.

^bThe standard deviation associated with Δz_{68} .

Because of the complicated selection for the photo- z samples, one concern is whether derived photo- z is representative of the entire population of galaxies. In Figures 5.9, we show the distribution of $U - B$, $B - V$, $i' - z'$, and $z' - K'$ colors for the multi-band selected sample and for those with z_{phot} determination. We find the best agreement at NIR wavebands and relatively good agreement in optical colors. Therefore, the photo- z samples that we use span a range of galaxy properties given their colors. The obvious limit is that lower mass galaxies are not probed given the current sensitivity limits of our data. This sensitivity will certainly vary with redshift, as sources of a given luminosity become dimmer.

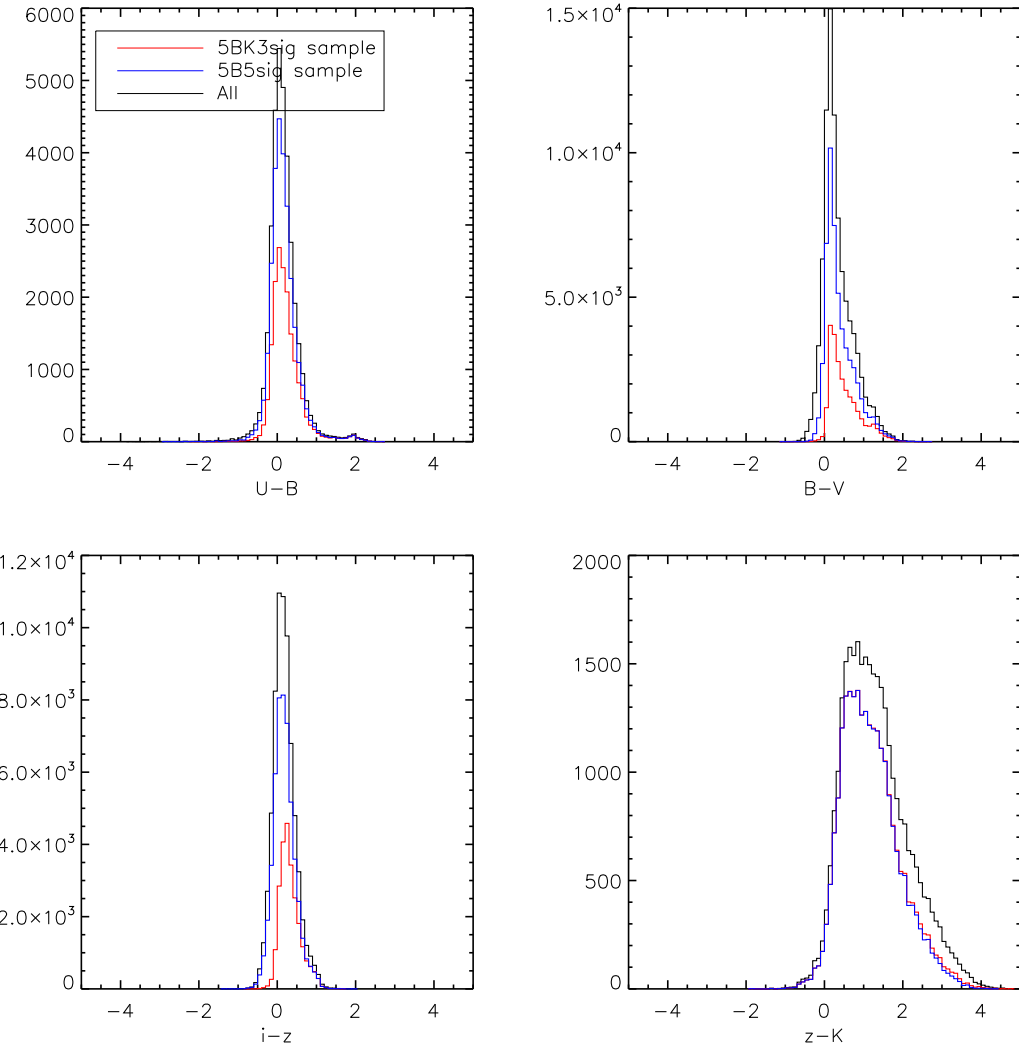


Figure 5.9 – The $U - B$ (upper left), $B - V$ (upper right), $i' - z'$ (lower left), and $z' - K'$ (lower right) colors for the photometric samples. The full sample (“All”) is shown by the black lines while the $5BK3\sigma$ and $5B5\sigma$ samples are shown by the red and blue lines. This shows that the population of galaxies that we have photo- z for span a similar range of colors as all the sources.

5.3.2 SED Modelling

To determine physical properties of our galaxies, the Fitting and Assessment of Synthetic Templates (FAST; [Kriek et al., 2009](#)) code is used to model the SED. Much like other SED modelling codes, FAST determines the best spectral synthesis model by minimizing χ^2 . The spectral synthesis models are generated from the [Bruzual & Charlot \(2003\)](#) or [Maraston \(2005\)](#) code,⁸ and consist of a star formation history that follows an exponential decay (i.e., a τ model). For simplicity, we choose $\log(\tau/\text{yr}) = 8.0, 9.0,$ and 10.0 . A larger range of τ models could have been used, but it would be more computationally intensive. Furthermore, the accuracy of distinguishing a $\log(\tau/\text{yr}) = 8.0$ from a $\log(\tau/\text{yr}) = 8.5$, for example, is difficult given the use of broad-band data and the number of degrees of freedom. These τ values were selected to span a bursty, intermediate, and roughly constant star formation history. In addition to the star formation history, the grid of models spans a range of stellar ages, $\log(\text{age}/\text{yr})$, between 7.0 and up to the age of the universe at a given redshift (increments of 0.1 dex), and dust extinction with $A_V = 0.0 - 3.0$ mag with 0.1 mag increments. FAST adopts [Calzetti et al. \(2000\)](#) for dust extinction corrections, and we only use the solar metallicity models and assume a Salpeter IMF.

Aside from these models, EAZY's z_{phot} , the photometric measurements, and the total system throughput for each filter (the same as those used in EAZY) are provided as inputs into the code and the best fitting stellar mass, stellar age, dust content, instantaneous SFR, and τ values are determined. The [Maraston \(2005\)](#) models include recent results on thermal pulsating (TP) AGB stars. On average, the [Maraston \(2005\)](#) models yield a factor of $\approx 0.5 - 1.3$ in stellar mass compared to the [Bruzual & Charlot \(2003\)](#) models when adopting the same IMF

⁸FAST is currently the only code that includes both these models, which minimizes systematic problems of using a secondary SED modelling code.

and metallicity. This ratio of stellar masses shows weak evolution with redshift, which is to be expected, since TB-AGB stars become important for young stellar populations, which is often the case at higher redshifts.

5.4 Photometric Techniques to Identify $z = 1 - 3$ Galaxies

To obtain a census of redshift desert galaxies, the following populations are selected: BX, BM, BzK (star-forming and passive), and LBG. Since the J -band data are shallower than the K , our ability to identify faint DRGs is poor. The DRG sample alone is ~ 200 in size for J -band flux $\geq 3\sigma$, so we do not discuss the is in the census. We refer readers to [Lane et al. \(2007\)](#) where a 0.5 deg^2 NIR survey was conducted and a large sample of bright ($K < 21.2 \text{ AB}$) DRGs was obtained and compared against other NIR selected galaxies. A summary of the sizes of these galaxy population selection samples is provided in Table [5.3](#).

5.4.1 The BX and BM Selection

[Steidel et al. \(2004\)](#) defined BX and BM galaxies by two polygons in the $U_n - G/G - R$ color space. For BX, it is

$$G - R \geq -0.2, \quad (5.2)$$

$$U_n - G \geq G - R + 0.2, \quad (5.3)$$

$$G - R \leq 0.2(U_n - G) + 0.4, \text{ and} \quad (5.4)$$

$$U_n - G \leq G - R + 1.0. \quad (5.5)$$

The BM selection consists of

$$G - R \geq -0.2, \quad (5.6)$$

$$U_n - G \geq G - R - 0.1, \quad (5.7)$$

Table 5.3. Summary of Photometric Selection Samples

Method	Eqn/Sections	N	$N_{z_{\text{phot}}}$	\bar{z}_{phot}	$z_{\text{phot}} < 1.0$	$z_{\text{phot}} < 0.5$
BX $R_C \leq 25.5$	5.12–5.15	5585	5082	2.271 ± 0.40	1718	1649
BX $R_C \leq 26.0$	5.12–5.15	8004	6934	2.249 ± 0.42	2084	1946
BM $R_C \leq 25.5$	5.16–5.20	6408	5952	1.598 ± 0.37	1363	1022
BM $R_C \leq 26.0$	5.16–5.20	8584	7542	1.609 ± 0.41	1781	1234
sBzK	§ 5.4.2	9796	8637	1.911 ± 0.64	1270	679
pBzK	§ 5.4.2	315	298	1.581 ± 0.51	7	0
$z \sim 3$ LBG $R_C \leq 25.5$	5.21–5.23	2375	2168	2.982 ± 0.46	424	400
$z \sim 3$ LBG $R_C \leq 26.0$	5.21–5.23	3823	3478	2.937 ± 0.44	572	536
$z \sim 2$ LBG $V \leq 25.4$	4.1–4.3	5563	5431	1.957 ± 0.40	87	63
$z \sim 2$ LBG $V \leq 26.0$	4.1–4.3	7999	7645	1.967 ± 0.39	115	66
$z \sim 1$ LBG	5.24–5.26	556	555	0.838 ± 0.13
Total (Shallow) ^{a,b}	...	30042	27568	...	4869	3813
Unique (Shallow) ^{a,b,d}	...	19434	17347	...	4241	3299
Total (Faint) ^{a,c}	...	38521	34534	...	5829	4461
Unique (Faint) ^{a,c,d}	...	25173	21929	...	5139	3910

^aThe combination of BX, BM, U -dropout ($z \sim 3$), sBzK, pBzK, and NUV -dropout ($z \sim 2$) samples.

^bBXs, BMs, and U -dropouts selected with $R_C \leq 25.5$, and NUV -dropouts selected with $V \leq 25.4$.

^cBXs, BMs, and U -dropouts selected with $R_C \leq 26.0$, and NUV -dropouts selected with $V \leq 26.0$.

^d“Unique” refers to the sample which accounts for overlap between the photometric selection samples.

$$G - \mathcal{R} \leq 0.2(U_n - G) + 0.4, \text{ and} \quad (5.8)$$

$$U_n - G \leq G - \mathcal{R} + 0.2. \quad (5.9)$$

However, the $U_nG\mathcal{R}$ system differs from existing filters of similar wavelengths for the SDF, so a transformation is necessary between $UBVR_Ci'$ and $U_nG\mathcal{R}$ (see Figure 5.10). The transformation is derived by using a [Bruzual & Charlot \(2003\)](#) spectral synthesis model representative of star-forming galaxies.⁹ A grid of the model is defined by redshifting the synthetic spectra between $z = 0.85$ and $z = 3.8$ and reddened it with a [Calzetti et al. \(2000\)](#) law with $E(B - V) = 0.0 - 0.4$ to produce mock galaxies. We also include H I IGM absorption following [Madau \(1995\)](#). Then magnitudes in the U_n , G , \mathcal{R} , U , B , V , R_C , and i' filters are determined for these 540 mock galaxies.¹⁰ Among the artificial galaxies that

⁹This model is identical that used in [Ly et al. \(2009\)](#) and is similar to [Steidel et al. \(1999\)](#).

¹⁰The $U_nG\mathcal{R}$ filter profiles were provided by Alice Shapley.

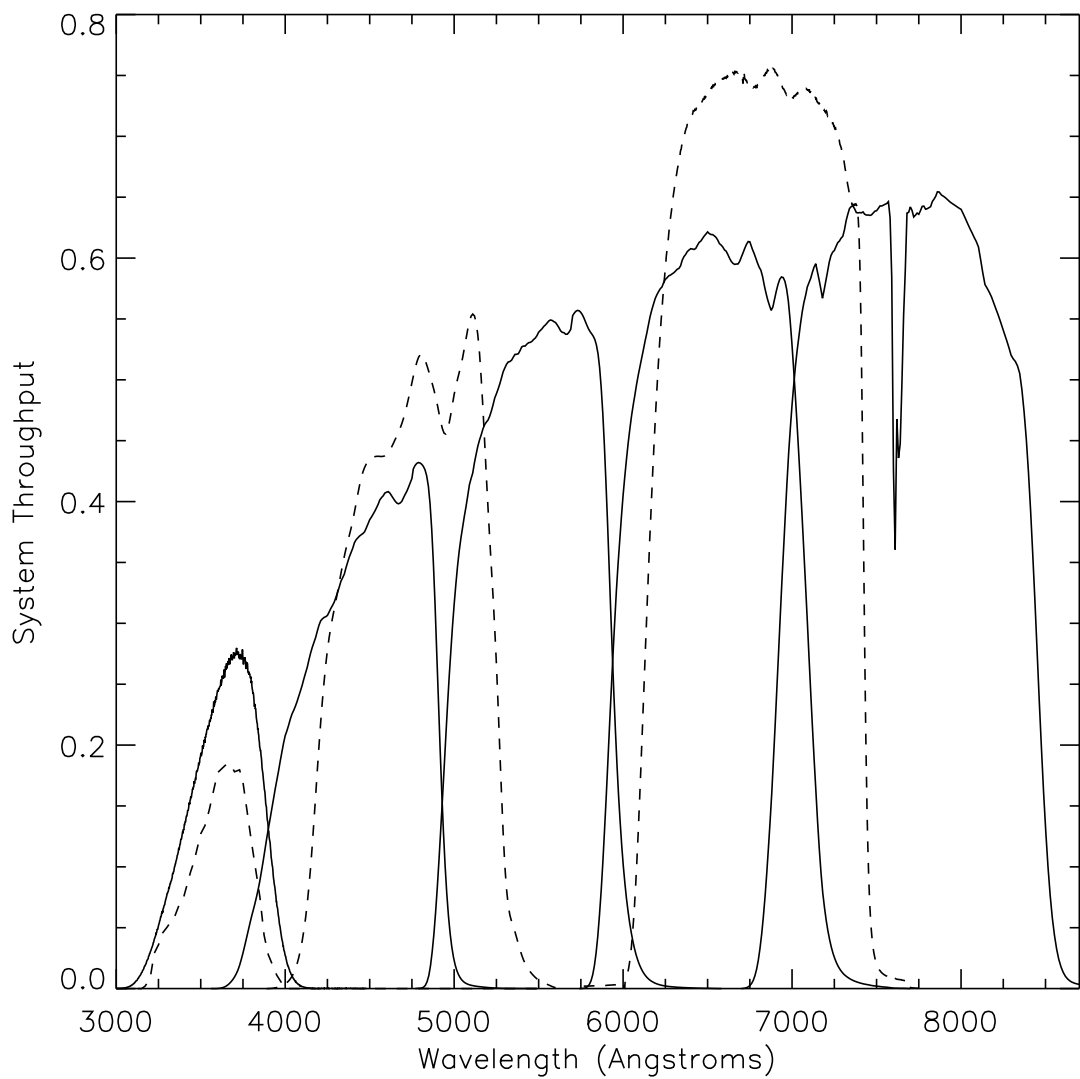


Figure 5.10 – The total system throughput for two different sets of filters. The SDF $UBVR_Ci'$ filters are shown as solid lines while the dashed lines are for the U_nGR filters.

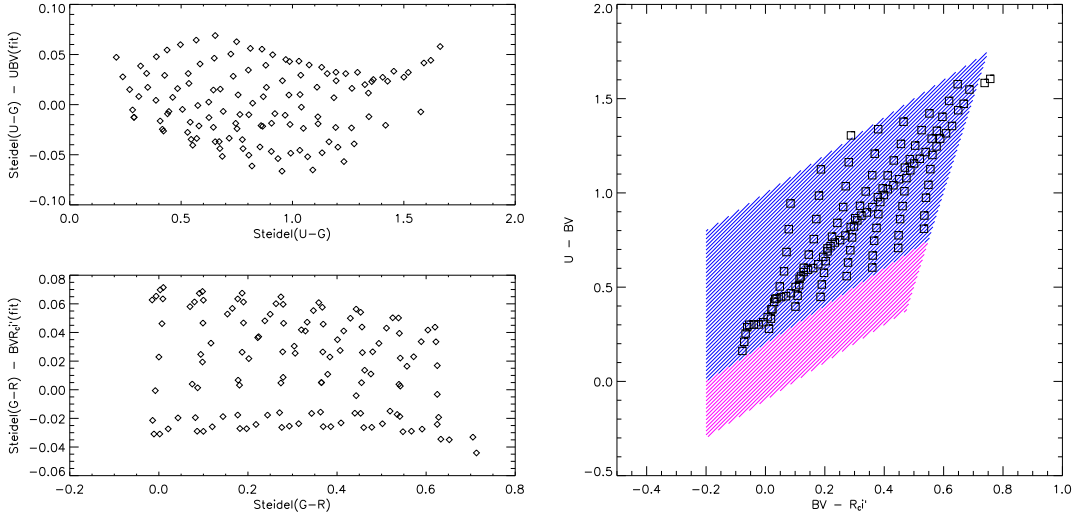


Figure 5.11 – (left) The residuals in $U_n - G$ and $G - \mathcal{R}$ colors for BX sources by adopting Equations 5.10 and 5.11 with $x_1 = 0.3135$ and $x_2 = 0.2073$. (right) The $U - BV$ and $BV - R_{\mathcal{C}}i'$ colors for BX sources overlayed on the $U_nG\mathcal{R}$ BX and BM selection region. These plots indicate a proper transformation has been made to select BX galaxies.

meet the original BX or BM selection, a least-squares fitting approach is used to represent the G -band with a combination of B and V and the \mathcal{R} -band as $R_{\mathcal{C}}$ and i' such that $U_n - G = U - BV$ and $G - \mathcal{R} = BV - R_{\mathcal{C}}i'$. Where

$$BV = -2.5 \log \left[\frac{x_1 f_B + (1 - x_1) f_V}{3630 \text{ } \mu\text{Jy}} \right], \text{ and} \quad (5.10)$$

$$R_{\mathcal{C}}i' = -2.5 \log \left[\frac{x_2 f_R + (1 - x_2) f_{i'}}{3630 \text{ } \mu\text{Jy}} \right]. \quad (5.11)$$

Here, f_X is the flux density per unit frequency ($\text{erg s}^{-1} \text{ cm}^{-2} \text{ Hz}^{-1}$) in band “ X .” An illustration of this technique is shown in Figure 5.11 for BX galaxies.

While different values of x_1 and x_2 can be adopted for the BX ($x_1 = 0.3135$ and $x_2 = 0.2073$) and BM ($x_1 = 0.4907$ and $x_2 = 0.7902$) selections, the net result is that some BX galaxies would also meet the BM selection and vice versa. This is because the $U - G$ and $G - \mathcal{R}$ colors spanned by two population samples are wide enough that they shift the transformation values, x_1 and x_2 . However,

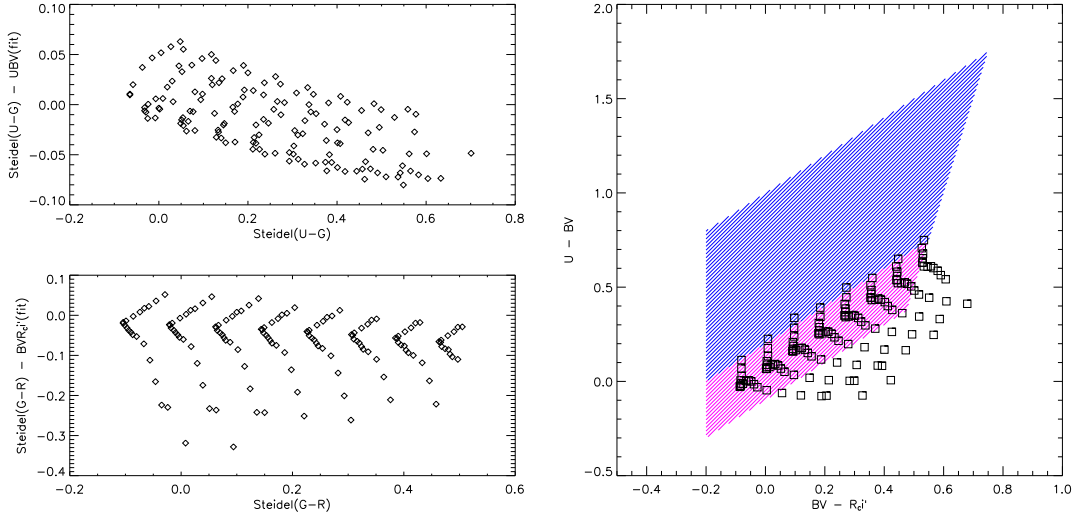


Figure 5.12 – Similar to Figure 5.11 but illustrated here for BM galaxies when adopting Equations 5.10 and 5.11 with $x_1 = 0.3135$ and $x_2 = 0.2073$. These plots indicate a reasonable transformation for BM when using the BX transformation except for $z \sim 1$ BM galaxies.

the BX and BM galaxies occupy distinct regions in the default U_nGR plane, so only *one* transformation set can be used to simultaneously identify the two galaxy populations. Adopting the BX transformation works well for the BX and U -dropouts; however, it has trouble reproducing the colors of $z \sim 1$ BM galaxies (see Figure 5.12). Likewise, the BM transformation produces noticeable residuals for the reddest $U_n - G$ objects. As a compromise, we decided to adopt the BX x_1 - x_2 transformation, since it occupies the region between the BM and U -dropout techniques. With this approach, the BX selection parallelogram remains roughly the same, while the BM and U -dropout selection regions are modified to capture the model galaxies that are identified as BM and U -dropouts in the U_nGR space. The only modification that we make to the BX transformation is to move the lower bound up by 0.03 mag in $U - BV$ color:

$$BV - R_{Ci'} \geq -0.2, \quad (5.12)$$

$$U - BV \geq BV - R_C i' + 0.23, \quad (5.13)$$

$$BV - R_C i' \leq 0.2(U - BV) + 0.4, \text{ and} \quad (5.14)$$

$$U - BV \leq BV - R_C i' + 1.0. \quad (5.15)$$

It should be noted that the BM transformation did change significantly when adopting the BX transformation (see Fig. 5.12). It now spans a wider range in $BV - R_C i'$ color, so more $z < 1$ sources could potentially contaminate our BM sample at the cost of identifying $z > 1$ BM galaxies. As a compromise, we choose not to extend the selection region to encompass the lowest-redshift BM galaxies, in order to exclude some low- z interlopers. While this may sound alarming, it is not surprising. Since the original BM selection spanned a small range of $G - R$ color for a given $U_n - G$ color that photometric scatter can lead to missed faint $z > 1$ galaxies and suffer from low- z interlopers. The final selection that we use for BM galaxies is:

$$BV - R_C i' \geq -0.2, \quad (5.16)$$

$$U - BV \geq -0.1, \quad (5.17)$$

$$BV - R_C i' \leq 0.382(U - BV) + 0.853, \quad (5.18)$$

$$BV - R_C i' \leq 0.70(U - BV) + 0.280, \text{ and} \quad (5.19)$$

$$U - BV \geq BV - R_C i' + 0.23. \quad (5.20)$$

The $U - BV$ and $BV - R_C i'$ colors for SDF galaxies are shown in Figure 5.13 for the selection of BX and BM galaxies. We defined a non-detection in the U -band when the U -band falls below the 1σ limit. This follows what was adopted by Steidel et al. (2003) in the selection of U_n -dropouts and likewise, BX and BM galaxies. In total, 6280 BX (5585 after stellar removal) and 6776 BM (6408 after stellar removal) galaxies are identified with $R_C \leq 25.5$. In § 5.5.2, we also discuss the BX and BM samples with $R \leq 26.0$, which consist of 8699 BX (8004

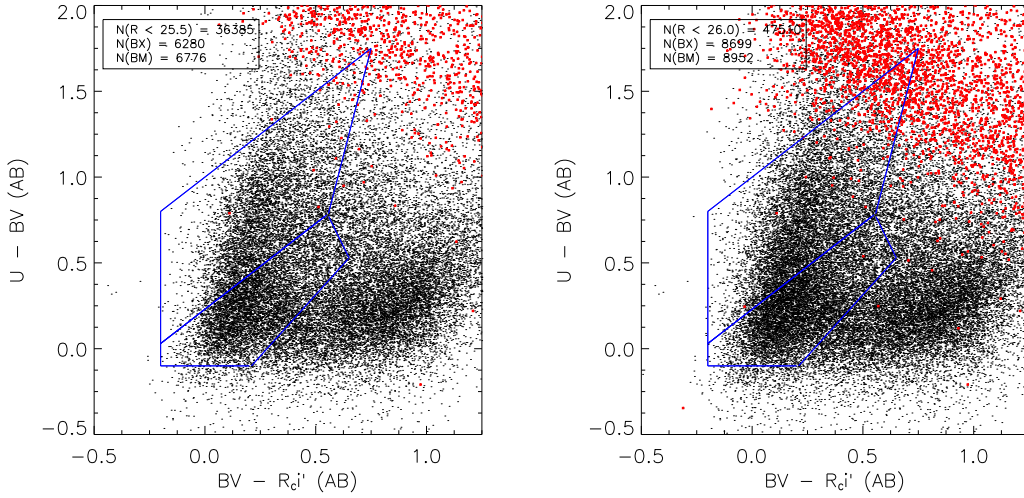


Figure 5.13 – $U - BV$ and $BV - R_{ci}'$ colors to select BX and BM galaxies. Red points are sources that are undetected in U at 1σ . Black lines indicate the selection box for the three galaxy populations. Selection is performed for $R_C \leq 25.5$ (left) and $R_C \leq 26.0$ (right).

after stellar removal) and 8952 BM (8584 after stellar removal). In Figure 5.14, the redshift distribution of the BX and BM technique is illustrated by $N(z)$ and $P(z)$. Also overlayed are the spectroscopic redshift distributions from Steidel et al. (2004) and Reddy et al. (2008), which demonstrates the accuracy of EAZY at $z \sim 2$ and shows that the filter transformations were done to sufficient accuracy. Although not illustrated in this figure, we find that a significant fraction of the BX and BM samples have $z_{\text{phot}} = 0.1 - 0.5$. The BX (BM) $R_C \leq 25.5$ sample has 1650 (1236) with $z_{\text{phot}} \leq 0.5$ corresponding to 32.5% and 21%. These numbers decrease to 28% and 16% when considering the sample with $R_C \leq 26.0$. These objects have average photometric redshift accuracy (Δz_{68}) at the 3.5% level, so one cannot argue that the redshifts for these sources were poorly determined and are at $z > 1$. Furthermore, we inspected the $B - z'$ and $z' - K$ colors and find that these objects occupy a region below the star-forming BzK selection (see § 5.4.2),

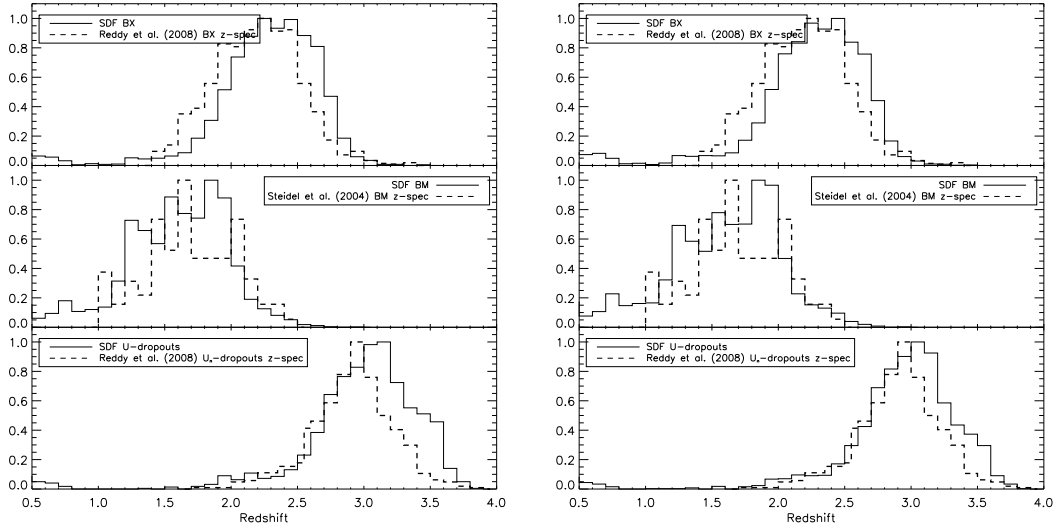


Figure 5.14 – The distribution of z_{phot} for the UV-selected BX, BM, and U -dropout (solid lines) compared to the spectroscopic samples of [Steidel et al. \(2004\)](#) or [Reddy et al. \(2008\)](#). We selected these galaxies down to $R_{\text{C}} = 25.5$ mag (left) and $R_{\text{C}} = 26.0$ mag (right).

which provides further evidence that they are at $z \lesssim 1.3$ (i.e., the Balmer/4000Å break is observed in the optical bands rather than the Lyman continuum break). The full z_{spec} distribution for BX and BM were not provided in [Steidel et al. \(2004\)](#), but the $z_{\text{spec}} < 1.0$ interloper statistics were determined to be 17.1% and 5.8% for BX and BM $\mathcal{R} \leq 25.5$ galaxies, respectively. Also, [Grazian et al. \(2007\)](#) discussed this issue for their sample of BX galaxies, so it appears that this interloper population is genuine.

Further evidence that the transformation was done correctly is the surface density of BXs, which is provided in Fig. 5.15. It is compared with measurements reported by [Reddy et al. \(2008\)](#) and shows good agreement over a range of ~ 3 mag.

5.4.2 The BzK Selection

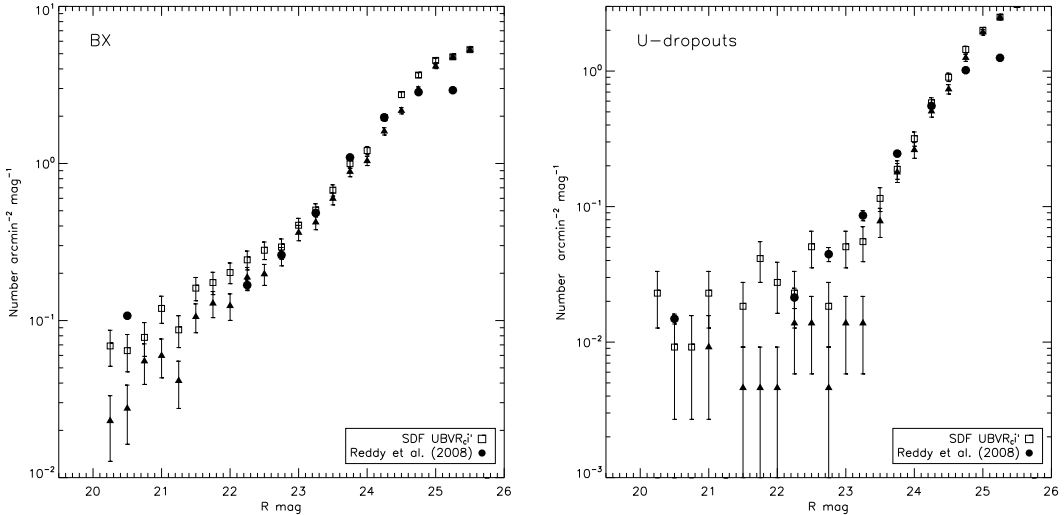


Figure 5.15 – The observed surface density of BX galaxies (left) and U -dropouts (right) shown as open squares. Triangles represent the SDF samples after removing stars. This shows good agreement with those reported by Reddy et al. (2008), which are shown as filled circles.

Daddi et al. (2004) defined star-forming BzK (sBzK) galaxies as those with $BzK \equiv (z - K) - (B - z) \geq -0.2$ with detection required in B and K . This corresponds to the solid line in Figure 5.16, and 9796 star-forming BzK (hereafter sBzK) galaxies are above this line. In addition, the selection of $z = 1 - 1.5$ passive BzK (pBzK), which have $BzK < -0.2$ and $z - K \geq 2.5$, yields 331 galaxies (315 after stellar removal). The photometric redshifts of the pBzK and sBzK populations are shown in Figure 5.17. They show good agreement with z_{phot} derived in the COSMOS field (McCracken et al., 2010). The COSMOS BzK sample probed $K < 23.0$ while our sample reaches to $K \sim 24.0$. We find better agreement at the $z_{\text{phot}} = 2.2 - 3.0$ range when limiting our sample to $K < 23.0$. The COSMOS and SDF samples of BzK galaxies independently confirm that sBzK galaxies are at $z \approx 1.5 - 2.5$ and pBzK galaxies are at $z \approx 1.0 - 1.5$.

The surface density of sBzKs appears higher than what has been reported

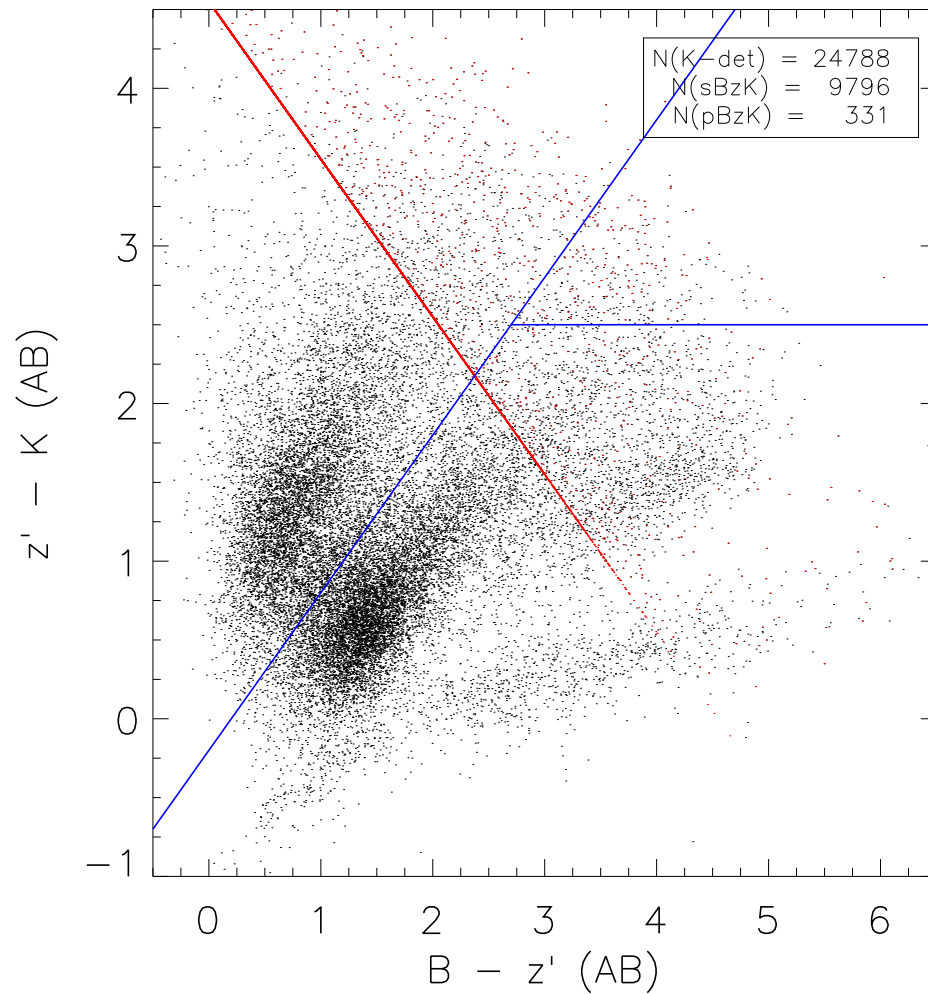


Figure 5.16 – The $B - z'$ and $z' - K$ colors for 24788 sources detected in the K -band above 3σ . Star-forming BzKs are identified as those above the slanted blue line ($BzK = -0.2$) while the selection of passive BzKs is through a combination of the horizontal blue line and the slanted line. Red points indicate sources that are undetected in the B -band at 3σ (lower limit on $B - z'$ color).

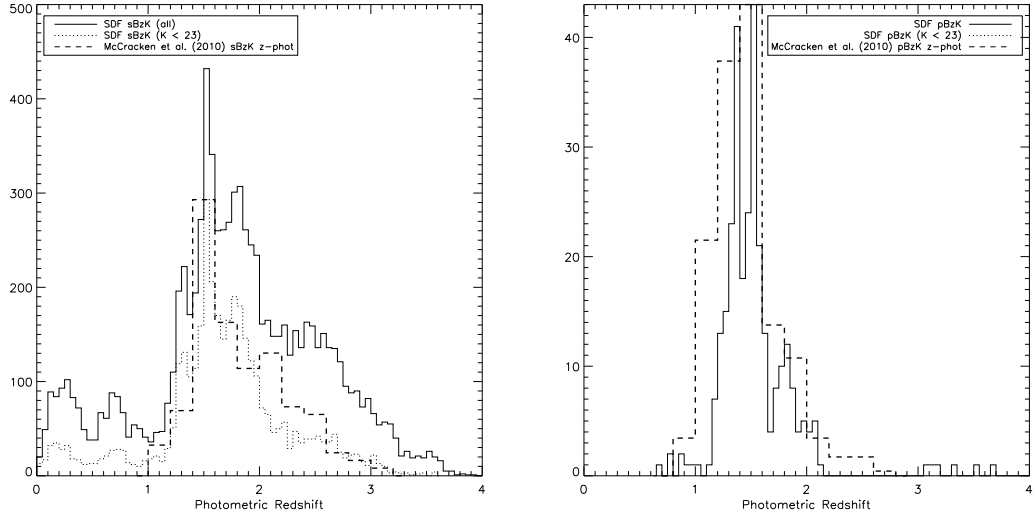


Figure 5.17 – The photometric redshift distribution for 8234 of 9796 sBzK galaxies (left) and 314 of 331 pBzK galaxies (right) indicated by the solid lines. The dotted lines are BzK galaxies with $K < 23$ mag to compare with the photo- z distribution of BzK galaxies from the COSMOS survey (McCracken et al., 2010), which are overlayed as dashed lines. The COSMOS distributions have been normalized to the peak in the SDF $K < 23$ mag z_{phot} distributions.

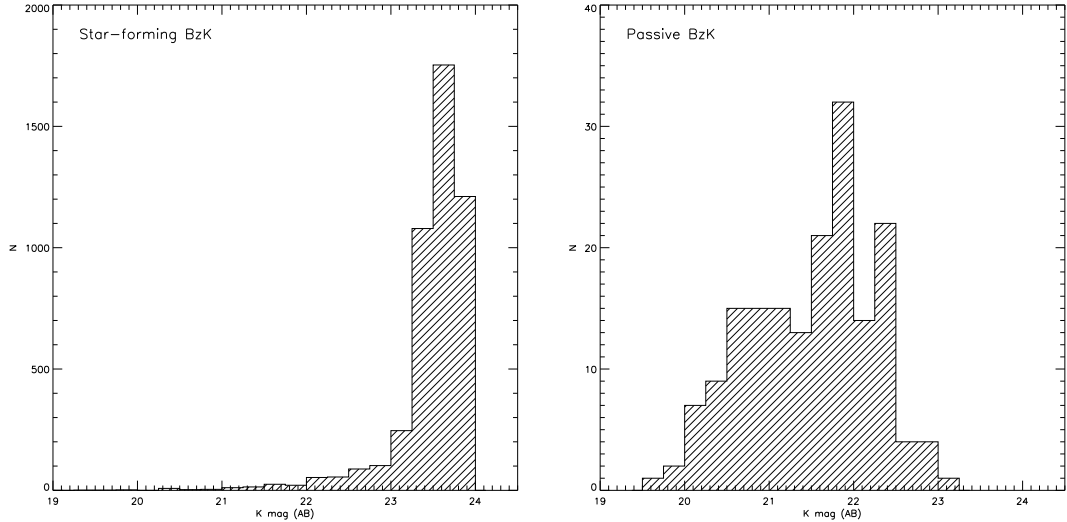


Figure 5.18 – The K -band magnitude for sBzK galaxies (left) and pBzK galaxies (right). These sources represent those that were identified in the multi-band selected sample, but were missed with the standard BzK selection procedure (multiple bands were not synthesized).

in other studies. We determined that the cause for this discrepancy is from the synthesis of multiple imaging bands. The BzK selection requires detection above the 3σ threshold in K , and is prone to incompleteness, as SExtractor will miss some faint sources. By combining multi-bands, some of these low-S/N K -band sources will be included since these sources may be detected in several of the optical bands. To illustrate this, we matched the B -, z' -, and K -band data and ran SExtractor in dual-image mode with the K -band as the reference image for detection (the same approach as other BzK studies). We then identified BzKs down to the same K threshold. selection. We found 5344 sBzKs and 169 pBzKs, of which 5228 and 169 are associated with sources in the multi-band selected catalog. Among the 5228 (169) sources, 112 (13) were photometrically scatter out of sBzK (pBzK) selection when adopting the measurements from the multi-band selected catalog. The net result is the 4680 sBzKs and 162 pBzKs in the multi-band selected catalog were missed compared to the common technique of just using the K -band image. The apparent K -band magnitude for these sources is shown in Figure 5.18, and illustrates that the majority of the sBzK sources are within 0.7 mag of the 3σ faint limit. These results indicate that future BzK searches should combine their optical and NIR bands to improve signal-to-noise and identify fainter (lower stellar mass) BzKs. Of course, not all BzK studies would have 9 optical bands, but combining, B , z' , and K would be advantageous at low luminosities.

5.4.3 The LBG Selection

The above techniques were designed to select $z = 1 - 3$ galaxies when the Lyman break technique could not be extended towards these redshifts. This has now changed since we discussed in Chapter 4 the first published survey of $z \sim 2$ LBGs

in the SDF. To fully span the $z = 1 - 3$ era with the Lyman break technique, we select U -, NUV -, and FUV -dropouts. Note that we will interchangeably use $U/NUV/FUV$ -dropout and $z \sim 1/2/3$ LBGs to refer to the Lyman-limit break selected sources.

5.4.3.1 U -dropouts

Using the $UBVR_{\mathrm{C}}i'$ to $U_nG\mathcal{R}$ transformation described in § 5.4.1, we identify U -dropouts in a similar manner as [Steidel et al. \(2003\)](#):

$$U - BV \geq -0.1, \quad (5.21)$$

$$BV - R_{\mathrm{C}}i' \leq 0.95, \text{ and} \quad (5.22)$$

$$U - BV \geq BV - R_{\mathrm{C}}i' + 1.0. \quad (5.23)$$

A modification was made to the right edge by shifting it 0.15 mag bluer in $BV - R_{\mathrm{C}}i'$. This selection spans the region above the BX selection window, and is illustrated in Figure 5.19. We consider sources with $R_{\mathrm{C}} \leq 25.5$ and identified 2578 U -dropouts (2375 after stellar removal). The surface density for our U -dropouts, as shown in Fig. 5.15, is similar to those reported by [Reddy et al. \(2008\)](#). Finally, we compared the z_{phot} for U -dropouts against the [Reddy et al. \(2008\)](#) sample in Figure 5.14. It appears that our distribution is shifted towards higher redshift by $\Delta z = 0.1 - 0.2$. The cause is still unknown.

5.4.3.2 NUV -dropouts

The selection of NUV -dropouts is discussed in Chapter 4.2.2. There are two corrections that we make to the previous selection of NUV -dropouts. First, a source is considered undetected in the NUV when it is below the 1σ threshold. Previously, we adopted 3σ to be conservative; however, we decided to be consistent

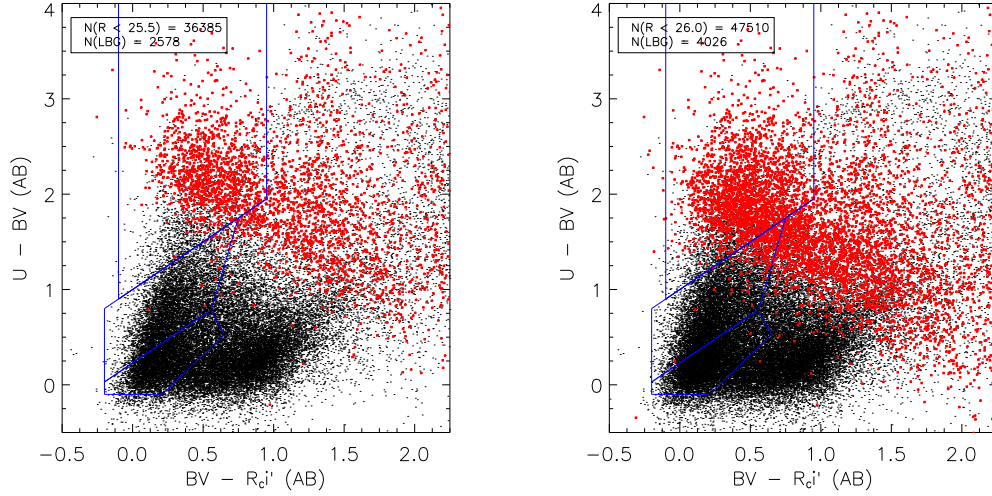


Figure 5.19 – $U - BV$ and $BV - R_{ci}'$ colors to select U -dropout galaxies. Red points are sources that are undetected in U at 1σ . Blue lines indicate the selection box for the BX, BM, and U -dropout galaxy populations.

with Steidel et al. (2003) for the final selection of all Lyman-limit galaxies. This will shift points in Figure 4.9 by 1.2 mag redder in $NUV - B$. Second, we failed to apply an aperture correction for undetected sources in Chapter 4. The aperture correction that we adopted previously was 1.81, and our latest calculation, which we now use, indicates 1.70, which leaves a 0.6 mag offset in the $NUV - B$ colors for faint galaxies.

We note that by adopting a 1σ threshold in the NUV, the $z \sim 2$ UV LF discussed in Chapter 4 may be different. We expect (to first order) that the completeness corrections were underestimated at $z = 2 - 2.5$ since some of the simulated galaxies that fell below our $NUV - B = 1.75$ mag will meet the $z \sim 2$ LBG selection region. However, by adopting a lower threshold, more sources will also enter our selection region that were bluer than $NUV - B = 1.75$ mag. We are still investigating this issue, but note that the comparisons between BX/BM and $z \sim 2$ LBG is more robust in this chapter than in Chapter 4 since direct

comparisons are made.

The $NUV - B$ and $B - V$ colors for $V < 25.4$ sources are shown in Figure 5.20, and 6071 NUV -dropouts (5563 after stellar removal) are identified. In § 5.5.2, we also discuss the NUV -dropout sample with $V \leq 26.0$, which consists of 8507 sources (7999 after stellar removal). The z_{phot} distribution is shown in Figure 5.20, and indicates that the selection identifies galaxies at $z = 1.5 - 2.5$, with 14% contamination from $z < 1.5$ interlopers. This small interloper fraction further supports our discussion in Chapter 4 where a small spectroscopic sample was used to estimate $\sim 30\%$ low- z contamination.

5.4.3.3 FUV -dropouts

Several studies (e.g., Burgarella et al., 2007) have used *GALEX FUV* imaging to select $z \sim 1$ LBGs. However, the selection of FUV -dropouts is often poorly described, and the FUV -dropout selection diagram has only been presented at conferences. The selection which has been adopted is:

$$FUV - NUV \geq 2.0, \quad (5.24)$$

$$NUV - U \leq 1.4, \text{ and} \quad (5.25)$$

$$FUV - NUV \geq 1.05(NUV - U) + 2.52. \quad (5.26)$$

The $FUV - NUV$ and $NUV - U$ colors are shown in Figure 5.21a. We limit ourselves to $U \leq 25.0$ mag and identified 578 FUV -dropouts (556 after stellar removal). We find that the z_{phot} distribution is skewed towards $z \sim 0.7 - 0.8$ (see Fig. 5.21). While FUV -dropouts have often been claimed to be at $z \sim 1$, the Lyman continuum breaks occurs at the FUV filter center at $z = 0.68$, reducing the flux by at least a half. This peak is not surprising due to the current FUV , NUV , and U sensitivities. The majority of $z \sim 1$ galaxies are $U > 25$ mag.

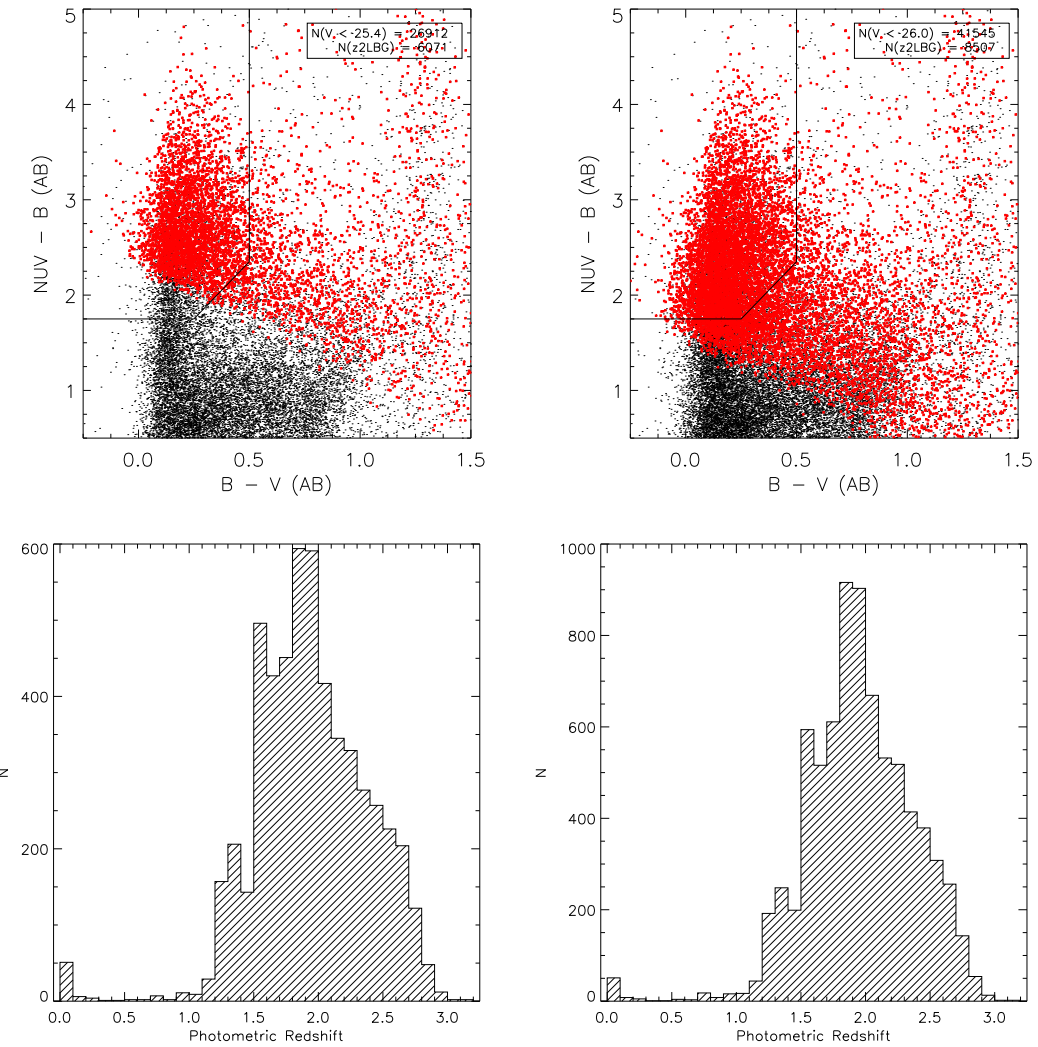


Figure 5.20 – The selection of $NUV - B$ and $B - V$ colors are shown in the top panels with $V \leq 25.4$ (left) and $V \leq 26.0$ (right). Objects marked in red indicate sources with 1σ upper limits in the NUV -band. For these samples, the z_{phot} distributions are shown in the bottom panels.

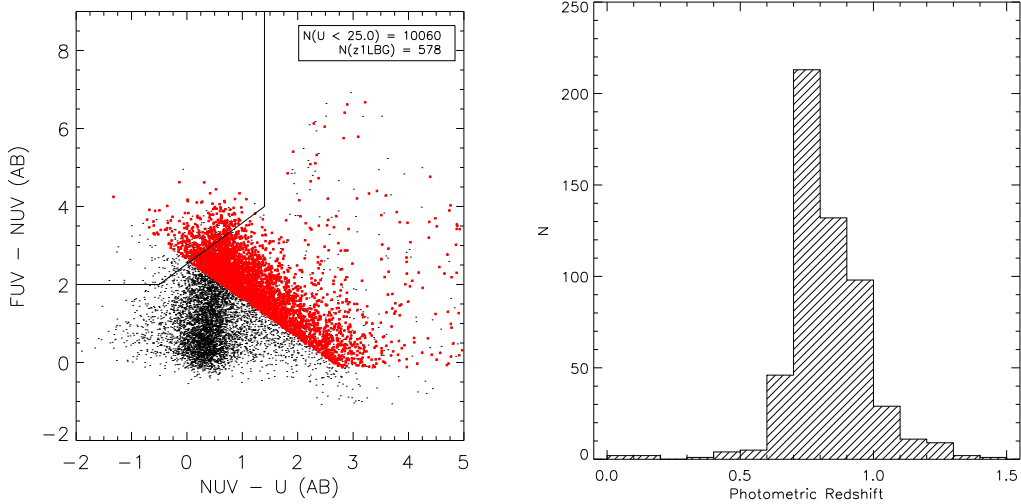


Figure 5.21 – The selection of $FUV - NUV$ and $NUV - U$ colors on the left panel. Objects marked in red indicate sources with 1σ upper limits in the FUV -band. The z_{phot} distribution for 555 of 556 FUV -dropouts are shown on the right.

5.4.4 Summary

We used photometric selection to identify 5585 BXs ($8004 R_C \leq 26.0$), 6408 BMs ($8584 R_C \leq 26.0$), 9796 sBzKs, 315 pBzKs, 2375 U -dropouts ($3823 R_C \leq 26.0$), 5563 NUV -dropouts ($7999 V \leq 26.0$), and 556 FUV -dropouts for a total of 30042 (adopting a shallower limit on R_C or V) or 38521 (adopting a fainter limit on R_C or V) of galaxies potentially at $z \approx 1 - 3$. However, since there is overlap between the different photometric samples, the non-redundant sample contains 19434 (17347 with z_{phot}) and 25173 (21929 with z_{phot}) galaxies in the Shallow and Faint samples, respectively.

5.5 Results

In this section we first discuss the properties of galaxies selected using a given photometric technique. We then compare the different photometric selection and discuss sample overlap and the selection bias associated with each technique. We then compare the photometric selection samples against photometric redshifts to access the completeness of using these techniques in acquiring a census of star-forming galaxies at $z = 1 - 3$.

For our analysis, we exclude the *FUV*-dropouts since the sample overlap with others are small and the z_{phot} distribution favors $z < 1$. Hereafter, we refer to the selections of BX/BM/*U*-dropout with $R_C \leq 25.5$ and *NUV*-dropouts with $V \leq 25.4$ as the “Shallow sample” while the “Faint sample” is designated for $R_C \leq 26.0$ and $V \leq 26.0$. The samples are further limited to galaxies with $z_{\text{phot}} > 0.5$ to remove any interlopers (particularly for the BX and BM samples) that strongly affect the sample overlap statistics.

5.5.1 The Physical Properties of $z = 1 - 3$ Galaxies

Using the photometric selection samples with z_{phot} and information from SED modelling, we illustrate in Fig. 5.22 the efficiency of these photometric techniques in terms of the relative fraction of the total number and “total SFR.” The total SFR is determined by the addition of SFRs determined from SED modelling for sources in the census. We find that the BX and BM methods are capable of identifying 60-80% of galaxies at the peak of their z_{phot} distribution, and the *U*-dropout technique identifies 90% of galaxies at $z \sim 3$, although this is overly optimistic since our “Total” sample is lacking low-mass $z \sim 3$ dusty galaxies with *K*-band detection. Likewise, it appears that the *NUV*-dropout technique has

similar efficiency as the BX/BM method, but with a smaller redshift coverage since lower redshift galaxies do not have a break in the *NUV*-band. Finally, the star-forming BzK selection is able to probe a wider range in redshift: yielding at least 30% at $z > 3$ and as much as 75% at $z \sim 1.5$. This illustrates that the vastly different methods to identify galaxies at this epoch are complementary, and that any single method is unable to identify all galaxies.

Our z_{phot} distributions can be used to determine the number and SFR fraction (of the photometric selection census) that is acquired by a given technique. The fraction of galaxies found in the Shallow sample: 50.4% (sBzK), 1.6% (pBzK), 28.7% (BX), 33.0% (BM), 12.2% (*U*-dropout), and 28.63% (*NUV*-dropout). The Faint sample consists of 38.9% (sBzK), 1.25% (pBzK), 31.8% (BX), 34.1% (BM), 15.2% (*U*-dropout), and 31.8% (*NUV*-dropout). The calculation normalized by SFRs yields for the Shallow sample: 47.3% (sBzK), 1.6% (pBzK), 28.1% (BM), 21.0% (BX), 10.3% (*U*-dropout), and 32.5% (*NUV*-dropout). The Faint sample consists of 36.0% (sBzK), 1.5% (pBzK), 28.6% (BM), 23.5% (BX), 13.8% (*U*-dropout), and 36.0% (*NUV*-dropout). The lower fraction for the *NUV*-dropout is because the technique sharply falls off at $z = 1.5$ and $z = 2.5$, whereas the other techniques (e.g., BM and sBzK) probe a much wider redshift range. LBGs at $z \sim 1$ would require UV imaging at $\approx 1800\text{\AA}$ (between the *FUV*- and *NUV*-band).

To further understand the selection bias of these techniques, we illustrate in Figure 5.23 the distribution of $E(B - V)$, stellar mass, SFR, and stellar ages for the BX, BM, sBzK, pBzK, *U*-dropout and *NUV*-dropout samples. These distributions are normalized to the census of these samples such that the fraction reported in a given bin is with respect all the galaxies with the property. We find that for galaxies with stellar masses above $6 \times 10^9 M_\odot$, the majority are

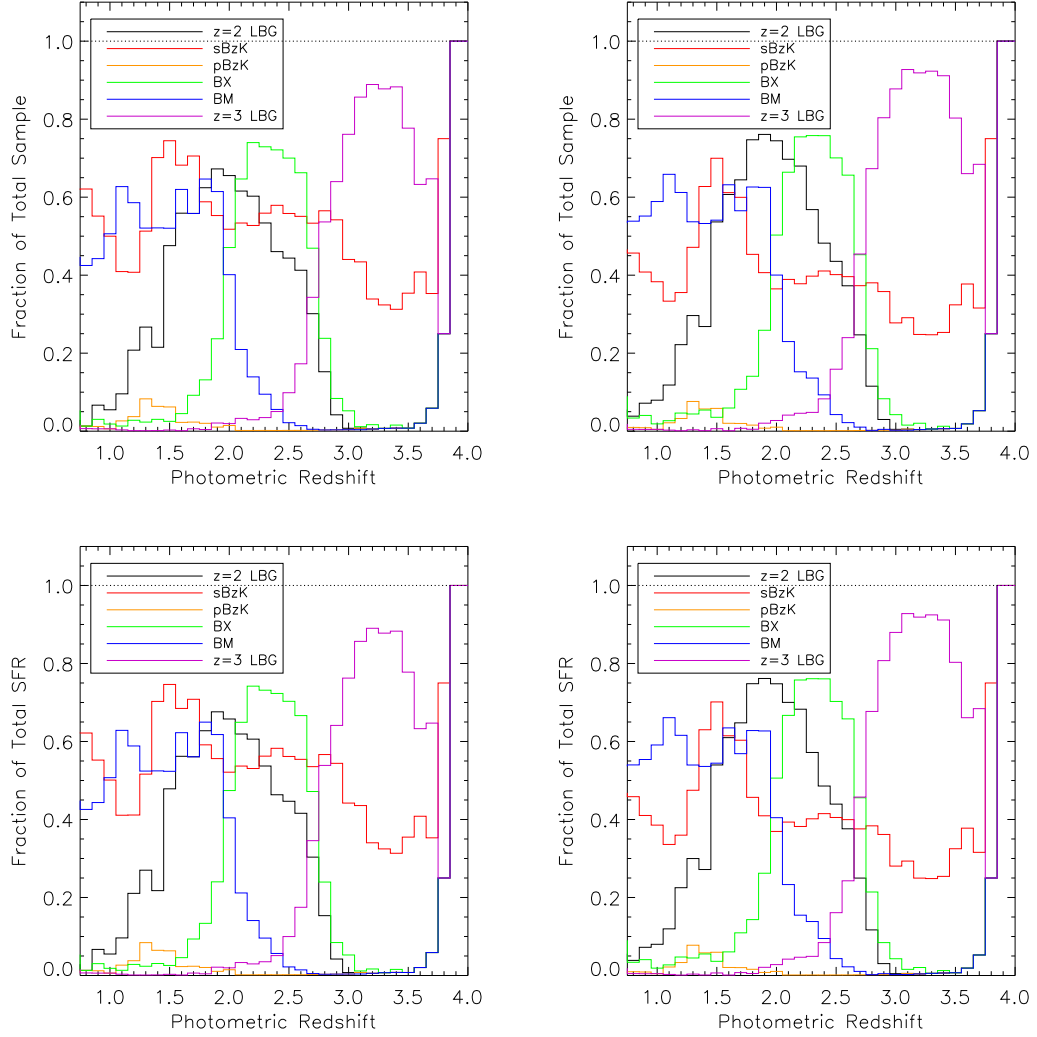


Figure 5.22 – The fraction of the Shallow (left) and Faint (right) samples versus redshift for the different photometric selection techniques: NUV -dropout (black), sBzK (red), pBzK (orange), BX (green), BM (blue), and U -dropout (purple). We illustrate the fraction in terms of the total number of galaxies (at a given redshift) in the top panels and in terms of the total SFR in the bottom panels.

acquired with the sBzK technique; below this UV selection methods are more efficient at selecting lower mass galaxies. The BzK technique is also able to identify the oldest galaxies and those with high dust extinction. UV techniques find young galaxies with little dust extinction and SFRs of $1 - 10 \text{ M}_\odot \text{ yr}^{-1}$. The $z \sim 2$ LBG population appears to span a wide range of $E(B - V)$ compared to the BX/BM method. We attribute this to the (1) larger range in rest-UV colors ($B - V < 0.5$ mag spans a larger $G - R$ color compared to the $G - R$ color of BX/BM galaxies) and (2) an ability to select massive galaxies. We discuss this further in § 5.5.2.1. Figure 5.23 also shows that the most actively star-forming galaxies³ will be identified using either the sBzK or *NUV*-dropout method. However, 85% of the photometric census consists of galaxies (between $z_{\text{phot}} = 1$ and $z_{\text{phot}} = 3$) with SFRs of $30 \text{ M}_\odot \text{ yr}^{-1}$ or lower, and 72% of this fraction is captured using the BX and BM methods with $R_C \leq 26.0$ mag.

5.5.2 A Direct Comparison of Photometric Selection Techniques

Previous studies (Reddy et al., 2005; Quadri et al., 2007; Grazian et al., 2007; Lane et al., 2007) have also investigated the completeness of photometric selection and the selection bias in the GOODS-N, GOODS-S/CDF-S, MUSYC, and UKIRT fields. However, each study has their own advantages and disadvantages in terms of area coverage, photometric selections used, and the accuracy of their redshifts. Thus the combination of these surveys provide a better understanding of the problem. We summarize in Table 5.4 how these surveys complement one another in terms of depth, redshift information, sample sizes, area coverage, and photometric selection techniques.

We note that these past surveys could not identify $z \sim 2$ LBGs, so most

³The high SFRs are due to large dust extinction corrections.

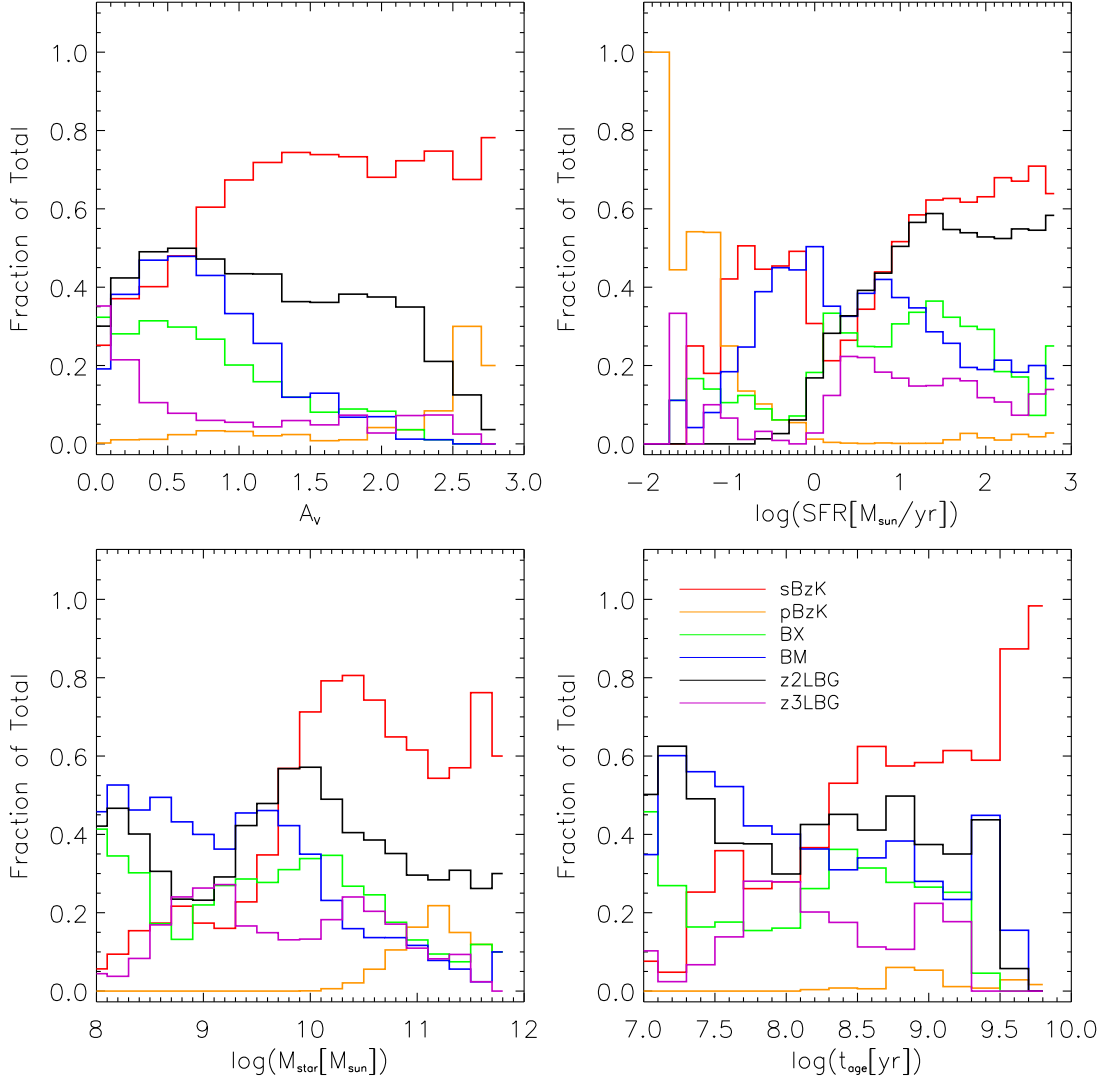


Figure 5.23 – The distribution of A_V , $\log(\text{SFR}/\text{M}_\odot \text{ yr}^{-1})$, $\log(M_{\star}/\text{M}_\odot)$, and $\log(\text{age}/\text{yr})$ for the different population. Color conventions follow those in Figure 5.22.

Table 5.4. Summary of Photometric Selection Census Surveys

	Field				
	GOODS	MUSYC	CDF-S	UDS ^a	SDF
Reference	Reddy05	Quadri07	Grazian07	Lane07	This Study
Area	72.3	400	90.2/143.2	2013	720/870
N _{total}	931	... ^b	2630	12503	19434
R depth	25.5	25.5		...	25.5
K depth	23.0	≈23.45	23.5 – 23.8	22.5	24.2
<i>z</i> _{phot}		9-band	12/13-band	No	15-band
<i>z</i> _{spec}		No	~1000	No	... ^c
BX	620	Yes ^b	1345	No	5585
BM	... ^d	Yes ^b	... ^d	No	8004
<i>U</i> -dropout	No	Yes ^b	... ^d	No	2375
sBzK	221	Yes ^b	747	6736	9796
pBzK	17	Yes ^b	89	816	315
DRG	73	Yes ^b	179	330	No
ERO ^e	No	No	No	4621	No
<i>NUV</i> -dropout	No	No	No	No	5563

^aUDS is short for the Ultra Deep Survey, which is part of the UKIRT Infrared Deep Sky Survey.

^bNumbers were not provided in the original paper, so a “Yes” or ellipses are used.

^cThe SDF *z*_{spec} is mostly limited to low-*z*, so we report nothing here.

^dThe number here is merged with the above number for BX.

^eEROs (extremely red objects) are often distinguished in the literature from DRGs. This selection consists of using a *R* – *K* > 5.3 mag criterion.

Note. — Abbreviated references: “Reddy05” for Reddy et al. (2005), “Quadri07” for Quadri et al. (2007), “Grazian07” for Grazian et al. (2007), and “Lane07” for Lane et al. (2007). Areas are in arcmin².

of these comparisons were made between the BX/BM/ U -dropout methods and the BzK/DRG methods given their redshift distribution, and it was assumed that BX/BM are lower redshift analogs of $z \sim 3$ LBGs. We discuss the overlap between BX/BM and $z \sim 2$ LBGs in § 5.5.2.1. In past photometric-selected census surveys, the phrase “LBG” has often been used to refer to the selection of U -dropouts. In our study, we make a clear distinction between the two.

A summary of the photometric selection sample overlap is provided in Tables B.2 and B.3, along with the average (and 1σ) z_{phot} , $E(B - V)$, stellar age, stellar mass, and SFR. We have created a 6-digit binary index to refer to the sample overlap. Each digit refers to a specific galaxy population in the order of: pBzK, sBzK, BM, BX, U -dropout, and NUV -dropout. So for example, sources that are classified as sBzK, BX, and NUV -dropout would be denoted as “010101”. Venn diagrams are provided to illustrate the sample overlap for both the Shallow (Figure 5.24) and Faint (Figure 5.25) samples. In these Venn diagrams, the BX, BM, and U -dropouts do not overlap given the selection via rest-UV colors. This is also the case for the passive and star-forming BzK-selected galaxies. Note that we have not placed any restrictions on the optical (K -band) magnitudes for NIR-selected (UV-selected) galaxies for these tables and these Venn diagrams. We do discuss the overlap with such restrictions in § 5.5.2.1 to compare with previous estimates.

5.5.2.1 Sample Overlap: Multi-Color Plots

To further understand and illustrate the selection effects of these techniques, it is natural to determine where each galaxy population/technique (e.g., BX) falls in the color-color selection of another (e.g., BzK). We first discuss the BzK selection, follow by the $U_n G\mathcal{R}$ methods, and finally the selection that we have developed to

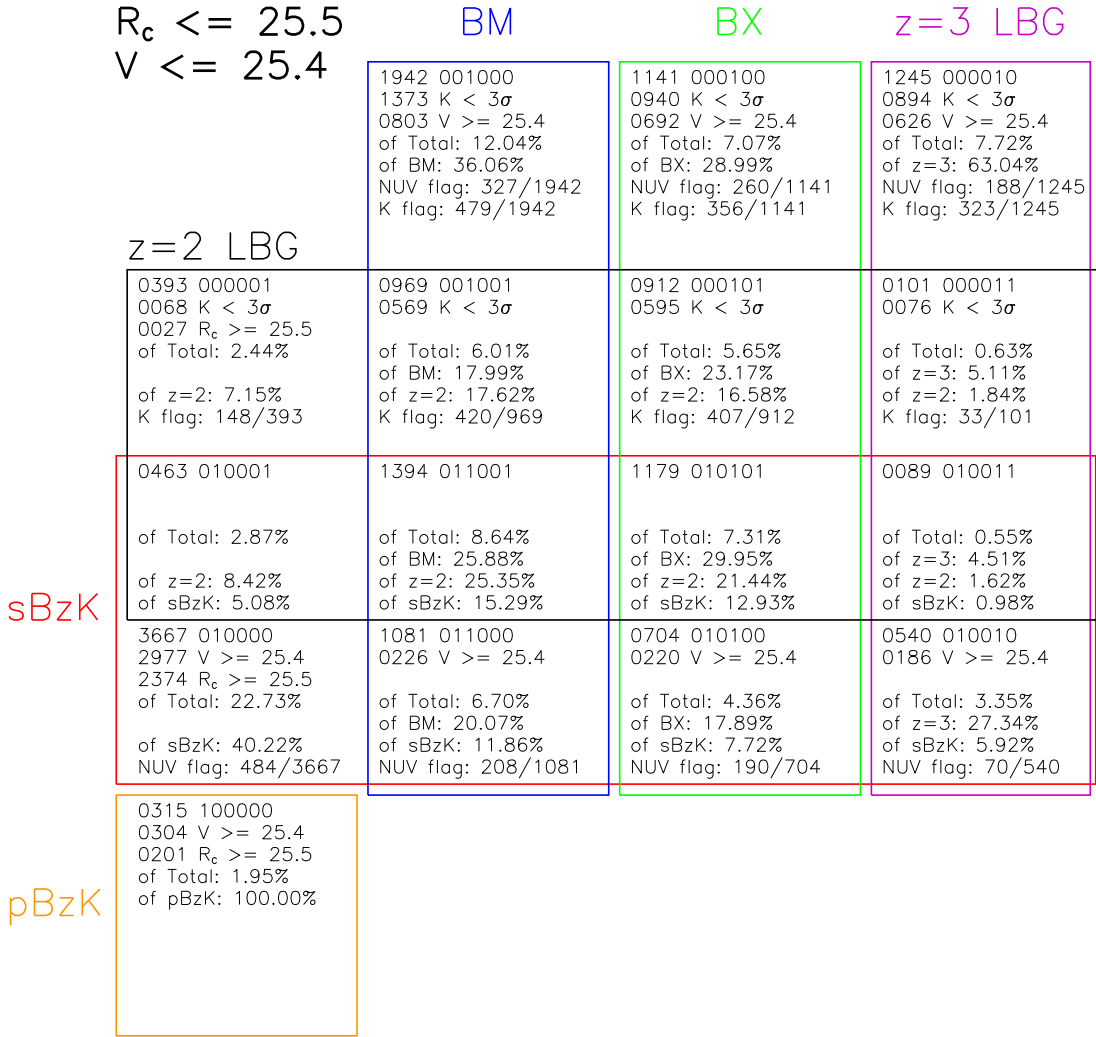


Figure 5.24 – A Venn diagram illustrating photometric galaxy sample overlap for the Shallow sample. The magnitude limits provided in the upper right are only for the optically selected objects. Redshift increases to the right for blue (BM), green (BX), and purple (U -dropout) rectangles and upwards from orange (pBzK) to red (sBzK). The black rectangle is for NUV -dropouts. The color coding is the same as that used in Figure 5.22. Statistics are provided in each box for the size of a given sample, and the fraction relative to the full and each photometric selection samples. “K flag” refers to sources that fall in a lower sensitivity region so they cannot be classified as sBzKs, and “NUV flag” indicates the fraction of sources (in a given box) that are affected by confusion in the NUV and could be NUV -dropouts. Typically, confusion is at the 15–20% level.

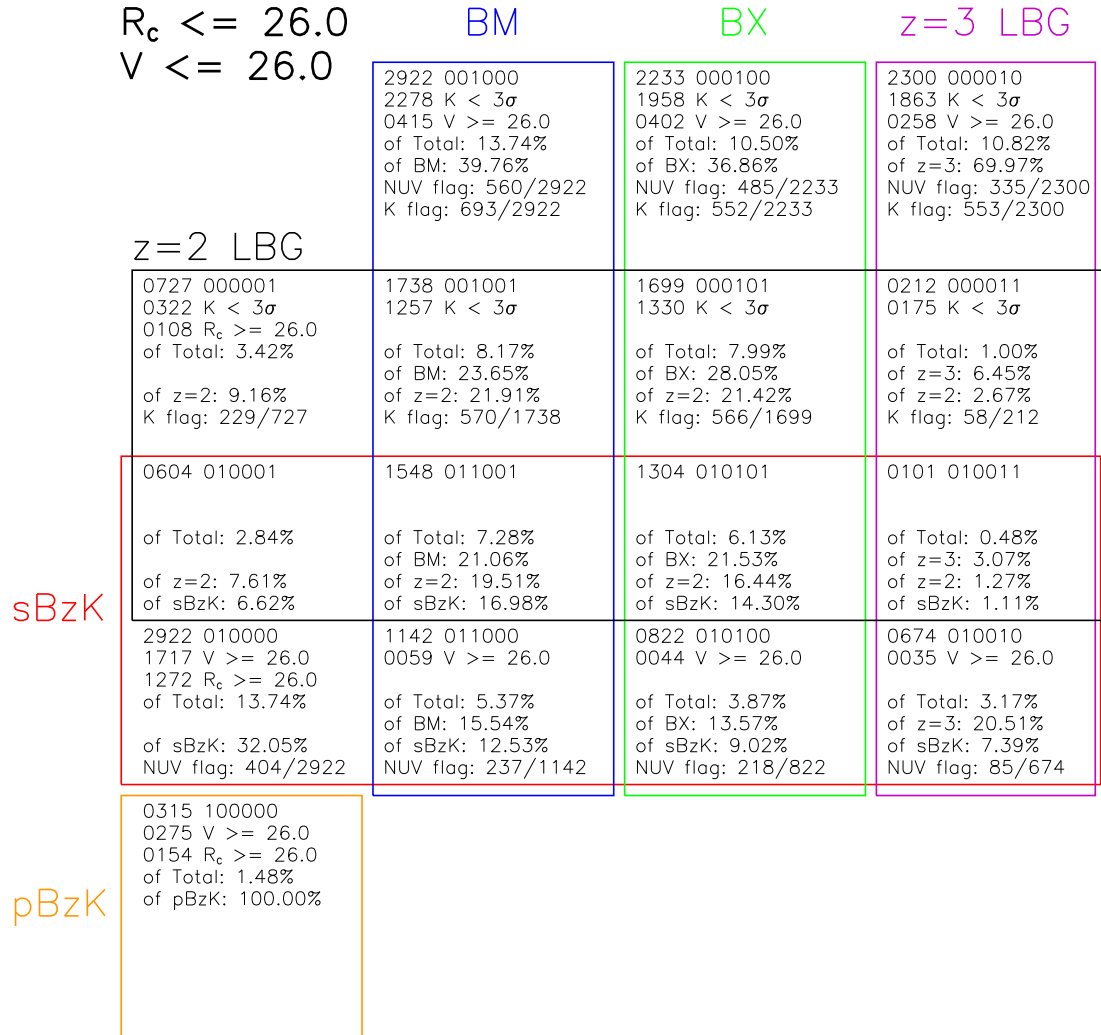


Figure 5.25 – A Venn diagram illustrating photometric galaxy sample overlap for the Faint sample. See the caption of Figure 5.24 for further details.

identify $z \sim 2$ LBGs. Note that the numbers below have excluded interlopers with $z_{\text{phot}} < 0.5$ (unless otherwise indicated). When computing the overlap fraction and providing the two-color distribution of sources, we place limits on either the V , R_C , or K , as we did when we generated the high- z photometric samples. We will discuss further this problem at the end of this section.

Near-IR selection: The BzK method. The $B - z'$ and $z' - K$ colors for BXs, BMs, NUV -dropouts, and U -dropouts are shown in Figure 5.26. Among 3173 BXs, 4487 BMs, 1619 U -dropouts, and 4492 NUV -dropouts, 1915, 2864, 815, and 3447 have K -band 3σ detection, respectively. Among these, 98.3%, 86.4%, 77.2%, and 90.7% meet the sBzK selection, which indicates that sBzK method is capable of selecting almost all high- z UV-selected galaxies having $K \lesssim 24$ mag. We note that if we did not exclude objects with $z_{\text{phot}} < 0.5$, the overlap fraction will be 78.6% (BX), 77.6% (BM), 71.9% (U -dropout), and 90.0% (NUV -dropout). As stated previously in § 5.4.3.2, the NUV -dropout method suffers from less $z < 1$ contamination than the U_nGR methods by examining for a Lyman break. Thus, to fully use the U_nGR method for high- z selection, accurate z_{phot} or z_{spec} or K data are needed to distinguish the population of low- z BX/BM/ U -dropout galaxies that are masquerading as high- z .

It appears that more than three-quarters of U -dropouts with K -band detections are also identified. The redshift where the Balmer/4000Å break begins to enter the K -band window is $z \approx 4$, so extremely deep K -band imaging ($K = 25 - 26$) can yield a mass-limited (and not SFR-limited) sample of $z \gtrsim 3 - 4$ galaxies with stellar masses above $\sim 10^{10} M_\odot$. These high- z sBzKs were also seen by [Grazian et al. \(2007\)](#), but with a much smaller sample. Unfortunately, they did not report a sBzK– U -dropout overlap fraction to compare. [Grazian et al. \(2007\)](#) did find that 86 – 100% of $z > 1.4$ BX/BM galaxies are sBzK galaxies, which is consistent with the above number. [Quadri et al. \(2007\)](#) determined that

80% of BX/BM/ U -dropout galaxies (regardless of z_{phot}) is sBzK selected, which agrees with our number without any constraints placed on z_{phot} . Likewise, similar numbers were reported by Reddy et al. (2005).

The majority of sources that are missed by the sBzK method are BM and NUV -dropout galaxies. We find that these non-sBzK galaxies have characteristic $z_{\text{phot}} \approx 1.9$, $E(B - V) \approx 0.1$, stellar masses of $\sim 10^{10} M_{\odot}$, SFRs of $\sim 10 M_{\odot} \text{ yr}^{-1}$, and stellar ages of 3×10^8 yrs. It is not surprising that the BzK technique misses such sources since it is sensitive to redder galaxies at $z \approx 1.5 - 2.5$.

None of the BX, BM, U -dropout, and NUV -dropout sources are classified as a passive BzK, indicating that these galaxies represent an orthogonal population to UV-selected galaxies. These sources are well detected in the B -band, so ambiguity cannot be invoked so that some of the sBzKs are pBzKs. This was also seen by Quadri et al. (2007). We further discuss this in Appendix B.1.

We find the fraction of sBzK galaxies that are BX, BM, or U -dropout varies with K -band magnitude with larger overlap at fainter K (see Fig. 5.27). This is to be expected as the UV selection techniques probe less reddened and young galaxies that are typically of lower masses. Our measurements agree with those of Reddy et al. (2005) at $K \approx 22 - 23$ mag and extends toward $K \approx 24$ to show a slightly larger fraction of overlap. However, our sBzK–BX/BM/ U -dropout overlap fraction is noticeably lower for $K < 22.0$ mag. Since the Reddy et al. (2005)’s sBzK sample is small ($N = 221$; total) and the bright end has a small number of sources, the apparent disagreement can be largely attributed to their small number statistics.

Non-ionizing UV continuum selection: The U_nGR method. For the selection of BX, BM, and U -dropout galaxies, the BzK galaxies and $z \sim 2$ LBGs are plotted on the $U - BV$ and $BV - R_C i'$ color space in Figure 5.28. We

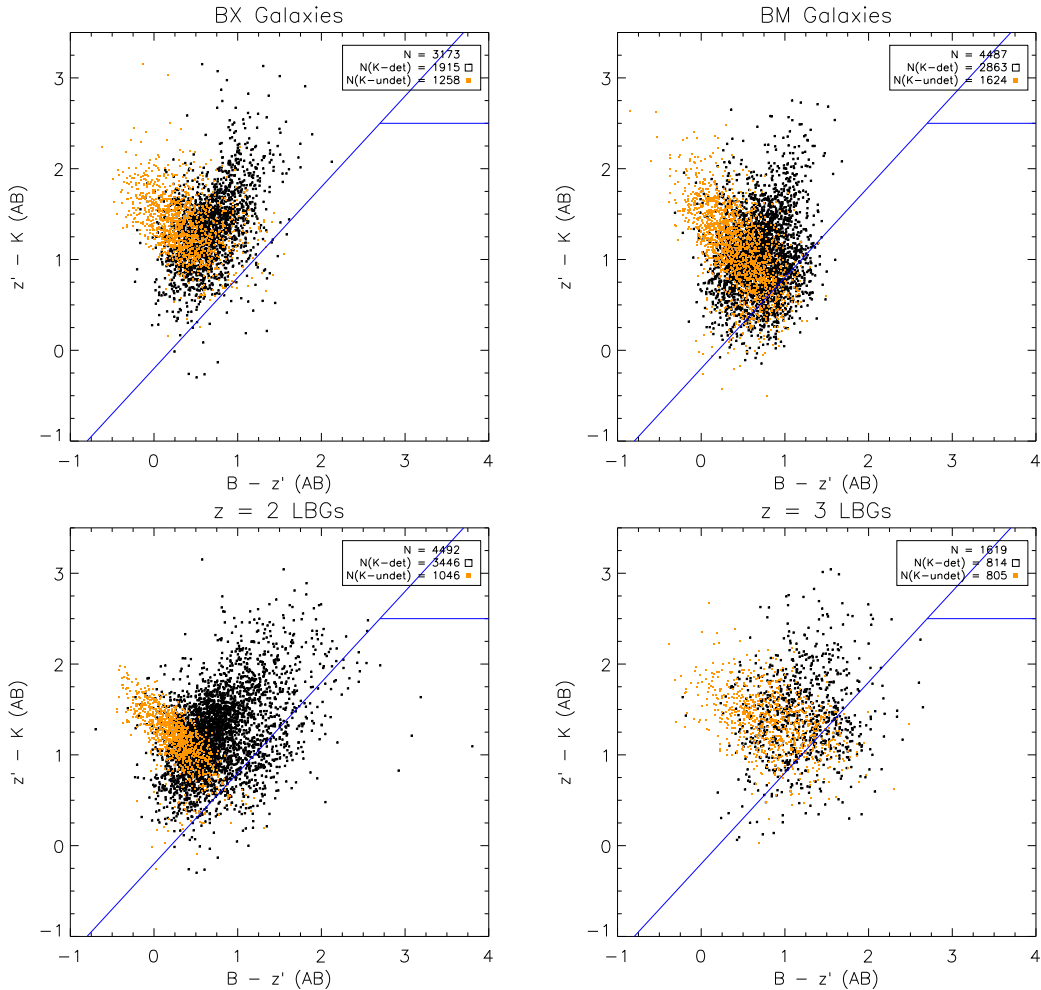


Figure 5.26 – The $B-z'$ and $z'-K$ colors for BX galaxies (upper left), BM galaxies (upper right), NUV -dropouts (upper left), and U -dropout galaxies (lower right). Sources shown as black are those with $> 3\sigma$ detection in K while those in orange are sources undetected in K . These undetected sources have upper limits on their $z'-K$ colors. Note that the axes scale differs from Figure 5.16.

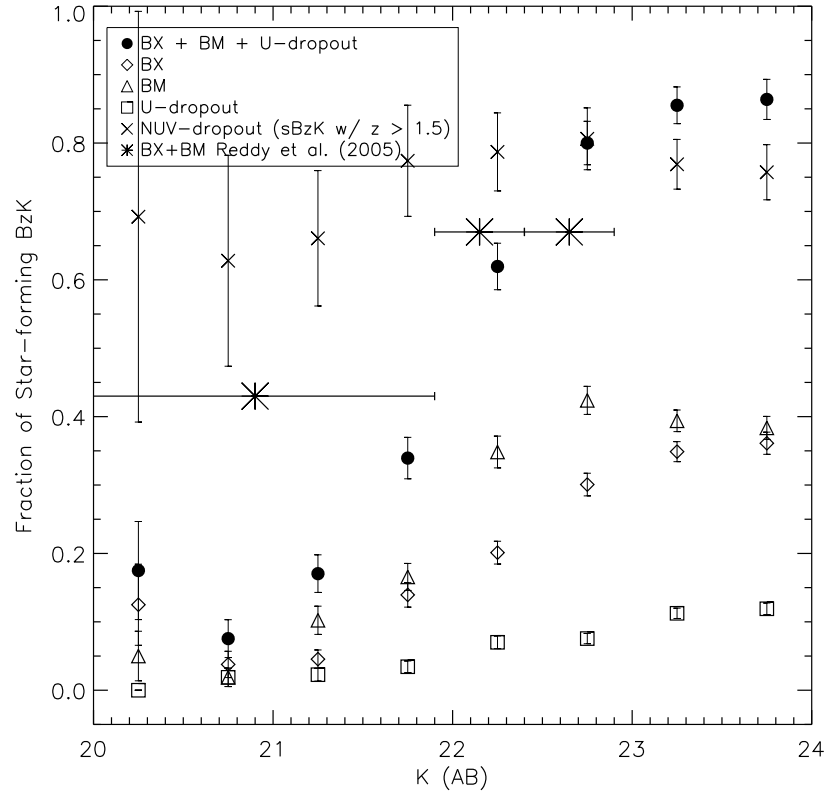


Figure 5.27 – The fraction of sBzK galaxies with $R_C < 25.5$ that meets the BX (diamonds), BM (triangles), or U -dropout (squares) selection. The combination of all three UV selection techniques is shown as filled circles. The sample overlap increases towards lower luminosities, which is expected given the selection bias that UV techniques target lower mass galaxies. Overlayed are estimates from [Reddy et al. \(2005\)](#). We also show $z_{\text{phot}} \geq 1.5$ sBzK galaxies that meet the NUV -dropout selection with crosses. This illustrate that the Lyman break technique is able to identify many massive $z \sim 2$ galaxies, which the BX/BM method fails.

find that among the sBzKs with $R_C \leq 25.5$, 27.9% (1883/6742) are BXs, 36.7% (2475/6742) are BMs, and 9.3% (629/6742) are U -dropouts for a total overlap of 74%. Quadri et al. (2007) determined $\sim 65\%$ for this fraction. To understand this small yet noticeable difference, we point out that our sample probes much fainter K magnitudes, by ≈ 1 mag. Since the majority of BX/BM galaxies have low stellar masses, many of them are expected to be faint in K . As a result, our survey is more complete in mass, and is weighted more toward the lower luminosity galaxies. We see this from the slightly higher overlap fraction in Figure 5.27 for $K > 23.0$ mag (AB).

Likewise, among 5472 NUV -dropouts with $R_C \leq 25.5$, 2091 (38.2%) are BXs, 2363 (43.2%) are BMs, and 190 (3.5%) are U -dropouts for a total overlap of 84.9%. The small overlap between NUV -dropouts and U -dropouts is to be expected since we intend to exclude $z \gtrsim 2.7$ blue galaxies with a $B - V \leq 0.5$ mag criterion (see Figure 4.13).

Recall that Steidel et al. (2004) defined the BX/BM selection to identify $z \sim 2$ galaxies that are analogous to $z \sim 3$ LBGs. The presence of this large overlap shows that this statement is *mostly* true. We find, however, that the LBG selection is able to identify redder and more massive galaxies. At least half of the $K < 21.5$ sBzK galaxies are selected using the NUV -dropout method. This was previously illustrated in Figure 5.26 with the NUV -dropout spanning redder $B - z'$ and $z' - K$ colors compared to the BX galaxies, again in Figure 5.27 where NUV -dropout method identified more K bright galaxies compared to BX/BM, and it also explains the slew of points at $BV - R_C i' = 0.5 - 1.3$ mag, which is also seen for sBzK galaxies.

Ionizing UV continuum selection: The NUV -dropout method. Finally, we show the $NUV - B$ and $B - V$ colors for BX, BM, U -dropouts, and BzK

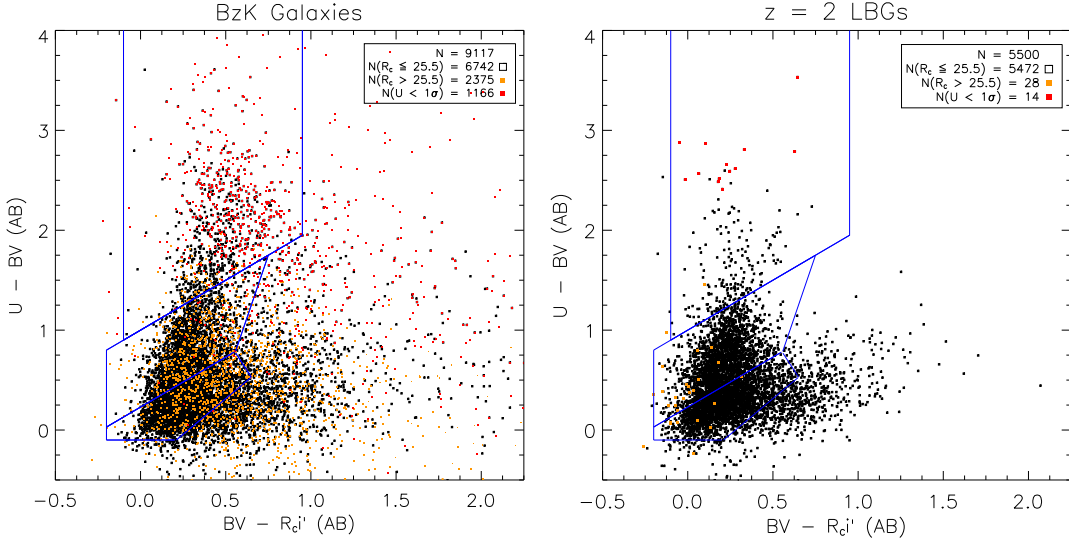


Figure 5.28 – The $U - BV$ and $BV - R_{ci}'$ colors for BzK galaxies (left) and $z \sim 2$ LBGs (right). Sources shown as black are those with $R_C < 25.5$ while those in orange are fainter than $R_C = 25.5$. Sources indicated in red are undetected in U .

galaxies in Figure 5.29. Among 3936 BXs, 5386 BMs, and 9117 sBzKs, 3024, 4357, and 5508 were brighter than $V = 25.4$, respectively. We further limit these samples to those with $z_{\text{phot}} = 1.5$, since the NUV will only be sensitive to a Lyman break above this redshift. The sample sizes are then 2653 (BX), 2618 (BM), and 3975 (sBzK). We find the fractions of BX, BM, and sBzK that meet the NUV -dropout criteria are 76.5%, 80.5%, and 72.1%, respectively. The high fraction of overlap strongly suggests that using a Lyman-limit break to select high- z galaxies of low and high stellar masses is successful.

Among the sources that were missed, 30–45% are affected by flux contamination from a nearby source, and thus did not meet the minimum $NUV - B = 1.75$ criteria. This fraction is similar to the incompleteness we derived (20%) in Chapter 4 from a MC simulation. Future higher resolution NUV imaging (e.g., with *Hubble*) will be able to select these sources that were missed due to their unlucky nature of being close (in projection) to another source that is detected in the

NUV. However, such surveys will only be able to probe small areas on the sky, so *GALEX* deep *NUV* surveys are still needed.

Summary. In general, we find that the overlap fraction between UV- and NIR-selected samples of $z = 1 - 3$ galaxies is high: 70–90%. The sample overlap was greater when examining the UV-selected samples in the BzK color space rather than vice versa. This illustrates that UV selection techniques, which are good at identifying blue high- z galaxies, miss the redder galaxies, particularly the more massive ones. This has been seen in previous studies (e.g., Quadri et al., 2007). Several comparisons made between the BX/BM galaxies and the $z \sim 2$ LBGs indicate that most (75–80%) BX/BM galaxies do show a Lyman-limit break. This implies that these UV-selected galaxies are nearly analogous to Lyman break selected galaxies. However, the *NUV*-dropout population does span a wider range in dust extinction and show greater sample overlap with bright (i.e., more massive galaxies) sBzK galaxies.

These comparisons were made by adopting limits on the V -, R_{C} -, and K -band magnitudes (e.g., requiring detection in K for UV-selected sources) in order to have reliable measurements of their colors. As illustrated in the Venn diagrams and in the two-color selection diagrams, a non-negligible fraction of sources do not meet such criteria. Such sources are of either lower masses or higher dust extinction. Thus, when considering the full sample of photometric-selected galaxies, the BX, BM, U -dropout, *NUV*-dropout, sBzK, and pBzK populations consist of 28.7%, 33.0%, 12.2%, 28.63%, 50.4%, and 1.6% of the Shallow photometric sample, respectively. These fractions are 31.8%, 34.1%, 15.1%, 31.8%, 38.9%, and 1.3% of the Faint photometric sample. This shows that a more comprehensive census of $z = 1 - 3$ is obtained by merging the different selection techniques. These percentages reflect the ability for the techniques to completely survey $z = 1 - 3$,

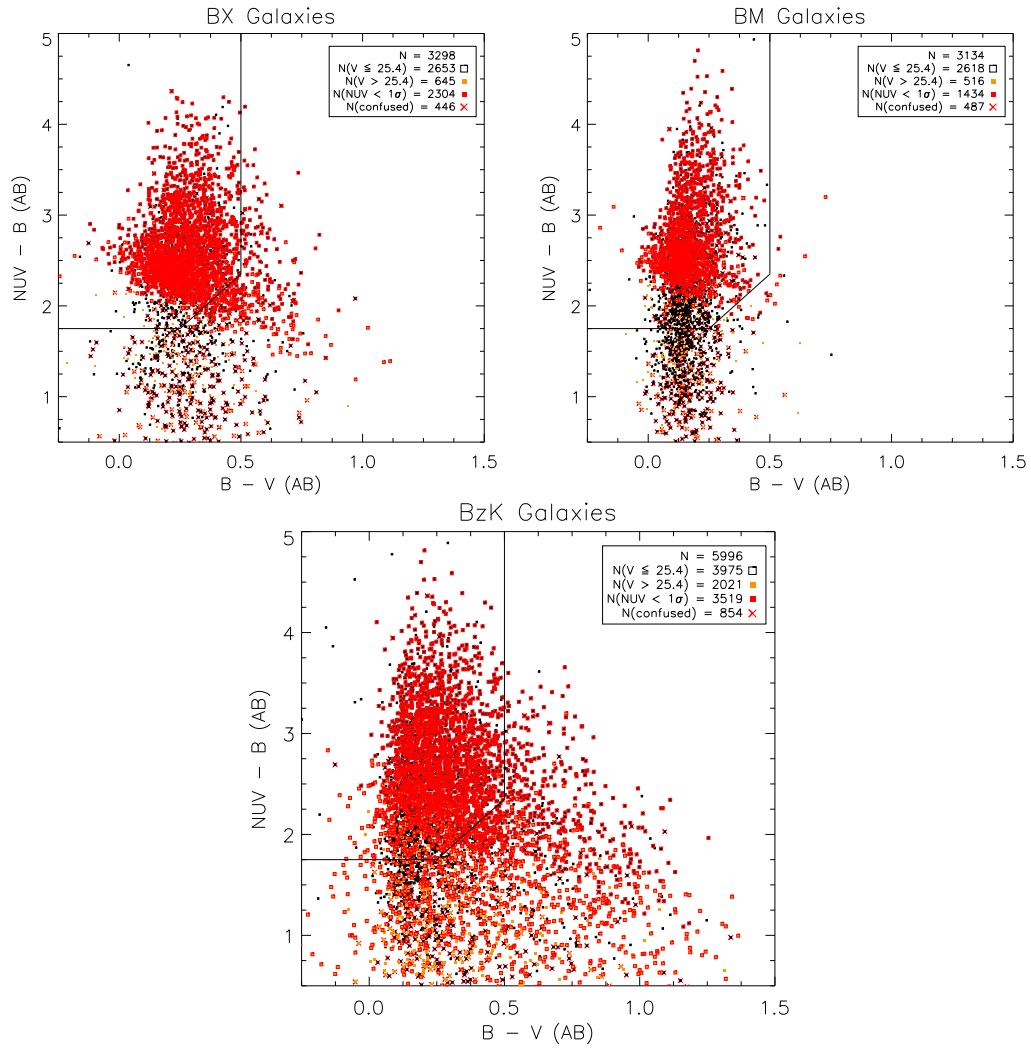


Figure 5.29 – $NUV - B$ and $B - V$ colors for BX-, BM-, and BzK-selected galaxies. We have limited these sources to those with $z_{\text{phot}} \geq 1.5$ since the NUV data is only able to see a break at $z \sim 1.5$. Orange crosses represent sources that are flagged as likely confused by a nearby source or sources in the NUV image.

and are a factor of ≈ 2 higher if you consider $\pm 1\sigma$ from the peak of their respective z_{phot} distribution.

5.5.3 The Star-Formation Rate Density from the Census

With a census of star-forming galaxies from photometric selection techniques, we can determine the SFR density from the results of our SED modelling with FAST. Reddy et al. (2005) were the first to estimate this with a census of DRGs, BX/BM galaxies, and sBzK galaxies at $1.4 < z_{\text{spec}} < 2.6$. We consider sBzK, BX/BM, and *NUV*-dropout galaxies and limit our sample to $1.5 < z_{\text{phot}} < 2.6$ since the *NUV*-dropout sample has a low percentage of $z < 1.5$ sources. We determine the accumulated SFR density versus K - and R_C -band magnitude for the sBzK, BX/BM, and *NUV*-dropout populations and the full census accounting for sample overlap. We only consider sources in the region ($\approx 720 \text{ arcmin}^2$) of deep K -band data. To normalize our SFR measurements by the effective surveyed volume, we assume that the completeness $C(z)$ of the census at any given redshift is proportional to the z_{phot} distribution with it normalized to unity at the z_{phot} peak. We note that this is a lower limit on incompleteness, so SFR density measurements reported here can be underestimated. The integral of the following equation,

$$V_{\text{eff}} = \Omega \int_{z=1.5}^{z=2.6} dz C(z) \frac{dV}{dz d\Omega}, \quad (5.27)$$

yields $1.2 \times 10^6 \text{ Mpc}^3$ and $1.5 \times 10^6 \text{ Mpc}^3$ when we consider sources with $K \lesssim 24$ and $R_C < 25.5$ mag, respectively. We determined a total SFR density of 0.14 ± 0.02 (0.11 ± 0.02) $M_{\odot} \text{ yr}^{-1} \text{ Mpc}^{-3}$ for sources brighter than $K = 24.0$ mag ($R_C = 25.0$ mag). The accumulated SFR density is illustrated in Figure 5.30a and 5.30b where the range of allowed values is 1σ from include uncertainties in the SFR due to the z_{phot} accuracy and cosmic variance (estimated from Somerville

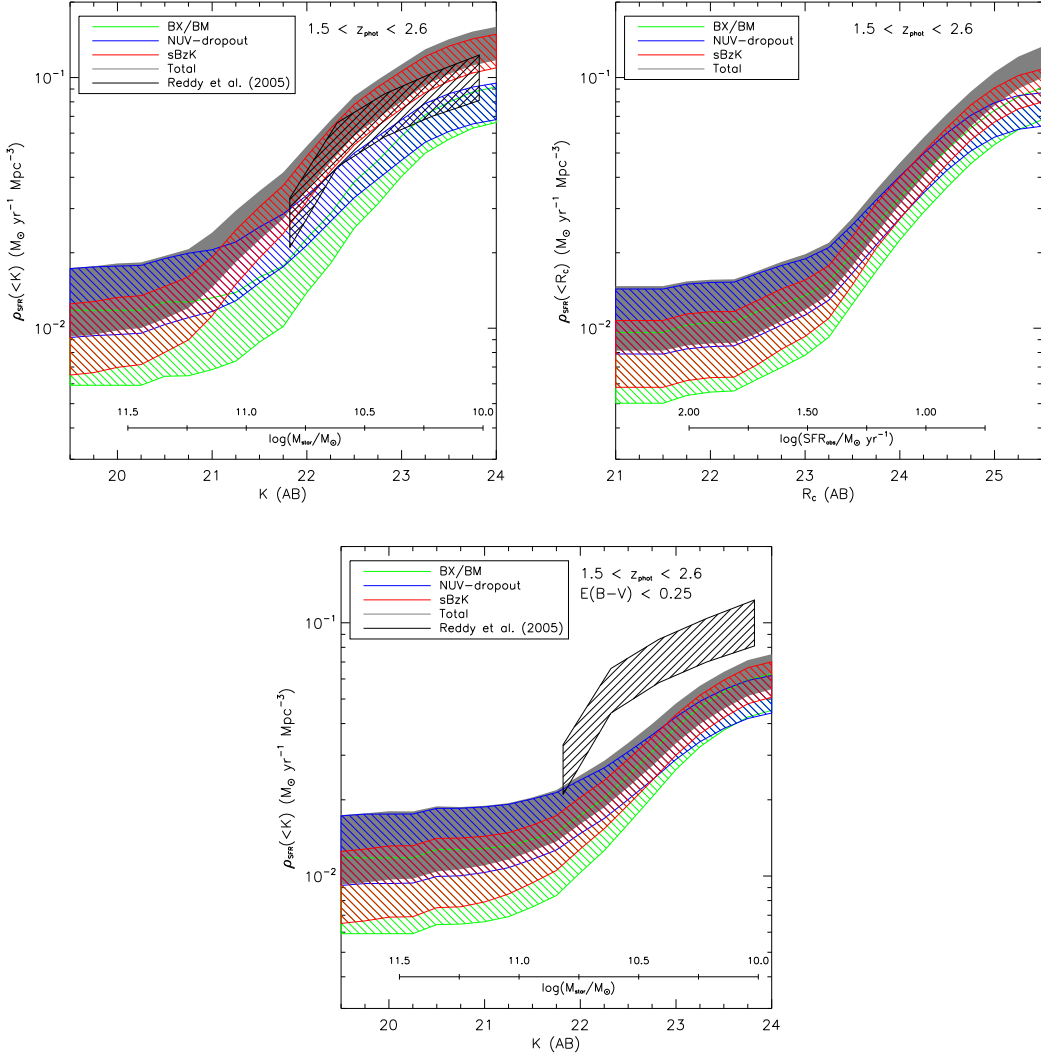


Figure 5.30 – The accumulated SFR density against K - (top left) and R_C -band (top right) magnitudes from a census of star-forming galaxies at $1.5 < z_{\text{phot}} < 2.6$. The bottom panel limits the K -band sample to sources with $E(B - V) < 0.25$ mag. Shaded regions include uncertainties in the SFR due to the z_{phot} accuracy and cosmic variance estimates from Somerville et al. (2004). The census total is shown by the shaded grey region while those determined using the sBzK, BX/BM, and NUV -dropout methods are shown by the hatched red, green, and blue regions, respectively. A stellar mass or observed 1700Å SFR scales are provided for guidance. The stellar mass is from Daddi et al. (2004) SED-fit relation. For the UV SFR, we adopt Kennicutt (1998) relation, which assumes a Salpeter IMF. This figure, combined with Figure 5.30a, illustrates that dusty star-forming galaxies contribute as much star formation as the low reddening galaxies.

et al., 2004). We find good agreement with Reddy et al. (2005) in the accumulated SFR density relative to K , $\rho_{\text{SFR}}(< K)$. It appears that the SFR density down to a stellar mass limit is mostly from sBzK galaxies. Such sources are not only numerous in the sky (13 arcmin^{-2} for $K \lesssim 24.0$), but have significant star formation.

To understand what fraction of the accumulated SFR density is from dusty or less dusty galaxies, we show the distribution of $\rho_{\text{SFR}}(< K)$ for $E(B - V) < 0.25$ mag in Figure 5.30c. A comparison with the total accumulated SFR density (regardless of the dust content) indicates that one-half of the census’s SFR density is from galaxies with relatively low dust content. In terms of number of galaxies, we have 3756 (1128) with $E(B - V) < 0.25$ mag ($E(B - V) > 0.25$). Therefore, while one-fourth of the census is composed of dusty star-forming galaxies, they contribute as much star formation as the remaining three-quarters with relatively little dust. If a cut of $E(B - V) = 0.4$ mag (recall that the BX/BM and *NUV*-dropout techniques are sensitive towards $E(B - V) < 0.4$ mag) is adopted to distinguish between dusty and “less” dusty galaxies, we have $\approx 70\%$ of the “total” SFR density from the latter.

5.5.4 The Completeness of Photometric Selection Techniques

In Figure 5.31, we show the redshift distribution for the different photometric selection techniques against the photo- z samples. It is apparent that the photometric selection techniques identify a subset of galaxies with $z_{\text{phot}} = 1 - 3$. Currently, no studies have discussed the completeness of such techniques by using photo- z samples as a reference. Our preliminary comparison between the two samples indicates that a noticeable ($\approx 40\%$) fraction of galaxies with $z_{\text{phot}} = 1.0 - 1.5$ are missed. This is due to (1) the BzK selection was designed to look at $z \gtrsim 1.5$,

(2) two-thirds of the BM galaxy population lie at $z_{\text{phot}} > 1.5$, (3) almost all BX galaxies are above $z_{\text{phot}} > 1.5$, and (4) the *GALEX*/NUV filter only detects a Lyman continuum break at $z_{\text{phot}} > 1.5$. However, as we discussed previously, recently available *Hubble*/WFC3 filters are beginning to be used to select galaxies via the Lyman break at $z \sim 1.3$, and such sample will be able to address this loss.

5.6 Discussion

In the previous section, we discussed about the sample overlap between the different techniques to photometrically select $z \approx 1 - 3$ galaxies and determined the SFR density from a census of LBGs, star-forming BzK galaxies, and BX/BM galaxies. We now discuss these results and their implications.

We emphasize the similarity between the z_{phot} distribution for sBzK and the K -band photo- z samples for $z > 1.5$. This shows that the sBzK method is able to identify almost all (85%) high- z galaxies selected through a K -band limited z_{phot} sample. This evidence, combined with the high fraction of overlap between BX/BM/ U -dropout and sBzK for $K \lesssim 24$ AB mag, and the likelihood that faint (blue) UV-selected galaxies will be detected with deeper K -band imaging, strongly suggests that future $z \approx 1 - 3$ studies should focus on a very deep K -band imaging (e.g., the Ultra-VISTA survey). But until such a deep ($K = 25 - 26$ AB) survey with multi-wavelength data (like the SDF) is available, the UV selection techniques (either the $U_nG\mathcal{R}$ or NUV -dropout method) are currently the only way to identify low stellar mass $z \sim 2$ galaxies. Optical data do not suffer from source confusion as much as the NUV data, so the BX/BM method has a better advantage for going deep in the rest-UV.

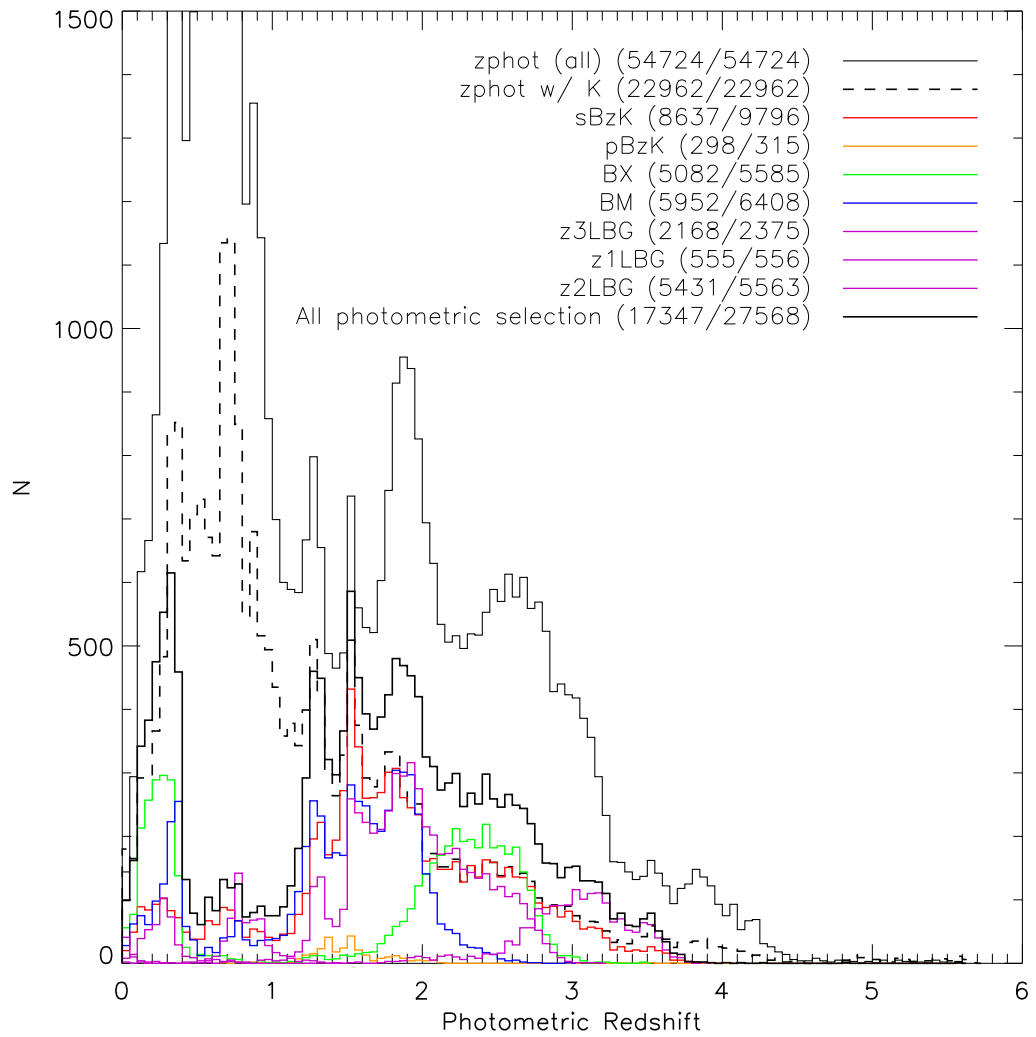


Figure 5.31 – The z_{phot} distribution for photo- z selected samples are shown by the dashed line (5BK3 σ) and solid top black line (full sample; 5B5 σ and 5BK3 σ). These are identical to those provided in Figure 5.8. The z_{phot} distributions are also shown for the different photometric selection techniques from the Shallow sample: sBzK (red), pBzK (orange), BX (green), BM (blue), and $z \sim 1$, $z \sim 2$, and $z \sim 3$ LBGs (all purple). The combination of these techniques gives the thick solid black line. Values in parentheses represent the fraction that have z_{phot} estimates except for the “All photometric selection” thick black solid line. The latter consists of the number with z_{phot} after removing sample overlap versus the full photometric selection sample with z_{phot} .

Our census of star-forming galaxies using the BzK ($K < 24$), Lyman break ($V < 25.4$), and BX/BM ($R_C < 25.5$) techniques shows that the UV selection methods is able to obtain 85% of the SFR density from galaxies with $E(B - V) < 0.25$ mag. This represents about three-quarters of our census by number. However, there appears to be a prominent population of galaxies with high ($E(B - V) > 0.25$ mag) dust extinction. These galaxies contribute 50% to the total SFR density that we derived from our census of star-forming galaxies with $K \lesssim 24$ mag ($\sim 10^{10} M_\odot$). Deeper optical selection (e.g., $R_C < 26.0$) for the BX/BM methods would be able to identify a fraction of the sBzK galaxies with $K \sim 24.0$ and $R - K < 2.0$.

5.7 Future Work

The results presented in this chapter were made possible with a large set of pan-chromatic deep data. We hope to further improve our photometric redshifts and strengthen many of our results through several means.

Mid-infrared data. While *Spitzer* data were acquired for most of the SDF and reduced, the inclusion of such data into our analyses was delayed. We attempted to take a PSF modelling approach but encountered problems with the poor spatial sampling of the *Spitzer*/IRAC point response functions. The *Spitzer*/IRAC data are expected to improve the accuracy of photometric redshifts since they cover the $1.6\mu\text{m}$ peak from the population of red giant stars at $z \approx 1 - 3$. Extremely deep IRAC data were obtained through one of our fellow SDF collaborators (E. Egami), and those data will be merged with the shallower, wider data that have been obtained. The $3.6\mu\text{m}$ data will prove rather useful in identifying star-forming massive galaxies at $z \gtrsim 2.5$ by using a similar two-color selection technique as the BzK method.

Narrow-band imaging. In addition, our photometric redshifts were derived from broad-band and intermediate-band data. Some preliminary work to include the measurements from imaging in five narrow-band filters did not show significant improvement, but this may be due to (1) the available emission-line templates used in EaZy did not span a broad range of parameter space (an updated [unreleased] version of EaZy has greater flexibility in emission lines; G. Brammer, priv. comm.), and (2) the greatest gain would be for the NB excess emitters, so it may appear that little improvement is seen for 90% of the photometric redshift sample. We hope to investigate this further and include these NB data to have at least 20-band photometry. Nevertheless, the z_{phot} derived for NB excess emitters show good agreement with what was predicted in Chapter 2.

Resolving source confusion in the NUV . As mentioned in § 5.2, measurements in the *GALEX* bands suffer from source confusion with the poor spatial resolution, and a simple procedure was developed to identify measurements affected by flux contamination from neighboring sources. A more sophisticated approach of modelling the sources with the PSF will be done in the near future. The modelling is simplified since almost all of the SDF sources appear unresolved, even typical galaxies that are $1''$ in size in the optical images. We expect that photo- z for some “outliers” will be improved. Furthermore, the ability to manage source confusion will allow us to increase the sample of $z \sim 2$ LBGs, as 20% are statistically expected to be missed (i.e., their $NUV - B$ color are observed to be bluer because of this problem).

Clustering analyses. Although not discussed in this chapter, we will investigate the spatial clustering of the different population of galaxies. Our field-of-view coverage samples a wide enough angular distance, and the samples sizes are unmatched by any other survey. One new investigation that we will consider is the two-point correlation function between two different sets of galaxy population,

for example, the sBzK sample against the UV-selected samples. This has yet to be done, and it would be interesting to examine how the low-mass UV-selected galaxies are spatially distributed relative to massive and reddened star-forming galaxies at $z \sim 2$.

Stellar mass density. Much of this chapter has focused on the SFRs of $z \sim 2$ galaxies, and the inclusion of the *Spitzer*/IRAC data into the modelling of the SEDs will provide better constraints on the stellar masses of our galaxies to obtain stellar mass function and densities at $z \sim 2$. This can then be compared to the integral of the SFR density for $z > 3$.

Extremely red objects. In our comparison of different photometric selection techniques, we were unable to include extremely red objects (EROs) using R and K data in our analyses due to time constraints. Such objects will be included, and we will be able to select using a $R - K > 5.3$ mag down to $K = 22.8$ mag. This will be one of the deepest surveys to date for EROs over a reasonable large area given the depth of the R_{C} -band data.

Additional spectroscopic redshifts. Finally, our comparison of photometric and spectroscopic redshifts in § 5.3.1 did not utilize all the spectra that we have obtained, as some of these data have yet to be fully analyzed. We hope to increase the spectroscopic sample by 50% with spectra from MMT/Hectospec, Keck/DEIMOS, and Subaru/MOIRCS.

5.8 Conclusions

We have conducted a large photometric survey of galaxies at $z = 1 - 3$ by synthesizing measurements from 15 broad- or intermediate-band filters covering observed wavelengths of 1500Å to 2μm. This survey is unique due to its size (0.25 deg²; 5.6×10^6 Mpc³ for $z = 1 - 3$), depth, and reliable photometric redshifts

derived for ≈ 23000 K -band selected sources (≈ 65000 if you include optically selected sources). The accuracy of our photo- z stems from the ability to cover both the Lyman continuum and Balmer/4000Å break at $z \sim 2$ and the multiple bands that we have. Most photo- z surveys use 10 photometric bands or less, are limited to accurate redshifts below $z \lesssim 1$ and $z \gtrsim 3$, and suffer from a common photo- z problem of miss-classifying high- z galaxies as $z \sim 0.3$. Compared to a spectroscopic sample, we find that our photometric redshifts are accurate to 2.4% (1σ) for $z \lesssim 1.8$. We have also examined the z_{phot} for ≈ 4500 NB excess emitters at $z \approx 0.25 - 1.5$, and found excellent to good agreement between our derived z_{phot} and the predictions from using simple multiple rest-frame optical colors (see Chapter 2). These evidences indicate that the photo- z that we have generated are reliable.

In addition, the combination of deep optical and relatively deep NIR data provides a large and representative sample of $z = 1 - 3$ galaxies covering a wide range in stellar mass, dust content, and SFR. With ≈ 25000 (≈ 22000 with z_{phot}) galaxies, we are able to study statistically the overlap of different galaxy populations (BX/BM, LBG, and BzK) obtained from photometric selection techniques. We also investigated the completeness of these techniques against a sample derived purely from photo- z . The main results for this chapter are:

Redshift distribution. We determined (with accurate photo- z) that 69.9% of BXs, 76.4% of BMs, 78.9% of U -dropouts, 84.4% of sBzKs, and 98.5% of NUV -dropouts have $z_{\text{phot}} = 1 - 3.5$, showing that these techniques do indeed select high-redshift galaxies. We find that the BX, BM, and U -dropout methods suffer from $z_{\text{phot}} < 0.5$ contamination at the 28.1%, 16.4%, and 15.4% levels, respectively. This problem is attributed to the Balmer/4000Å break occurring between the U and B filters, rather than a Lyman break. We also find that the NUV -dropout technique has low (9.2%) contamination from “interlopers” at

$z = 1.0 - 1.5$, which resolves a previous concern that contamination fractions in Chapter 4 could be underestimated. Also, the technique does not suffer from $z < 0.5$ interlopers, since the Balmer break is redward of the NUV. We have also selected *FUV*-dropouts, but found that the majority of them are at $z < 1$. This is likely due to the limited depth in the *FUV* that we were able to survey.

Selection bias and completeness of techniques. We confirmed a common hypothesis, that each photometric selection is biased towards some subset of galaxies not fully representative of the entire galaxy population. By modelling the SED of thousands of photometrically-selected galaxies, we find that the BzK method targets more massive and dusty galaxies, while the BX, BM, and *U*-dropout methods identify galaxies of lower stellar mass with little reddening. Compared to a combined census of photometrically selected galaxies (BX/BM, LBG, and BzK), we find that any UV or IR techniques find at most 60 – 80% at the peak of their redshift sensitivity. However, these techniques are optimized for a certain redshift range, so relative to a full $z = 1 - 3$ photometric census, the BX/BM, *NUV*-dropout and sBzK obtain about 30%. This strongly indicates that combining multiple techniques is favored for a census of high-redshift galaxies and their SFRs. We determined that the BX/BM method is capable of identifying 72% of galaxies with SFR of $30 M_{\odot} \text{ yr}^{-1}$ or lower, and this represents 61% of the overall SFR for the census.

Sample overlap between galaxy populations. Among the star-forming BzK-selected galaxies, the overlap fraction with the BX/BM/*U*-dropout increases at fainter *K* luminosities, consistent with Reddy et al. (2005). However, with a larger sample of massive sBzK galaxies, we determined that the overlap fraction is much smaller by $\lesssim 5$ times than what was reported in Reddy et al. (2005) for bright *K* magnitudes. We argue that this is due to the smaller sample that they used. Our study also show that 60 – 80% of $z \geq 1.5$ sBzK galaxies have a Ly-

man break, thus meeting the *NUV*-dropout criteria. Unlike the BX/BM method, this overlap fraction is independent of K mag, indicating that the Lyman break technique is relatively more sensitive to massive galaxies. Furthermore, we found that 79.3% of $z \sim 2$ LBGs are either BX or BM galaxies. This fraction increases to 83.7% when excluding objects that are below $z_{\text{phot}} \leq 1.5$ since such sources do not have a break in the *NUV*. This evidence indicates that the 912Å break is ubiquitous in $z \sim 2$ galaxies. Thus the *NUV*-dropout selection differs from the BX/BM selection with the ability to identify more massive and reddened galaxies.

SFR density from a census of UV- and NIR-selected galaxies. We determined that the comoving SFR density at $z_{\text{phot}} = 1.5 - 2.6$ is $0.14 \pm 0.02 \text{ M}_{\odot} \text{ yr}^{-1} \text{ Mpc}^{-3}$ from a joint census of BzK galaxies, BX/BM galaxies, and LBGs. This census was limited to galaxies with $K \lesssim 24$ (corresponds to $\approx 10^{10} \text{ M}_{\odot}$). Our measurement of the SFR density agrees reasonably well with [Reddy et al. \(2005\)](#). We examined the contribution to the SFR density relative to the dust properties of our galaxies, and find that galaxies below and above $E(B - V) = 0.25$ mag contribute equally to the SFR density. This indicates that dusty galaxies are important for a full census of star formation at $z \sim 2$.

CHAPTER 6

The State of Star Formation Rate Estimates and Conclusions

In this dissertation, we used narrow-band imaging, photometric selection, and photometric redshift to efficiently identify star-forming galaxies from $z \approx 0.07$ to $z \approx 3.0$. These samples allow us to measure the SFR density over a significant fraction of the universe (≈ 10 Gyrs). We find that the comoving SFR density (ρ_{SFR}) evolves strongly with redshift, $\rho_{\text{SFR}} \propto (1+z)^{\sim 3-4}$, implying a factor of 10 increase from $z \sim 0$ to $z \sim 1$. Our census study also shows that a significant population of dusty galaxies exists at $z \sim 2$, and represents one half of the SFR density at $z \sim 2$. We now discuss these observational measurements in the context of predictions from cosmological simulations and remark on the systematic issues affecting both observations and theoretical predictions. We conclude with a discussion of future prospects of high redshift star formation surveys.

6.1 SFR Estimates from Cosmological Simulations

Several simulations have provided estimates of the SFR density. In general, these simulations begin with the initial conditions set forth by cosmological constraints on the energy/matter density of the universe.¹ They differ in the numerical tech-

¹Note that most simulations adopted the concordance Λ CDM cosmology, but there are some that use more recent determination of the cosmological parameters.

niques that were used, the volume simulated, and certain physical behaviors that could affect the growth of galaxies. One of the first models to predict the SFR density was Cole et al. (2000). Their model used the semi-analytical approach where they combined realizations of merger trees with prescriptions for gas cooling, star formation, feedback, and stellar population. More recently, Croton et al. (2006) used the Millennium simulation, the largest N-body simulation of dark matter, and combined it with their own semi-analytical code that included AGN feedback through a so called “radio mode.” Also, Somerville et al. (2008) have provided estimates for the SFR density using their own semi-analytical model with and without feedback.

Aside from semi-analytical models, SPH simulations have been developed to provide constraints on the SFR density. These simulations avoid dealing with simplistic equations for many of the underlying physics, and look at the thermodynamics and kinematics of gas within halos. The largest simulations are those developed by Nagamine et al. (2006) and Choi & Nagamine (2009). These simulations surveyed volumes with 60 and 100 h^{-1} Mpc on a side.

6.2 A Comparison between Theory and Observation

We illustrate in Figure 6.1 the predictions from these models compared to our SFR density measurements and some of those present in the literature. We note that some of our measurements differ from those published in previous chapters. Our [O III] measurements have been updated to adopt the M_B -dependent $F([O\ III])/F(H\alpha)$ ratio, which was described in Chapter 2. The net result is a higher SFR density measurements at $z \approx 0.64$ and $z \approx 0.84$, since at these redshifts more luminous galaxies are probed (thus a lower [O III]/H α flux ratio is used). The SFR density from a census of $z = 1.5 - 2.6$ star-forming galaxies only consider

galaxies with $K < 24$ ($\sim 10^{10} M_\odot$), so this should be treated as a lower limit.

The majority of the models adopted a Salpeter IMF except for those generated by [Somerville et al. \(2008\)](#) and the Fossil model of [Nagamine et al. \(2006\)](#). To consistently compare with our SFR density measurements, which adopted a Salpeter IMF, we have scaled their numerical predictions by a factor of 1.7. We find that almost all of the models appear to agree with observational measurements at $z \lesssim 1$ to within the observed scatter. Note that SFR density measurements below $z \sim 0.5$ disagree at the factor of two level. These measurements are all determined using H α , so systematic issues due to different SFR indicators is not the reason for the discrepancy. However, with these measurements being at low- z , it is likely that the surveyed volumes are not sufficient enough to be less affected by cosmic variance (we discuss this later).

There is one model by [Somerville et al. \(2008\)](#) that significantly disagrees with observations at low redshift by having prescriptions for feedback turned off. They argue that feedback is important for producing the decline in the SFR density over the past ≈ 7 Gyrs. While many of the models appear consistent at low- z , they typically fall below measurements at $z = 1 - 3$ at the 2σ significance level. That is, the models only show a factor of $2 - 5$ ($2.3 - 7$) in the SFR density between $z = 0$ and $z = 1$ ($z = 1.5$). The [Somerville et al. \(2008\)](#) “halo quenching” model with feedback agrees with measurements between $z = 1 - 2$ given the uncertainties in the measurements; however, it disagrees with our low- z SFR density measurements.²

These comparisons illustrate that there are still some disagreements between measured SFR density and those estimated from cosmological simulations. Our measurements, taken at face value, show a more rapid evolution in the SFR den-

²This model does agree with other $z \sim 0$ SFR density measurements that are ~ 2 times higher.

sity than those reported elsewhere. Certainly, an underlying assumption is that observational measurements and numerical simulations can *both* be trusted. We discuss below systematic problems that might arise to cause these discrepancies and suggest future improvements.

6.3 Potential Problems with Observations

Measurements of the SFR density suffer from many systematic corrections. These include field-to-field fluctuations, dust correction, the faint-end slope of the LF, and the reliability of using a given SFR indicator.

It should be indicated that a few studies (e.g., Hopkins & Beacom, 2006) have compared SFR density measurements with measurements of the stellar mass densities. The basic idea is that the integral of the cosmic star formation history above a given redshift should yield the stellar mass densities determined from summing the stellar masses at the same redshift. However, discrepancies have been found at $z > 1$ in the form of SFR density being higher than it should to produce the observed stellar mass densities. These studies have proposed for an evolution in the stellar IMF such that at high- z , the IMF is more “top heavy.” This implies that the SFR densities are in fact lower since it is normalized with respect to a Salpeter IMF. We note that before invoking any evolution in the stellar IMF, some of these issues must be addressed and understood before such a possibility is further considered.

6.3.1 Cosmic Variance

Observational surveys can be strongly affected by the inherent variations due to their spatial distribution. We have noticed this in individual NEWFIRM

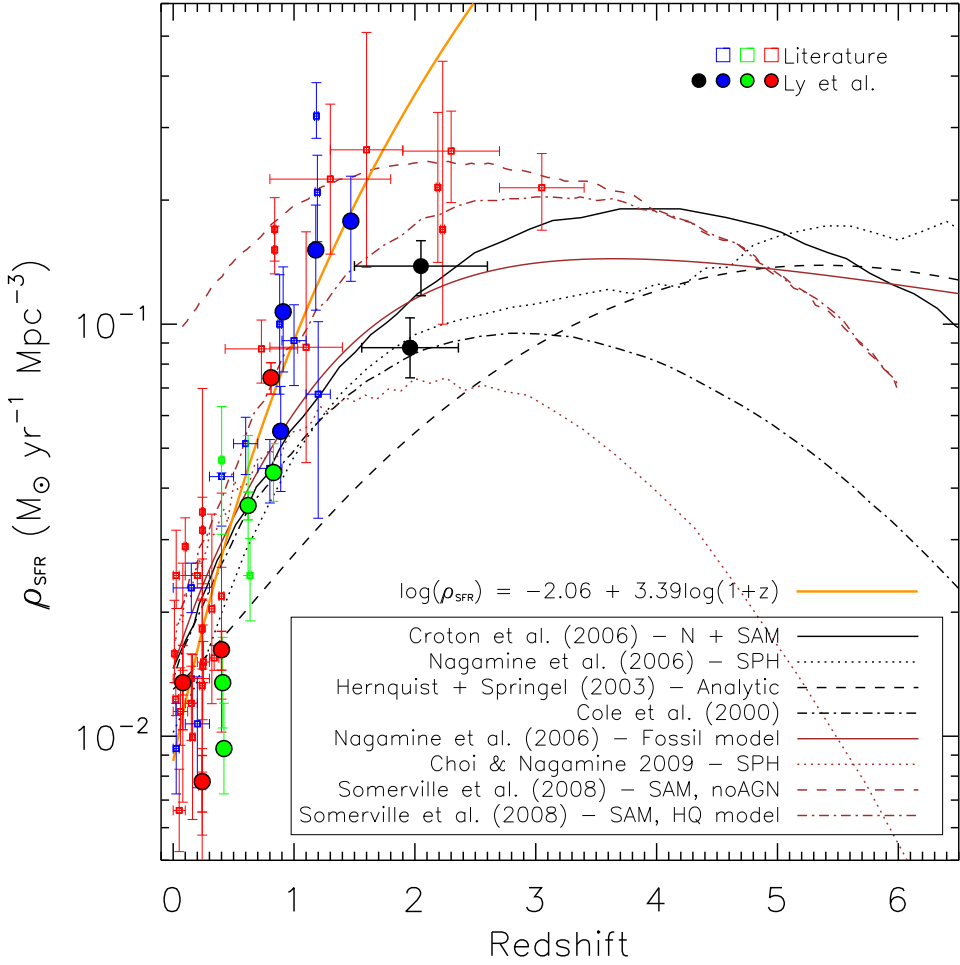


Figure 6.1 – The star formation history from measurements determined in this dissertation (filled circles) and some measurements found in the literature (open squares). The color of these points corresponds to the SFR indicators that were used. Red is H α , green is [O III], and blue is [O II]. The two black circles are the SFR density of $z \sim 2$ LBGs and the census of $z_{\text{phot}} = 1.5 - 2.6$ star-forming galaxies with $K < 24$. The latter is the higher of the two points. Predictions from numerical simulations are indicated by either the black or brown curves. They are: [Croton et al. \(2006\)](#) (solid black), [Nagamine et al. \(2006\)](#) (dotted black), [Hernquist & Springel \(2003\)](#) (long-dashed black), [Cole et al. \(2000\)](#) (dot-dashed black), Fossil model by [Nagamine et al. \(2006\)](#) (solid brown), [Choi & Nagamine \(2009\)](#) (dotted brown), [Somerville et al. \(2008\)](#) model without AGN feedback (dashed brown), and [Somerville et al. \(2008\)](#) ‘halo quenching’ model (HQ; dot-dashed brown). The orange line is a least squares fit that [Dale et al. \(2010\)](#) determined for a set of $z < 2$ SFR density measurements. This was also plotted in Figure 3.13.

pointings for H α survey discussed in Chapter 3. As pointed out in Chapter 2, H α measurements at $z \approx 0.24$ show a factor of 2 scatter due to the small areas that are subtended. These field-to-field fluctuations affect the bright-end of the LF, hence Φ_* and L_* of the Schechter fits. Certainly larger surveys are the answer, but there is a point of diminishing return. Using the $z = 0.81$ H α and $z = 1.47$ [O II] LFs as a proxy for the expected LF, we find that narrow-band surveys of bright galaxies ($> 0.5L_*$) as large as 5 deg 2 suffer from cosmic variance at the $\sigma_{\text{CV}} = 0.2 - 0.3$ level. Thus, NB surveys must image ~ 10 deg 2 or use multiple filters to probe enough comoving volume.

6.3.2 Dust Attenuation

Observations of young stars are always attenuated by dust that are embedded in star-forming regions. For measurements reported using emission lines, we have adopted a luminosity-dependent extinction correction developed by Hopkins et al. (2001). To determine if this correction is reasonable, a comparison was made between the SFR derived from SED modelling and the H α SFR with Hopkins et al. (2001) extinction for 300 $z \approx 0.4$ H α emitters. We found good agreement with 0.28 dex scatter. Furthermore, we found that using the $E(B - V)$ estimated from SED modelling and adopting the Calzetti et al. (2000) extinction law provided a better agreement ($\sigma = 0.20$ dex). The latter yielded a SFR–H α extinction-corrected luminosity conversion value of $10^{-41.0 \pm 0.2}$ ergs s $^{-1}$ /M $_{\odot}$ yr $^{-1}$, which is consistent with Kennicutt (1998)'s $10^{-41.1}$ ergs s $^{-1}$ /M $_{\odot}$ yr $^{-1}$. Ideally, estimates of the Balmer decrement are needed to address dust attenuation at the individual source level. While this is spectroscopically tedious, having the Balmer decrement and $E(B - V)$ from SED modelling for a subset of sources may suffice to obtain the H α luminosity.

6.3.3 The Faint-end Slope

In general, estimates for the “total” SFR density have extrapolated the faint-end slope (α) to account for the population of galaxies that fall below their observation limit. And in some studies where their data are not deep enough, a particular value for the slope (that other studies have reported) has been adopted. These approaches were fine 10 years ago, but measurements now show scatter at the 0.3 dex level, requiring more detailed attention to the faint galaxies for improved accuracy. For example, an uncertainty of $\Delta\alpha = 0.1$ for $\alpha = -1.6$ ($\alpha = -1.8$) would correspond to 0.1 dex (0.3 dex) uncertainties associated with the luminosity/SFR density. We note that recent measurements (Reddy et al., 2008; Bouwens et al., 2006) have found that the UV LF is steep ($\alpha \approx -1.8$) at $z \sim 2$ and $z \sim 6$. This strongly suggests that deep surveys at high redshift are needed to better constrain the contribution of star formation from faint galaxies.

Our measurements reported in Chapter 2 are the most sensitive to low-SFR galaxies compared to any other existing NB surveys at similar redshifts. And large-format CCDs will provide significant gains towards imaging large areas at unprecedented depth. The measurements provided in Chapters 3 and 4 were more difficult to obtain and were limited to brighter galaxies. More sensitive higher spatial resolution NIR detectors will be able to probe down to $\sim 0.1L_*(\text{H}\alpha)$ at $z \sim 1 - 2$. For our $z \sim 2$ LBG survey, the biggest problem that prevented us from going deeper was the spatial resolution of *GALEX*. Recently, *Hubble*/WFC3 UV data were obtained (Hathi et al., 2010). These measurements went 1 magnitude deeper with much higher spatial resolution, but surveyed ~ 50 arcmin 2 . The combination of using *GALEX* to probe the more luminous end and *Hubble* for the faint-end will provide strong leverage on the LF Schechter parameters for the majority of star-forming galaxies at $z \sim 2$.

6.3.4 Using [O II] and [O III] as SFR Indicators

Like most other $z \gtrsim 0.5$ emission-line surveys, other nebular lines were used in place of H α . We were fortunate to have simultaneous measurements of H α and [O III] at $z = 0.4$, allowing [O III] to be used as an indicator. The amount of scatter in this relation is 0.20 dex, which we included within the uncertainties of our H α SFR density measurements that were derived from [O III]. One assumption that we do make is that the [O III]/H α – M_B relation does not evolve from $z = 0.40$ to $z = 0.84$. One piece of preliminary evidence that supports this is the [O III]/H α flux ratio determined from optical spectroscopy and NB1187 measurements for $z \sim 0.81$ H α emitters. They show, to first order, reasonable agreement with what we found at $z \sim 0.4$ when extrapolated to the absolute B -band magnitude of these H α emitters at $z \sim 0.8$.

In the local universe, the [O II]/H α flux ratio is known to within 30% (Kenricutt, 1998). Thus, the uncertainties for [O II] measurements reported in Figure 6.1 have been inflated to account for this systematic uncertainty. As such, it cannot be argued that our measurements are systematically too high. NIR spectroscopy for a representative sample of $z \sim 1 - 1.5$ is prudent to obtain H α measurements for such high redshift galaxies so that [O II] surveys can be reliably used.

6.4 Potential Problems with Numerical Simulations

6.4.1 Resolution

The processes that drive star formation have yet to be fully understood with smooth-particle hydrodynamical simulations due to the complexity involved. Such simulations must account for heating and cooling, gas compression, turbulence,

and shock effects, to name a few physical phenomena. The current SPH cosmological simulations are intended to probe a large cosmological volume, thus limiting spatial and particle mass resolutions. However, star formation happens on scales much smaller than the resolution limit. Therefore, while the amount of baryonic matter that has accumulated in dark matter halos is approximately known, how this cold material is further converted to stars is poorly understood. Unfortunately, the current computational power is incapable of simulating the resolution needed to study star formation in a cosmological context. More sophisticated techniques must be developed by theorists to push towards higher resolution yet surveying large volumes.

6.4.2 Pitfalls of Semi-Analytical Models

Much of the comparisons discussed previously utilized semi-analytical models to provide theoretical predictions on the cosmic star formation history. This technique has been viewed unfavorably by some members of the astronomical community, since the model parameters are adjusted to match a set of data. While the semi-analytical models have been able to reproduce certain observed properties, they also have failed to produce many other observed properties. Continued improvements to the prescriptions used by semi-analytical models and additional observations are both needed to maintain viability of semi-analytical models.

6.5 Star Formation at Higher Redshifts

This dissertation has discussed SFR density measurements below a redshift of 3 using nebular emission lines and the UV continuum. To further trace the cosmic

star formation history, measurements must be pushed to higher redshifts. Studies have already extended the UV techniques to redshift above $z = 3$. However, as discussed previously, the use of the UV suffers from more dust extinction, which could introduce systematics into the measurements. One of the goals of our NewH α survey is to extend H α SFR measurements to $z \sim 2$. At this redshift, we will be able to compare the SFRs derived by both H α and the UV. Such future work could lead to an ability to calibrate high- z measurements since H α at $z > 3$ will not be easily available in the near future.

We note that it has been speculated that SFR density measurements could be used as a cosmological probe if they were reliable ([Robinson & Silk, 2000](#)). This is driven by the idea that the SFR density above $z = 3$ is dominated by the initial conditions, since the majority of halos have not fully grown to a point where feedback and other processes may regulate the star formation in galaxies. Thus the SFR in the early universe is strongly correlated with the matter density and the expansion rate of the universe. Such a possibility is intriguing, but measurements are far from the precision necessary to accomplish this goal.

APPENDIX A

Chapter 4: Individual Sources of Special Interest

In most cases, the confirmed LBGs showed no unique spatial or spectral properties. However, 3 cases are worth mentioning in more detail.

1. SDFJ132431.8+274214.3 (179350). Upon careful examination of the 2-D spectra, it appears that the Ly α emission from this source is offset by $\approx 1.1''$ (9 kpc at 107° east of north) from the continuum emission, which is shown in Figure A.1a. The extended emission appears in the individual exposures of 15 – 30 minutes. The deep ($3\sigma = 28.45$) *B*-band image (Figure A.1b) reveals that there are no sources in this direction and at this distance, assuming that the continuum emission in the spectrum corresponds to the bright source in the *B*-band image. The two sources located below the bright object in Figure A.1b are too faint for their continuum emission to be detected with LRIS. Also, absorption features seen in the 1-D spectra (see Figure 4.3a) are at nearly the same redshift as Ly α . This indicates that the Ly α emission is associated with the targeted source, rather than a secondary nearby companion.

Extended Ly α emission galaxies are rare (e.g., [Saito et al., 2006](#), have the largest sample of 41 objects), and the extreme cases are extended on larger (~ 100 kpc) scales, such as LAB1 and LAB2 of [Steidel et al. \(2000\)](#). In addition, extended Ly α emission has been seen in some cases that show evidence for energetic

galactic winds (Mas-Hesse et al., 2003). Either this source is a fortuitous discovery from a dozen spectra, or perhaps a fraction of *NUV*-dropouts have extended Ly α emission. The physical significance of this source is not discussed here, given limited information.

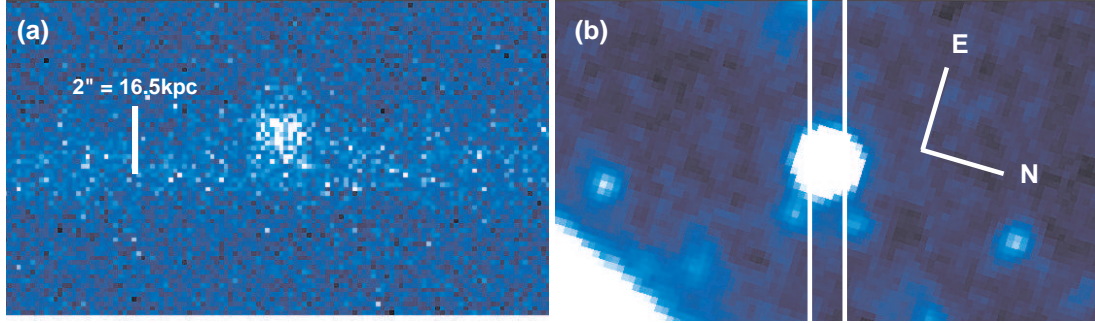


Figure A.1 – (a) The 2-D spectrum with wavelength increasing to the right shows Ly α emission offset by $\approx 1''$ from the center of the continuum. The vertical white line corresponds to $2''$. (b) The Suprime-Cam *B*-band image centered on the targeted source shows that there are no sources in the direction of the extended emission. The two white vertical lines correspond to the slit, so (b) is rotated to have the same orientation as (a), and the vertical scales are the same.

2. SDFJ132452.9+272128.5 (62056). The 1- and 2-D spectra for this source reveal an asymmetric emission line, as shown in Figure A.2a, but with a weak “bump” about 10Å blue-ward from the peak of Ly α emission. The *B*-band image (see Figure A.3) shows two nearby sources where one is displaced $\approx 2''$ nearly in the direction of the slit orientation while the other source is displaced in the direction perpendicular to the slit orientation. It may be possible that the blue excess is originating from the latter source due to a slight misalignment of the slit to fall between the two sources (i.e., they are physically near each other). To confirm this hypothesis, spectroscopy with a 90° rotation of the slit would show two sources with Ly α emission $\approx 800 \text{ km s}^{-1}$ apart.

3. SDFJ132450.3+272316.24 (72012). This object is not listed in Table 4.1, as it was serendipitously discovered. The slit was originally targeting a

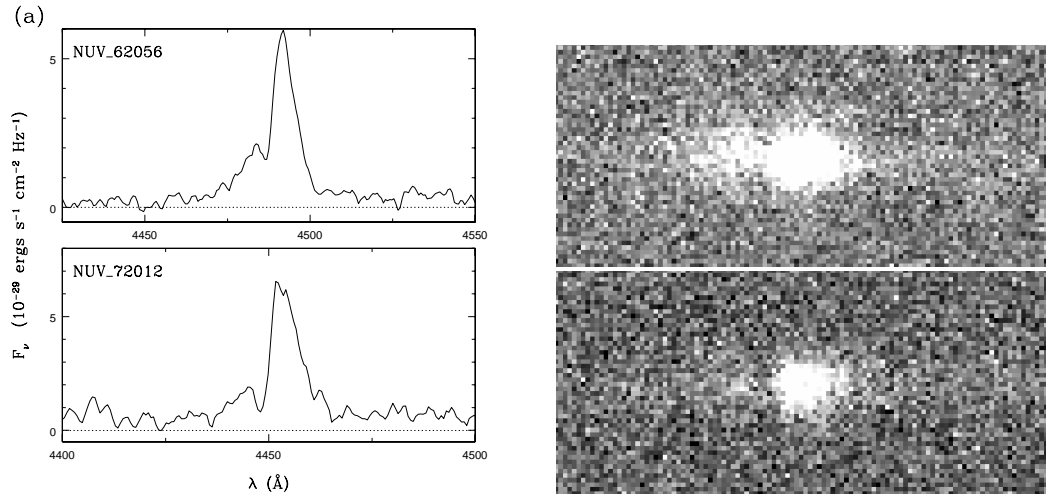


Figure A.2 – (a) One- and (b) two-dimensional spectra for 62056 (top) and 72012 (bottom) centered on the Ly α emission. These objects appear to show weak emission blue-ward of Ly α . See § A for a discussion.

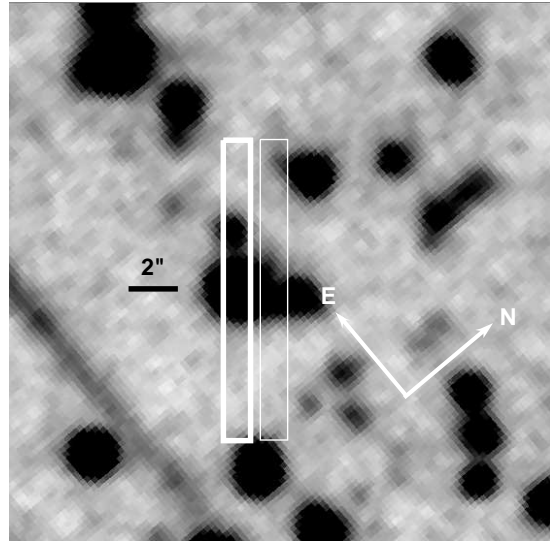


Figure A.3 – B-band image of object #62056. The white box with thick lines is the LRIS slit intended to target the bright object. However, a $1.5''$ offset of the slit in the north-west direction (as shown by the thin white box) may explain the blue excess seen in the 1-D and 2-D spectra (Figure A.2) by including both objects.

narrow-band (NB) emitter. The LRIS-R spectrum showed an emission line at 7040Å, but the blue-side showed a strong emission line that appears asymmetric at \approx 4450Å. One possibility is that the 4450Å feature is Ly α , so that the 7040Å emission line is the redshifted C III] λ 1909, but at $z = 2.6634$, C III] is expected at \approx 6994Å. This \approx 40Å difference is not caused by poor wavelength calibration, as night sky and arc-lamps lines are located where they are expected in both the blue and red spectra. In Figure A.4, the *B*-band image reveals two sources, one of which is moderately brighter in the NB704 image, as expected for a NB704 emitter. These two sources were too close for SExtractor to deblend, but the coordinate above has been corrected. Because the NB704 emitter is a foreground source, the measured *NUV* flux for the other source is affected, and results in a weak detected source in the *NUV*. Thus, this source is missed by the selection criteria of the ver. 1 catalog and those described in § 4.2.2. It is excluded from the spectroscopic sample discussed in § 4.1.

This source is of further interest because it also shows a blue excess bump (shown in Figure A.2) much like 62056, but weaker. This blue bump does not correspond to a different emission line with the same redshift as the 7040Å emission line. Since the bump is 10Å from the strong Ly α emission, it is likely associated with the source producing Ly α . Both 62056 and 72012 were obtained on the second mask. These blue bumps are not due to a misalignment of single exposures when stacking the images together, as other equally bright sources in the mask with emission lines do not show a secondary blue peak. Other studies have also seen dual peak Ly α emission profiles (e.g., Tapken et al., 2004, 2007; Cooke et al., 2008; Verhamme et al., 2008). In addition, high resolution spectra of 9 LBGs have also revealed 3 cases with double-peaked Ly α profile (Shapley et al., 2006), which indicates that such objects may not be rare.

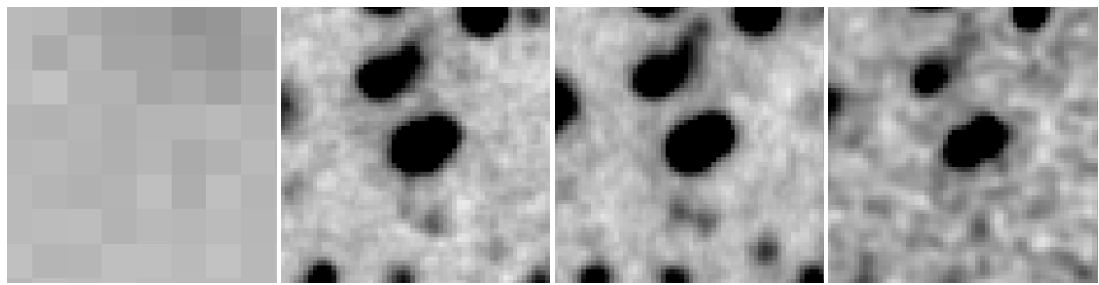


Figure A.4 – From left to right is NUV , B , R_C , and $NB704$. North is up and east is to the left. The source on the right shows a weak excess in $NB704$ relative to the broad-band images.

APPENDIX B

Chapter 5

B.1 Unique Sources from Photometric Selection

About one-half of the Shallow and Faint samples consists of sources that are uniquely selected by only one photometric selection. These sources are of the greatest interest since they indicate that a particular technique is advantageous in culling a galaxy sample that is unavailable by any other techniques. We summarize the uniqueness below:

Passive BzK galaxies. We find that the entire pBzK sample do not overlap with any of the other techniques. These galaxies (at $z \approx 1 - 2$) have the oldest ages $\log(t_{\text{age}}/\text{yr}) \approx 9.0$, the highest stellar mass $\log(M_{\text{stellar}}/M_{\odot}) \approx 11.0$, and span $E(B - V) = 0.0 - 0.4$. Their stellar ages imply that they formed $\Delta z = 0.75$ earlier (median formation redshift is $z = 2.34$), and are likely the descendants of luminous infrared galaxies or massive LBGs with $\text{SFR} \sim 100 M_{\odot} \text{ yr}^{-1}$. These galaxies are important for a stellar mass census survey, but contribute little to the SFR density since their SFR is roughly $0.1 M_{\odot} \text{ yr}^{-1}$.

Star-forming BzK galaxies. We find that the sample of purely sBzKs, compared to UV-selected samples, have similar SFRs ($\sim 10 M_{\odot} \text{ yr}^{-1}$) but are more massive ($\sim 10^9 - 10^{11} M_{\odot}$), cover a broader range in dust extinction ($E[B - V] \approx 0.0 - 0.4$), and are 0.5 dex older. As expected, this technique is therefore capable of identifying massive galaxies with noticeable SFRs at $z = 1 - 2.5$.

BX, BM, and U -dropout galaxies. The UV selection techniques of Steidel et al. appear to identify a unique set of galaxies with relatively younger stellar ages (2×10^8 yr with the lowest at 3×10^7 yr), lower stellar mass ($\sim 10^9 M_\odot$), and $E(B - V) \approx 0.1$. We find that the SFR is systematically lower for the BM and BX techniques, although this is likely a manifestation of redshift dependence of the sample as the SFRs for U -dropout is 0.2 – 0.3 dex higher than the BX or BM galaxies. The poor U -dropout overlap with NIR techniques can be attributed to the redshift of the sample as well as the lack of deep NIR data. It would be prudent to identify a sample of higher redshift BzK galaxies using a set of different filters (e.g., R , J , and $3.6\mu\text{m}$; [Daddi et al., 2004](#)) to investigate the overlap of LBGs at higher redshift with $3.6\mu\text{m}$ -selected galaxies.

$z \sim 2$ Lyman break galaxies. The methodology that we developed to identify LBGs at $z = 1.5 - 2.5$ appears to have significant overlap with the BX/BM or BzK techniques with $\approx 90\%$ of them being identified by any other means. It appears that remaining 10% are galaxies with stellar mass of $10^{10 \pm 1} M_\odot$, cover the same stellar age as other techniques, has an average SFR of $\sim 20 M_\odot \text{ yr}^{-1}$, and span $E(B - V) = 0.1 - 0.4$ (the majority below 0.2 mag). The reason for why these sources were uniquely identify is due to their redshift (about half of them are below $z = 1.5$ where the sBzK and BM technique are less sensitive) and stellar masses. We note that the higher SFRs of NUV -dropout is likely due to the limit adopted for the V -band (our limit is comparable brighter than $R = 25.5$ for BX/BM). The fainter limit yielded a SFR that is systematically lower by 0.3 dex due to the higher contribution of lower SFR LBGs.

B.2 Additional Tables

Table B.1. Summary of Wave-band Detection for the 5BK3 σ Sample

N	FUV	NUV	U	B	V	IA598	R _C	IA679	i'	z'	z _b	z _r	J	H	K
6256	1	1	1	1	1	1	1	1	1	1	1	1	1	1	1
4316	0	1	1	1	1	1	1	1	1	1	1	1	1	1	1
2719	0	0	1	1	1	1	1	1	1	1	1	1	1	1	1
1251	1	1	1	1	1	1	1	1	1	1	1	1	1	0	1
1215	0	1	1	1	1	1	1	1	1	1	1	1	1	0	1
1080	0	0	1	1	1	1	1	1	1	1	1	1	1	0	1
860	1	0	1	1	1	1	1	1	1	1	1	1	1	1	1
620	0	0	0	1	1	1	1	1	1	1	1	1	1	1	1
368	1	0	1	1	1	1	1	1	1	1	1	1	1	0	1
368	0	0	1	1	1	1	1	1	1	1	1	1	0	0	1
280	0	1	1	1	1	1	1	1	1	1	1	1	0	0	1
248	0	0	1	1	1	1	1	1	1	1	1	1	0	1	1
243	1	1	1	1	1	1	1	1	1	1	1	1	0	0	1
226	0	0	0	1	1	1	1	1	1	1	1	1	1	0	1
206	0	1	1	1	1	1	1	1	1	1	1	1	0	1	1
193	0	1	0	1	1	1	1	1	1	1	1	1	1	1	1
175	1	0	0	1	1	1	1	1	1	1	1	1	1	1	1
169	0	0	0	1	1	1	1	1	1	1	1	1	0	0	1
157	1	1	1	1	1	1	1	1	1	1	1	1	0	1	1
141	1	1	0	1	1	1	1	1	1	1	1	1	1	1	1
124	1	0	1	1	1	1	1	1	1	1	1	1	0	0	1
94	1	0	1	1	1	1	1	1	1	1	1	1	0	1	1
92	0	0	0	1	1	1	1	1	1	1	1	1	0	1	1
71	1	0	0	1	1	1	1	1	1	1	1	1	1	0	1
57	0	1	0	1	1	1	1	1	1	1	1	1	1	0	1
57	0	0	0	1	1	0	1	1	1	1	1	1	1	1	1
49	0	0	1	1	1	1	1	1	1	1	1	0	0	0	1
48	1	0	0	1	1	1	1	1	1	1	1	1	0	0	1
48	0	0	0	1	1	1	1	1	1	1	1	0	0	0	1
44	0	0	1	1	1	1	1	1	1	1	1	0	1	0	1
42	1	1	0	1	1	1	1	1	1	1	1	1	1	0	1
35	0	1	0	1	1	1	1	1	1	1	1	1	0	0	1
31	0	0	0	1	1	1	1	1	1	1	1	0	1	0	1
30	0	0	0	1	1	1	1	1	1	1	1	0	1	1	1
28	1	0	0	1	1	1	1	1	1	1	1	1	0	1	1
27	0	0	1	1	1	1	1	1	1	1	1	0	1	1	1
26	1	1	0	1	1	1	1	1	1	1	1	1	0	0	1
26	0	1	0	1	1	1	1	1	1	1	1	1	0	1	1
25	0	0	0	1	1	1	1	1	1	1	1	0	0	1	1
24	0	0	1	1	1	1	1	1	1	1	1	0	0	1	1
22	0	0	0	1	1	0	1	1	1	1	1	1	0	0	1
21	1	0	0	1	1	1	1	1	1	1	1	0	0	0	1

Table B.2. Summary of Photometric Technique Overlap: Shallow Sample

Type	N	z_{avg}	$E(B - V)_{\text{avg}}$ (mag)	$\log(M)_{\text{avg}}$ (M_{\odot})	$\log(\text{SFR})_{\text{avg}}$ ($M_{\odot} \text{ yr}^{-1}$)	$\log(t_{\text{age}})_{\text{avg}}$ (yr)
100000	298	1.581±0.508	0.238±0.181	10.987±0.344	-1.396±2.294	8.986±0.251
010000	2787	1.767±0.760	0.224±0.176	10.140±0.816	0.816±0.728	8.850±0.574
011000	977	1.464±0.357	0.147±0.087	9.668±0.579	0.909±0.418	8.596±0.509
010100	588	2.278±0.485	0.160±0.109	10.237±0.537	1.174±0.461	8.701±0.461
010010	515	2.938±0.414	0.115±0.105	10.538±0.372	1.263±0.419	8.873±0.384
010001	460	1.565±0.170	0.260±0.143	10.510±0.614	1.436±0.615	8.563±0.486
011001	1382	1.764±0.204	0.149±0.083	10.046±0.386	1.167±0.417	8.578±0.414
010101	1160	2.259±0.269	0.132±0.087	10.242±0.397	1.302±0.401	8.714±0.377
010011	89	2.509±0.377	0.121±0.111	10.936±1.246	1.617±0.641	8.792±0.517
000001	372	1.445±0.322	0.248±0.160	10.154±1.012	1.317±0.707	8.430±0.619
001001	931	1.807±0.243	0.136±0.077	9.642±0.864	1.137±0.455	8.343±0.769
000101	874	2.309±0.253	0.100±0.080	9.561±0.817	1.150±0.533	8.195±0.777
000011	100	2.656±0.263	0.089±0.146	9.847±1.330	1.371±1.227	8.171±0.606
001000	1640	1.418±0.431	0.125±0.084	9.072±0.656	0.712±0.492	8.233±0.665
000100	811	2.243±0.561	0.097±0.095	9.316±0.790	0.839±0.498	8.160±0.724
000010	1064	3.074±0.461	0.060±0.085	9.783±0.744	1.064±0.554	8.372±0.565

Note. — Average properties are reported.

Table B.3. Summary of Photometric Technique Overlap: Faint Sample

Type	N	z_{avg}	$E(B - V)_{\text{avg}}$ (mag)	$\log(M)_{\text{avg}}$ (M_{\odot})	$\log(\text{SFR})_{\text{avg}}$ ($M_{\odot} \text{ yr}^{-1}$)	$\log(t_{\text{age}})_{\text{avg}}$ (yr)
100000	298	1.581±0.508	0.238±0.181	10.987±0.344	-1.396±2.294	8.986±0.251
010000	2199	1.691±0.776	0.235±0.185	10.131±0.861	0.792±0.781	8.841±0.593
011000	995	1.451±0.391	0.146±0.088	9.632±0.630	0.878±0.446	8.604±0.525
010100	652	2.277±0.494	0.162±0.107	10.240±0.551	1.143±0.458	8.726±0.469
010010	633	2.912±0.419	0.116±0.103	10.527±0.364	1.208±0.417	8.912±0.392
010001	593	1.568±0.170	0.272±0.144	10.464±0.594	1.378±0.601	8.574±0.488
011001	1516	1.768±0.208	0.150±0.084	10.044±0.382	1.135±0.428	8.600±0.423
010101	1269	2.250±0.274	0.133±0.088	10.240±0.390	1.271±0.411	8.737±0.387
010011	101	2.493±0.394	0.123±0.112	10.874±1.190	1.540±0.652	8.823±0.507
000001	691	1.541±0.351	0.195±0.167	9.552±1.181	1.006±0.700	8.248±0.708
001001	1607	1.851±0.243	0.125±0.076	9.392±0.864	0.985±0.455	8.258±0.801
000101	1596	2.267±0.247	0.091±0.072	9.322±0.829	0.982±0.528	8.141±0.807
000011	206	2.567±0.273	0.065±0.112	9.442±1.081	1.010±0.952	8.142±0.604
001000	2190	1.392±0.467	0.115±0.086	8.935±0.692	0.569±0.533	8.234±0.671
000100	1471	2.215±0.604	0.086±0.092	9.142±0.810	0.681±0.519	8.131±0.731
000010	2002	3.006±0.434	0.050±0.076	9.595±0.692	0.875±0.507	8.367±0.548

Note. — Average properties are reported.

BIBLIOGRAPHY

- Adelberger, K. L., Steidel, C. C., Shapley, A. E., Hunt, M. P., Erb, D. K., Reddy, N. A., & Pettini, M. 2004, ApJ, 607, 226
- Ajiki, M., et al. 2003, AJ, 126, 2091
- Ajiki, M., et al. 2006, PASJ, 58, 113
- Aragón-Salamanca, A., Alonso-Herrero, A., Gallego, J., García-Dabó, C. E., Pérez-González, P. G., Zamorano, J., & Gil de Paz, A. 2003, ASP Conf. Ser. 297: Star Formation Through Time, 297, 191
- Arnouts, S., et al. 2005, ApJL, 619, L43
- Baugh, C. M. 2006, Reports on Progress in Physics, 69, 3101
- Bershady, M. A., Charlton, J. C., & Geoffroy, J. M. 1999, ApJ, 518, 103
- Bertin, E., & Arnouts, S. 1996, A&AS, 117, 393
- Bouwens, R. J., Illingworth, G. D., Blakeslee, J. P., & Franx, M. 2006, ApJ, 653, 53
- Bouwens, R. J., Illingworth, G. D., Franx, M., & Ford, H. 2007, ApJ, 670, 928
- Boylan-Kolchin, M., Springel, V., White, S. D. M., Jenkins, A., & Lemson, G. 2009, MNRAS, 398, 1150
- Brammer, G. B., van Dokkum, P. G., & Coppi, P. 2008, ApJ, 686, 1503
- Brinchmann, J., Charlot, S., White, S. D. M., Tremonti, C., Kauffmann, G., Heckman, T., & Brinkmann, J. 2004, MNRAS, 351, 1151

- Burgarella, D., et al. 2007, MNRAS, 380, 986
- Bruzual, G., & Charlot, S. 2003, MNRAS, 344, 1000
- Calzetti, D., Armus, L., Bohlin, R. C., Kinney, A. L., Koornneef, J., & Storchi-Bergmann, T. 2000, ApJ, 533, 682
- Capak, P., et al. 2004, AJ, 127, 180
- Cardelli, J. A., Clayton, G. C., & Mathis, J. S. 1989, ApJ, 345, 245
- Casali, M., et al. 2007, A&A, 467, 777
- Chapman, S. C., Blain, A. W., Smail, I., & Ivison, R. J. 2005, ApJ, 622, 772
- Choi, J.-H., & Nagamine, K. 2009, arXiv:0909.5425
- Cole, S., Lacey, C. G., Baugh, C. M., & Frenk, C. S. 2000, MNRAS, 319, 168
- Connolly, A. J., Szalay, A. S., Dickinson, M., Subbarao, M. U., & Brunner, R. J. 1997, ApJL, 486, L11
- Cooke, J., Barton, E. J., Bullock, J. S., Stewart, K. R., & Wolfe, A. M. 2008, ApJL, 681, L57
- Cowie, L. L., Songaila, A., Hu, E. M., & Cohen, J. G. 1996, AJ, 112, 839
- Cowie, L. L., Songaila, A., & Barger, A. J. 1999, AJ, 118, 603
- Cowie, L. L., Barger, A. J., Hu, E. M., Capak, P., & Songaila, A. 2004, AJ, 127, 3137
- Croton, D. J., et al. 2006, MNRAS, 365, 11
- Daddi, E., Cimatti, A., Renzini, A., Fontana, A., Mignoli, M., Pozzetti, L., Tozzi, P., & Zamorani, G. 2004, ApJ, 617, 746

- Dale, D. A., Giovanelli, R., Haynes, M. P., Hardy, E., & Campusano, L. E. 1999, AJ, 118, 1468
- Dale, D. A., et al. 2008, AJ, 135, 1412
- Dale, D. A., et al. 2010, ApJL, 712, L189
- Davé, R. 2008, MNRAS, 385, 147
- Dekel, A., et al. 2009, Nature, 457, 451
- Doherty, M., Bunker, A., Sharp, R., Dalton, G., Parry, I., & Lewis, I. 2006, MNRAS, 370, 331
- Dressler, A., Hare, T., Bigelow, B. C., & Osip, D. J. 2006, Proc. SPIE, 6269, 13
- Drozdovsky, I., Yan, L., Chen, H.-W., Stern, D., Kennicutt, R. J., Spinrad, H., & Dawson, S. 2005, AJ, 130, 1324
- Erb, D. K., Shapley, A. E., Steidel, C. C., Pettini, M., Adelberger, K. L., Hunt, M. P., Moorwood, A. F. M., & Cuby, J.-G. 2003, ApJ, 591, 101
- Faber, S. M., et al. 2003, Proc. SPIE, 4841, 1657
- Fabricant, D., et al. 2005, PASP, 117, 1411
- Foucaud, S., et al. 2003, A&A, 409, 835
- Franx, M., et al. 2003, ApJL, 587, L79
- Fujita, S. S., et al. 2003, ApJL, 586, L115
- Furusawa, H., et al. 2008, ApJS, 176, 1
- Gabasch, A., et al. 2004, A&A, 421, 41

- Gabasch, A., et al. 2006, A&A, 448, 101
- Gallego, J., Zamorano, J., Aragon-Salamanca, A., & Rego, M. 1995, ApJL, 455, L1
- Gallego, J., Zamorano, J., Rego, M., & Vitores, A. G. 1997, ApJ, 475, 502
- Gallego, J., García-Dabó, C. E., Zamorano, J., Aragón-Salamanca, A., & Rego, M. 2002, ApJL, 570, L1
- Geach, J. E., Smail, I., Best, P. N., Kurk, J., Casali, M., Ivison, R. J., & Coppin, K. 2008, MNRAS, 388, 1473
- Geach, J. E., et al. 2010, MNRAS, 402, 1330
- Giavalisco, M. 2002, ARAA, 40, 579
- Giavalisco, M., et al. 2004, ApJL, 600, L103
- Glazebrook, K., Blake, C., Economou, F., Lilly, S., & Colless, M. 1999, MNRAS, 306, 843
- Glazebrook, K., Tober, J., Thomson, S., Bland-Hawthorn, J., & Abraham, R. 2004, AJ, 128, 2652
- Grazian, A., et al. 2007, A&A, 465, 393
- Gunn, J. E., & Stryker, L. L. 1983, ApJS, 52, 121
- Hammer, F., et al. 1997, ApJ, 481, 49
- Hanish, D. J., et al. 2006, ApJ, 649, 150
- Hathi, N. P., et al. 2010, ApJ, submitted (arXiv:1004.5141)

- Hayashi, M., Shimasaku, K., Motohara, K., Yoshida, M., Okamura, S., & Kashikawa, N. 2007, ApJ, 660, 72
- Hayashi, M., et al. 2008, ApJ, in press, (arXiv:0809.5100)
- Hayes, M., Schaerer, D., & Östlin, G. 2010, A&A, 509, L5
- Hernquist, L., & Springel, V. 2003, MNRAS, 341, 1253
- Hicks, E. K. S., Malkan, M. A., Teplitz, H. I., McCarthy, P. J., & Yan, L. 2002, ApJ, 581, 205
- Hildebrandt, H., et al. 2007, A&A, 462, 865
- Hippelein, H., et al. 2003, A&A, 402, 65
- Hogg, D. W., Cohen, J. G., Blandford, R., & Pahre, M. A. 1998, ApJ, 504, 622
- Hopkins, A. M., Connolly, A. J., & Szalay, A. S. 2000, AJ, 120, 2843
- Hopkins, A. M., Connolly, A. J., Haarsma, D. B., & Cram, L. E. 2001, AJ, 122, 288
- Hopkins, A. M. 2004, ApJ, 615, 209
- Hopkins, A. M., & Beacom, J. F. 2006, ApJ, 651, 142
- Hu, E. M., Cowie, L. L., McMahon, R. G., Capak, P., Iwamuro, F., Kneib, J.-P., Maihara, T., & Motohara, K. 2002, ApJL, 568, L75
- Hu, E. M., Cowie, L. L., Capak, P., McMahon, R. G., Hayashino, T., & Komiyama, Y. 2004, AJ, 127, 563
- Ichikawa, T., et al. 2006, Proc. SPIE, 6269,

- Ilbert, O., et al. 2009, ApJ, 690, 1236
- Iwamuro, F., et al. 2000, PASJ, 52, 73
- Iwata, I., Ohta, K., Tamura, N., Akiyama, M., Aoki, K., Ando, M., Kiuchi, G., & Sawicki, M. 2007, MNRAS, 376, 1557
- Iye, M., et al. 2004, PASJ, 56, 381
- Jansen, R. A., Fabricant, D., Franx, M., & Caldwell, N. 2000, ApJS, 126, 331
- Jansen, R. A., Franx, M., & Fabricant, D. 2001, ApJ, 551, 825
- Jones, D. H., & Bland-Hawthorn, J. 2001, ApJ, 550, 593
- Kaifu, N. 1998, Proc. SPIE, 3352, 14
- Kashikawa, N., et al. 2002, PASJ, 54, 819
- Kashikawa, N., et al. 2004, PASJ, 56, 1011
- Kashikawa, N., et al. 2006, ApJ, 648, 7
- Kennicutt, R. C. 1983, ApJ, 272, 54
- Kennicutt, R. C. 1992, ApJ, 388, 310
- Kennicutt, R. C. 1998, ARAA, 36, 189
- Kereš, D., Katz, N., Weinberg, D. H., & Davé, R. 2005, MNRAS, 363, 2
- Kewley, L. J., Geller, M. J., & Jansen, R. A. 2004, AJ, 127, 2002
- Kobulnicky, H. A., Kennicutt, R. C., & Pizagno, J. L. 1999, ApJ, 514, 544
- Kodaira, K., et al. 2003, PASJ, 55, L17

- Kodama, T., Balogh, M. L., Smail, I., Bower, R. G., & Nakata, F. 2004, MNRAS, 354, 1103
- Komatsu, E., et al. 2010, arXiv:1001.4538
- Kriek, M., van Dokkum, P. G., Labb  , I., Franx, M., Illingworth, G. D., Marchesini, D., & Quadri, R. F. 2009, ApJ, 700, 221
- Kurtz, M. J., & Mink, D. J. 1998, PASP, 110, 934
- Landolt, A. U. 1992, AJ, 104, 340
- Lane, K. P., et al. 2007, MNRAS, 379, L25
- Lee, J. C., Kennicutt, R. C., Funes, S. J., Jos   G., Sakai, S., & Akiyama, S. 2007, ApJL, 671, L113
- Lee, J. C., et al. 2009, ApJ, 706, 599
- Lee, J. C., Ly, C., et al. 2010, in preparation
- Lilly, S. J., Le Fevre, O., Hammer, F., & Crampton, D. 1996, ApJL, 460, L1
- Lilly, S. J., et al. 2007, ApJS, 172, 70
- Ly, C., et al. 2007, ApJ, 657, 738
- Ly, C., et al. 2009, ApJ, 697, 1410
- Madau, P. 1995, ApJ, 441, 18
- Madau, P., Ferguson, H. C., Dickinson, M. E., Giavalisco, M., Steidel, C. C., & Fruchter, A. 1996, MNRAS, 283, 1388
- Madau, P., Pozzetti, L., & Dickinson, M. 1998, ApJ, 498, 106

- Malkan, M., Teplitz, H., & McLean, I. 1995, ApJL, 448, L5
- Malkan, M. A., Teplitz, H., & McLean, I. S. 1996, ApJL, 468, L9
- Maraston, C. 2005, MNRAS, 362, 799
- Martin, D. C., et al. 2005, ApJL, 619, L1
- Mas-Hesse, J. M., Kunth, D., Tenorio-Tagle, G., Leitherer, C., Terlevich, R. J., & Terlevich, E. 2003, ApJ, 598, 858
- Massarotti, M., Iovino, A., & Buzzoni, A. 2001, ApJL, 559, L105
- McCarthy, P. J., et al. 1999, ApJ, 520, 548
- McCracken, H. J., et al. 2010, ApJ, 708, 202
- Meisenheimer, K., & Wolf, C. 2002, Astronomy and Geophysics, 43, 15
- de Mello, D. F., Wadadekar, Y., Dahlen, T., Casertano, S., & Gardner, J. P. 2006, AJ, 131, 216
- Miyazaki, S., et al. 2002, PASJ, 54, 833
- Momcheva, I., et al. 2010, in preparation
- Moorwood, A. F. M., van der Werf, P. P., Cuby, J. G., & Oliva, E. 2000, A&A, 362, 9
- Morioka, T., Nakajima, A., Taniguchi, Y., Shioya, Y., Murayama, T., & Sasaki, S. S. 2008, PASJ, 60, 1219
- Morrissey, P., et al. 2007, ApJS, 173, 682
- Moustakas, J., & Kennicutt, R. C., Jr. 2006, ApJS, 164, 81

- Muller, G. P., Reed, R., Armandroff, T., Boroson, T. A., & Jacoby, G. H. 1998,
Proc. SPIE, 3355, 577
- Nagamine, K., Ostriker, J. P., Fukugita, M., & Cen, R. 2006, ApJ, 653, 881
- Nagao, T., et al. 2008, ApJ, 680, 100
- Nakamura, O., Fukugita, M., Brinkmann, J., & Schneider, D. P. 2004, AJ, 127,
2511
- O'Donnell, J. E. 1994, ApJ, 437, 262
- Oke, J. B. 1974, ApJS, 27, 21
- Oke, J. B., & Gunn, J. E. 1983, ApJ, 266, 713
- Oke, J. B. 1990, AJ, 99, 1621
- Oke, J. B., et al. 1995, PASP, 107, 375
- Osterbrock, D. E. 1989, Astrophysics of Gaseous Nebulae and Active Galactic
Nuclei (Mill Valley, CA: University Science Books)
- Ouchi, M., et al. 2003, ApJ, 582, 60
- Paltani, S., et al. 2007, A&A, 463, 873
- Pascual, S., Villar, V., Gallego, J., Zamorano, J., Pelló, R., Díaz, C., & Aragón-
Salamanca, A. 2005, Revista Mexicana de Astronomía y Astrofísica Conference
Series, 24, 268
- Pérez-González, P. G., Zamorano, J., Gallego, J., Aragón-Salamanca, A., & Gil
de Paz, A. 2003, ApJ, 591, 827
- Persson, S. E., et al. 2008, Proc. SPIE, 7014,

- Pettini, M., Steidel, C. C., Adelberger, K. L., Dickinson, M., & Giavalisco, M. 2000, ApJ, 528, 96
- Probst, R. G., et al. 2004, Proc. SPIE, 5492, 1716
- Probst, R. G., George, J. R., Daly, P. N., Don, K., & Ellis, M. 2008, Proc. SPIE, 7014,
- Quadri, R., et al. 2007, AJ, 134, 1103
- Reddy, N. A., Erb, D. K., Steidel, C. C., Shapley, A. E., Adelberger, K. L., & Pettini, M. 2005,
- Reddy, N. A., Steidel, C. C., Pettini, M., Adelberger, K. L., Shapley, A. E., Erb, D. K., & Dickinson, M. 2008, ApJS, 175, 48
- Richmond, M. 2005, PASJ, 57, 969
- Robin, A. C., Reylé, C., Derrière, S., & Picaud, S. 2003, A&A, 409, 523
- Robinson, J., & Silk, J. 2000, ApJ, 539, 89
- Rodriguez-Eugenio, N., Noeske, K. G., Acosta-Pulido, J., Barrena, R., Prada, F., Manchado, A., & EGS Teams 2006, in press (astro-ph/0604027)
- Saito, T., Shimasaku, K., Okamura, S., Ouchi, M., Akiyama, M., & Yoshida, M. 2006, ApJ, 648, 54
- Salpeter, E. E. 1955, ApJ, 121, 161
- Savaglio, S., et al. 2004, ApJ, 602, 51
- Sawicki, M., & Thompson, D. 2006a, ApJ, 642, 653
- Sawicki, M., & Thompson, D. 2006b, ApJ, 648, 299

- Schechter, P. 1976, ApJ, 203, 297
- Schlegel, D. J., Finkbeiner, D. P., & Davis, M. 1998, ApJ, 500, 525
- Scoville, N., et al. 2007, ApJS, 172, 1
- Shapley, A. E., Steidel, C. C., Pettini, M., & Adelberger, K. L. 2003, ApJ, 588, 65
- Shapley, A. E., Steidel, C. C., Pettini, M., Adelberger, K. L., & Erb, D. K. 2006, ApJ, 651, 688
- Shim, H., Im, M., Choi, P., Yan, L., & Storrie-Lombardi, L. 2007, ApJ, 669, 749
- Shim, H., Colbert, J., Teplitz, H., Henry, A., Malkan, M., McCarthy, P., & Yan, L. 2009, ApJ, 696, 785
- Shimasaku, K., et al. 2003, ApJL, 586, L111
- Shimasaku, K., et al. 2004, ApJL, 605, L93
- Shimasaku, K., Ouchi, M., Furusawa, H., Yoshida, M., Kashikawa, N., & Okamura, S. 2005, PASJ, 57, 447
- Shimasaku, K., et al. 2006, PASJ, 58, 313
- Shioya, Y., et al. 2008, ApJS, 175, 128
- Skrutskie, M. F., et al. 2006, AJ, 131, 1163
- Sobral, D., et al. 2009, MNRAS, 398, 75
- Somerville, R. S., Lee, K., Ferguson, H. C., Gardner, J. P., Moustakas, L. A., & Giavalisco, M. 2004, ApJL, 600, L171

- Somerville, R. S., Hopkins, P. F., Cox, T. J., Robertson, B. E., & Hernquist, L. 2008, MNRAS, 391, 481
- Spergel, D. N., et al. 2003, ApJS, 148, 175
- Spergel, D. N., et al. 2006, submitted (astro-ph/0603449)
- Springel, V., et al. 2005, Nature, 435, 629
- Steidel, C. C., Giavalisco, M., Pettini, M., Dickinson, M., & Adelberger, K. L. 1996, ApJL, 462, L17
- Steidel, C. C., Adelberger, K. L., Giavalisco, M., Dickinson, M., & Pettini, M. 1999, ApJ, 519, 1
- Steidel, C. C., Adelberger, K. L., Shapley, A. E., Pettini, M., Dickinson, M., & Giavalisco, M. 2000, ApJ, 532, 170
- Steidel, C. C., Adelberger, K. L., Shapley, A. E., Pettini, M., Dickinson, M., & Giavalisco, M. 2003, ApJ, 592, 728
- Steidel, C. C., Shapley, A. E., Pettini, M., Adelberger, K. L., Erb, D. K., Reddy, N. A., & Hunt, M. P. 2004, ApJ, 604, 534
- Sullivan, M., Treyer, M. A., Ellis, R. S., Bridges, T. J., Milliard, B., & Donas, J. 2000, MNRAS, 312, 442
- Szalay, A. S., Connolly, A. J., & Szokoly, G. P. 1999, AJ, 117, 68
- Taniguchi, Y., et al. 2003, ApJL, 585, L97
- Taniguchi, Y., et al. 2005, PASJ, 57, 165
- Tapken, C., Appenzeller, I., Mehlert, D., Noll, S., & Richling, S. 2004, A&A, 416, L1

- Tapken, C., Appenzeller, I., Noll, S., Richling, S., Heidt, J., Meinköhn, E., & Mehlert, D. 2007, A&A, 467, 63
- Teplitz, H. I., et al. 2000, ApJ, 542, 18
- Teplitz, H. I., Collins, N. R., Gardner, J. P., Hill, R. S., & Rhodes, J. 2003, ApJ, 589, 704
- Tresse, L., & Maddox, S. J. 1998, ApJ, 495, 691
- Tresse, L., Maddox, S. J., Le Fèvre, O., & Cuby, J.-G. 2002, MNRAS, 337, 369
- Treyer, M. A., Ellis, R. S., Milliard, B., Donas, J., & Bridges, T. J. 1998, MNRAS, 300, 303
- Treyer, M., et al. 2005, ApJL, 619, L19
- Trump, J. R., et al. 2007, ApJS, 172, 383
- Umeda, K., et al. 2004, ApJ, 601, 805
- Verhamme, A., Schaerer, D., Atek, H., & Tapken, C. 2008, A&A, in press
(arXiv:0805.3601)
- van Dokkum, P. G., et al. 2004, ApJ, 611, 703
- van Dokkum, P. G. 2008, ApJ, 674, 29
- van Dokkum, P. G., et al. 2009, PASP, 121, 2
- van der Werf, P. P., Moorwood, A. F. M., & Bremer, M. N. 2000, A&A, 362, 509
- Villar, V., Gallego, J., Pérez-González, P. G., Pascual, S., Noeske, K., Koo, D. C., Barro, G., & Zamorano, J. 2008, ApJ, 677, 169

- Wadadekar, Y., Casertano, S., & de Mello, D. 2006, AJ, 132, 1023
- Westra, E., & Jones, D. H. 2008, MNRAS, 383, 339
- Westra, E., Geller, M. J., Kurtz, M. J., Fabricant, D. G., & Dell'Antonio, I. 2010, ApJ, 708, 534
- Wilson, G., Cowie, L. L., Barger, A. J., & Burke, D. J. 2002, AJ, 124, 1258
- Wyder, T. K., et al. 2005, ApJL, 619, L15
- Yan, L., McCarthy, P. J., Freudling, W., Teplitz, H. I., Malumuth, E. M., Weymann, R. J., & Malkan, M. A. 1999, ApJL, 519, L47
- Yip, C. W., et al. 2004, AJ, 128, 585
- Yoshida, M., et al. 2006, ApJ, 653, 988
- Zhu, G., Moustakas, J., & Blanton, M. R. 2009, ApJ, 701, 86